HELLENIC REPUBLIC
National and Kapodistrian University of Athens
EST. 1837
School of Science
Faculty of Geology and Geoenvironment

Mineralogical, petrographic and geochemical study of hydrothermal alteration zones and related porphyry-epithermal mineralization at Sapes-Kirki area, NE Greece.

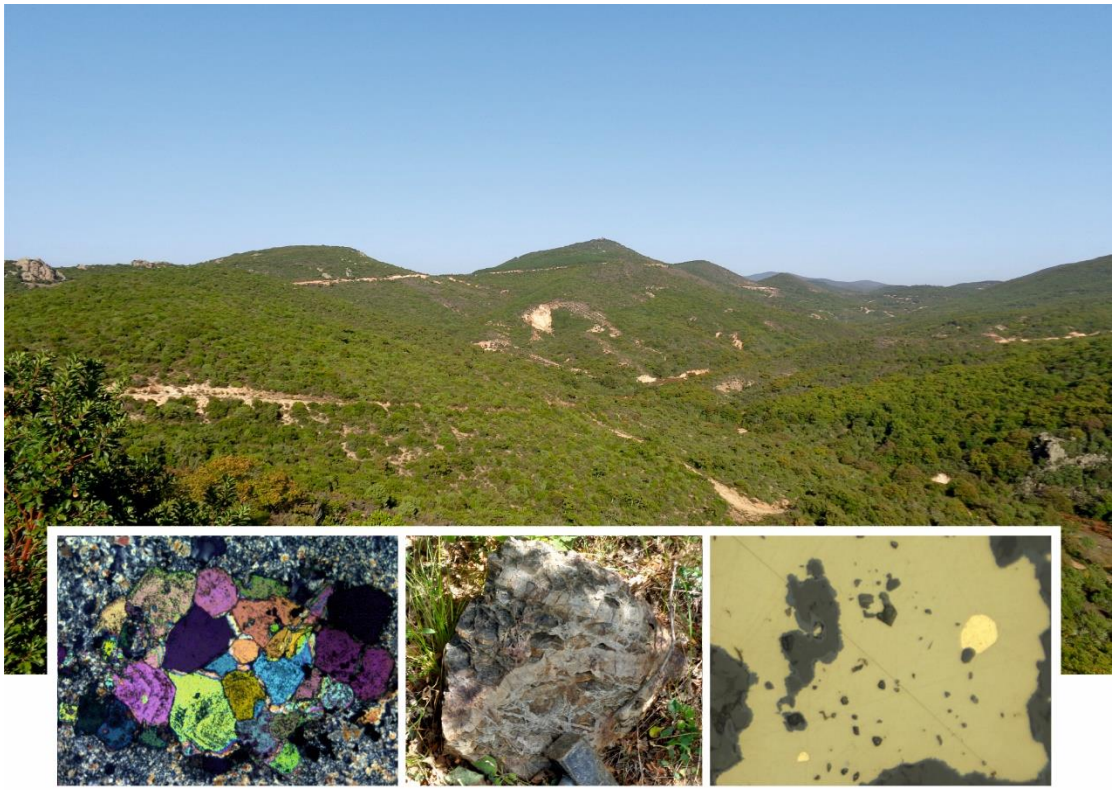

A Dissertation Submitted for Award of the Degree of
Doctor of Philosophy

by

Constantinos G. Mavrogonatos

“The approval of this Dissertation by the Faculty of Geology and Geoenvironment, School of Science, National and Kapodistrian University of Athens, does not imply the acceptance of the author's views (Act 5343/1932, Article 202, § 2)”

- **Advisory committee:**

Supervisor:

Dr Panagiotis Voudouris, Professor
Faculty of Geology and Geoenvironment, University of Athens, Greece

Members:

Dr Paul G. Spry, Professor
Department of Geological and Atmospheric Sciences, Iowa State University, USA

Dr Vasilios Melfos, Associate Professor
Faculty of Geology, Aristotle University of Thessaloniki, Greece

- **Examination committee:**

Dr Panagiotis Voudouris, Professor
Faculty of Geology and Geoenvironment, University of Athens, Greece

Dr Paul G. Spry, Professor
Department of Geological and Atmospheric Sciences, Iowa State University, USA

Dr Vasilios Melfos, Associate Professor
Faculty of Geology, Aristotle University of Thessaloniki, Greece

Dr Federica Zaccarini, Senior Scientist
Department of Applied Geosciences and Geophysics, University of Leoben, Austria

Dr Andreas Magganas, Professor
Faculty of Geology and Geoenvironment, University of Athens, Greece

Dr Konstantinos Kyriakopoulos, Professor
Faculty of Geology and Geoenvironment, University of Athens, Greece

Dr Christina Stouraiti, Assistant Professor
Faculty of Geology and Geoenvironment, University of Athens, Greece

ATHENS 2020

I. Table of contents

II. Acknowledgments

It has been a long time since I first started to admire the world of minerals, when I bought for the first time an amethyst specimen, during my visit to a museum. Ever since, my only dream was to become a geologist. With this dissertation, my ambition is fullfilled! So, at this point, I must express my gratitude to all the people who helped me and made my deams come true.

A few years ago, when I applied for a PhD degree, I knew that it was going to be a long, difficult journey. Fortunately, I was lucky to meet wonderful people during this demanding period, and to make a network of excellent collaborators, who were always eager to provide me with useful advice, every time my brain was unable to think even about the easiest things on Earth.

I am indebted to my supervisors, Profs. Panagiotis Voudouris, Paul G. Spry and Vasilios Melfos, for their enlightening guidance throughout my PhD studies. Above all, I thank them for their patience, and for being always available to help me at any matter.

Among them, my supervisor Dr Panagiotis Voudouris, was one of the first persons to meet and collaborate with, since my undergraduate years. Everything that I have achieved until now, is a result of his teaching. I had the really big luck to take part in many of his field trips, from the very early years of my studies, fact that made my love for Geology to grow bigger constantly. I would like to sincerely thank him for giving me so much, both as a teacher and as a friend.

A large part of analytical work was conducted at the laboratories of the Department of Geology and Geoenvironment, National and Kapodistrian University of Athens. Further, demanding analytical methods, that were a necessity for the completion of my PhD work, were conducted at the laboratories of the Institute of Mineralogy, Westfalisches-Wilhelms Universität Münster (Germany) and the Department of Applied Geosciences and Geophysics, Montanuniversität Leoben (Austria). I must sincerely thank Prof. Stephan Klemme and Dr Jasper Berndt-Gerdes from the Institute of Mineralogy, Westfälische Wilhelms-Universität Münster, who generously provided to me full access to their laboratories. Their kind help and

support is highly appreciated. Both of them did their best to make me feel comfortable whenever I visited Münster, and helped me a lot while I was using their analytical facilities; They honor me with their friendship and collaboration. For the same reason, I must also thank Dr. Federica Zaccarini, from the Department of Applied Geosciences and Geophysics, Montanuniversität Leoben, who was really helpful and gave me access to the "Eugen F. Stumpfl" analytical laboratory. She organized perfectly all the details of my visit at Leoben, and allowed me a full access to the EPMA facility.

Professors Andreas Magganas, Constantinos Kyriakopoulos and Ass. Professor Christina Stouraiti, from the Department of Geology and Geoenvironment, National and Kapodistrian University of Athens, are kindly thanked for accepting the invitation to become members of my examination committee. Ass. Prof. Marianna Kati is also thanked, for being always eager to offer her advice whenever I was seeking for support. I must also thank Assoc. Professor Ioannis Baziotis, from the Agricultural University of Athens, whom I met during my PhD studies. He helped me really much in many aspects. Dr Christos Papatrechas and Dr Georgios Economou from the Hellenic Survey of Geology and Mineral Exploration, are also thanked for providing access to their labs and for their kind advice. I express my gratitude to Dr Konstantinos Soukis, who provided valuable advice on various matters regarding the tectonic regime in my study area.

Life is always tasteless without friends! In my case, while being a PhD candidate, the fact that I shared my thoughts and made endless conversations about geology (and many more!) with friends and colleagues, made my effort to finish my PhD to be much easier. I would like to thank my good friends Ifigeneia Megremi, Stathis Vorris, Christos Kanellopoulos, Elena Moustaka, Marianthi Anstasatou, Aggelos Galanopoulos, Petros Chatzimpaloglou, Stamatios Xydous, Argyrios Periferakis and Aggeliki Papoutsa for their support during my studies. I would also like to thank my friend Stamatios Flemetakis, for providing me hospitality, during my stay in Münster, and for providing useful advice in various matters.

I feel honored that I was granted a full scholarship for my PhD studies by the Onassis Foundation. Without this financial support, I would have not been able to finish my studies, and I would sincerely like to thank the Onassis Foundation for giving

me the chance to do so. I must also thank the Eldorado Gold Corporation, for providing me financial support during my field campaigns and for covering the costs for a large part of the geochemical analyses of the present work. They were conducted under a very fruitful collaboration, under the guidance of Dr Tim Baker, to whom I am grateful. Dr Georgios Falalakis is finally thanked, for being so helpful every time I was staying in Alexandroupolis.

Finally, yet importantly, my most sincere thanks go to my parents, Grigorios Mavrogonatos and Eirini Petraki for their love, faith and support, during this whole "journey". I dedicate my PhD thesis to both of them, as an express of my gratitude.

III. Εκτεταμένη περίληψη (Extended abstract in Greek)

Στην περιοχή μεταξύ Σαπών και Κίρκης (Θράκη), έγινε λεπτομερής εργασία υπαίθρου και χαρτογράφηση, γύρω από τα πορφυρικά/επιθερμικά μεταλλοφόρα κέντρα των Σαπών (Κώνος) και της Κίρκης (Παγώνη Ράχη). Πέραν των ήδη γνωστών αυτών ζωνών μεταλλοφορίας, ανακαλύφθηκαν νέες θέσεις με αντίστοιχου τύπου μεταλλοφορίες (π.χ. Παπαδοκορυφή).

Η περιοχή μελέτης καλύπεται από ηφαιστειοκλαστικούς σχηματισμούς, που έχουν αποτεθεί σε τεκτονικές λεκάνες διεύθυνσης Α-Δ, οι οποίες οφείλουν την δημιουργία τους σε εφελκυστκή τεκτονική, και πιο συγκεκριμένα σε έκταση λόγω οπισθοχώρησης (slab roll-back) της υποβυθιζόμενης λιθόσφαιρας του ωεκανού της Ανατολικής Μεσογείου κάτω από το Ευρασιατικό περιθώριο, ήδη από το Ηώκαινο. Βορειότερα της περιοχής μελέτης, εμφανίζονται τα μεταμορφωμένα πετρώματα της Ροδοπικής μάζας, ενώ προς Νότο, υπάρχουν εμφανίσεις πετρωμάτων που ανήκουν στην Περιροδοπική ζώνη (π.χ. ενότητα Μάκρης κλπ.). Οι μεταλοφορίες που ερευνήθηκαν, φιλοξενούνται σε διεισδύσεις Ολιγοκαινικής ηλικίας, ενδιάμεσης έως όξινης σύστασης και υψηλού Καλίου ασβεσταλκαλικό γεωχημικό τύπο.

Τρία διαφορετικά μαγματικά σώματα ανπτύσσονται στην περιοχή μελέτης. Ο γρανοδιοριτικός πορφύρης αποτελείται από φαινοκρυστάλλους βιοτίτη, αμφιβόλων/κεροστίλβης, πυροξένου/αυγίτη, τιτανίτη και σπανιότερα χαλαζία με την μορφή αποστρογγυλωμένων κόκκων (resorbed quartz/quartz eyes), που φιλοξενούνται σε μία λεπτόκοκκη κύρια μάζα αστρίων και χαλαζία. Το σώμα αυτό φαίνεται να είναι η παλαιότερη διείσδυση στην περιοχή, ενώ σχεδόν πάντα συναντάται έχοντας υποστεί ισχυρή επίδραση από υδροθερμικές εξαλοιώσεις και φιλοξενεί τις μελετηθείσες μεταλλοφορίες. Ακολουθεί ο χαλαζιακός μονζοδιορίτης, ο οποίος έχει μεγάλη ανάπτυξη στο βόρειο τμήμα της περιοχής μελέτης, χωρίς όμως να φιλοξενεί κάποια μεταλλοφορία. Πρόκειται για ένα λεπτόκοκκο πέτρωμα, κατά βάση ισοκοκκώδες, αποτελούμενο από διάφορες αναλογίες αμφιβόλων, πυροξένων, βιοτίτη και αστρίων. Στην περιοχή μελέτης ανευρίσκεται είτε χωρίς να έχει υποστεί εξαλλοίωση, είτε με προπυλιτικού τύπου εξαλλοίωση, ή ακόμα και σερικιτίωση, ειδικά κατά μήκος ζωνών ρηγμάτων. Τέλος, στην περιοχή συναντώνται διάσπαρτα ρυολιθικά (μικρογρανιτικός πορφύρης) σώματα, κατά κανόνα μικρών διαστάσεων (μερικές δεκάδες τετραγωνικά μέτρα). Τα σώματα αυτά δείχνουν έναν προτιμητέο

προσανατολισμό Β0-20°Δ, ενώ όπως στην περιοχή Παγώνης Ράχης, αναπτύσσονται και σε διεύθυνση Α-Δ. Συνήθως έχουν υποστεί ισχυρή σερικιτική εξαλλοίωση. Γεωχημικές αναλύσεις των πιο πάνω μαγματιτών (αφορά κυρίως στα δύο πρώτα σώματα και στις λιγότερο εξαλλοιωμένες εμφανίσεις τους), έδειξαν ότι πρόκειται για πετρώματα της ασβεσταλκαλικής σειράς, με ένα χαρακτηριστικό μετα-συγκρουσιακό (post-collisional) χαρακτήρα.

Η πορφυρικού τύπου μεταλλοφορία της περιοχής Κώνου, εμφανίζεται σε τεκτονικά ελεγχόμενη ζώνη διεύθυνσης Β10°Δ και αναπτύσσεται με την μορφή πλέγματος χαλαζιακών φλεβιδίων (stockwork), αλλά και διασπορών. Στα βαθύτερα τμήματα του συστήματος, εντοπίστηκαν υπολείμματα ζώνης νατριούχου μετασωμάτωσης, με την κυρίαρχη παρουσία αλβίτη και λιγότερο χλωρίτη, με σημαντική όμως επικάλυψη από σερικιτίωση, η οποία είναι και η πιο διαδεδομένη ζώνη εξαλλοίωσης στην περιοχή.

Κατά θέσεις, οι χαλαζιακές φλέβες (που είναι κυρίως Α-τύπου) εμφανίζουν ζωνώδη δομή (banded veins), με χαρακτηριστικές επάλληλες αναπτύξεις λευκού και σκουρόχρωμου χαλαζία. Φιλοξενούν σιδηροπυρίτη, χαλκοπυρίτη, πλούσιο σε ρήνιο μολυβδαινίτη, ρηνιίτη, καθώς και μικρές ποσότητες εναργίτη, μαγνητίτη, κολουζίτη, σφαλερίτη, γαληνίτη και τετραεδρίτη/τενναντίτη. Πολλές από τις φλέβες αυτές, φέρουν μία κεντρική ζώνη σιδηροπυρίτη, ο οποίος αποτέθηκε σε μεταγενέστερο επεισόδιο (D-event), με το οποίο σχετίζεται και η ζώνη σερικιτίωσης στην περιοχή. Σπάνια, φλεβίδια γύψου με μεταλλοφορία γαληνίτη, σφαλερίτη, σιδηροπυρίτη και τετραεδρίτη/τενναντίτη εντοπίζονται στην περιοχή.

Η πορφυρικού τύπου μεταλλοφορία χαρακτηρίζεται από ανωμαλίες σε μολυβδαίνιο και ρήνιο, και επικαλύπτεται από σύστημα επιθερμικού τύπου υψηλής θείωσης (lithocap) με κύριο χαρακτηριστικό τις ζώνες πυριτίωσης και την διαδεδομένη παρουσία ορυκτών της υπερ-ομάδας του αλουνίτη, καολινίτη, δικίτη, διάσπορου, πυροφυλλίτη, καθώς και του σπάνιου ορυκτού ζουνιίτη.

Η περιοχή της Παπαδοκορυφής έδωσε ενθαρρυντικά αποτελέσματα για την πιθανή ύπαρξη νέου πορφυρικού κέντρου. Εκεί αναπτύσσεται ζώνη καλιούχου μετασωμάτωσης (με κύριο ορυκτό τον δευτερογενή βιοτίτη), που συνοδεύει πλέγμα φλεβιδίων χαλαζία και μαγνητίτη. Τα φλεβίδια, αν και εμφανίζουν περιορισμένη επιφανειακή ανάπτυξη, φιλοξενούν μεταλλοφορία χαλκοπυρίτη, βορνίτη,

σιδηροπυρίτη και μολυβδαινίτη, ενώ γεωχημικές αναλύσεις έδωσαν σημαντικές ανωμαλίες μολυβδαίνιου.

Η μεταλλοφορία πορφυρικού τύπου της Παγώνης Ράχης, αναπτύσσεται με εντυπωσική μορφή πυκνού πλέγματος χαλαζιακών φλεβιδίων. Συνοδεύεται από νατριούχο και/ή καλιούχο (και λιγότερο ασβεστούχο) μετασωμάτωση, με χαρακτηριστικά δευτερογενή ορυκτά τον Κ-άστριο, αλβίτη, βιοτίτη, αμφίβολο, επίδοτο, χλωρίτη, τιτανίτη και ασβεστίτη. Στα υψηλότερα τοπογραφικά σημεία, επικρατεί έντονη σερικιτίωση. Τα κύρια μεταλλικά ορυκτά είναι σιδηροπυρίτης, χαλκοπυρίτης, βορνίτης, μολυβδαινίτης (πλούσιος σε ρήνιο), ρηνιίτης, χρυσός, κλπ.

Τουλάχιστον 4 τύποι πορφυρικών φλεβών/φλεβιδίων διακρίθηκαν: πρώιμα φλεβίδια μαγνητίτη (Μ-τύπου) αλλά και ζωνώδεις (banded), κυματοειδείς χαλαζιακές φλέβες (Α-τύπου), σχετιζόμενα με νατριούχο/καλιούχο εξαλλοίωση, ευθύγραμμες, Β-τύπου χαλαζιακές φλέβες, συνοδευόμενες από νατριούχο/καλιούχο εξαλλοίωση, D-τύπου φλέβες σιδηροπυρίτη (+χαλκοπυρίτη+μολυβδαινίτη), που επικαλύπτουν προηγούμενους τύπους φλεβιδίων και σχετίζονται με ισχυρή σερικιτική εξαλλοίωση (σερικίτης, ασβεστίτης).

Το πορφυρικό σύστημα επικαλύπτεται κατά θέσεις από επιθερμικού τύπου μεταλλοφόρες φλέβες και ρήγματα, που αποτελούνται από χαλαζία και ασβεστίτη, και σχετίζονται με αργιλική εξαλλοίωση (σερικίτης, χαλαζίας, ασβεστίτης). Οι επιθερμικές αυτές φλέβες (Ε-τύπου) φιλοξενούν γαληνίτη, σφαλερίτη, σιδηροπυρίτη, κράμα αργύρου-χρυσού (Ag-Au alloy), τετραεδρίτη/τεναντίτη (πλούσιες σε Zn ποικιλίες).

Περιφερειακά των πορφυρικών συστημάτων, αναπτύσσονται ζώνες προπυλιτικής εξαλλοίωσης, με κυμαινόμενα ποσοστά πλαγιοκλάστου, επιδότου, αμφιβόλων, χλωρίτη και ασβεστίτη, που αναπτύσσονται κατά κύριο λόγο εις βάρος πρωτογενών μαφικών ορυκτών και αστρίων.

Ορυκτοχημικές αναλύσεις πρωτογενούς και υδροθερμικού βιοτίτη (τόσο από την Παγώνη Ράχη, όσο και από την περιοχή Παπαδοκορυφής αλλά και Κασσιτερών-Σαπών, για λόγους σύγκρισης χημισμού) έδειξαν σημαντικές διαφορές στην ορυκτοχημεία. Οι υδροθερμικοί βιοτίτες είναι πλούσιοι σε μαγνήσιο (φλογοπίτες), εμφανίζουν κυμαινόμενη συμμετοχή τιτανίου, υψηλές περιεκτικότητες σε αλογόνα (έως 5.21% φθόριο και 0.36% χλώριο), σε αντίθεση με τους μαγματικούς, οι οποίοι

είναι τυπικοί (σιδηροπλούσιοι) βιοτίτες. Αναλύσεις LA-ICP-MS που γίνονται για πρώτη φορά σε δείγματα υδροθερμικών βιοτιτών από πορφυρικό σύστημα του Ελλαδικού χώρου, έδειξαν ότι αυτοί εμφανίζονται εμπλουτισμένοι σε συγκεκριμένα ιχνοστοιχεία (π.χ. Cs, La, Th κλπ.). Χαρακτηρίζονται από σχετικά ομοιογενή κατανομή σπανίων γαιών, αν και τα δείγματα δευτερογενούς βιοτίτη της Παγώνης Ράχης εμφανίζουν τον μεγαλύτερο εμπλουτισμό.

Αξιοσημείωτη είναι και η αύξηση της συμμετοχής φθορίου (έως 0.8 apfu) σε συστάσεις δευτερογενών αμφιβόλων, οι οποίοι ανεξαρτήτως προέλευσης (μαγματική/υδροθερμική) ταξινομούνται πάντα ως ασβεστούχοι. Συγκριτικές αναλύσεις επιδότων από ζώνες προπυλιτικής και καλλιούχου/ασβεστούχου εξαλλοίωσης δεν έδειξαν διαφορές στο χημισμό, με τις αναλυθείσες συστάσεις να εμπίπτουν στο πεδίο του κλινοζωισίτη (αργιλοπλούσιες). Αντίστοιχη ομοιότητα συστάσεων ανακαλύφθηκε και στο χημισμό χλωριτών από τις δύο αυτές ζώνες εξαλλοίωσης, όμως, οι χλωρίτες από την καλλιούχο/ασβεστούχο εξαλλοίωση δείχνουν μία μεγαλύτερη διακύμανση στο περιεχόμενό τους σε σίδηρο.

Αυτοφυής χρυσός δεν ανακαλύφθηκε στην μεταλλοφορία του Κώνου, όμως στην περιοχή της Παγώνης Ράχης, στο σύστημα καταγράφεται μία σημαντική διακύμανση στην περιεκτικότητά του. Πρώιμες Μ-τύπου φλέβες φιλοξενούν ήλεκτρο (μ. ό. 78% at. Au). Στη συνέχεια, το ποσοστό του αργύρου μειώνεται, ώστε σε φλέβες D-τύπου να ανευρίσκεται αυτοφυής χρυσός (μ. ό. 88% at. Au), ενώ τέλος, οι επιθερμικού τύπου φλέβες φιλοξενούν κράμα αργύρου/χρυσού (μ. ό. 30% at. Au) καταγράφοντας μία σημαντική μείωση του περιεχόμενου χρυσού στην μεταλλοφορία. Η πορεία αυτή αντικατοπτρίζεται πολύ καλά και σε γεωχημικές αναλύσεις μεταλλεύματος.

Και στα δύο πορφυρικά συστήματα, εντοπίστηκε το σπάνιο θειούχο ορυκτό ρηνιίτης, ενώ ο μολυβδαινίτης εμφανίζεται εξαιρετικά εμπλουτισμένος σε ρήνιο (μέχρι 2.20 και 3.15 wt% Re, σε Κώνο και Παγώνη Ράχη αντίστοιχα). Στην Παγώνη Ράχη, η περιεκτικότητα ρηνίου στο σύτημα ακολουθεί αυτή του χρυσού, με σημαντικό εμπλουτισμό του μετάλλου στις D-τύπου φλέβες, έναντι των υπολοίπων τύπων φλεβών. Ο χαλκοπυρίτης, εμφανίζεται σχεδόν πάντα καθαρός από προσμίξεις, με στοιχειακές αναλογίες πολύ κοντά στις ιδανικές.

Εναργίτης, σφαλερίτης, γαληνίτης, κολουζίτης και ορυκτά μέλη της ομάδας του τετραεδρίτη/τενναντίτη, ανευρίσκονται είτε εντός επιθερμικού τύπου φλέβών

χαλαζία/ασβεστίτη (Ε-τύπου), είτε διάσπαρτα, επικαλύπτοντας συνήθως πορφυρικού τύπου μεταλλοφορία. Συστάσεις κολουζίτη που αναλύθηκαν στην παρούσα εργασία έδειξαν σημαντική συμμετοχή Sn στη δομή του ορυκτού, ενώ τετραεδρίτες και τενναντίτες εμφανίζονται πάντα ως ποικιλίες πλούσιες σε ψευδάργυρο (έως 2 apfu).

Γεωχημικές αναλύσεις μεταλλευμάτων έδειξαν εμπλουτισμό των πορφυρικού τύπου μεταλλοφοριών σε μία πληθώρα κρίσιμων και πολύτιμων στοιχείων όπως Au, Ag, Bi, Te, Se, Mo, Re, In, Sn και V. Ξεχωρίζουν οι συσχετίσεις μεταξύ Mo-Re και Au-Se.

Η περιεκτικότητα του πορφυρικού συστήματος Κώνου σε χρυσό εμφανίζεται πολύ χαμηλή (έως 0.12 g/t), ενώ η μέση περιεκτικότητα χρυσού της Παγώνης Ράχης αγγίζει τα 0.36 g/t, με έναν εξαιρετικό εμπλουτισμό χρυσού στις D-τύπου φλέβες (έως 6.3 g/t Au).

Σε αντίθεση με τις πορφυρικού τύπου μεταλλοφορίες, οι επιθερμικού τύπου φλέβες από το σύνολο της περιοχής μελέτης εμφανίζουν εμπλουτισμό σε Ag, Ga, In, Sn, Te, Bi, Se και V.

Στην προσπάθεια να διαπιστωθούν χωρικοί/γενετικοί συσχετισμοί μεταλλοφόρων ζωνών και διαφόρων τύπων εξαλλοιώσεων, που θα μπορούσαν να χρησιμοποιηθούν ως δείκτες, ένα τμήμα της παρούσας διατριβής αφιερώθηκε στην χαρτογράφηση και περιγραφή της ζώνης προχωρημένης εξαλλοίωσης που εμφανίζεται στα ανατολικά κράσπεδα της περιοχής μελέτης. Το πορφυρικό σύστημα του Κώνου, εμφανίζει μία σημαντική επικάλυψη (telescoping) από ζώνη προχωρημένης αργιλικής εξαλλοίωσης. Η ζώνη αυτή τοποθετείται στα υψηλότερα τοπογραφικά επίπεδα της περιοχής Κώνου και σχετίζεται με επιθερμική μεταλλοφορία τύπου υψηλής θείωσης. Ζώνη σκωριώδους πυριτίωσης στο κεντρικό τμήμα της περιοχής, συνοδεύεται από διάφορες παραγενέσεις ορυκτών προχωρημένης αργιλικής εξαλλοίωσης και κατανέμεται σε ζώνες Β-Ν, ΒΒΔ-ΝΝΑ και Α-Δ, οι οποίες και σχετίζονται με ρήγματα αντίστοιχων διευθύνσεων. Οι ζώνες αυτές προς τα κάτω και πλευρικά εξελίσσονται σταδιακά σε εξαλλοίωση πλούσια σε σερικίτη (σερικιτίωση). Η λεπτομερής ορυκτολογική εξέταση ανέδειξε την ύπαρξη του σπάνιου ορυκτού ζουνιίτης (το οποίο ανευρίσκεται για πρώτη φορά σε περιβάλλον πορφυρικού/επιθερμικού συστήματος στον Ελλαδικό χώρο), σε

συνύπαρξη με ορυκτά της ομάδας αλουνίτη (συμπεριλαμβανομένων και αλούμινο-φοσφωρικών-θειικών ορυκτών/APS), καολινίτη, δικίτη, διάσπορο και πυροφυλλίτη.

Ορυκτοχημικές αναλύσεις ζουνιίτη έδειξαν κυμαινόμενα ποσοστά φθορίου και χλωρίου, ενώ τα ορυκτά της ομάδας του αλουνίτη (συμπεριλαμβανομένων και APS) εμφανίζουν μία πολύ μεγάλη διακύμανση στο χημισμό, από K-πλούσια έως και Na-πλούσια μέλη. Από τις αναλύσεις, οι συστάσεις που προέκυψαν ταξινομούνται στις υποομάδες αλουνίτη, μπεουδαντίτη και πλουμπογκουμίτη, με Sr-, Ca-, Ba-, και REE-πλούσια μέλη, όπως για παράδειγμα ο φλορενσίτης-Ce, που περιγράφεται για πρώτη φορά από τον Ελληνικό χώρο.

Η μεταλλοφορία στη ζώνη προχωρημένης αργιλικής εξαλλοίωσης του Κώνου χαρακτηρίζεται από ένα σχετικό εμπλουτισμό σε στοιχεία όπως Se, Mo, και Bi, τα οποία υποδηλώνουν μία μαγματική πηγή προέλευσης, επιβεβαιώνοντας έτσι τη γενετική σχέση με την υποκείμενη πορφυρική μεταλλοφορία. Επίσης, καταδεικνύουν την χρησιμότητα χαρτογράφησης αντίστοιχων ζωνών υδροθερμικής εξαλλοίωσης στην ευρύτερη περιοχή, αφού σηματοδοτούν εγγύτητα σε μαγματικές διεισδύσεις που δύνανται να έχουν αξιόλογο μεταλλευτικό δυναμικό.

Προς την ίδια κατεύθυνση, του εντοπισμού δηλαδή ορυκτοχημικών/γεωχημικών εργαλείων που να εμφανίζουν συστηματική σχέση με ζώνες μεταλλοφορίας υψηλής περιεκτικότητας σε χρυσό και άλλα πολύτιμα/κρίσιμα μέταλλα, ερευνήθηκε λεπτομερώς και ο χημισμός του μαγνητίτη σε επίπεδο ιχνοστοιχείων.

Ο μαγνητίτης αποτελεί κοινό ορυκτό στην περιοχή μελέτης και εμφανίζεται με δύο μορφές: (α) ως επουσιώδες μαγματικό ορυκτό (σε υγιή έως προπυλιτιωμένα πετρώματα), αλλά και ως βασικό ορυκτολογικό συστατικό των πρώιμων σταδίων πορφυρικής μεταλλοφορίας της Παγώνης Ράχης (δεν εντοπίστηκε αντίστοιχο στάδιο στη μεταλλοφορία του Κώνου). Η ευκολία με την οποία ενσωματώνει ιχνοστοιχεία στην σύστασή του, αποτέλεσε τη βάση για ανάλυση μαγματικού και υδροθερμικού μαγνητίτη στο πλαίσιο της παρούσας διατριβής, με τη μέθοδο LA-ICP-MS, για πρώτη φορά σε μεταλλοφορία του Ελληνικού χώρου.

Οι δύο τύποι μαγνητίτη εμφανίζουν σημαντικές ιστολογικές και χημικές διαφορές. Ο πρωτογενής (μαγματικός) μαγνητίτης, συναντάται με την μορφή ευεδρικών κρυστάλλων, σε φρέσκο/ελαφρά προπυλιτιωμένο γρανοδιοριτικό πορφύρη. Αντίθετα, ο υδροθερμικός μαγνητίτης σχηματίζει λεπτομερείς ανεδρικούς

κρυστάλλους, που συναντώνται με τη μορφή διασπορών ή/και φλεβιδίων (Μ-τύπου). Σχετίζεται δε με νατριούχο (αλβίτη)/καλιούχο (ορθόκλαστο, βιοτίτη, χλωρίτη) εξαλλοίωση του γρανοδιοριτικού πορφύρη, ενώ συνυπάρχει με άλλα μεταλλικά ορυκτά όπως χαλκοπυρίτης, σιδηροπυρίτης, μολυβδαινίτης, ήλεκτρο. Οι ορυκτοχημικές αναλύσεις έδειξαν ότι ο υδροθερμικός μαγνητίτης είναι εμπλουτισμένος σε μία σειρά ιχνοστοιχείων όπως V, Pb, W, Mo, Ta, Zn, Cu, Nb, σε αντίθεση με τον πρωτογενή, ο οποίος συνηθέστερα χαρακτηρίζεται από υψηλότερες περιεκτικότητες Ti, Cr, Ni, και Sn. Ειδικά η μείωση τιτανίου στον υδροθερμικό μαγνητίτη, αντικατοπρίζει την μετάβαση από το μαγματικό στο υδροθερμικό περιβάλλον, και αποτελεί ένα ιδιαίτερο χαρακτηριστικό του μαγνητίτη σε πολλούς τύπους μεταλλοφοριών.

Ένα ασυνήθιστο γνώρισμα για πορφυρικού τύπου υδροθερμικό μαγνητίτη είναι ο εμπλουτισμός του σε Mo, Pb και Zn. Η διαπίστωση αυτή αποτελεί ένα ιδιαίτερο γνώρισμα του υδροθερμικού μαγνητίτη από την Παγώνη Ράχη και μπορεί να χρησιμοποιηθεί ως ορυκτοχημικό εργαλείο για την ιχνηλάτηση ζωνών με υψηλό δυναμικό σε μεταλλοφορία στην ευρύτερη περιοχή και όχι μόνο.

Αντίστοιχη εφαρμογή επικεντρώθηκε και σε ένα άλλο πολύ διαδεδομένο ορυκτό, αυτή τη φορά και στα δύο συστήματα. Ο σιδηροπυρίτης είναι παρών σε όλα τα στάδια μεταλλοφορίας. Ανάλογα με το στάδιο με το οποίο συνδέεται, ο σιδηροπυρίτης εμφανίζει σημαντικές μορφολογικές και χημικές διαφοροποιήσεις.

Μορφολογικά, στα στάδια μεταλλοφορίας πορφυρικού τύπου, ο σιδηροπυρίτης σχηματίζει μικρούς ανεδρικούς κρυστάλλους με σπογγώδη ιστό. Σε πλήρη αντιδιαστολή, οι επιθερμικού τύπου εμφανίσεις περιέχουν ευεδρικούς και ευμεγέθεις σιδηροπυρίτες.

Μελέτη διαφορετικών γενεών φλεβών που περιέχουν σιδηροπυρίτη (Μ-τύπου από Παγώνη Ράχη, D-, και Ε-τύπου από Κώνο και Παγώνη Ράχη), έδειξε ότι ο πορφυρικού τύπου σιδηροπυρίτης εμφανίζεται εμπλουτισμένος σε Co, Se, Cu, και λιγότερο Zn, χωρίς την παρουσία λοιπών ιχνοστοιχείων. Οι επιθερμικού τύπου σιδηροπυρίτες εμφανίζονται εμπλουτισμένοι σε στοιχεία όπως As, Bi, Pb, Ni και Se. Το περιεχόμενο σε χρυσό των μελετηθέντων σιδηροπυριτών φτάνει μέχρι 4ppm (αφορά σε D-τύπου φλέβες από Παγώνη Ράχη), ενώ αποδεικνύεται ότι ο χρυσός

εμφανίζεται με την μορφή του μη στοιχειομετρικού υποκαταστάτη στη δομή του σιδηροπυρίτη, και όχι ως μικρο-εγκλείσματα.

Το αυξανόμενο περιεχόμενο σε As σιδηροπυριτών της περιοχής Κώνου, από τις D-τύπου στις επιθερμικές (Ε-τύπου) φλέβες είναι σε συμφωνία με παρατηρήσεις αντίστοιχων μεταλλοφοριών σε άλλα κοιτάσματα, όμως η αύξηση αυτή στην περίπτωση της Παγώνης Ράχης αφορά (εκτός από τη μετάβαση προς το επιθερμικό στάδιο) και τη μετάβαση από πρώιμες Μ-τύπου φλέβες σε D-τύπου φλέβες, και βρίσκεται σε συμφωνία με την περιεκτικότητα σε χρυσό.

Οι χημικές μεταβολές αυτές έρχονται σε συμφωνία με αντίστοιχες παρατηρήσεις από άλλα πορφυρικά/επιθερμικά κοιτάσματα σε παγκόσμια κλίμακα, γεγονός που αναδεικνύει την αξία της χημικής σύστασης του σιδηροπυρίτη ως εργαλείο εξερεύνησης και στις μεταλλοφορίες της Θράκης. Περαιτέρω, ο εμπλουτισμός του σιδηροπυρίτη από την περιοχή μελέτης σε Se δείχνει να είναι υψηλότερος από άλλα πορφυρικά κοιτάσματα παγκοσμίως, καθιστώντας τον ένα μοναδικό γεωχημικό χαρακτηριστικό και καθοδηγητικό στοιχείο για ζώνες υψηλής περιεκτικότητας σε χρυσό, μιας και οι γεωχημικές αναλύσεις έχουν ήδη αποδείξει την πολύ ισχυρή συσχέτιση μεταξύ των δύο στοιχείων.

Συνοψίζοντας, η λεπτομερής γεωχημική και ορυκτοχημική μελέτη σε ζώνες εξαλλοίωσης και μεταλλοφορίες πορφυρικού/επιθερμικού τύπου περιοχής Σαπών/Παγώνης Ράχης, αναδεικνύει το ελπιδοφόρο μεταλλευτικό δυναμικό της εν λόγω περιοχής.

Επιπλέον αποδεικνύει τη συνεισφορά των όξινων διεισδυτικών σωμάτων (μικρογρανιγτικών πορφυρών) στις μεταλλοφορίες, με τη συνεισφορά π.χ. αλογόνων, κασσίτερου, κλπ, τόσο σε μεταλλικά, όσο και σε ορυκτά εξαλλοίωσης, πιστοποιώντας έτσι, μία πολύπλοκη μαγματική/υδροθερμική εξέλιξη των μελετηθέντων συστημάτων.

Οι πορφυρικές μεταλλοφορίες εμφανίζουν επίσης εξαιρετικό εμπλουτισμό σε ρήνιο, που μαζί με το μολυβδαίνιο και τον χρυσό, αποτελούν τα κύρια μέταλλα ενδιαφέροντος. Σε πλήρη αντιδιαστολή με άλλα πορφυρικά συστήματα της χώρας (π.χ. Σκουριές), η μειωμένη συμμετοχή χαλκούχων ορυκτών (π.χ. χαλκοπυρίτη, βορνίτη) έναντι του σιδηροπυρίτη, είναι ένα ιδιαίτερο χαρακτηριστικό των μελετηθέντων συστημάτων. Το ιδιαίτερο αυτό γνώρισμα, πρόσφατα έχει βρεθεί να

χαρακτηρίζει μία νέα κλάση πορφυρικών κοιτασμάτων: τα πορφυρικά κοιτάσματα-Au (π.χ. Kişladağ, Τουρκία, Biely Vrch, Σλοβακία). Αντιστοίχως, η παρουσία ζωνωδών πορφυρικών φλεβιδίων (banded quartz veins), είναι έντονη τόσο στον Κώνο όσο και στην Παγώνη Ράχη, και αποτελεί και αυτή, άλλο ένα χαρακτηριστικό των πορφυρικών κοιτασμάτων χρυσού. Με δεδομένο την ήδη υψηλή μέση περιεκτικότητα σε χρυσό, τουλάχιστον για το σύστημα της Παγώνης Ράχης (0,36 g/t), από δείγματα επιφανείας και μόνο, είναι εμφανές ότι τα συστήματα αυτά πρέπει να αποτελέσουν άμεσο μελλοντικό στόχο για γεωτρητική έρευνα στη βόρεια Ελλάδα.

IV. List of figures

Chapter 1

Chapter 2

Chapter 3

Chapter 4

Chapter 5

Chapter 6

Chapter 7

V. List of tables

Chapter 4

Chapter 5

Chapter 6

Chapter 7

Chapter 8

Chapter 1:

Structure of the Thesis

1.1 Aims of the Thesis

The present Thesis aims to investigate the distribution of porphyry/epithermal mineralization and their associated hydrothermal alteration zones, in an attempt to further expand our knowledge in a very promising metallogenic province, namely the Sapes-Kirki area, NE Greece. Detailed geological mapping and collection of samples aims to

- record (and identify any new) mineralized centers in the study area
- distinguish and describe their associated hydrothermal alteration types
- investigate the petrography and geochemistry of the magmatic host rocks (both fresh and altered)
- obtain mineral-chemical data from alteration and ore minerals
- acquire bulk ore geochemical data and evaluate the precious and critical metal content of the studied mineralization
- identify any possible mineral-chemical vectors as exploration tools
- propose a genetic model for the studied mineralization, by combining all data acquired through the present study, with the available literature, and
- compare the studied mineralization with analogous/similar ore deposits and prospects, in Greece and elsewhere.

1.2 Field campaigns, mapping and sampling

For the needs of the present dissertation, a total of 198 samples were collected from the study area. Thirty (30) of these samples comprise various types of magmatic rocks, while the rest of them are mineralized. A recconaisance field visit and sampling took place in August 2013, and was followed by three more sampling campaigns during October 2013, June 2014, and Septemeber-October 2014, summing a total of

84 days spent in the field. Two short field visits also took place during October 2017 and November 2018.

One hundred and twenty-three (123) polished thin sections and two hundred and twenty-seven (227) polished block sections were constructed for detailed alteration and ore petrography, as well as for mineral-chemical analyses.

Mapping of the study area was based on topographic maps at scale 1:5000, supplied by the Hellenic Military Geographical Service. Field data were imported in ArcGIS 9.3 for the production of georeferenced geological and alteration maps. Sampling in the targeted areas was conducted under a fixed sampling protocol throughout the study.

1.3 Organization of the Thesis

The present Thesis comprises three introductory (Chapters 1, 2 and 3), four research (Chapters 4, 5, 6 and 7) and one concluding (Chapter 8) chapters.

The first chapter (Chapter 1) describes the organization of the Thesis, which is graphically illustrated in the flow chart of Figure 1.1. A brief description of previous work regarding the mineralization/alteration in the study area is also presented. The second chapter (Chapter 2) is an informative chapter, presenting an introduction to the Poprhyry/Epithermal deposits. In Chapter 3, the Geological framework of Greece is discussed, with emphasis given on the geology of the study area. The next four chapters, largely present the results of this Thesis. The detailed methodology that was used, is described separately in every chapter, since different analytical techniques were implemented each time. A combination of field observations and laboratory work produced an important volume of new data that were organized as follows:

Chapter 4 describes in detail the mineralization and alteration types found in the whole study area, based on mineralogical, petrographic and geochemical data. The results of field-mapping are presented through geological and alteration maps. The mineralogical content of various alteration assemblages is presented, based on petrographic, X-ray diffraction and spectroscopic (SWIR) examination.

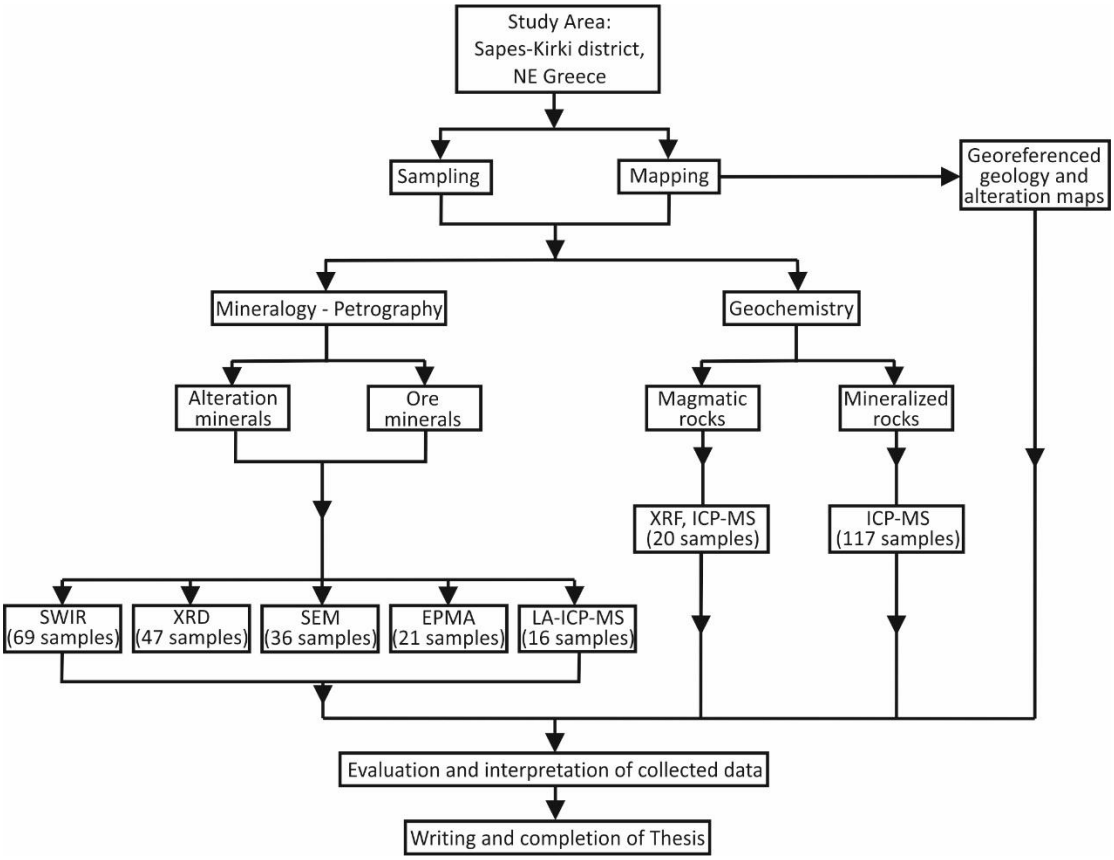

Figure 1.1: Flowchart illustrating the methodological steps followed for the completion of this dissertation.

Mineral-chemical studies (EPM and LA-ICP-MS analyses) of both alteration and ore minerals are discussed in detail, along with an extended dataset of geochemical data (obtained from the analysis of magmatic host rocks and mineralized samples). The trace element content of hydrothermal biotite from the Pagoni Rachi prospect, is the first to be documented from a porphyry mineralization in Greece.

Chapter 5, focuses on the eastern part of the study area, specifically the Konos Hill prospect. The Chapter comprises a detailed mineralogical/geochemical study of a lithocap superimposed on a porphyry system. Owing to its mineralogical and mineral-chemical importance, the advanced argillic alteration zone at Konos is here separately discussed, reporting at the same, the first occurrence in Greece of the APS mineral florencite-Ce, and the first presence of the mineral zunyite, in a porphyry-related environment (which constitutes the second occurrence of this rare, halogen-bearing silicate in Greece).

In Chapter 6, the chemistry of magmatic and hydrothermal magnetite is discussed. The Chapter contains a petrographic description and the first trace elements dataset of magnetite from a Greek porphyry prospect, namely the Pagoni Rachi Cu-Mo-Re-Au system. The distribution of trace elements is discussed and genetic implications are made, followed by a comparative study to other magmatic and/or hydrothermal magnetite from similar deposits and prospects elsewhere. Finally, the use of magnetite chemistry as a potential mineralogical vector towards fertile intrusions is proposed for the Greek prospects/deposits.

The Chapter 7 contains a detailed, comparative geochemical study of various pyrite generations, originating from the two most important porphyry/epithermal prospects of the study area, namely the Konos Hill and the Pagoni Rachi prospects. Documentation of the trace element content of porphyry-, and epithermal-style pyrite, aims to provide knowledge on the metal endowment of the precipitating fluids. The transition from the porphyry to the epithermal environment is also investigated, as it is reflected by the enrichment/depletion of certain elements in pyrite. Important geochemical similarities to other porphyry/epithermal-style pyrite from elsewhere are remarked, as well as a few differences. A notable Se-enrichment, mainly in porphyry-style pyrite compared to other deposits/prospects worldwide, emerges as a characteristic feature and is further evaluated as a potential exploration tool, towards high-grade mineralization zones.

The final Chapter 8, comprises a summary and presents the most important concluding remarks of the Thesis. Further work on the studied prospects, as well as in nearby deposits/prospects is suggested, aiming to fully document the metallogenetic context of NE Greece, which remains up to date, one of the most promising, yet unexplored, areas in southern Europe.

From the above-mentioned, the chapters 5 and 6 have been published in peer-reviewed form as follows: Chapter 5: Mavrogonatos, C. et al.: Mineralogical study of the advanced argillic alteration zone at the Konos Hill Mo–Cu–Re–Au porphyry prospect, NE Greece. Minerals 8, 479.

Chapter 6: Mavrogonatos, C.; et al.: Trace Elements in Magnetite from the Pagoni Rachi Porphyry Prospect, NE Greece: Implications for Ore Genesis and Exploration. Minerals 2019, Volume 9(12), 725.

Both chapters, are integral parts of this dissertation. Any mineral abbreviations used throughout this manuscript, are those proposed by Whitney and Evans, (2010).

1.4 Summary of previous work

During the past few decades, research, exploration for new mineral resources and development of new mining areas in Greece, has gained significant attraction. At the same time, it has emerged as one of the major political matters, mainly in relation to the environmental impact of the mining activities.

Among others, the broad area of northeastern Greece is considered to be one of the most promising target areas for exploration, as it hosts significant mineralization of various types (e.g., Arikas and Voudouris 1998; Melfos et al. 2002; Voudouris, 2006; Melfos and Voudouris, 2017; Voudouris et al., 2019a).

In the broad area of Sapes, over 20 prospects/targets have been identified since the mining companies "Greenwich" and "Glory Resources" conducted exploration activities. An important part of the area, owned now (since 2013) by the Eldorado Gold Corp., and coinciding to the "E5-Sapes Lease", comprises mainly epithermal Au-Ag mineralization, with the most important Au-bearing bodies being the Viper, Scarp and St Demetrios. Au-Ag epithermal mineralization at Sapes, and especially the Viper deposit, has attracted the scientific interest from a number of researchers over the last few decades (e.g., Bridges et al., 1997; Border et al., 1999; Shaw and Constantinidis, 2001; Voudouris, 1993; Michael, 1993, 2004; Voudouris et al., 2006; Kilias S.P. et al., 2013). Another important epithermal Au-Ag deposit is the Perama Hill, located South of the Sapes area (e.g., Voudouris and Skarpelis, 1998; Lescuyer et al., 2003; Voudouris et al., 2010, 2019a), while a number of other deposits/and prospects are scattered in the broader region (e.g., Mavrokoryphi, Perama South, etc., cf. Voudouris, 2011; Melfos and Voudouris, 2017; Voudouris et al., 2019a).

Beyond the above mentioned deposits/prospects, the area presents a strong potential for porphyry-style mineralization as well, with the Konos Hill porphyry/epithermal prospect being a prominent example (e.g., Voudouris 1993, Voudouris et al., 2006, 2019a; Ortelli et al., 2009, 2010; Melfos and Voudouris, 2017).

At the western part of the Sapes Kirki area, the high-intermediate sulfidation epithermal deposits of St Philippos and Achla Tarla occur. Both deposits are

characterized by a complex mineralogy and an extreme enrichment in a plethora of metals like Pb, Zn, Ag, Bi, Sn, Ga, Ge, In, etc. (e.g., Moëlo et al., 1985; Vavelidis et al., 1989; Dimou, 1993; Skarpelis, 1999; Voudouris et al., 2013b, 2019a). Further to the southeast, the Pefka deposit is characterized by a high-intermediate sulfidation, uncommon, Cu-Au-Ag-Te mineral assemblage (Voudouris, 2006; Repstock et al., 2015, 2016; Voudouris et al., 2019a).

Beyond epithermal-style mineralization, at the eastern part of the Sapes-Kirki area, lies the significant Pagoni Rachi porphyry/epithermal prospect. Fisrt described by Arikas (1991), this prospect has already been subject to a number of studies (e.g., Voudouris et al., 2009, 2013a,b; 2019a). Voudouris et al., (2009, 2013a,b) identified an extreme enrichment in Re, and the presence of the rare sulfide rheniite, in the porphyry-style mineralization, and presented data for the alteration, mineralization and the physico-chemical conditions of formation of the prospect, based on fluid inclusion studies.

Recently, Perkins (2018), provided an extended dataset on the petrology, geochemistry and geochronology of magmatic rocks of the Maronia Magmatic Corridor, focusing on the origin of the ore-bearing magmas.

Finally, Melfos and Voudouris (2017) provided a review paper summarizing the mineralization types throughout Greece, while Voudouris et al., (2019a) focused on porphyry/epithermal mineralization types only.

Chapter 2

Porphyry – Epithermal deposits

2.1 General information, age and distribution of porphyry deposits

Porhyry (Cu-Au-Mo) deposits, despite being low-grade systems, are among the major ore sources producing almost three-quarters of the world's Cu, the vast majority of the Mo, one-fifth of the Au, most Re, and minor amounts of a number of other other metals (Ag, Pd, Te, Se, Bi, Zn, and Pb; e.g., Sinclair, 2007; Sillitoe, 2010).

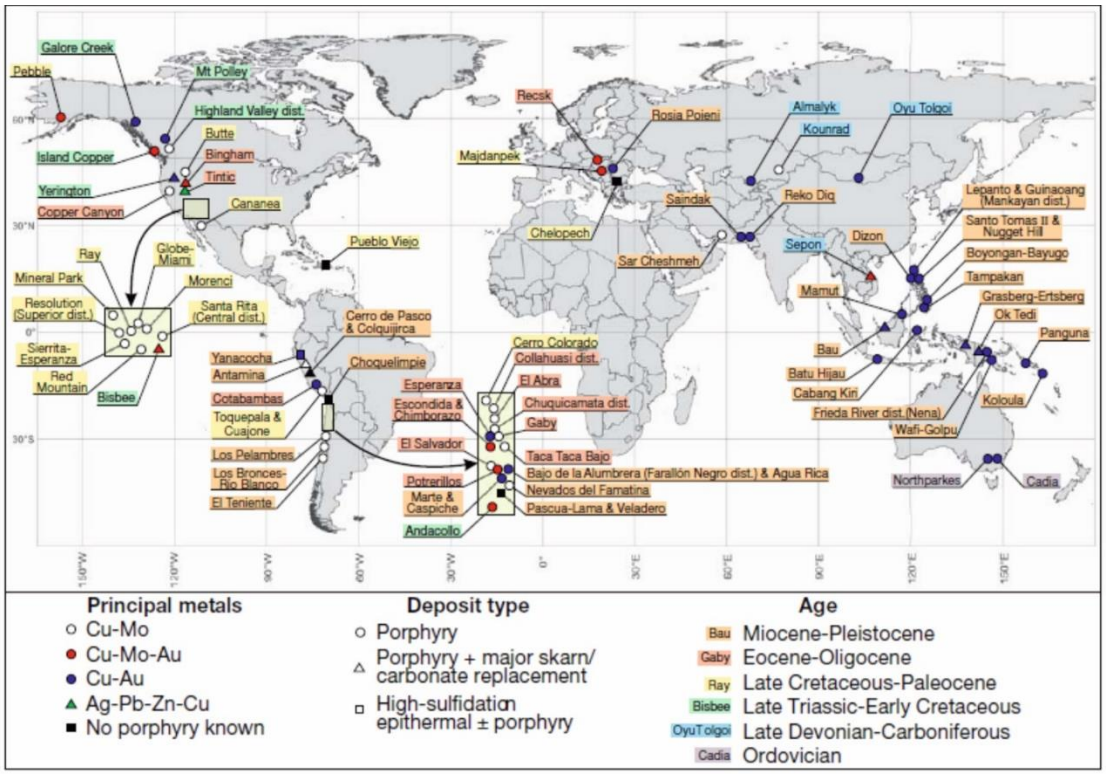

Figure 2.1: Worldwide distribution, metal characterization and age of the major porphyry systems (from Sillitoe 2010).

The deposits themselves are usually hosted in small (<1 km wide) intrusions, which form finger-shaped stocks and dykes, rooting to an underlying batholith. However, metal enrichment and associated hydrothermal alteration of the magmatic/hydrothermal system, usually occupy significantly larger areas, ranging in volume between 10 and 100 km^3 (e.g., Lowell and Guilbert, 1970; Beane and Titley, 1981; Sillitoe, 2010). Pophyry deposits are thought to be consistent with effusive rather than explosive magmatism, since the latter case implements the release of

magmatic volatiles, thus preventing them from condensating and forming ore deposits (e.g., Cloos 2001; Cooke et al. 2005; Richards, 2005). However, in many cases magmatic rocks that host porphyry-style mineralization, are interpreted to represent the deeper parts of ancient stratovolcanoes (e.g., Hattori and Keith, 2001; Sinclair 2007; Sillitoe 2010), that are now mostly erroded.

Many examples of porphyry deposits and prospects worldwide display a cogenetic relation to a number of other mineralization types, including skarns, epithermal (high, intermediate-, or low-sulfidation) base and precious metal mineralization and carbonate replacement deposits (e.g., Seedorf et al., 2005; Sillitoe 2010).

Magmatic rocks associated with the formation of porphyry deposits are mostly I-type granitoids of the magnetite-series (Ishihara 1981; Seedorff et al. 2005). They display calc-alkaline to alkalic affinity, and are chracterized by distinct alteration and mineralization patterns and host variable Cu, Au and Mo contents (Wilson, 2003). In many cases, magmatic rocks of intermediate composition lead to the formation of porphyry deposits with mixed characteristics between the two end-member types (Lang et al., 1995).

Rocks with calc-alkaline affinities display a compositional range from diorite to granodiorite and quartz monzonite, while alkaline intrusions, usally range between diorite and monzodiorite (Sillitoe, 2010). The calk-alkaline porphyries are the most widespread type, while alkalic-rocks hosted systems are rare, and mostly occur in the British Columbia, as well as in Australia, Philippines, Papua New Guinea, and Fiji (Sillitoe, 2010; Bissig and Cooke, 2014).

More fractionated (felsic) host rocks preferably host porphyry-Mo, Sn or W deposits, in contrast to Au-rich deposits, which tend to be hosted in more mafic lithologies. Hoewever, there are exceptions to this empeirical rule, like the quartz-monzonite hosted, Au-rich Mamut deposit, Malaysia (Kósaka and Wakita, 1978).

Poprhyry deposits display a worldwide distribution (Figure 2.1) and form linear, orogen-parallel belts (Sillitoe 2010). Their age of formation spans from the Archean to recent, however, the majority of porphyry deposits is characterized by ages since Jurassic and onwards (Singer et al. 2005; Sinclair 2007; Sillitoe 2010).

2.2 Geotectonic regime of formation

The majority of porphyry deposits was thought to form over subduction zones (Sillitoe 2010), however, the existence of a significant number of porphyries both in continent-continent collisional, and post-collisional environments was recently documented (e.g., Richards 2009; Richards 2011; Chen et al. 2015). In both cases, their formation is inextricably related the generation of hydrous calc-alkaline to alkaline magmas (e.g., Seedorff et al., 2005; Sillitoe, 2010; Richards, 2009, 2011; Kouzmanov and Pokrovski, 2012).

In the subduction-related porphyry deposits, that form in arc environments (Fig. 2.2.a), volatile/metal-enriched magma is generated by solute-rich aqueous fluids that originate either from melting, or dehydration of the subducting slab (Dreyer et al. 2010). The metal endowment of such magmas is attributed to originate from the mantle (e.g., Wilkinson 2013), except for molybdenum, which is believed to have a crustal origin (Farmer and Depaolo, 1984). However, partial contribution to the metal budget from pre-existing ore deposits and/or sulfide cumulates (from earlier subduction cycles) cannot be ruled out (Core et al., 2006; Lee et al. 2012). These sources alone would not be enough to generate a porphyry deposit; a fertilizing mechanism is needed to concentrate the metals from the exsolving fluids. Examples of such mechanisms are (i) the crystallization of magnetite, which leads to the formation of an immiscible sulfide melt (Jenner et al. 2010), that can incorporate metals like Fe, Au, Pd, Pt and to a lesser extent Cu (e.g., Sun et al. 2004; Nadeau et al. 2010), or (ii) the assimilation of reduced country rocks, (e.g., shales, carbonates), which act as an additional metal-providing source (Cloos, 2001).

In the case of post-collisional porphyry formation (Figure 2.2.b-d), despite the fact that the main features of the deposits remain the same to those formed over subduction zones, (Richards 2009; Richards 2011), the magma sources are totally different. Magmatism in the post-collisional setting is volumetrically restricted and commonly short-lived, compared to the arc-environment. It also tends to be more alkaline and leads to the formation of Au-, and PGE-enriched porphyry deposits, with the Skouries deposit in Greece being a prominent example (e.g., Siron et al. 2016).

Hydrous magmas form in the post-collisional environment due to partial remelting of subduction-metasomatised lithospheric mantle and hydrous cumulate zones of former arc systems. This procedure is triggered by extension occuring at a pos-collisional environment, and leads to the generation of shoshonitic magmas (Richards 2009; Moritz et al. 2016).

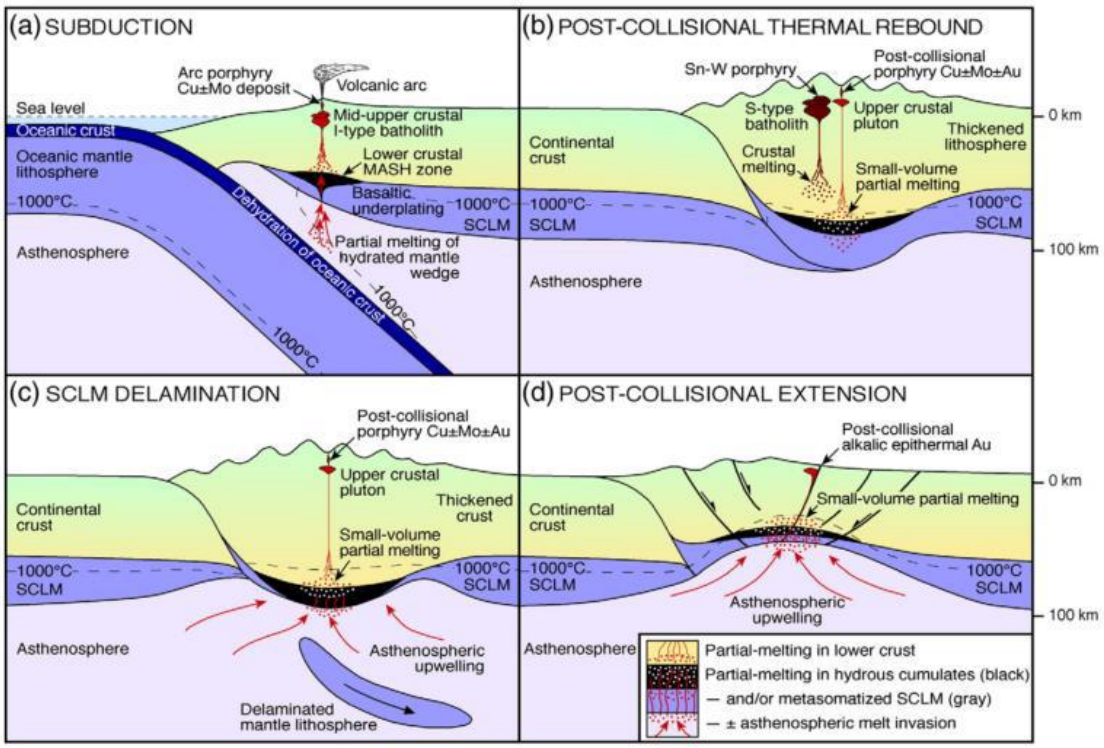

Figure 2.2: Schematic diagram illustrating the geoectonic environments of porphyry deposits formation in (a) subduction and (b-d) post-collitional setting (from Richards 2011).

As Richards (2009) suggested, enrichment of these magmas in Au is due to its more siderophile nature compared to Cu, and because crustal assimilation is more likely to happen in an extensional regime, adding to the magma fertility, through contamination by a crustal component. A number of mechanisms have been proposed to explain magma upwelling: lithospheric thickening, thermal rebound, stress relaxation following slab-rollback, subcontinental lithospheric mantle delamination or lithospheric extension (Richards 2009; Delibaş et al. 2016).

In the same context, crutal-scale fault structures, that accomondate extension during the post-collisional stage, favor the ascend of fertile magmas, and thus lead to

the formation of porphyry-style deposits that display a significant tectonic control, as has been described for porphyry-mineralization in the Rhodope Massif, in Bulgaria and Greece (Marchev et al. 2005).

2.3 Alteration and mineralization patterns

Owing their name to the porphyrytic texture of their host rocks, which is thought ot be the result of sudden crystallisation, due to volatiles release (Cloos 2001), porphyry deposits are characterised by intense and large-volume hydrothermal alteration of their host and surrounding rocks (Sillitoe, 2010).

It has long been recognized that hydrothermal alteration in the porphyry deposits shows a sequential distribution both laterally and vertically (Figure 2.3), followed by a zonation of metals (Lowell and Guilbert 1970; Meyer and Hemeley, 1967; Rose and Burt 1979; Sillitoe 2000, 2010; Watanabe and Hedenquist 2001; Seedorff et al. 2005; Halley et al., 2015). As a general rule, alteration types often display overprninting, and tend to become younger towards the shallower parts of a porphyry system (Sillioe 2010).

Most porphyry deposits are characterized by a core occupied by potassic alteration, where biotite and K-feldspar are the dominant minerals. Potassic alteration zones coincide with the largest part of the hypogene mineralization, comprising commonly chalcopyrite, bornite and gold (Sillitoe 2010). In more acidic systems (e.g., porphyry Mo, Sn etc.,) potassic alteration may be characterized by partial or complete absence of biotite, and the predominance of K-feldspar. Alteration zones that surround the mineralized core of porphyry systems are significantly variable, fact that depends on the geochemistry of magmatic/hydrothermal fluids and the composition of the host rocks.

Upwards, potassic assemblages grade into chlorite-sericite and sericite alteration zones, the latter commonly hosting pyrite, chalcopyrite, enargite, bornite, chalcocite and sphalerite mineralization (Sillitoe 2010). Sericitic alteration (also described as “phyllic”) is widespread in many deposits and may cause partial or pervasive desctruction of earlier alteration assemblages (e.g., potassic alteration, Sillitoe, 2010). Furthermore, it may be associated with structural features, e.g., faults, thus forming geometrical zones, or it may show irregular distribution.

A propylitic alteration zone is widespread in many porphyry deposits. It consists of variable amounts of actinolite, albite, epidote, hematite, pyrite and carbonates, surrounding the porphyrytic stock and grading outwards into albite-actinolite, and a more distal/low temperature chlorite-rich alteration assemblage (Sillitoe 2010).

Many porphyry deposits, especially those hosted in calk-alkaline rocks, are characterized by the presence of a vertically-, and laterally extensive lithocap (e.g., Sillitoe, 1995; Muntean and Einaudi 2001; Khasgherel et al., 2008), comprising advanced-argillic alteration minerals (e.g., quartz, alunite, dickite, kaolinite, pyrophyllite, aluminosilicates).

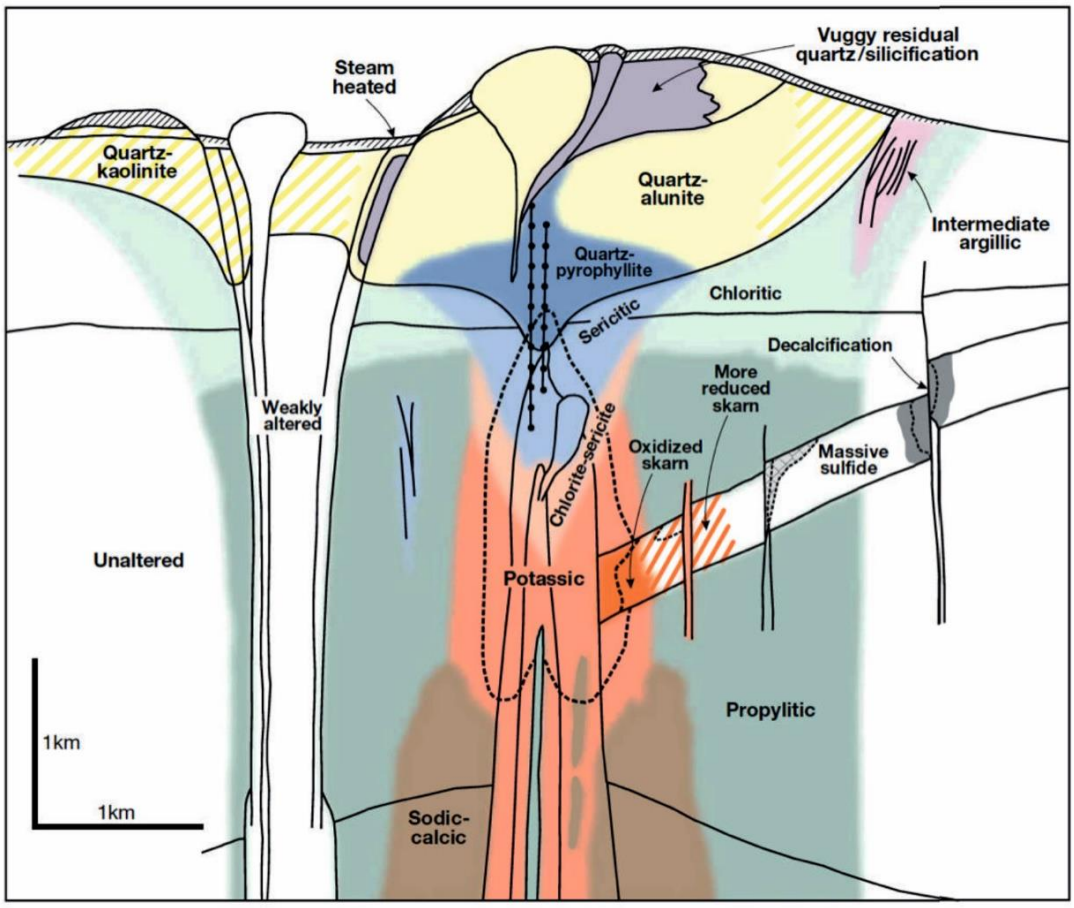

Figure 2.3: Generalized alteration-mineralization zoning pattern for telescoped porphyry Cu deposits (from Sillitoe, 2010).

These areas, if not eroded away, are favorable environments for high-sulfidation, epithermal-style pyrite-enargite ± chalcocite-covellite, Au-rich mineralization (Watanabe et al., 1997; Sillitoe 1999, 2010). Lithocaps are useful vectors towards (blind/burried) porphyry deposits as they usually exhibit large-scale characteristic Zn-

Pb-Ag-rich areas, surrounding a central Cu-Au rich zone (Landtwing et al. 2010; Sillitoe 2010).

Lithocaps are typically absent from porphyry deposits that develop in alkaline intrusions (e.g., Lang et al., 1995; Sillitoe, 2002; Holliday and Cooke, 2007). Such sytems comprise sodic, albite-dominated, calc-potassic and/or potassic alteration styles and host pyrite-chalcopyrite ± bornite mineralization at their cores. Moreover, they are typically depleted in quartz, especially when they are hosted within silica-undersaturated intrusives (Lang et al., 1995; Wilson, 2003; Holliday and Cooke, 2007), and display a prominent Au±PGE enrichment, mainly of platinum and palladium (Eliopoulos and Economou-Eiopoulos 1991; Bissig and Cooke, 2014; McFall et al., 2016).

Sodic-calcic alteration assemblages also characterize some porphyry deposits. They are commonly found in the deeper parts (roots) of some systems and are considered to be sulfide and metal poor (e.g., the Ann-Mason deposit, Yerington, Dilles et al., 1995). However, sodic-calcic and hybrid potassic-calcic assemblages (e.g., biotite-actinolite-magnetite) may host significant mineralization in Au-rich deposits (e.g., Cotabambas deposit, Peru, Perelló et al., 2004).

Mineralization in the porphyry deposits occurs mostly in the form of veins (stockworks), as well as disseminations of sufides (mostly) in the potassic zone. Despite their multi-phase genetical history, that causes reopening and overprinting of various vein genarations, vein types are commonly used for classification of porphyry-style deposits. Numerous works have been published suggesting various classification schemes of veining in the porphyry deposits (e.g., Arancibia and Clark, 1996; Gustafson and Hunt 1975; Dilles and Einaudi, 1992; Gustafson and Quiroga, 1995; Redmond et al., 2001; Pollard and Taylor, 2002; Cannell et al., 2005; Masterman et al., 2005; Monecke et al., 2018). The complexity of veining in the vast majority of the porphyry systems makes it almost impossible to propose a unique succession of veining/mineralizing events.

However, most porphyries comprise early veins associated with biotite (EB-veins), K-feldspar, magnetite (M-veins) and/or actinolite, that commonly lack of sulfides and quartz. These vein types are followed by sulfide-hosting quartz veins with narrow or absent alteration selvages. They display a wavy geometry and contain magnetite (A

type), or can be straight-sided and host molybdenite (B type). This group hosts the majority of the metal content of deposits. The above-mentioned vein-types are associated with potassic alteration assemblages. In many deposits, they are overprinted (crosscut and/or reopened) by sulfide veins (with crystalline or no quartz) associated with feldspar destructive alteration, dominated by sericite (D type veins).

Metals in the porphyry systems, exsolve from the parental intrusion, and are hydrothermally transported either as sulfide complexes or as chlorine ligands (Hedenquist and Lowenstern 1994; Audétat et al. 2008; Tooth et al. 2008). They commonly display a zoned pattern of distribution. Normally, Cu-Au enrichment characterizes the central parts of a porphyry system (potassic, chlorite-sericite, and sericite-altered rocks). At some deposits, PGE-bearig phases are also present, mostly in the potassic zones, often in the form of tellurides (e.g., Tarkian and Stribrny, 1999; McFall et al., 2016). Outwards, anomalous content of metals like Pb, Zn, and Ag may characterize the propylitic alteration zones, reflecting dropping temperature conditions (Sillitoe 2010).

2.4 Relation to epithermal deposits

As discussed before, high-sulfidation epithermal mineralization may occur in the uppermost part of a porphyry system, commonly hosted in volcanic (e.g., phreatomagmatic deposits) and/or clastic and other sedimentary lithologies (Sillitoe 2010). They are characterized by a very shallow depth of emplacement (commonly <1.5km). As a consequence, epithermal-style deposits are highly susceptibile to erosion processes, and this is probably reflected to their geologically younger ages, compared to porphyry deposits, as Paleozoic or older epithermal deposits are highly uncommon (Seedorff et al., 2005; Simmons et al., 2005).

Contrary to epithermal-style deposits, and as evidenced by isotopic studies, epithermal deposits owe their genesis to mixing of both magmatic and non magmatic fluids (e.g., Giggenbach 1992; White and Hedenquist 1995)

These deposits are characterized by high average Au concentrations (average 1 to 3 g/t Au), especially compared to the porphyry deposits, but they sometimes contain no or minor recoverable Cu, which is usually depleted due to supergene removal

(Sillitoe, 2010). However, not all epithermal deposits are essentialy mineralized. Three types of epithermal-style mineralization are usually distinguished: High sulfidation (acid-sulfate/pyrophyllite-kaolinite) Au-Cu epithermal systems usually occur above and proximal to the intrusion, while low-sulfidation Au-Ag (adularia-sericite), and base-metal rich intermediate sulfidation (Ag-Zn-Pb) deposits are preferably found peripherally to the intrusion.

Mineralization in the high-sulfidation environment is mostly structurally controlled, as the ascent of the acidic hydrothermal fluids is enhanced through structural corridors (fault and fracture zones). In some cases, massive polymetallic sulfide lodes tend to develop in the deeper feeder structures of such lithocaps, while less commonly, intermediate sulfidation epithermal mineralization, mainly in the form of veins, may occur in the periphery of the lithocaps (Sillitoe 2010).

In many deposits, porphyry-style stockworks are overprinted and crosscut by late, base metal-rich veins that are known as E-type veins and are probably deep equivalents of the shallow epithermal structures (Masterman et al., 2005; Voudouris et al., 2013b; Maydagán et al., 2015). Also known as Cordilleran-style veins, they may host significant mineralization comprising pyrite and sphalerite, as well as chalcopyrite, enargite-famatinite, galena, and tennantite-tetrahedrite. A prominent example of such ineralization style, is the Butte system in Montana (Rusk et al., 2008a, b). Furthermore, E-type veins have been recently recognized to occur in a number of Greek porphyry deposits and prospects (see Voudouris et al., 2013b, 2019a).

.

Chapter 3.

Geological context

3.1 Geodynamic evolution of the Greek region

The Hellenic Orogen, or the "Helenides" as it is widely known, composes an integral part of the Alpine-Himalayan orogenetic chain. The Hellenides represent a critical link that connects the southern Balkan Peninsula in the northwest (e.g., the Dinarides/Albanides) to the Turkey (e.g., Pontides, Anatolides) in the East.

Their formation took place as a result of the subduction-accretionof the African and Eurasian plates, that initiated during the Late Jurassic. This procedure, which is still on-going above the north-dipping Hellenic subduction zone, produced a thrust pile of SW-verging nappe (Figure 2.1), comprising continental blocks (e.g., Pelagonia, Rhodope Massif), and their in-between Neotethyan oceanic domains (Vardar and Pindos oceans), now represented by ophiolitic relics (Robertson, 2002, Jolivet and Brun, 2010; Ring et al., 2010; Jolivet et al., 2013; Kydonakis et al., 2015a, b; Menant et al., 2016; Brun et al., 2016; Schmid et al., 2008, 2019).

Early evolution of the Hellenides region (Late Precambrian to Late Jurassic) is characterized by a repeated opening and closure of oceanic domains and subsequent continental crust generation above the relevant subduction zones (Anders et al., 2006; Himmerkus et al., 2006; Reischmann and Kostopoulos, 2007). A first cycle related to the subduction of the Paleotethys beneath the European continental margin is reflected to a Permian/Carboniferous igneous event interpreted to record the evolution of an active continental margin in the Precambrian-Silurian basement of the Hellenides (Anders et al., 2006; Reischmann and Kostopoulos, 2007).

During Late Triassic-Early Jurassic, the evolution of the Hellenides region is marked by the opening of the Vardar oceanic domain, in-between the Rhodope and Pelagonian continental blocks (Robertson et al., 2013). Its subduction gave rise to a Late Jurassic magmatic arc in the southern parts of the Rhodope. The final closure of the Vardar oceanic domain and the subsequent collision between the European margin and the Pelagonian continental block occurred at Late Ceataceous and is

highlighted by Jurassic ophiolites that are obducted on the Pelagonian region. (Robertson et al., 2013). This accretion procedure was followed by subduction initiation in the Pindos oceanic domain, during the Paleocene times (60–55 Ma), which ended at ~35 Ma, with the collision between Adria and Pelagonian microcontinents (Brun and Faccenna, 2008; Ring et al., 2010; Jolivet et al., 2013; Menant et al., 2016).

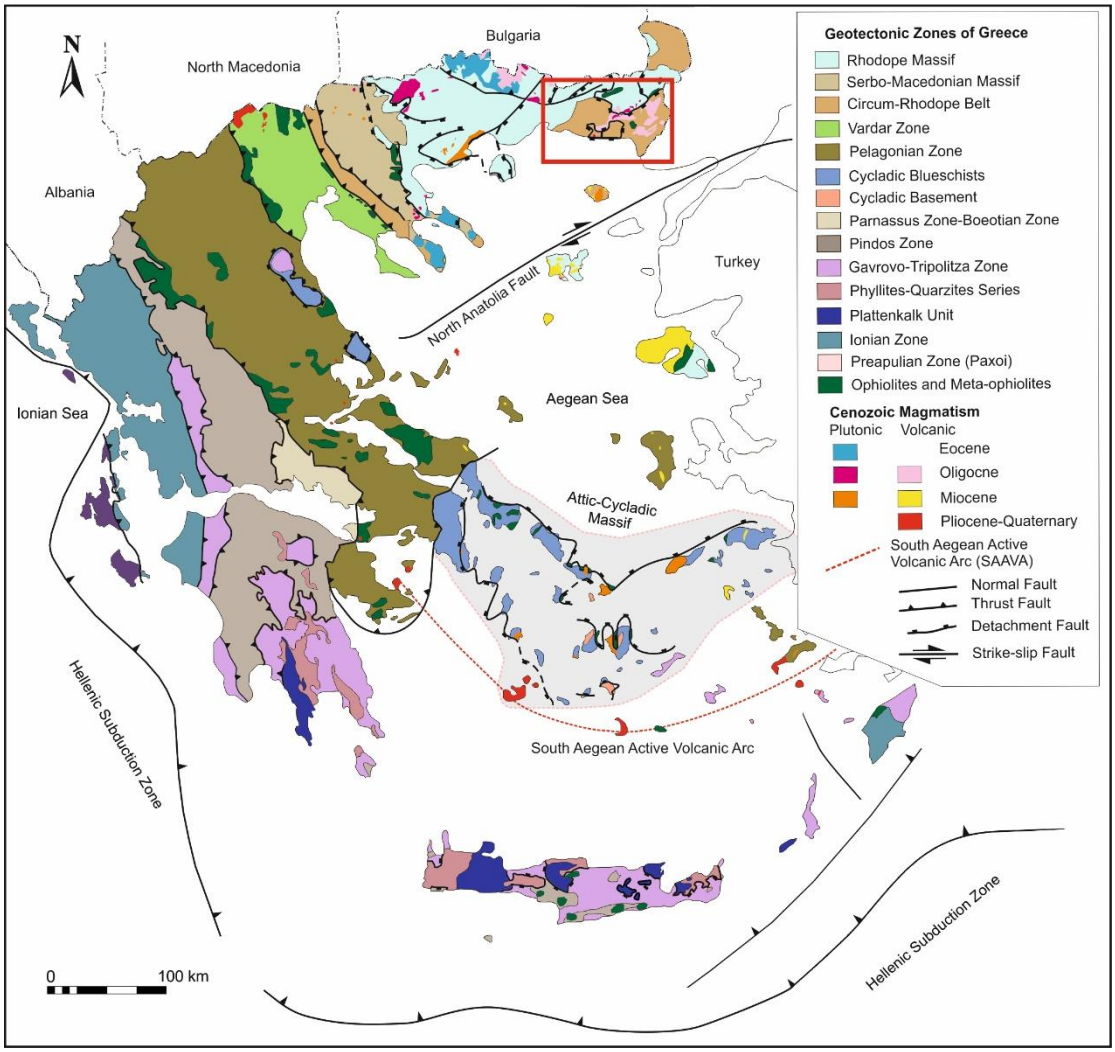

Figure 3.1: Simplified geological map of Greece (adopted with minor modifications from Ottens and Voudouris, 2018). The study area is highlighted.

The geodyamic context in the area since Early Creatceous, is marked by the presence of a single operating subduction zone, where both oceanic and continental lithospheric mantle subducted beneath the Aegean domain (van Hinsbergen et al., 2005; Brun and Faccenna, 2008; Ring et al., 2010; Jolivet et al., 2013; Menant et al.,

2016; Brun et al., 2016). Futrther evolution is marked by slab roll-back during Eocene times, and a slab tearing, that is believed to have happened below western Anatolia in Miocene (Menant et al., 2016). The slab roll-back caused the collapse of the accretionary wedge, and the opening of a plethora of back-arc, supra-detachment basins. In such basins, post-orogenic extension accomondated by crustal-scale detachment faults, exhumed deep-seated crustal parts onto the surface forming metamorphic core complexes, and gave rise to widespread magmatism with a pronounced post-collisional signature (e.g., Wortel and Spakman, 2000; Brun and Sokoutis, 2010; Ring et al., 2010; Jolivet et al., 2013; Kilias A. et al., 2013; Menant et al., 2016).

Characteristic examples of such exhumed complexes are the Rhodope Massif in northern Greece and the Attic-Cycladic Massif in the central Aegean area (Menant et al., 2016).

3.2 Geology of the Rhodope Massif

The Rhodope Massif records a long and rather complex tectonometamorphic history (Brun and Sokoutis 2018). It extends alongside the Greek-Bulgarian borders and together with other major units of the Balkanides, is believed to represent an integral part of the European continental margin (Schmid et al., 2008, 2019; Himmerkus et al., 2009; Burg, 2012; Kydonakis et al., 2015a, b). Structurally bond to both its northern and southern margins, the Rhodope massif comprises three major sub-domains (Figure 3.2), known as the Southern Rhodope Core Complex (also including the Kerdylion unit), the Chalkidiki Block, better known as “Serbo-Macedonian Massif” (excluding the Kerdylion unit), and the Northern Rhodope Domain (Kydonakis et al., 2015a, b).

The Southern Rhodope Core Complex is built by a massive succession of Triassic marbles intercalated with amphibolites and metapelites, as well as orthogneisses of Permian/Carboniferous age (Dinter et al., 1995; Brun and Sokoutis, 2007; Turpaud and Reischmann, 2010). The Complex has partially been exposed to anatexis, as suggested by the existence of migmatites found in Thassos island and the Kerdylion unit.

The Chalkidiki block largely coincides with the former-known Serbo-Macedonian Massif (with the exception of the Kerdylion unit). It comprises a thrust-system built up

by four NW-trending sub-units: The Vertiskos Unit (interpreted as a Godwana-derived domain, accreted to the European margin by the end of the Palaeozoic, cf. Himmerkus et al., 2009) including the Thermes-Volvi-Gomati (TVG) complex, the Circum–Rhodope Belt, the Chortiatis Magmatic Suite, and the eastern Vardar ophiolites (Bonev et al., 2015; Kydonakis et al., 2015a,b; Siron et al., 2016).

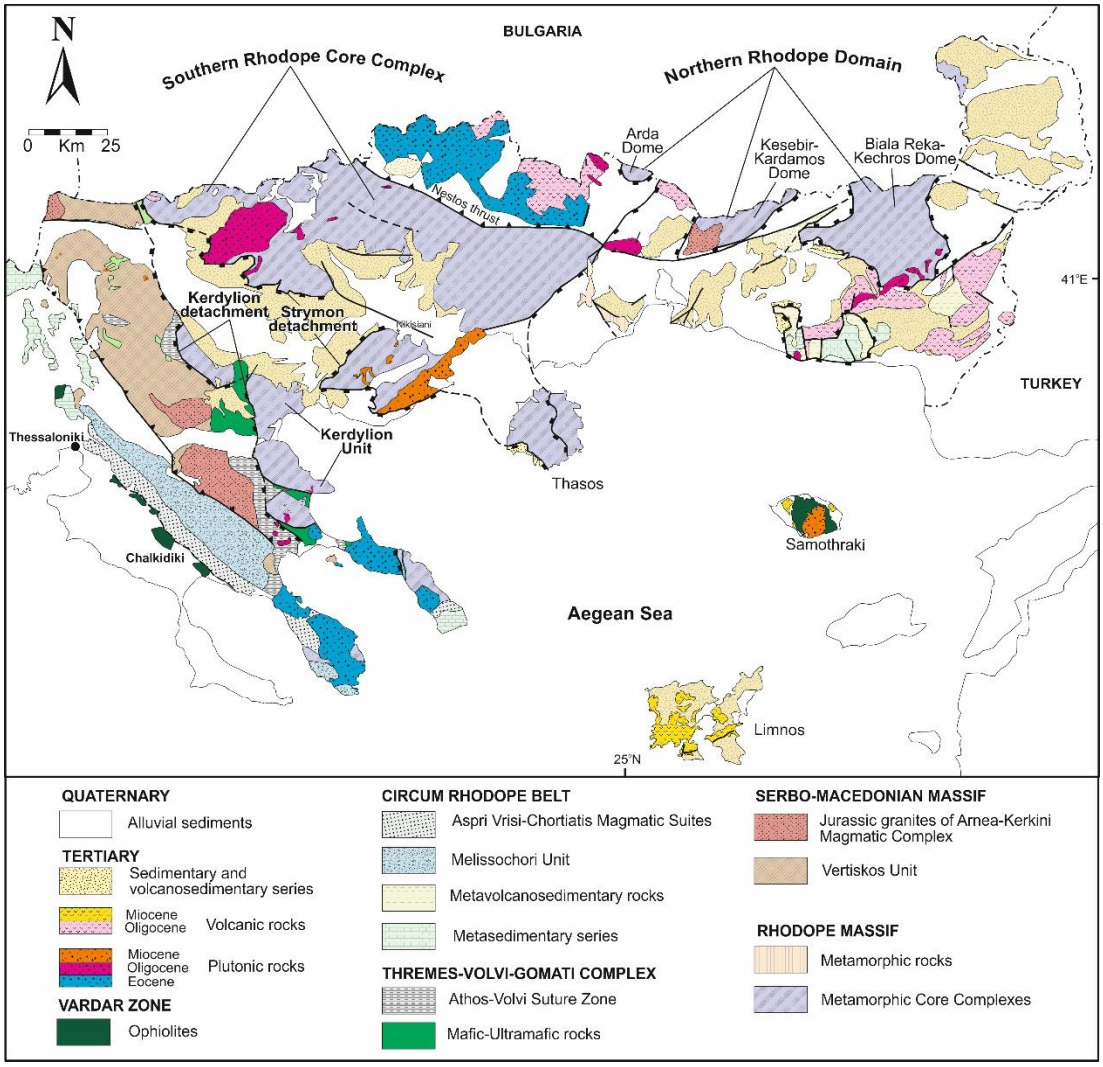

Figure 3.2: Simplified geological map of the Rhodope, the Serbomacedonian Massif and the Circum-Rhodope belt at northeastern Greece (from Melfos and Voudouris, 2017).

The Northern Rhodope Domain occupies a major part of northeastern Greece (Figure 3.2) and is further subdivided into three parts (Kydonakis et al., 2015a, b):

The lower unit comprises high metamorphic-grade basement rocks (orthogneisses) with protoliths of Permo-Carboniferous ages, and includes the Arda, Biala Reka-Kechros, and Kesebir-Kardamos migmatitic domes.

The intermediate unit, comprises again high-grade rocks, sharing both continental and oceanic affinities. The ages of their protoliths span in two periods, from Neoproterozoic to Ordovician, and Permo-Carboniferous to Early Cretaceous.

The structurally upper unit comprises low-grade rocks of Mesozoic age, known as the Circum-Rhodope Belt, including several sub-units (e.g., Drymos-Melia, Makri unit etc.), as well as and the Evros ophiolitic rocks (Magganas et al., 1991; Magganas, 2002; Turpaud and Reischmann, 2010; Kirchenbaur et al., 2012; Meinhold and Kostopoulos, 2013; Bonev et al., 2015).

3.3. Magmatism and mineralization in the Rhodope Massif

As indicated by mantle tomographic images, a single slab was subducted beneath the Aegean domain since at least the latest Cretaceous, and was largely responsible for its tectonomagmatic evolution (Jolivet and Brun, 2010).

Asthenospheric mantle upwelling and thermal disturbance of the crust and underlying mantle produced voluminous post-subduction magmatism in Oligocene to Miocene times, associated with the formation of core complexes. Magmatic rocks of this age are of calc-alkaline to shoshonitic and ultra-potassic affinities, and cover a compositional range from mafic to felsic (Pe-Piper and Piper 2002; Ersoy and Palmer, 2013; Menant et al., 2016; Perkins et al., 2018). Magmatic activity in northern Greece culminated in two periods: at about 34-26 Ma, and at ~22-19 Ma (Gilg and Frei, 1994; Christofides et al., 2004; Moritz et al., 2010; Kaiser-Rohrmeier et al. 2013; Siron et al., 2016). It is characterized by a decreasing crustal component through time, while a mantle cotrnibution grows larger, with the Skouries plutonite being a prominent example of a mantle-enriched magmatic source (e.g., Kroll et al., 2002; Siron et al., 2016).

Marchev et al. (2005) first recognized that the hydrothermal alteration and ore genesis, the formation of the metamorphic core complexes, and the widespread Late Eocene to Early Miocene basic to felsic magmatism, share a genetic relation. This fact

was later denoted by a number of other researchers (e.g., Moritz et al., 2010; Melfos and Voudouris, 2017; Voudouris et al., 2019a; Tsirambidis and Filppidis, 2019).

Significant mineralization in the Rhodope massif is mostly focused on the Thrace and Chalkidiki districts (e.g., Melfos and Voudouris, 2017; Voudouris et al., 2019a), and comprises various mineralization types, like porphyry, epithermal, carbonate-replacement, reduced intrusion-related gold, etc. A prominent characteristic of these deposits/prospects is their significant enrichment in precious and critical metals (e.g., Voudouris, 2006; Melfos and Voudouris, 2012, 2017; Tsirambides and Filippidis, 2012; Voudouris et al., 2019a).

Chapter 4

Porphyry/Epithermal mineralization and alteration, and critical/precious metals enrichment in the study area

Abstract: Detailed field mapping in the Sapes-Kirki area in northeastern Greece, resulted in new discoveries of porphyry-, and epithermal-style mineralization in addition to the already known Konos Hill and Pagoni Rachi prospects. Porphyry Cu-Mo-Re±Au systems and associated high/intermediate sulfidation epithermal ores are hosted in Oligocene post-collisional intermediate-to-acidic intrusives with high-K calc-alkaline affinities. The porphyry mineralization at Konos Hill, Pagoni Rachi and the newly discovered Papadokoryphi prospect, is temporally related to sodic/potassic-calcic, sodic/potassic and sericitic alteration of the host rocks, and propylitic alteration in the periphery of the systems. All three porphyry prospects are characterized by several generation of quartz stockwork veins with various amounts of magnetite, pyrite, chalcopyrite, molybdenite and native gold. High- (HS) and intermediate-(IS) sulfidation epithermal-style mineralization at Konos Hill and Pagoni Rachi is spatially associated with zunyite-alunite-APS minerals-diaspore-bearing lithocaps and underlying sericitic alteration zones, respectively, and resulted in significant overprinting of the former sodic/potassic-calcic and sodic/potassic assemblages. Enargite-colusite and tetrahedrite/tennantite along with tellurides are the main metallic minerals characterizing the HS and IS epithermal ore, respectively. Mineral-chemical analyses revealed a significant presence of F (up to 5.67 wt%) and Cl (up to 0.36 wt%) in hydrothermal biotite (phlogopite), compared to its magmatic counterpart. K- and Na-rich (orthoclase, albite to oligoclase) feldspar varieties dominate the sodic/potassic-calcic and sodic/potassic alteration assemblages respectively, while propylitic-related feldspar share a compositional range from albite to oligoclase as well. Secondary amphiboles (commonly actinolite) incorporate F in their structure (up to 0.8 apfu), compared to their magmatic precursors. Epidote and chlorite do not display significant chemical variation between the various alteration

styles. Rheniite is present at both Konos Hill and Pagoni Rachi prospects. Molybdenite in both areas is extremely Re-enriched (values up to 2 wt% and 3.15 wt% respectively). Geochemical data suggest significant enrichment of porphyry-epithermal ores in several precious and critical metals including Au, Ag, Bi, Te, Se, Mo, Re, In, Sn, and V. Close correlations between Mo-Re and Au-Se, suggest the contemporaneous introduction of these metals to the ore systems. In contrast to the low gold content in the Konos Hill porphyry system, in the exposed parts of the deposit, significant gold introduction in the Pagoni Rachi was related to at least three types of alteration and associated porphyry mineralization: early sodic-calcic/potassic assemblages (average 0.15 g/t); Quartz stockworks associated with sodic alteration and late massive pyrite veins associated with sericitic alteration display significant enrichment in gold (average of 0.20 g/t and 3.68 g/t respectively), combined with highest content of Se. Epithermal-style mineralization at Pagoni Rachi and Konos Hill is characterized by an enrichment in Ag, Ga, In, Sn, Te, Bi, Se, and V. A classification of the studied porphyry systems is a matter of further research, as they display several features that are not common to any other known type of porphyry deposit, with an extreme enrichment in Re being the most prominent.

Keywords: Porphyry-epithermal; Critical and precious metals; Re-rich molybdenite; Alteration mineralogy; LA-ICP-MS; Exploration; Greece

---

4.1 Introduction

The demand of modern industry for precious and critical metals (e.g., Au, Ag, PGE, REE, Ga, Te, Mo, Re, Se, Te, Bi) is dramatically increasing (Sillitoe 2010; Melfos and Voudouris, 2012; Kelley and Spry, 2016) despite the downturn in the discovery of ore deposits containing these metals. Of these deposits, porphyry-style systems are very important ore providers, producing the majority of the world's Cu and Mo, one-fifth of the Au, most Re, and minor amounts of other metals like Ag, Pd, Te, Se, Bi, Zn, and Pb (e.g., Sillitoe 2010).

The study of alteration zones is critical for understanding the temporal and spatial distribution of economic metals in porphyry and associated epithermal ore systems,

and provides significant information on the ore-forming processes (e.g., Meyer and Hemley 1967; Lowell and Guilbert 1970; Rose and Burt 1979; Sillitoe 2000, 2010); Watanabe and Hedenquist 2001; Seedorff et al. 2005). Detailed field work and mapping, microscopic examination of the alteration assemblages coupled with mineral-chemistry of alteration and ore minerals, geochemistry and spectroscopic examination of outcrops (based mainly on short-wave infrared spectroscopy and X-ray diffraction) have proven to be critical to understanding the different types of alteration assemblages and ore mineralization.

In northeastern Greece, widespread Tertiary magmatism and associated hydrothermal alteration have produced a wide variety of magmatic-hydrothermal ore deposits (Arikas and Voudouris 1998; Melfos et al. 2002, 2017; Marchev et al. 2005; Voudouris et al., 2019a), including porphyry-style at Maronia, Sapes-Kassiteres, Myli, Aisymi and Melitena (Melfos et al. 2002, 2020; Voudouris et al. 2006, 2009, 2013a,b; 2016a,b; Galanopoulos et al., 2018), and epithermal Au-Ag-Te at Sapes, Perama Hill, Pefka and St Philippos (e.g, Dimou, 1993; Shaw et al., 2001; Voudouris 2006; Voudouris et al., 2011; Kilias S.P. et al., 2013). Previous research on the Sapes and Kirki area reported various alteration types associated with porphyry Cu-Mo-Re-Au and epithermal Ag-Au ore systems (Voudouris 2006; Voudouris et al. 2009, 2013a,b; Ortelli et al. 2009, 2010; Mavrogonatos et al., 2018a, b, c; 2019).

The abundance of different types of mineralization in Greece that display significant enrichment in a number of precious and critical metals, has been a matter of recent research (e.g., Voudouris, 2006; Melfos and Voudouris, 2012, 2017; Stergiou et al., 2018; Voudouris et al., 2019a; Tsirambides and Filippidis, 2019). Within the Serbomacedonian and Rhodope metallogenic districts, enrichment in Sb, Te, Mo, Re Ga, In, PGE, Au and Ag have been identified in porphyry-, epithermal-, and reduced intrusion-related ore systems (e.g., Voudouris, 2006; Melfos and Voudouris 2012; Voudouris et al., 2019a). One of the most promising areas for exploration of precious and critical metals in Greece, is the Sapes - Kirki area in the Rhodope metallogenic district, which hosts both porphyry-, and epithermal-style mineralizations (Arikas and Voudouris 1998; Voudouris et al. 2013a,b; 2019a).

In the present chapter new gological and alteration maps of the studied area are presented. A detailed description of the petrographic, lithogeochemical and

geochemical characteristics of fresh and hydrothermally altered magmatic rocks, and associated porphyry-epithermal style mineralization is made. Further detailed investigations are made regrding the mineral chemistry of the major alteration and ore minerals, based on EPMA and LA-ICP-MS studies. The main aim is to determine the ore forming processes and the alteration phenomena in the area. Moreover, lithogeochemical data are used to determine whether a geochemical fingerprint of metallic elements in alteration zones can be used as an exploration guide to precious and critical elements in northeastern Greece.

4.2 Regional Geology

The Sapes-Kirki area is part of the Rhodope metallogenic district. It is located in northeastern Greece, where lithologies of the Rhodope Massif and the Circum-Rhodope Belt are exposed to the north and south of the study area, respectively (Figure 4.1). The study area is dominated by volcaniclastic rocks of middle-to-upper Eocene age that uncomformably cover the metamorphic rocks (Figure 4.1).

The Sapes-Kirki area mainly comprises conglomerates, marls, sandstones and volcaniclastic material (e.g., tuffs) of Priabonian age (Figure 4.2a) as well as a series of magmatic rocks. The volcaniclastic sequence is intruded by four types of subvolcanic rocks with subalkaline to alkaline affinities that form stocks and dykes (Arikas and Voudouris, 1998). These rocks are, (from the oldest to the youngest, based on cross-cutting relations; Ortelli et al., 2010; Voudouris, 2014) hornblende-biotite granodiorite porphyry, pyroxene-biotite microdiorite porphyry, quartz monzodiorite, and microgranite porphyry. The hornblende-biotite granodiorite porphyry occupies the major part of the study area, and forms E-trending elongated stocks that host both the Konos Hill and the Pagoni Rachi porphyry-epithermal prospects (Figures 4.1 and 4.2).

The broader Sapes area represents a deeply eroded stratovolcano, where the following types of intrusive rocks occur: hornblende-biotite granodiorite porphyry, pyroxene-hornblende diorite porphyry, pyroxene-biotite microdiorite porphyry, quartz monzodiorite, and microgranite porphyry.

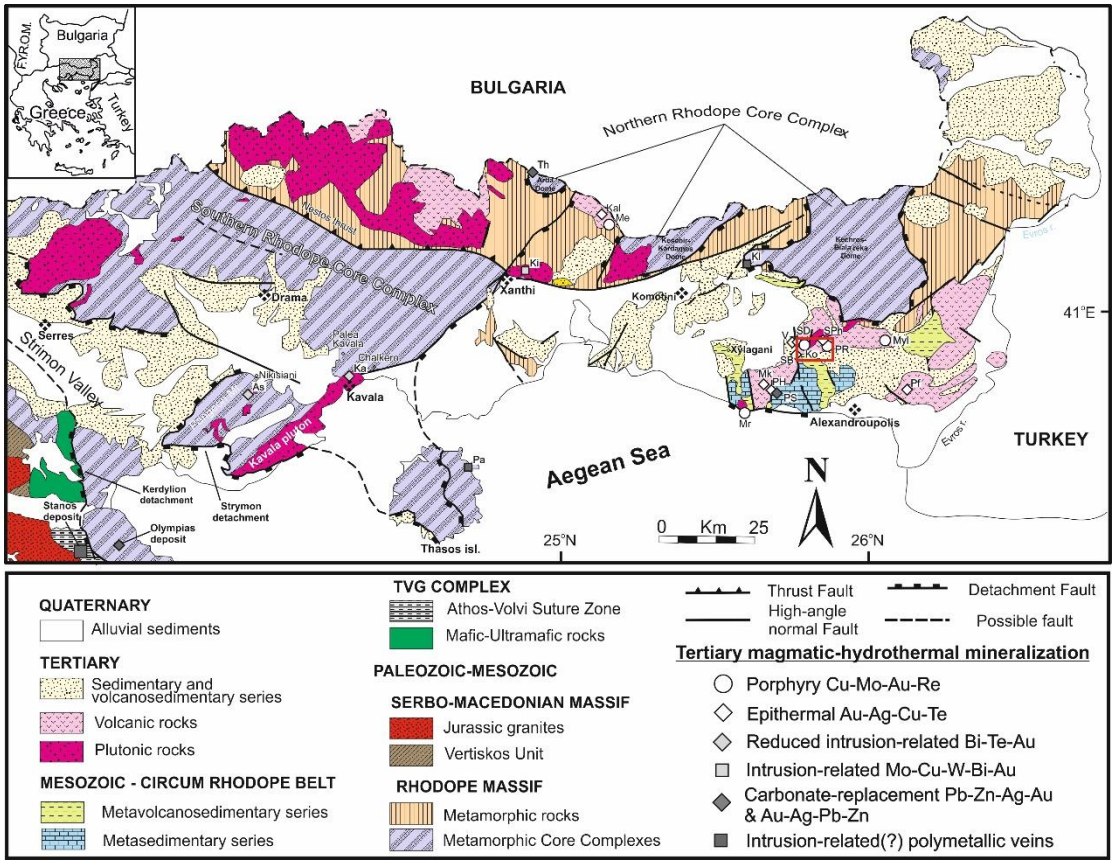

Figure 4.1. Simplified geological map of the Rhodope metallogenic province in NE Greece, also displaying the major Tertiary ore deposits and prospects (after Voudouris et al., 2016a). The study area is highlighted. Abbreviatied names of ore deposits and prospects: Th = Thermes, Ki= Kimmeria/Xanthi, Klt = Kalotycho, Me = Melitena, Mr = Maronia, Ko = Konos/Sapes, SB = St. Barbara/Kassiteres, SD = St. Demetrios/Sapes, V = Viper, PH = Perama Hill, Mk = Mavrokoryphi, PR = Pagoni Rachi/Kirki, SPh = St Philippos/Kirki, Pf = Pefka, Ltr = Loutros, Kl = Kallintiri, Myl = Myli/Esymi.

Of these intrusive rocks, the pyroxene-hornblende diorite porphyry does not crop out in the study area. Fresh rocks are almost absent in the area, being hydrothermally-altered, with sericitic alteration being the most widespread type. The hornblende-biotite granodiorite porphyry is the most common lithology in the area and comprises a microlitic feldspar matrix (orthoclase, plagioclase and minor quartz) with embedded phenocrysts of hornblende, plagioclase, biotite and rare quartz, along with minor opaque phases. Small bodies of pyroxene-biotite microdiorite occur mainly north of the Papadokoryphi Hill (Figure 4.2), where they hosts porphyry-type mineralization (Mavrogonatos et al., 2018a). Quartz monzodiorite occupies the northern part of the study area and is a granular to porphyritic intrusive rock consisting mainly of plagioclase, pyroxene, hornblende, biotite, and minor amounts of ilmenite and

magnetite. The microgranite porphyry is the latest intrusive phase and its emplacement is facilitated by NW-, and rarely E-trending faults. Mostly altered, this rock is characterized by phenocrysts of plagioclase, orthoclase, rare biotite and resorbed quartz and hosts porphyry-style stockworks and associated base metal mineralization at Koryphes Hill, to the west of the study area (Voudouris, 2014). Radiometric data from the area are quite limited and refer to ages of 31.9±0.5 Ma (Rb/Sr on biotite; Del Moro et al., 1988) and 32.05±0.07 Ma (U-Pb zircon age; Perkins et al., 2018) for the quartz monzodiorite, and 32.6±05 Ma for the granodiorite porphyry (Ortelli et al. 2010). Regarding the late microgranite porphyry dykes, available K-Ar ages are available only from the Eastern Bulgarian Rhodopes, at about 28-25.5 Ma (Lilov et al., 1987).

The tectonic regime in the area is expressed mainly by four sets of fault directions: N-S, E-W, ENE-WSW and NNW-SSE (Figure 4.2). The latter is related to major ore-bearing structures, including the St Phillipos polymetallic deposit (Vavelidis et al. 1989; Michailidis et al. 1989, Dimou 1993; Skarpelis 1999; Voudouris et al. 2005b).

4.3 Materials and methods

Detailed mapping of the study area was based on topographic maps at 1:5000, supplied by the Hellenic Military Geographical Service. In the absence of drilling data, mapping and sampling was based on surface outcrops in an area that covers approximately 35km^2. Field data were imported in ArcGIS 9.3 for the production of georeferenced geological and alteration maps. A total of 198 samples from altered and mineralized rocks were collected from the Sapes and Kirki areas. From those samples, 123 thin-and-polished sections of fresh and altered host rocks, and 227 polished ore sections underwent detailed mineralogical investigation using transmitted and reflected light optical microscopic techniques (including samples B26, P62 and SP20, kindly provided by Dr. P. Voudouris). Moreover, 117 mineralized and 20 fresh to propylitic-altered samples were analyzed in order to study their geochemical characteristics. Analyses of both altered and mineralized samples were conducted at the ACME analytical laboratories, Canada. An analytical protocol of 1:1:1 Aqua Regia digestion and Ultra trace ICP-MS analytical method was used for the

mineralized samples, while a combination of XRF (for the major) and ICP-MS (for the trace elements) methods was used for the magmatic rocks. Alteration assemblages were also determined using short-wave infrared spectroscopy (SWIR) and X-rays diffraction (XRD) on selected representative samples.

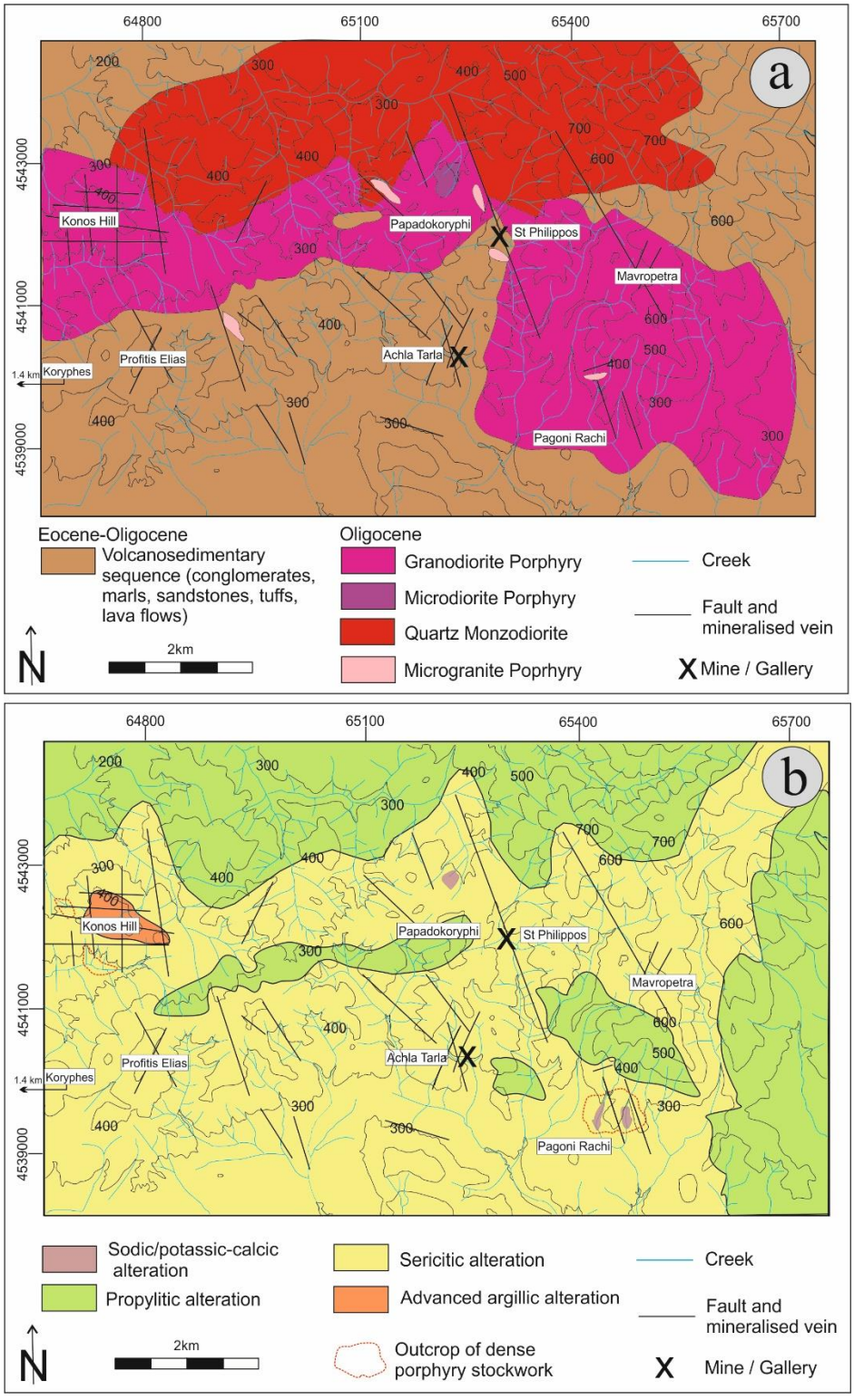

Figure 4.2: Geological (a) and alteration (b) map of the study area.

SWIR analyses were conducted in selected altered rock chips using a portable TerraSpec 4 Standard-Res mineral analyzer at the Eldorado Gold's core yard in Sapes. Spectra were processed through the TSG Pro mineral analysis software for interpretation of the detected alteration minerals. Powders of selected altered samples were processed by X-ray diffraction, using a Brooker (Siemens) 5005 X-ray diffractometer, in conjunction with the DIFFRACplus software. All samples were scanned between 3^o and 65^o 2θ angle with 1^o/min velocity (step size ~0.01^o/sec), using the Kα radiation of a Cu X-ray tube, operated at a voltage of 40 kV and a current of 40 mA. The obtained X-ray diffraction patterns were evaluated with the EVA software, version 10.0.

Petrographic remarks on alteration minerals were made with an Axio Scope. A1 (Zeiss) transmitted light optical microscope and, a JEOL JSM 5600 scanning electron microscope equipped with back-scattered imaging capabilities (which also provided semi-quantitave analyses of mineral phases), at the Department of Mineralogy and Petrology, University of Athens, Greece. The chemical composition of alteration minerals was determined using a JEOL 8530F instrument (Field emission electron probe microanalyzer, FEG-EPMA), at the Institute of Mineralogy, University of Münster, Germany. Analytical conditions included a 15-kV accelerating voltage, a 5-nA beam current, and counting times of 10 s for peaks and 5 s for the background signal. Natural (for Na, Mg, Al, Si, Mn, Fe, Sr, Cl, Ba, K, Ca, P, and S) and synthetic (for F, Ti, Cr, La, Ce, Nd, and Pb) mineral standards were used for calibration prior to quantitative analyses. The phi-rho-z correction was applied to all data. Standard deviations of the major oxides are within 1-2%. Oxides and elements that were analyzed and their average (1σ) detection limits are: Na_2O (0.046 wt %), MgO (0.43 wt %), Al_2O_3 (0.038 wt %), SiO_2 (0.058 wt %), MnO (0.054 wt %), FeO (0.057 wt %), Cr_2O_3 (0.20 wt%), SrO (0.082 wt %), Cl (0.021 wt %), BaO (0.094 wt %), K_2O (0.032 wt %), CaO (0.038 wt %), P_2O_5 (0.049 wt %), SO_3 (0.063 wt %), F (0.14 wt %), TiO_2 (0.13 wt %), La_2O_3 (0.25 wt %), Ce_2O_3 (0.20 wt %), Nd_2O_3 (0.20 wt %), and PbO (0.05 wt %).

Metallic minerals (oxides, sulfides, sulfosalts, native elements) were studied with reflected-light microscopy and a JEOL JSM 5600 scanning electron microscope equipped with back-scattered imaging capabilities, at the Department of Mineralogy and Petrology, University of Athens, Greece. Their chemical composition was

determined using a JEOL JXA 8200 Superprobe electron-microprobe at the "Eugen F. Stumpfl" Laboratory, Leoben University, Austria. The operating conditions were: accelerating voltage 20 kV, beam current 10 nA, beam size ≈ 1 µm. Counting times were 20 s on the peak and 10 s on the backgrounds for major elements. The counting times were increased to 60 s and 30 s for peak and backgrounds, respectively, when analyzing the trace elements. The following X-ray lines were used: AsLα, SeLα, SKα, FeKα, SbLα, BiMα, AgLα, AuLa, PbLα, GeLα, GaKα, ZnKα, InLα, CuKα, TeLα, MoLα, WLα, ReLα, SnLα, MgKα, AlKα, SiKα, CaLα, TiKα, VKα, CrKα, MnLα, CoKα, and NiLα, with respect to the following standards (average (1σ) detection limits are given in parenthesis): synthetic GAaS for As (350 ppm) and Ga (150 ppm), synthetic $AgBiSe_2$ for Se (200 ppm) and Bi (450 ppm), natural pyrite for S and Fe (150 ppm), natural stibnite for Sb (350 ppm), synthetic electrum for Au and Ag (100 ppm), natural galena for Pb (700 ppm), synthetic Ge 100% for Ge (150 ppm), natural sphalerite for Zn (400 ppm), synthetic In 100% for In (250 ppm), natural chalcopyrite for Cu (150 ppm), synthetic Bi_2Te_3 for Te (150 ppm), natural molybdenite fro Mo (500 ppm), synthetic W 100% for W (300 ppm), synthetic Re 100% for Re (300 ppm), synthetic cassiterite for Sn (150 ppm), corundum for Al (200 ppm), wollastonite for Si (270 ppm) and Ca (270 ppm), rutile for Ti (700 ppm), synthetic V 100% for V (150 ppm), natural chromite for Mg (250 ppm) and Cr (250 ppm), rhodonite for Mn (400 ppm), natural skutterudite for Co (150 ppm), and natural millerite for Ni (150 ppm). Corrections were applied using the PAP online program (Pouchou and Pichoir, 1991).

Laser ablation-ICP-MS analyses of the selected samples were conducted at the Institute of Mineralogy, University of Münster, Germany, with a pulsed 193 nm ArF excimer laser (Analyte G2, Photon Machines). Pre-defined areas of the polished sections were ablated using a 35 µm-sized spot diameter. A repetition rate of 10 Hz and an energy of ~4 J/cm^2 were used throughout the session. The laser system was coupled to an Element 2 mass spectrometer (ThermoFisher). Forward power was 1250 W and reflected power <1 W, gas flow rates were 1.2 L/m for He carrier gas, 0.9 L/m and 1.2 L/m for the Ar-auxiliary and sample gas, respectively. The argon cooling gas flow rate was set to 16 L/min. Before starting an analysis, the system was calibrated to a NIST 612 reference glass measuring ^{139}La, ^{232}Th and $^{232}Th^{16}O$ to get stable signals

and high sensitivity, as well as low oxide rates ($^{232}Th^{16}O/^{232}Th < 0.1\%$) during ablation. The NIST 612 glass was used as internal standard.

For biotite 43 elements (^{7}Li, ^{9}Be, ^{11}B, ^{43}Ca, ^{45}Sc, ^{47}Ti, ^{51}V, ^{53}Cr, ^{55}Mn, ^{59}Co, ^{60}Ni, ^{66}Zn, ^{69}Ga, ^{72}Ge, ^{85}Rb, ^{88}Sr, ^{89}Y, ^{90}Zr, ^{93}Nb, ^{111}Cd, ^{118}Sn, 133Cs, 137Ba, 139La139, 140Ce140, $^{141}Pr141$, ^{146}Nd, ^{147}Sm, ^{153}Eu, ^{157}Gd, ^{159}Tb, ^{163}Dy, ^{165}Ho, ^{166}Er, ^{169}Tm, ^{172}Yb, ^{175}Lu, ^{178}Hf, $^{181}Ta1$, ^{208}Pb, ^{232}Th, ^{238}U) were analysed, using Si previously defined by EPM analyses as internal standard. For sphalerite, 20 elements (^{55}Mn, ^{56}Fe, ^{59}Co, ^{60}Ni, ^{63}Cu, ^{69}Ga, ^{73}Ge, ^{75}As, ^{77}Se, ^{95}Mo, ^{107}Ag, ^{111}Cd, ^{115}In, ^{118}Sn, ^{121}Sb, ^{182}W, ^{197}Au, ^{205}Tl, ^{208}Pb, and ^{209}Bi) were analysed, using sulfur previously determined by EPM analyses, as the internal standard. For magnetite, 26 elements (^{25}Mg, ^{27}Al, ^{29}Si, ^{43}Ca, ^{45}Sc, ^{49}Ti, ^{51}V, ^{53}Cr, ^{55}Mn, ^{59}Co, ^{60}Ni, ^{63}Cu, ^{66}Zn, ^{69}Ga, ^{85}Rb, ^{88}Sr, ^{89}Y, ^{90}Zr, ^{93}Nb, ^{95}Mo, ^{118}Sn, ^{137}Ba, ^{178}Hf, ^{181}Ta, ^{182}W and ^{208}Pb) were quantitatively analyzed using stoichiometric Fe (97% wt.% FeO) as internal standard, since total concentration of minor elements is <3 wt.% (cf. Milani et al., 2017). For pyrite, a total of 20 elements (^{55}Mn, ^{59}Co, ^{60}Ni, ^{63}Cu, ^{66}Zn, ^{69}Ga, ^{73}Ge, ^{75}As, ^{77}Se, ^{95}Mo, ^{107}Ag, ^{111}Cd, ^{115}In, ^{118}Sn, ^{121}Sb, ^{182}W, ^{197}Au, ^{205}Tl, ^{208}Pb, and ^{209}Bi) were quantitatively analyzed, using sulfur previously determined by EPM analyses, as the internal standard.

Run time of the single ablation pattern was 60 s (20 s for background, 40 s for peak after switching the laser on). Concentrations of measured elements were calculated using the Glitter software (van Achterbergh et al., 2001; Griffin et al., 2008). Standard reference glasses BHVO-2G and BIR1-G were analyzed in order to monitor for precision and accuracy. The results obtained from these glasses matched the published range of concentrations (standard deviation in the range of 5%), given in the GeoReM database (version 23, Jochum et al., 2005).

Average detection limits for the analyzed elements are as follows (in ppm): Li = 2.47, Be = 1.16, B = 3.46, Ca = 505, Sc = 1.13, Ti = 31, V = 2.48, Cr = 16, Mn = 0.8, Fe = 4.2, Co = 0.3, Ni = 4, Cu = 0.5, Zn = 4, Ga = 0.2, Ge = 1.3, Rb = 0.57, Sr = 0.27, Y = 0.11, Zr = 2.01, Sn = 0.53, Cs = 0.18, Ba = 0.47, La = 0.03, Ce = 0.004, Pr = 0.03, Nd = 0.12, Sm = 0.19, Eu = 0.04, Gd = 0.20, Tb = 0.02, Dy = 0.10, Ho = 0.02, Er = 0.07, Tm = 0.02, Yb = 0.12, Lu = 0.02, Hf = 0.08, Ta = 0.04, Nb = 0.06, As = 1.9, Se = 5.6, Mo = 0.15, Ag = 0.8, Cd = 0.8, In = 0.06, Sn = 0.3, Sb = 0.19, W = 0.04, Au = 0.04, Tl = 0.02, Pb = 0.06, Bi = 0.03.

4.4. Geochemistry of magmatic rocks

Fifteen representative samples (10 samples of granodiorite porphyry, with the least intense propylitic overprint possible) and 5 samples of monzodiorite (fresh to slightly propylitised) were selected for geochemical analyses. Furthermore, 5 (4 sericitic-, and 1 potassic-altered) microgranite porphyry samples were also analyzed for comparison. The geotectonic classification and chemical variations of the magmatic rocks are illustrated in Figures 4.3, 4.4 and 4.5, while the full dataset of the chemical analyses is presented in the Appendix D.

In the TAS classification diagram (Le Bas et al., 1986), the analyzed samples are characterized as intermediate to acidic and plot in the field of subalkaline/tholeiitic rocks (Figure 4.3a). Samples from both Pagoni Rachi and Sapes area plot at the borders between diorite and granodiorite (Figure 4.3c), while the microgranite porphyry samples fall slightly outside their predicted field, thus reflecting their strong alteration. In the K_2O versus SiO_2 plot (Figure 4.3b) after Peccerillo and Taylor (1976), all samples scatter between the calk-alkaline and high-K calk-alkaline series, due to their varying K_2O content, which is a result of different degrees of hydrothermal alteration. Al_2O_3 values seem to correlate with slightly decreasing total amount of CNK values ($CaO+Na_2O+K_2O$), and thus the analyzed samples plot in both metaluminous and peraluminous fields in the A/CNK vs A/NK diagram (Shand 1943).

Moreover, the studied rocks are characterized by a relatively fixed Y+Nb content, coupled with slightly varying Rb content and plot in a narrow area of the Rb vs. (Y+Nb) (Pearce at al., 1984, 1996) reflecting their post-collisional affinities (Figure 4.3d).

The trace elements concentrations of the studied magmatic rocks, were normalized to the primitive mantle values of McDonough and Sun (1995). Figure 4.3e shows that samples from both areas show relatively identical patterns, with the exception of a few notable differences. A highly variable Cs content is recorded in the samples, fact that also holds true, but to a lesser extend for Ba and Th. A relatively strong Nb anomaly is recorded in all samples. Varying Sr content characterizes the granodiorite and monzodiorite samples, while a depletion in Sr is recorded by the microgranite porphyries. Finally, all rock samples display a prominent Ti depletion, which is more significant in the microgranite porphyry samples.

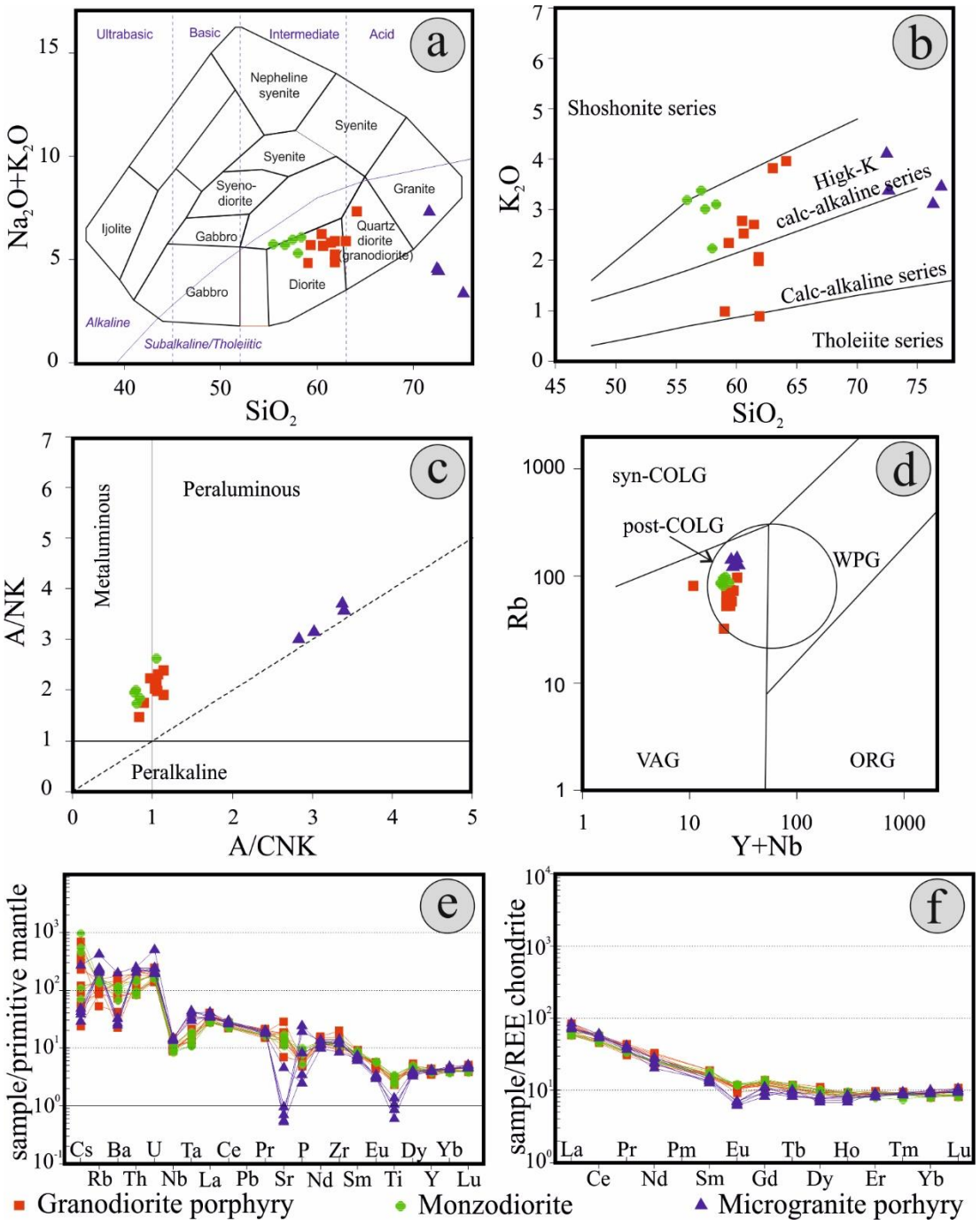

Figure 4.3: Classification of magmatic rocks in the study area: (a) Total alkali versus silica plot, rock fields are from Le Bas et al. (1986). The boundary between the alkaline and subalkaline fields is from Irvine and Baragar (1971); (b) SiO_2 vs K_2O diagram (Peccerillo and Taylor, 1976); (c) A/CNK vs A/NK plot from Shand (1943). (A/NK=molar ratio of $Al_2O_3/(Na_2O+K_2O)$; A/CNK=molar ratio of $Al_2O_3/(CaO+Na_2O+K_2O)$; (d) Rb versus Y+Nb diagram after Pearce et al. (1984). VAG, Volcanic Arc Granite; Syn-COLG, Syn-collisional Granite; WPG, Within-Plate Granite; ORG, Ocean Ridge Granite, post-COLG, Post-collisional Granite. The field of post-collisional granite (Post-COLG) is from Pearce (1996); (e) Primitive mantle-normalized (McDonough and Sun, 1995) trace

element and (f) Chondrite-normalized (Boynton, 1984) rare earth element patterns of the studied rocks.

Rare earth elements (REE) values of the studied lithologies normalized to REE-chondrite (Boynton, 1984) reveal that magmatic rocks from the Sapes and Pagoni Rachi areas share common patterns (Figure 4.3f), characterized by light REE enrichment compared to the heavy REE's and relatively weak negative Eu anomalies, which are more prominent in the microgranite porphyry.

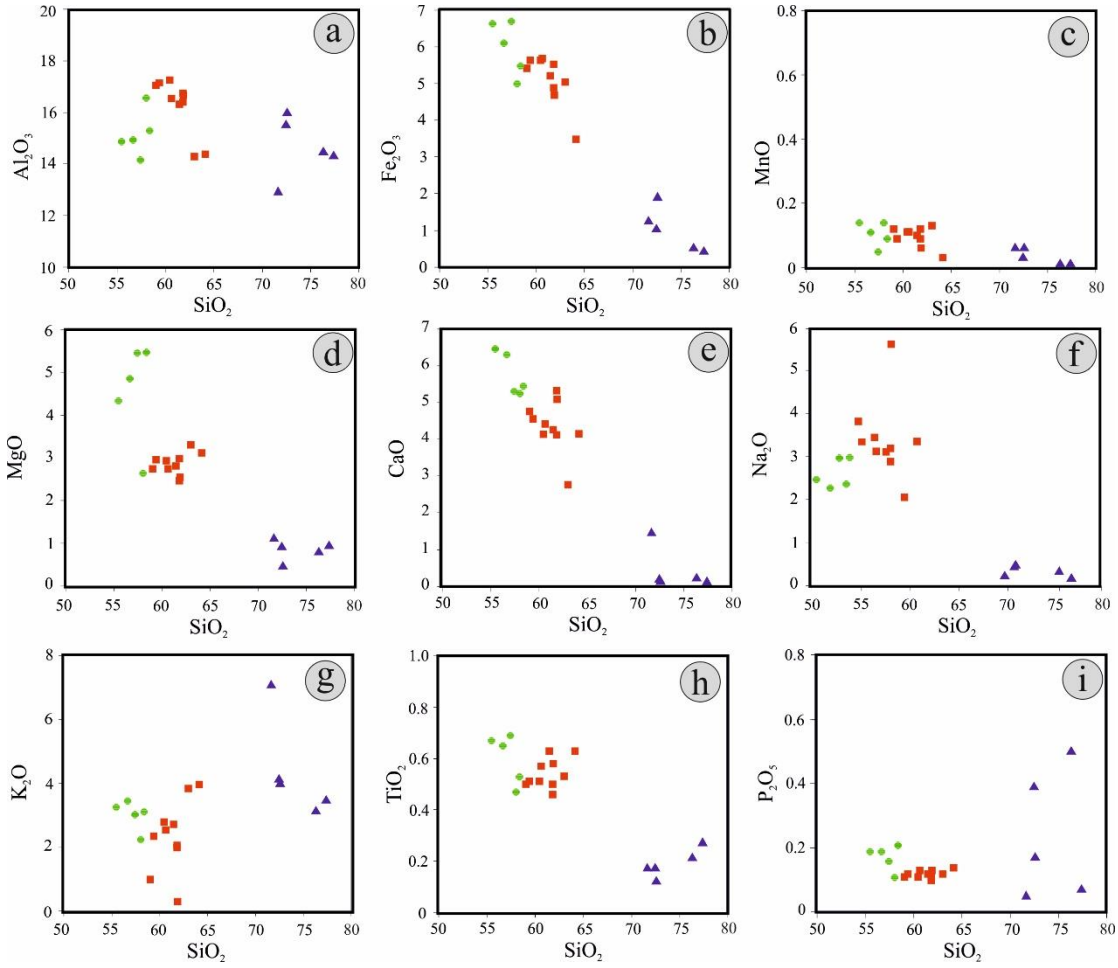

Figure 4.4: Selected oxides Harker plots for the magmatic rocks of the study area. Symbols as in Figure 4.3.

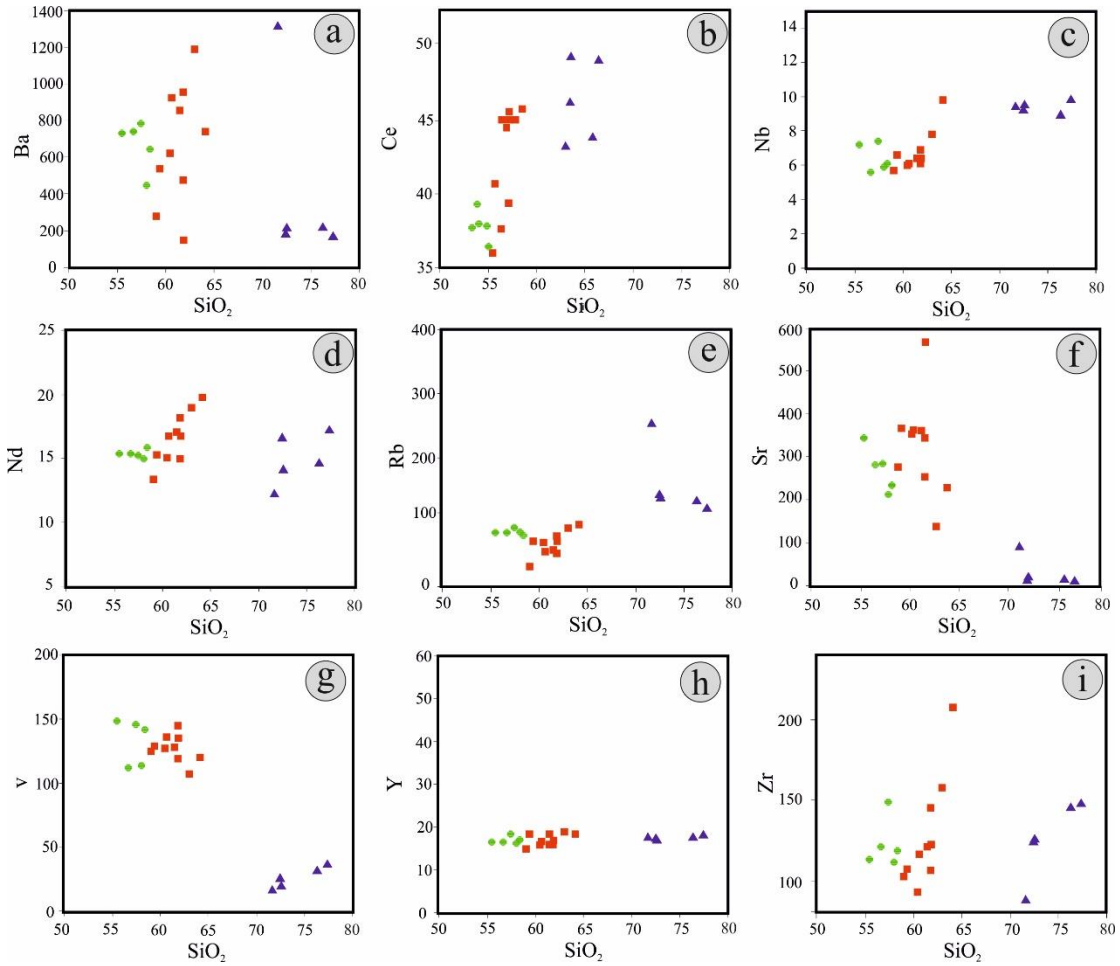

Figure 4.5: Selected trace elements Harker plots for the magmatic rocks of the study area. Symbols as in Figure 4.3.

Harker plots made for selected oxides (Figure 4.4) and trace elements (Figure 4.5) reflect the significant variation of these elements in the studied rocks. Moreover, the majority of the samples in most of the plots are set in linear trends, thus indicating their chemical differentiation due to fractionation, as for example stated by the compatible elements, like Fe and Ti, whose content decreases in respect to an increase of the SiO_2 content.

4.5. Alteration and mineralization

Porphyry-, and spatially associated epithermal-style mineralization occurs in the western, central and eastern parts of the Sapes-Kirki area. Magmatic rocks that host mineralization were subjected to different styles of alteration. The mineralogy of each

type of alteration and related ore mineralization is summarized in Table 4.11, while field, hand-specimen, alteration and ore assemblages photographs are illustrated in pictures 4.6 to 4.12.

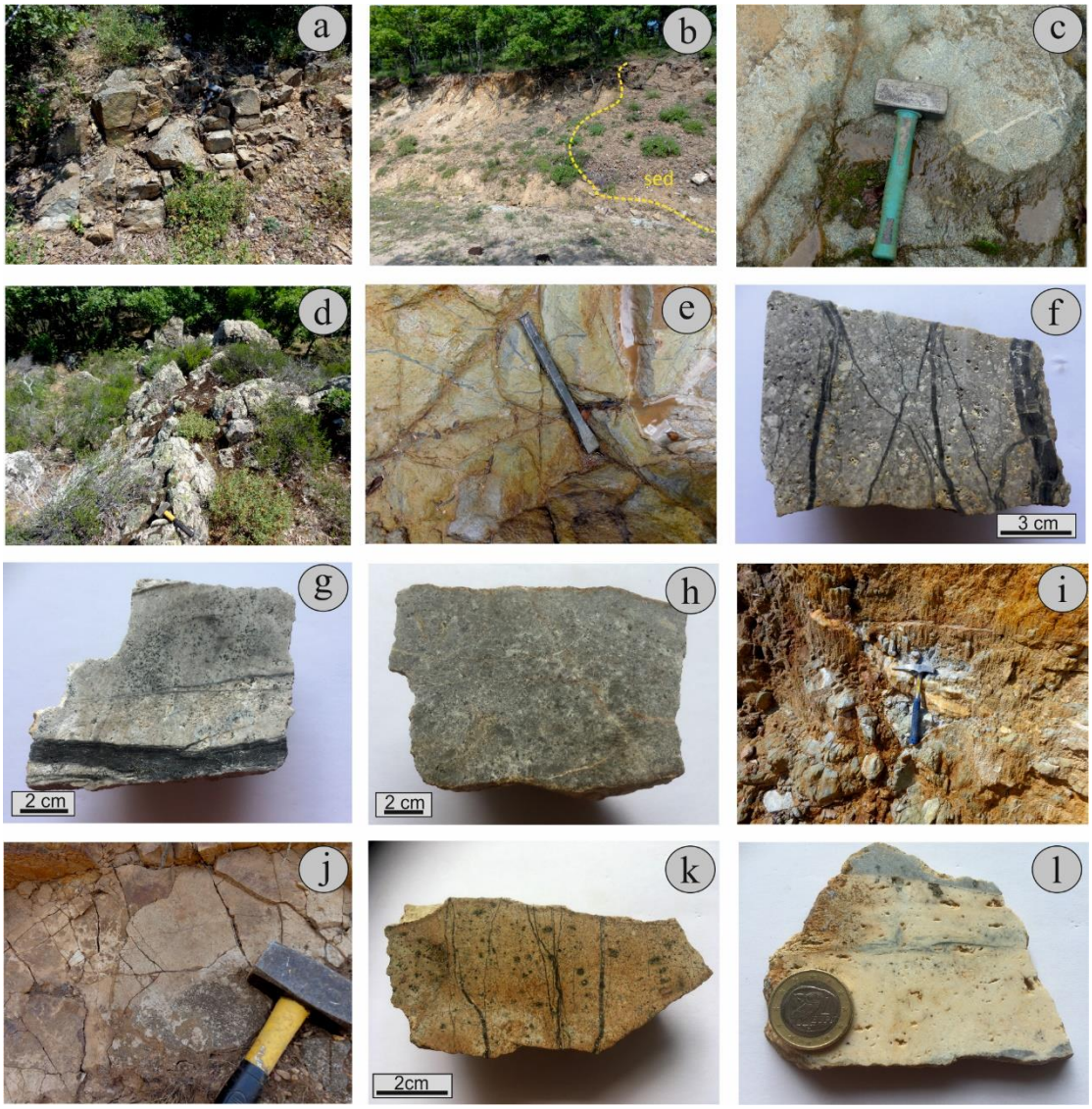

Figure 4.6: Field and hand-specimen photographs of porphyry/epithermal mineralization and alteration at the broad Sapes area. (a) Fresh to propylitic-altered granodiorite porphyry; (b) Marls uncomformably onerlying the sericitic-altered granodiorite porphyry; (c) Monzodiorite, slightly propylitized; (d) N10°W-trending microgranite porphyry dyke, close to Papadokoryphi hill; (e) Dense quartz porphyry stockwork, from the eastern slopes of Konos Hill; (f, g) Hand-specimen of quartz stockowokr from Konos Hill. Note in g, the banded appearance of the vein and the pyrite center-line; (h) Sodic (albite)-altered granodiorite; (i) Gypsum vein (early anhydrite?) with base metal mineralization; (j,k) Weak quartz porphyry sotockwork

associated with calcic/potassic altered granodiorite porphyry, Papadokoryphi Hill; (l) Epithermal-style (E-type) quartz-calcite vein.

Table 4.1: Typology and alteration characteristics of mineralization stages, from the Konos Hill, Papadokoryphi, and Pagoni Rachi porphyry/epithermal prospects.

Prospect	Vein type	Vein assemblage	Alteration assemblage	Form, texture, zonation
Konos Hill	A-, B-type/ D-type, overprint on earlier quartz veins	Qz + Py + Ccp ± Mol + Rhe + Bn + Po + Hem + Ser	Ser + Qz ± Cal ("Sericitic")	Continuous (banded) quartz/ pyrite veins / pyrite-molybdenite±chalcopyrite veins reopening and overprinting earlier quartz veins
	"Epithermal" (E-type)	Qz + Cal + Sp + Gn + Py + Ccp ± Col + Tnt/Ttr ± Eng ± Ag-Au	Qz + Cal + Ser ± Kln ("Argillic")	Continuous straight-sided, up to 15 cm wide, quartz-carbonate veins with sharp parallel walls
Papadokoryphi	A-type	Qz + Py + Ccp ± Mol+Ep	Qz + Or/Ab + Ep + Bt + Chl ± Ser ("Potassic-Calcic")	Narrow, irregular-shaped, wispy veinlets
Pagoni Rachi	M-type	Mag + Ccp + Hem + Py + Bn + Or/Ab + Bt + Act + Ep + Mol + Au	Qz + Or/Ab + Act + Ep + Bt + Chl + Cal + Mag ("Sodic/Potassic-Calcic")	Narrow (width less than 0.5 cm), irregular in shape and discontinuous and/or straight-sided veinlets
	A-type	Qz + Mag + Py + Or/Ab + Bt + + Act + Ep + Ccp ± Bn ± Mol ± Po ± Chl ± Fl	Qz + Bt + Or/Ab + Act + Ep + Tit + Mag ± Chl ± Cal ("Sodic/Potassic-Calcic")	Continuous, wispy quartz veins, locally, centerlines of magnetite and/or pyrite. At places banded texture.
	B-type	Qz + Py + Ccp + Mol ± Rhn ± Hem ± Po ± Mag ± Ab ± Chl ± Cal ± Ser	Qz ± Ab/Or ± Chl ± Cal ± Ser ("Sodic/Potassic")	Continuous, quartz veins with sharp parallel walls, up to 20cm wide, locally banded
	D-type	Py + Ccp ± Mol + Po + Hem + Ser ± Qz ± Au + Cal ± Rhe ± Bn ± Gn	Qz + Ser + Py ± Cal ("Sericitic")	Continuous, up to 10cm wide, massive pyrite veins and reopening and overprinting earlier quartz veins
	"Epithermal" (E-type)	Qz + Cal + Sp + Gn + Ccp + Py ± Tnt/Ttr ± Ag-Au alloy ± Ser ± Kln	Qz + Cal + Ser ± Kln ("Argillic")	Continuous straight-sided, up to 20 cm wide, quartz-carbonate veins with sharp parallel walls

Western part (Konos Hill)

The Konos Hill area at Sapes (Figure 4.2) occupies the W-NW part of the study area and is dominated by a granodiorite porphyry intrusion, which hosts porphyry Cu-Mo-Re, disseminated sulfide, and polymetallic base metal vein mineralization (Voudouris et al. 2006; Ortelli et al. 2009, 2010). Unaltered magmatic rocks are almost absent from the area due to widespread hydrothermal alteration (Figure 4.6). Propylitic alteration of granodiorite porphyry was recognized north of Konos Hill (Figure 4.6a), whereas further to the northeast propylitic assemblages also occur in the quart-monzodiorite (Figure 4.6c). The propylitic altered monzodiorite is an equigranular, fine-grained rock characterized by abundant epidote, plagioclase, biotite, hornblende, ortho-, and clinopyroxene, and chlorite, whereas propylitized porphyritic granodiorite is characterized by abundant epidote, hornblende, plagioclase, and quartz (Figure 4.7a,b). Epidote in propylitic-altered granodiorite is volumetrically more common towards the central part of the alteration zone, closer to widespread sericite-altered granodiorite of the Konos Hill porphyry. Where epidote is less abundant, chlorite and calcite tend to be more common at the more distal parts.

Advanced argillic alteration assemblages are exposed at the higher topographic levels of Konos Hill (see Chapter 5), mostly surrounding vuggy silica zones along N-S and E-W trending faults (Voudouris et al. 2006; Ortelli et al. 2009; Voudouris, 2014; this study). These zones are characterized by a core dominated by vuggy (and/or massive silica), grading into zones dominated by alunite and quartz, with minor amounts of diaspore, pyrophyllite, and dickite/kaolinite and zunyite (Figure 4.7de-f). Relics of sodic alteration dominated by quartz-albite-chlorite (Figure 4.6h) assemblages were observed at the NW and SE foothills of Konos Hill, although a sericitic overprint is often present in the whole area. The sodic-altered rocks have a characteristic grey-colored appearance and a fine-grained texture, dominated by albite (Figure 4.6h). The sericite overprint becomes pervasive at Konos Hill mainly in areas of major N-S, NW-SE and E-W trending faults, or in areas that quartz stockwork is present.

Two surface outcrops of very dense porphyry style stockwork veins were mapped at Konos Hill, and occur in a linear direction that trends N0-20°W.

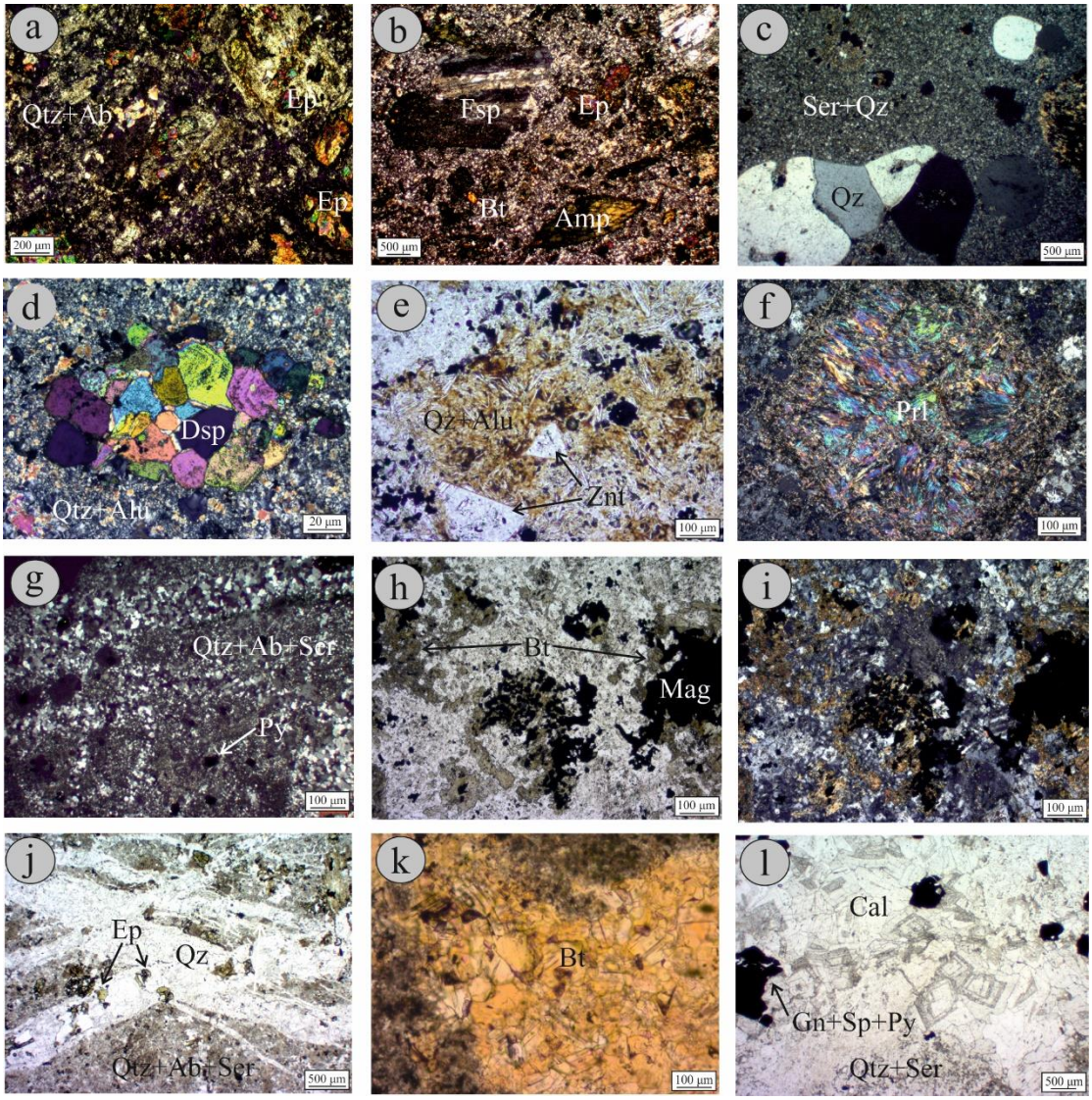

Figure 4.7: Transmitted light photomicrographs of various ateration assemblages from the Sapes (a to h, l), Papadokoryphi (i, j) and Koryphes (k). All photomicrographs but e, j, k, and l, taken under cross-polarized light: (a,b) Propylitic-altered granodiorite porphyry. Mafic magmatic phenocrysts, commonly amphibole-hornblende (amph) and biotite (Bt) are altered to epidote (Ep) and set in a quartz (Qz) and albite (Ab) dominated matrix; (c) Sericitic altered microgranite porphyry. Note the resorbed quartz (Qz) phenocrysts (quartz eyes) scattered in the fine grained, sericitic-altered matrix (Ser+Qz); (d-e) Diaspore (Dsp), alunite (Alu), zunyite (Znt) and pyrophyllite (Prl) from the advanced argillic alteration zone of Konos Hill; (g) Quartz stockwork veins crosscutting sodic-altered granodiorite porphyry. A sericitic (Ser) overprinting is obvious; (h,i) Weak potassic/calcic alteration with shreddy hydrothermal biotite (bt) accompanying magnetite (Mag); (j) Quartz (Qz) porphyry stockwork veinlets crosscutting potassic/calcic altered granodiorite porphyry; (k) Pervasive potassic alteration (biotite, bt) from the Koryphes prospect; (l) Zoned calcite (Cal) including base metal sulfides (galena-Gn, sphalerite-Sp, and pyrite-Py) from E-type vein, associated with quartz (Qz) and sericite (Ser) alteration of the wall rock.

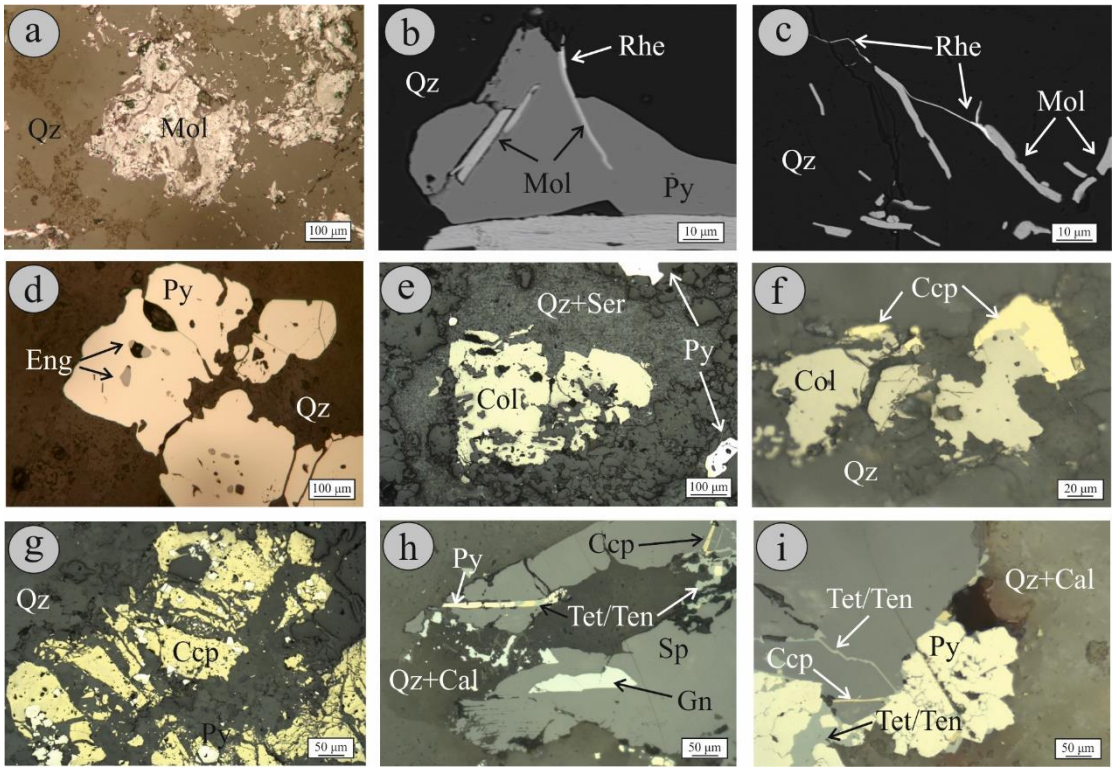

Figure 4.8: Refleceted-light photomicrographs and back-scattered electron images (b, c) from ore mineral assemblages at the Sapes area. (a) Molybdenite (mol) in quartz (Qz) stockwork vein; (b,c) Rheniite (Rhe) crystals in association with molybdenite (Mol) and pyrite (Py), embedded in quartz (Qz); (d) Enargite (Eng) included in pyrite (py); (e, f) Colusite (in figure f, associated with chalcopyrite, Ccp), set in quartz (Qz) and sericite (Ser) altered granodiorite porphyry; (g) Chalcopyrite (Ccp) in quartz (Qz) – calcite epithermal style (E-type) vein; (h,i) Fahlores (Tet/Ten) associated with sphalerite (Sp), galena (Gn), pyrite (Py) and chalcopyrite (Ccp), in quartz (Qz) - calcite (Cal) epithermal stye vein.

Stockwork is formed by wavy to planar, granular quartz veins (A-, and B-type veins, Figure 4.6 e-g). In many cases, alternating zones of clear/milky and black-colored quartz result in a banded appearance of these veins (Figure 4.6f,h). A pyrite center-line is commonly found inside these veins, and along with pyrite-molybdenite veins, they represent a subsequent mineralization stage (D-event), associated with pervasive sericitic alteration (Figure 4.6g).

Ore minerals occur either as disseminations in the matrix of the host rock, or are carried in the quartz veins. Pyrite, molybdenite, rheniite, magnetite, pyrrhotite, chalcopyrite, and minor amounts of colusite, bornite and enargite were identified (Figure 4.8a-f). The ore minerals are spatially associated with sericitic alteration, which

is dominated by illitic sericite, also verified by SWIR spectroscopy (Appendix G). Rheniite is associated with Re-rich molybdenite and forms microscopic hair-like crystals embedded in quartz and/or pyrite (Figure 4.8b,c). At places enargite was identified as inclusion in pyrite, while colusite occurs as disseminated grains in the sericitic-altered granodiorite (Figure 4.8e-f). In a few places, gypsum veins host pyrite, Se-galena and fahlores, and probably represent earlier anhydrite veins, associated with the D-type mineralization event (Figure 4.6i). Locally, N-S, to N10°W trending epithermal-style (E-type) quartz-carbonate veins crosscut both the granodiorite porphyry and the monzodiorite and are related to meter-sized lateral zones of argillic alteration. These veins are composed by quartz and calcite, and contain chalcopyrite, pyrite, sphalerite, and minor amounts of tennantite-tetrahedrite group minerals (Figures 4.6l, 4.7l, 4.8g-i).

South of Konos Hill, the area is dominated by Eocene sandstones and conglomerates subjected to intense sericitic alteration and host fault-related and disseminated oxidized epithermal mineralization (e.g., Profitis Elias area, Figure 4.2). Sericite altered microgranite porphyry bodies intrude both the granodiorite porphyry and the sedimentary sequence along N0-20°W trending faults. The most characteristic feature of this rock is the abundance of resorbed quartz and sericite-altered orthoclase phenocrysts, set in a very fine-grained quartz-sericite matrix (Figure 4.6d, 4.7c). No mineralization was found in these bodies in the study area, but minor disseminations of pyrite.

The absence of potassic alteration assemblages is characteristic for the Konos Hill area. As stated before, only minor relict zones of albitic (sodic) alteration were identified. However, in the nearby area of Koryphes hill, surface outcrops have been identified, dominated by the presence of hydrothermal biotite and associated with porphyry-style mineralization (Voudouris 1994; Voudouris and Arikas 1994). K-alteration occurs in selective or pervasive form (Figure 4.7k), and such biotite samples were studied in the present work for mineral chemical-comparison to magmatic and hydrothermal biotite from the Pagoni Rachi and the Papadokoryphi prospects.

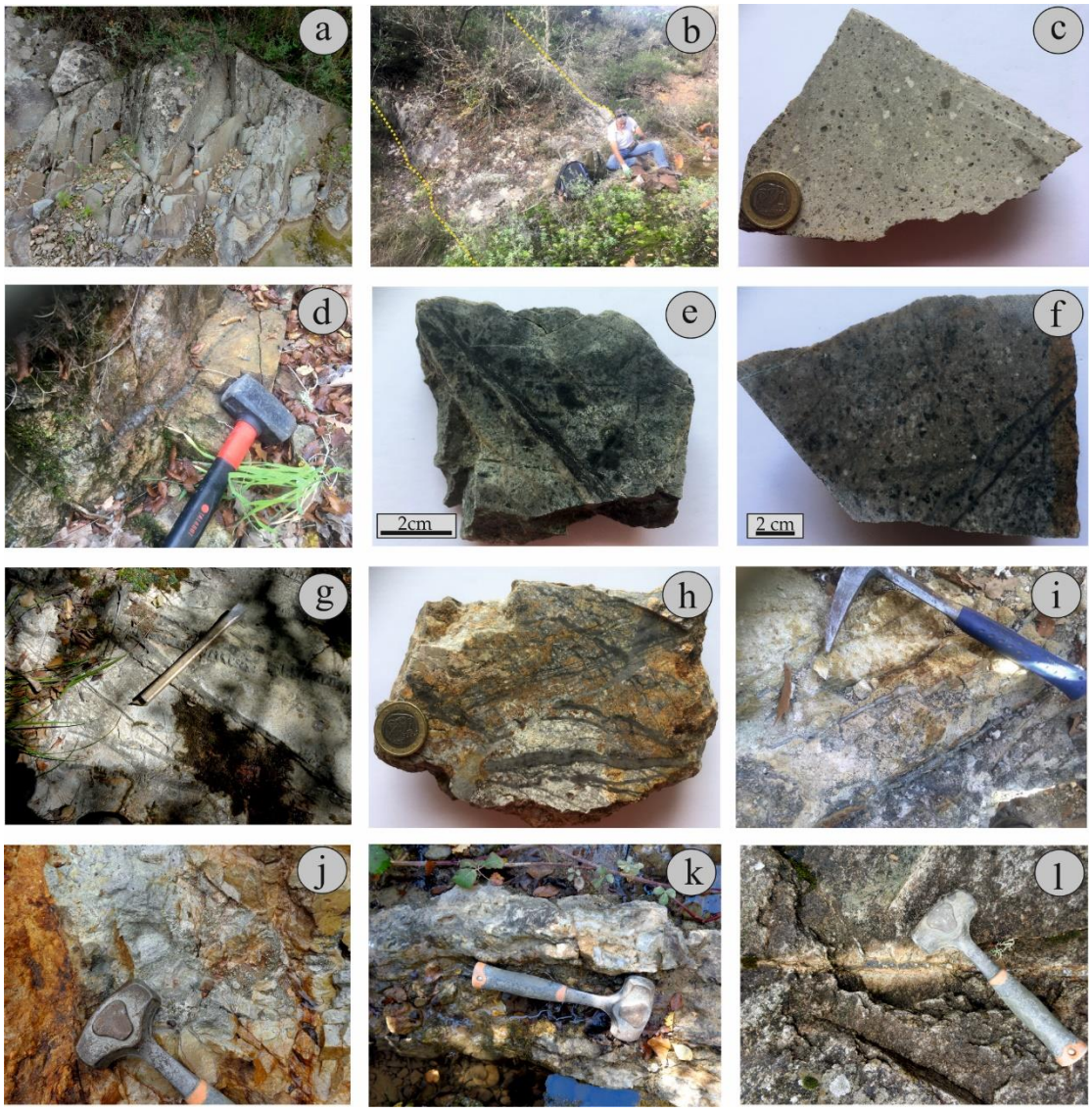

Figure 4.9: Field and hand-specimen photographs from porphyry/epithermal mineralization and alteration at the Pagoni Rachi area: (a) Fresh to propylitic altered granodiorite porphyry; (b) E-trending microgranite porphyry crosscutting granodiorite; (c) Hand-specimen of K-feldspar(±sericite) altered microgranite porphyry dyke); (d-f) Sodic/potassic-calcic altered granodiorite porphyry crosscut by magnetite (M-type veins, figure e) and quartz stockwork (A-type veins, figures d and f) veins; (g) Sharp B-type quartz stockwork veins crosscutting sodic/potassic altered granodiorite porphyry; (h) Hand specimen of banded B-type quartz veins hosting molybdenite-pyrite-rheniite mineralization; (i) Banded B-type quartz veins crosscutting sericitic altered granodiorite porphyry; (j) Massive pyrite veins (D-type) associated with pervasive sericitic alteration of the host granodiorite porphyry; (k, l) NW-trending quartz-calcite, epithermal-style veins (E-type), hosting base/precious metal mineralization (e.g., see sphalerite at the center of the vein in figure l).

Central part (Papadokoryphi Hill)

Papadokoryphi Hill (Figure 4.2) dominates the central part of the study area and is occupied mostly by propylitic-, and minor sericitic-altered granodiorite porphyry. In the northern foothills, a new occurrence of quartz porphyry stockwork was discovered, and spatially associated with the sodic/calcic altered granodiorite porphyry, characterized by epidote, actinolite, chlorite and albite, partly altered to sericite (Figure 4.6j-k). Wavy black silica veins (A-type) contain minor amounts of pyrite and chalcopyrite. Towards the NE of this new porphyry occurrence, a small microdioritic body intrudes the sericitic-altered granodiorite porphyry. The microdiorite is a fine-grained equivalent to the quartz monzodiorite, exhibits selective potassic alteration expressed mainly by hydrothermal biotite (Figure 4.7h-i) and minor K-feldspar, associated with chlorite and abundant secondary magnetite. As in the Konos Hill area, epithermal-style E-, and N20°W trending quartz-calcite veins (Fig. 4.6k), crosscut at places the granodiorite porphyry and host base metal mineralization, consisting of pyrite, galena, sphalerite, and minor amounts of chalcopyrite and tetrahedrite/tennantite. Alongside these veins, argillic alteration occurs, composed of quartz, sericite and calcite, and grades outwards within a few meters in propylitic alteration of the host rocks.

Eastern part (Pagoni Rachi)

The Pagoni Rachi Cu-Mo-Au-Re porphyry prospect (Figure 4.2) is hosted by hydrothermally altered granodiorite (Arikas, 1981; Voudouris et al., 2009; 2013b). The area of the prospect is dominated by the granodioritic intrusion, while further to the south sedimentary lithologies (marls, conglomerates) occur. Peripheral to the prospect, the granodiorite porphyry is affected by varying assemblages of propylitic alteration (Figure 4.9a). A few microgranite porphyry bodies also occur in the area, commonly set along N-, and N20°W-trendig zones and are characterized by intense serictitc alteration. In the NW part of the prospect, a microgranite porphyry intrusion crosscuts the Pagoni Rachi prospect, trending E-W, and is characterized by potassic (±sericitic) alteration (Figure 4.9b,c). The rocks exhibit a porphyrtitic texture, composed of resorbed quartz and K-feldspar phenocrysts, set in a fine-grained matrix consisting of K-feldspar, quartz and minor sericite.

At the higher topographic levels of the Pagoni Rachi system, a very dense oxidized quartz vein stockwork is associated with sericitic alteration. At the lower levels, close to where the core of the system is believed to occur, sodic-calcic/potassic, sodic/potassic and sericitic alteration assemblages occur and host significant porphyry-style mineralization (Figure 4.9d-j).

Sinuous magnetite-rich veins (M-type, according to Seedorf et al., 2005) crosscut the sodic/potassic-calcic altered granodiorite porphyry (Figures 4.9e-f, 4.10a, 4,11a). In these veins, early, anhedral magnetite (±hematite, pyrrhotite) predominates and is post-dated by pyrite, chalcopyrite and minor bornite, molybdenite, and electrum. Along with the M-type veins, A-type quartz, banded veins also occur (Figure 4.9d, 4.11b-c) and host the same ore minerals. The quartz veins contain various proportions of K-feldspar, epidote, actinolite, chlorite and minor fluorite, and are ssociated with variable combinations of K-feldspar/albite, biotite, amphibole, epidote, chlorite, titanite and calcite alteration of the host rock, which exhibits pervasive recrystallization and obliteration of its primary texture (Figure 4.10b-j). Secondary K-feldspar and biotite in association with epidote, and chlorite form mm-scaled masses/laths, while biotite commonly appears as isolated aggregates of pseudo-hexagonal or “shreddy”-shaped crystals.

The wavy veins of granular quartz (A-type veins) locally crosscut the magnetite-rich veins and reach a size of up to 2cm wide. Sometimes, a re-opening event is assigned by the presence of sulfides (e.g., pyrite, chalcopyrite etc.) and alteration minerals along the central parts of the veins.

In certain areas, tectonically controlled, NW- trending planar quartz (B-type veins) were observed (Figure 4.9g-i). These veins, which are an uncommon feature to many porphyry deposits, are very well expressed in the Pagoni Rachi system. They may reach a size of up to 0.5 meters, and exhibit banded texture. The veins are associated with sodic/potassic, albite-, and orthoclase-dominated alteration of the wall rocks, that overprint the pre-existing sodic/potassic-calcic alteration. The veins contain variable amounts of magnetite, albite, orthoclase, chlorite, fluorite, calcite and minor sericite, and are associated with molybdenite, pyrite, rheniite, chalcopyrite and pyrite mineralization (Figure 4.10k, 4.11d). It is noteworthy that molybdenite at this stage is volumetrically more compared to the M/A-type veins. The above-mentioned ore

minerals occur disseminated in the veins, at the wall rocks and also crosscut the quartz veins themselves, thus postdating the quartz crystallization. The veins commonly display reopening texture and are filled with pyrite along center-lines.

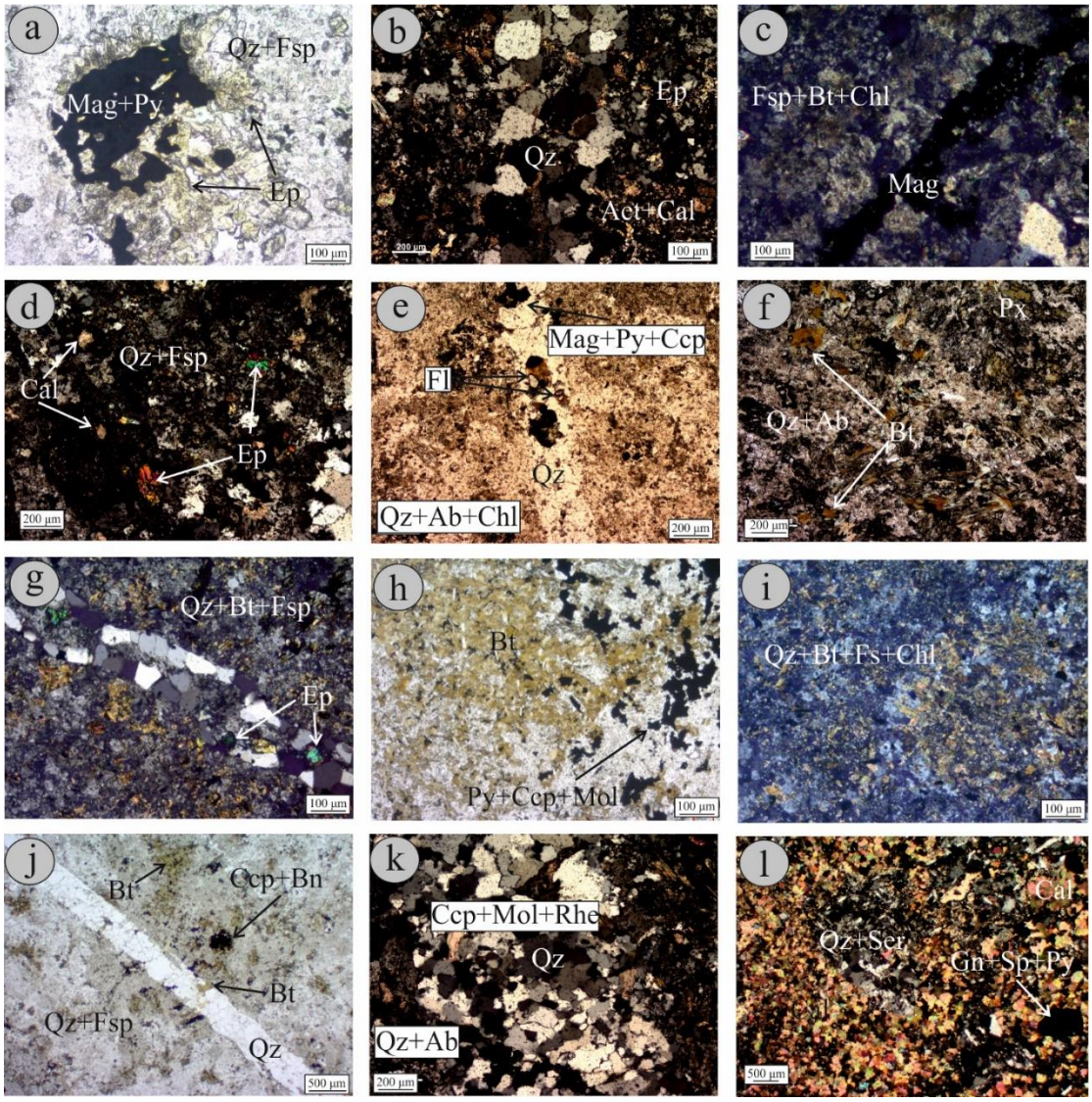

Figure 4.10 Transmitted light photomicrographs of various alteration assemblages from the Pagoni Rachi area (all figures but , e, h and j, taken under crossed-polarized light): (a) Magnetite (Mag) and pyrite (Py) associated with epidote (Ep), set in an albite/orthoclase (Fsp) and quartz (Qz) altered granodiorite matrix; (b) Quartz vein (Qz) crosscutting epidote (Ep), actinolite (Act), and calcite (Cal)-altered granodiorite porphyry; (c) Magnetite vein (M-type) crosscutting albite (Fsp)-biotite (Bt)-chlorite (Chl) altered granodiorite porphyry; (d) Sodic-potassic/calcic altered granodiorite porphyry matrix dominated by quartz (Qz), albite and orthoclase (Fsp), epidote (Ep) and calcite (Cal); (e) Quartz (Qz) vein with pyrite (Py), chalcopyrite (Ccp) and fluorite (Fl) deposited at a centerline, in quartz vein (Qz), crosscutting albite (Ab)-chlorite (Chl) altered granodiorite porphyry; (f-i) Hydrothermal biotite from the sodic/potassic-

calcic alteration associated with quartz (Qz), albite (Fsp, Ab), chlorite (Chl), and minor pyroxene (Px), accompanying pyrite (Py), chalcopyrite (Ccp) and molybdenite (Mol) mineralization; (j) B-type quartz vein (Qz) associated with hydrothermal biotite (Bt), quartz (Qz) and albite/orthoclase (Fsp) alteration and disseminations of chalcopyrite (Ccp) and bornite (Bn); (k) Sodic/potassic atered granodiorite porphyry crosscut by chalcopyrite (Ccp), molybdenite (Mol) and rheniite (Rhe) bearing B-type quartz vein; (l) Quartz (Qz)-sericite (Ser)-calcite (Cal) altered granodiorite hosting base metal mineralization (galena, Gn; pyrite, Py, and sphalerite, Sp) from epithermal-style (E-type) vein.

A fourth type of veining, attributed to a subsequent mineralizing stage, is massive pyrite and/or pyrite-chalcopyrite-molybdenite veins, associated with pervasive sericitic alteration of the host rocks (Figure 4.9j). The veins (that are described as as D-type) reach a width of some tens of centimeters, and may incorporate fragments of sericite-altered granodiorite porphyry. Pyrite carries inclusions of pyrrhotite associated with chalcopyrite, while molybdenite and native gold are abundant at this stage. These minerals are commonly included in pyrite or occur as fracture-, and open-space filling phases.

The final stage of mineralization consists of N- and/or NW-trending epithermal-style (E-type) quartz-calcite veins (Figure 4.9k,l) hosting base-, and precious metal mineralization, which is related to quartz-sericite-calcite (± minor kaolinite) alteration (argillic alteration, Figure 4.10l). These veins contain pyrite that is accompanied by varying amounts of sphalerite, chalcopyrite, galena, and tetrahedrite/tennantite group minerals (Figure 4.11j-k). Rarely Ag-rich electrum (Ag-Au alloy) is included in galena, forming microscopic anhedral grains (Figure 4.11l). Although pyrite was deposited throughout the evolution of the Pagoni Rachi porphyry system, it is more abundant in the later vein stages, in contrast to its minor presence in the early veins that are characterized by the abundance of magnetite.

Finally, several epithermal-style polymetallic deposits/prospects surround the Pagoni Rachi deposit, most important being Aghios Philippos (also named St Philippos), Achla Tarla, and Mavropetra (Figure 4.2). These deposits/prospects are not examined in the presnt study, however a brief description is given, so that the reader may acquire a better understanding of the mineralization in the broader area.

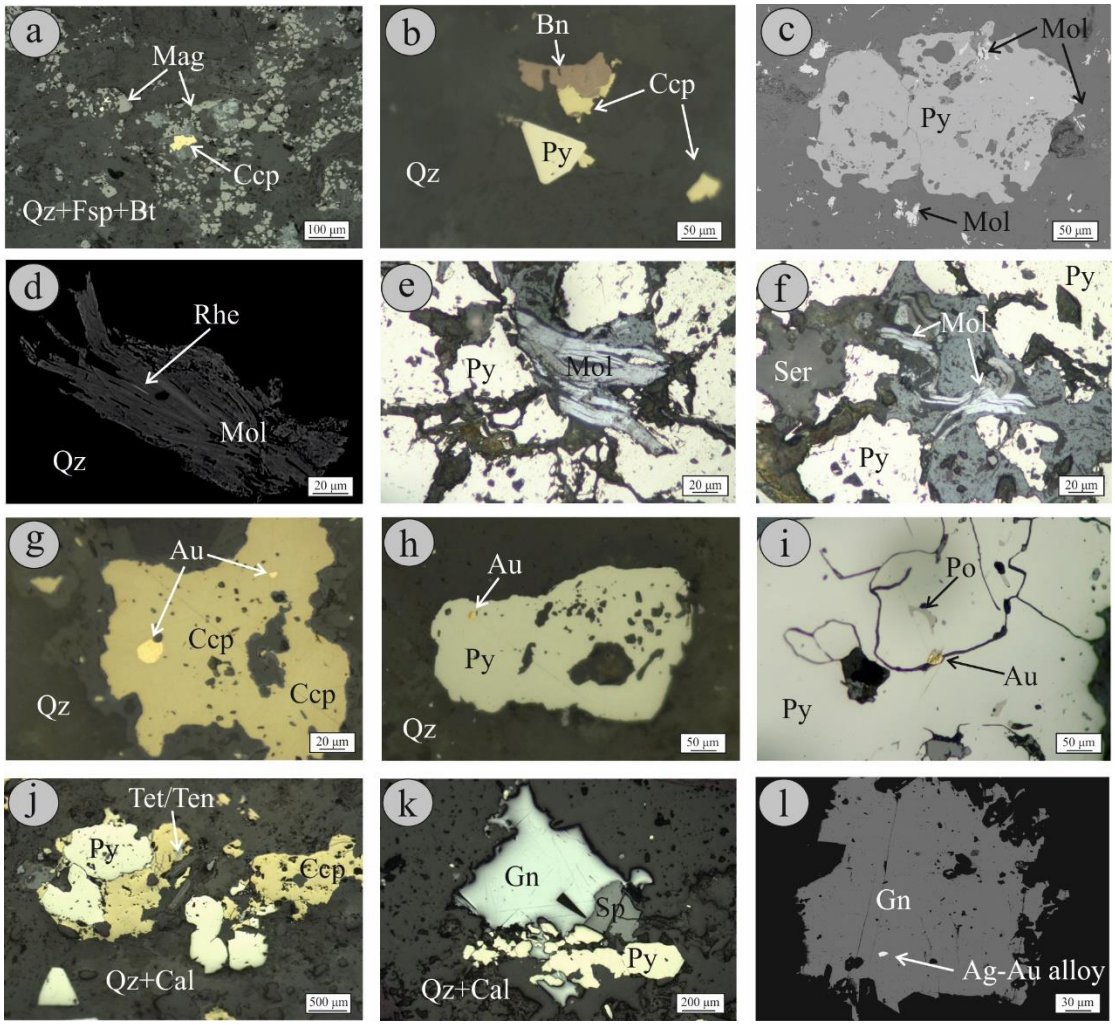

Figure 4.11: Refleceted-light photomicrographs and back-scattered electron images (d, l) from ore mineral assemblages at the Pagoni Rachi area. (a) Magnetite (Mag) vein (M-type) carrying minor chalcopyrite (Ccp), crosscutting sodic/potassic-calcic altered granodiorite porphyry (quartz-Qz, albite/orthoclase-Fsp, and biotite-Bt); (b) Intergrowth of bornite (Bn) and chalcopyrite (Ccp), along with minor pyrite (Py), set in A-type quartz (Qz) veinlet; (c) Pyrite (Py) associated with molybdenite (Mol), A-type quartz vein; (d) Molybdenite (Mol) and rheniite (Rhe) in B-type quartz vein; (e-f) Molybdenite (Mol) and pyrite (Py) associated with sericite (Ser) from D-type vein; (g) Electrum (Au), associated with sodic/potassic-calcic alteration; (h-i) Native gold (Au) fom D-type vein, associated with sericite alteration; (j, k) E-type vein composed of quartz (Qz) and calcite (Cal) hosting pyrite (Py), chalcopyrite (Ccp), fahlores (Tet/Ten), galena (Gn) and sphalerite (Sp); Ag-Au alloy included in ganlena (Gn) from the same E-type vein.

The Mavropetra prospect occurs along N0-20°W and N30°E trending faults (e.g. Mavropetra fault) and is associated with quartz-pyrite veins with minor chalcopyrite and galena. Advanced argillic (quartz, kaolinite) and sericitic alteration of the

granodiorite porphyry host rock accompanies the ores. The Achla Tarla deposit , at the NW part of the Pagoni Rachi porphyry prospect (Figure 4.2), is hosted in sericitic-altered conglomerates and sandstones. The mineralization is fault-controlled and associated with advanced argillic alteration (kaolinite, dickite) and, an intermediate-sulfidation epithermal assemblage dominated by abundant galena, sphalerite, pyrite, chalcopyrite and tetrahedrite/tennantite series minerals (e.g., Dimou, 1993). Quartz, barite and carbonates are the most common gangue minerals.

The St Philippos intermediate-(high)-sulfidation polymetallic deposit occurs along a N20°W-trending fault system developed in advanced argillic (alunite-pyrophyllite) and sericitic-altered sandstones and conglomerates. Ore mineralogy consists of galena, sphalerite/wurtzite, chalcopyrite, members of the tetrahedrite/tennantite group and Sn-bearing sulfosalts hosted in massive sulfide ore and quartz-barite±carbonate veins (Skarpelis 1999; Voudouris et al., 2005b, 2013; 2019a).

4.6. Mineral chemistry

Mineral chemical analyses of alteration and ore minerals are summarized in appendices B (EPMA data) and C (LA-ICP-MS data). Selected mineral-chemical analyses are presented on the Tables 4.2 to 4.7 of the present chapter, while chemical variations of different mineral comonents are depicted in Figures 4.12 to 4.17.

4.6.1 Alteration minerals

4.6.1.1 Biotite

Biotite of two different origins was analyzed in the present study. Magmatic biotite from the granodiorite porphyry, is typically Fe-rich and classified as biotite in the #Fe versus Al_{iv} plot of Figure 4.12, in contrast to the rest of biotite, which are of hydrothermal origin and all plot in the field of phlogopite. The magmatic biotite is characterized by a fixed TiO_2 content (average 4 wt%), and low halogens concentration, namely F up to 0.47 wt% and Cl up to 0.12 wt%.

Four distinct types of hydrothermal biotite were analysed in order to compare their chemical composition: secondary biotite from (i) pervasive and (ii) selective potassic alteration at the Koryphes prospect, (iii) secondary biotite in potassic alteration of microdiorite from the Papadokoryphi prospect and (iv) secondary biotite

from the sodic/potassic-calcic alteration zone in granodiorite porphyry of the Pagoni Rachi prospect. All of them are classified as Mg-rich phlogopite, but are characterized by significant chemical variations, that probably reflect the chemistry of the host rock (as previously stated by Voudouris, 2001; Mavrogonatos et al. 2018a). Hydrothermal biotite exhibits a wide range of TiO_2 content: biotite from the pervasive potassic alteration zone at Koryphes is characterized by the lowest TiO_2 content (average 2.46 wt%), while the other types of hydrothermal biotite display wider Ti contents, which is comparable (and in some cases higher) to the TiO_2 content of magmatic biotite from the granodiorite porphyry. Specifically, biotite from the selective potassic alteration at Koryphes has a TiO_2 content around 5.34 wt%, the one from the potassic-altered microdiorite at Papadokoryphi has an average TiO_2 content close to 4.2 wt%, while average Ti content in biotite from the Pagoni Rachi is close to 3.8 wt%. Figure 4.12b graphically depicts these variations, and for the case of the Pagoni Rachi prospect, it is evident that Ti content of the hydrothermal biotite partially coincides with the Ti content of its magmatic counterpart. The F content is highly variable between the various types of hydrothermal biotite. The higher amount of F characterizes the biotite from the pervasive potassic zone at Koryphes (up to 5.67 wt%, average 4.61 wt%). In the selective potassic alteration, biotite carries significantly lower F, up to 3.41 wt % (average 2.65 wt%). The other two types of hydrothermal biotitite share roughly the same F content (average 1.02 wt% and 1.06 wt% for biotite from the Papadokorfyphi and Pagoni Rachi prospect, respectively). It is notable that the higher Cl content does not coincide with the higher F concentration, and is remarked in the Pagoni Rachi hydrothermal biotite (up to 0.38 wt%). The other hydrothermal biotite do not show variation in their Cl content (values around 0.18 wt% to 0.26 wt%), which is still higher at all cases compared to the Cl content of magmatic biotite.

Trace elements analyses in the four different hydrothermal biotite types revealed some variations (Table 4.2). In Figure 4.12c, where the average trace element content of each type of biotite is normalized to primitive mantle, the hydrothermal biotite from the pervasive potassic alteration at Koryphes displays an enrichment in Th and Nb compared to the other types. However it appears to be depleted in Ta, while th other biotites display a positive anomaly for the same element.

Table 4.2. LA-ICP-MS data of hydrothermal biotite from Papadokoryphi (KMSP80), Koryphes (B26, pervasive potassic alteration; P62, selective potassic alteration) and the Pagoni Rachi (KMPR60) prospects.

Type	**KMSP80**			**B26**			**P62**			**KMPR60**		
Type	Hydrothermal (n=10)			Hydrothermal (n=10)			Hydrothermal (n=20)			Hydrothermal (n=8)		
(ppm)	aver	min	max	aver	min	max	aver	min	max	aver	min	max
Li	111	67	168	19	14	26	9.84	3.21	37	53	46	61
Be	0.37	0.19	0.54	0.51	0.45	0.59	1.14	0.74	1.70	0.69	0.37	1.00
B	3.82	3.82	3.82	3.43	3.43	3.43	8.94	8.94	8.94	bdl	bdl	bdl
Ca	422	317	617	508	409	606	1278	801	5932	2346	585	5853
Sc	3.55	2.86	4.41	13	8.48	19	36	16	87	7.72	5.51	9.92
Ti	14208	13598	14742	28480	23724	31035	18785	2005	31735	25369	17263	31513
V	407	368	436	909	616	1634	427	230	785	126	107	148
Cr	49	36	65	68	36	254	32	22	38	18	8.71	26
Mn	201	191	213	261	248	284	1038	676	2670	572	325	1081
Co	1.25	0.70	1.75	6.84	5.81	7.94	31	17	45	63	55	68
Ni	bdl	bdl	bdl	5.9	5.9	5.9	19	14	23	50	44	57
Zn	20	17	23	32	27	36	369	206	1156	68	45	102
Ga	23	20	26	30	27	33	41	27	59	35	28	44
Rb	554	529	586	650	601	691	421	63	524	791	580	951
Sr	4.60	3.17	5.67	2.83	2.47	3.55	24	1.70	67	6.29	1.96	23
Y	0.15	0.04	0.44	0.14	0.06	0.28	4.42	0.11	24	1.71	0.11	3.42
Zr	24	1.38	152	2.33	1.54	4.43	62	1.89	788	3.05	2.76	3.37
Nb	434	1.69	1679	14	3.46	22	29	2.94	44	20	13	27
Sn	0.28	0.27	0.28	2.52	1.43	3.67	20	1.79	49	5.42	4.22	6.69
Cs	5.31	4.69	5.78	9.89	8.25	12	13	3.15	32	21	11	36
Ba	402	280	568	741	603	878	867	84	1779	665	347	1059
La	0.03	0.01	0.04	0.02	0.01	0.03	70.01	0.03	1296	0.12	0.01	0.26
Ce	0.04	0.01	0.10	0.03	0.01	0.06	3.73	0.04	38	0.25	0.01	0.85

Pr	0.01	bdl	0.01	0.01	bdl	0.02	0.52	0.03	4.78	0.04	0.01	0.11
Nd	0.04	0.02	0.06	0.03	0.01	0.05	1.84	0.06	19	0.39	0.02	0.76
Sm	0.04	0.01	0.08	0.03	0.01	0.05	0.59	0.05	3.94	0.16	0.02	0.30
Eu	0.02	bdl	0.03	0.02	0.01	0.04	0.20	0.02	0.47	0.05	0.02	0.13
Gd	0.03	0.01	0.05	0.04	0.03	0.07	0.89	0.02	3.34	0.18	0.02	0.46
Tb	bdl	bdl	bdl	0.00	bdl	0.01	0.11	0.00	0.51	0.04	bdl	0.12
Dy	0.05	0.02	0.07	0.02	0.01	0.09	0.64	0.02	3.42	0.28	0.02	0.70
Ho	0.01	bdl	0.02	0.01	bdl	0.02	0.15	bdl	0.69	0.07	bdl	0.17
Er	0.03	bdl	0.09	0.03	bdl	0.07	0.34	0.01	2.12	0.16	0.01	0.49
Tm	0.01	bdl	0.05	0.01	bdl	0.02	0.08	0.01	0.47	0.04	0.01	0.10
Yb	0.05	0.02	0.20	0.04	0.01	0.15	0.50	0.02	4.22	0.40	0.02	1.12
Lu	0.01	bdl	0.05	0.01	bdl	0.01	0.09	0.01	0.58	0.03	bdl	0.07
Hf	0.61	0.03	4.66	0.08	0.02	0.13	1.72	0.07	22	0.14	0.08	0.21
Ta	0.08	0.04	0.12	716	0.28	1296	75	0.16	1394	302	0.85	1332
Pb	13	1.32	62	16	1.89	41	7.72	0.69	25	0.51	0.26	0.77
Th	105	0.03	1049	0.01	bdl	0.03	0.54	0.01	5.35	0.04	0.01	0.14
U	0.10	0.02	0.49	0.03	0.01	0.06	0.95	0.09	12	0.05	0.02	0.10

n = number of analyses; aver =average value; min = minimum value; max = maximum value; bdl = below detection limit.

A positive anomaly for the elements Pb, Zr and Ti characterizes all types of hydrothermal biotite. Regarding their REE content, it is clear from the Figure 4.12d that all types of hydrothermal biotite are characterized by relatively parallel and flat distribution patterns for all the REE's, however it appears that hydrothermal biotite from the Pagoni Rachi prosepcts is slightly enriched in all elements (and especially the LREE) compared to the rest of the hydrothermal biotite.

Selected EPMA analyses are presented in the Appendix B1, and the LA-ICP-MS analyses are presented in the Appendix C1.

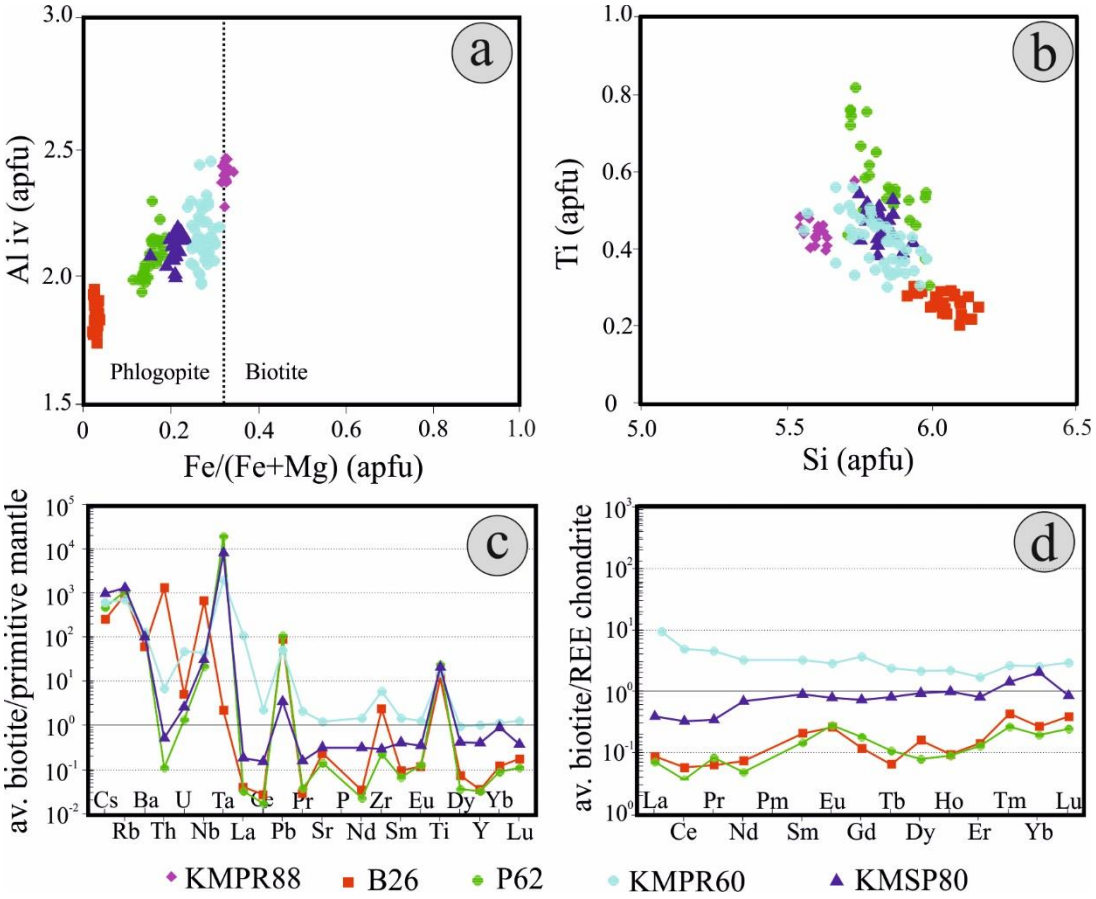

Figure 4.12: Chemical variation of biotite (a) #Fe versus Al_{iv} and (b) Si versus Ti plots of magmatic and hydrothermal biotite; (c) Primitive mantle-, and (d) REE chondrite-normalized patterns of average composition of hydrothermal biotite. B26 = pervasive-, and P62 = selective-potassic alteration, Koryphes prospect; KMPR60 = sodic/potassic-calcic alteration, Pagoni Rachi prospect; KMSP80 = potassic/calcic alteration, Papadokoryphi prospect.

4.6.1.2. Feldspar group minerals

Felsdpars are very common mineralogical cosntituents in various alteration assemblages, mostly at Pagoni Rachi. The analysed chemical compositions of secondary feldspar from the Pagoni Rachi prospect are plotted in Figure 4.13a and summarized in Table 4.3. Plagioclase compositions from the propylitic alteration of the granodiorite porphyry, vary between Ab_{93} and Ab_{75} (albite to oligoclase). At the sodic/potassic-calcic alteration, both orthoclase and Na-rich plagioclase are present, but this time the compositional range of plagioclase is slightly more wide compared to plagioclase from the propylitic alteration, ranging between Ab_{96} and Ab_{70}. Regarding the feldspar from the sodic/potassic alteration, again orthoclase is present together with plagioclase, however, the compositional range of the latter is restricted between Ab_{98} and Ab_{84}. Selected EPMA analyses of feldspar group minerals are presented in the Appendix B2.

Table 4.3 Compositional variation of feldspar group minerals from sodic/potassic-calcic, sodic/potassic and propylitic alteration of the study area.

Alteration	**Sodic/Potassic-Calcic**			**Sodic/potassic**			**Propylitic**		
End member	Or	Ab	An	Or	Ab	An	Or	Ab	An
min	0.24	2.45	0.01	0.14	75.04	6.43	0.25	83.26	0.00
max	97.47	97.25	25.96	1.32	93.31	24.82	4.51	98.13	16.06

4.6.1.3. Chlorite

Chlorite is common in the propylitic alteration, and an important mineralogical component of the sodic/potassic-calcic alteration and sodic/potassic alteration. Mineral chemical analyses of chlorite from the Pagoni Rachi prospect, revealed a relatively restricted compositional range from the sodic/potassic-calcic and the propylitic alteration types. As shown in Figure 4.13b, chlorite from the propylitic alteration belongs to the variety of pycnochlorite, according to the classification scheme of Hey (1954). However, chlorite from the sodic/potassic-calcic alteration is characterized by wider Fe_{tot} content and thus is classified as both pycnochlorite and clinochlore.

Selected EPMA analyses of chlorite are presented in the Appendix B3.

4.6.1.4. Amphibole group minerals

Amphibole is present in both the propylitic alteration and the sodic/potassic-calcic alteration at Pagoni Rachi. Analysed compositions (Table 4.4.) reveal that it never exceeds the composition of calcic amphiboles, and that chemical variations occur between amphiboles of the two distinct altearation styles. Amphibole from the propylitic alteration is more Fe-, and Al-rich compared to the one from the potassic assemblage, and is characterized as Fe-hornblende, Mg-hornblende and tschermakite (Figure 4.13c). The hydrothermal type of apmhibole exhibits higher content of Si, Mg, Ca and Na and varies compositionally between Fe-actinolite, which is the most common amphibole type in the sodic/potassic-calcic alteration, Fe-hornblende and Mg-Hornblende. Interestingly, amphibole from the sodic/potassic-calcic alteration incorporates certain amounts of F, which reach up to 0.8 wt%, corresponding to 0.368 apfu (Figure 4.13d).

Selected EPMA analyses of amphibole are presented in the Appendix B4.

4.6.1.5 Epidote group minerals

Epidote is one of the most important mineralogical components of the propylitic alteration of the granodiorite porphyry, replacing commonly mafic minerals and/or feldspars. In addition, it is widespread in the sodic/potassic-calcic alteration zone at the Pagoni Rachi prospect. No significant chemical variations were remarked between epidote from the two distinct alteration styles (Table 4.4). All the compositions that were analysed, plot in a restricted area in the field of clinozoisite (Figure 4.13e).

EPMA analyses of epidote are presented in the Appendix B5.

4*.6.1.6. Sericite*

As sericitic alteration in the broad study area is widespread, sericite is one of the most common mineralogical constituents. In this study, sericite that is associated with D-type veins at Konos Hill and Pagoni Rachi was analysed. Figure 4.13f graphically depicts chemical variation of sericite, as a function of its Na+K content. No significant variations are obvious between sericite from the two prospects, however, a slight negative correlation between the Si and Na+K content is evident.

EPMA analyses of sericite associated with D-type mineralization from the Konos Hill and the Pagoni Rachi prospects are presented in the Appendix B6.

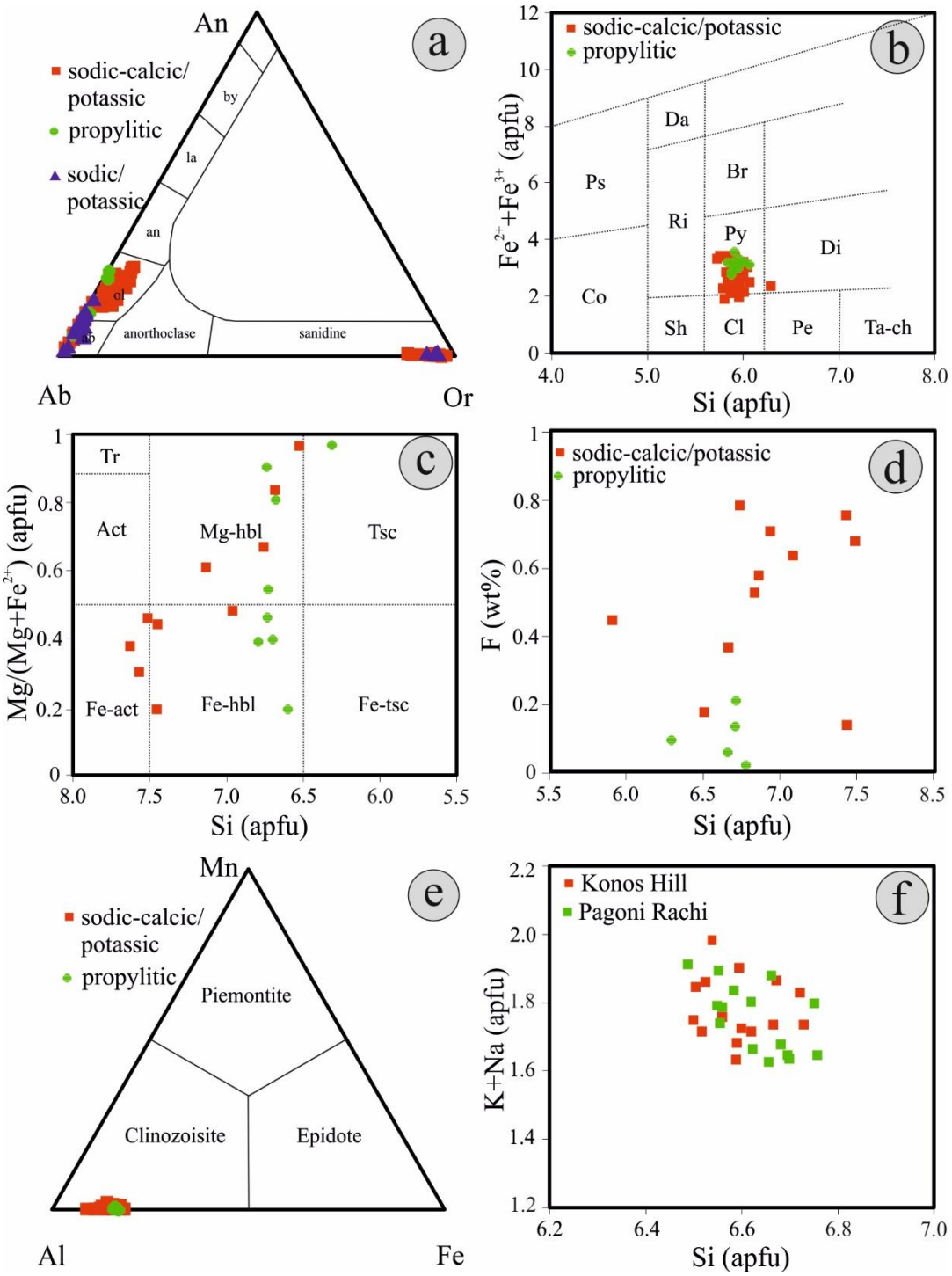

Figure 4.13: Chemical variation plots of various alteration minerals. (a) Feldspar Classification plot of feldspar group minerals from the Pagoni Rachi prospect (after Deer et al., 1992); (b) Si versus Fe_{tot} classification plot for chlorite from the Pagoni Rachi prospect (after Hey, 1954); (c) Si versus #Mg classification plot (after Leak et al., 1997) and (d) Si versus F plot for amphibole group minerals from the Pagoni Rachi

prospect; (e) Ternary Mn-Al-Fe classification plot for epifdote group minerals from the Pagoni Rachi prospect; (f) Si versus K+Na plot for sericite from D-type veins at the Konos Hill and Pagoni Rachi prospects.

Table 4.4. Average composition of amphibole and epidote group minerals from the sodic/potassic-calcic (Pot, sample KMPR74) and the propylitic (Prop, sample KMPR88) alteration zone at the Pagoni Rcahi prospect; bdl = below detection; n = number of analyses.

Amphibole group			**Epidote group**		
Alter.	Pot	Prop	Alter.	Pot	Prop
n =	44	12	n =	10	8
SiO_2	50.00	46.72	SiO_2	38.45	38.43
TiO_2	1.50	1.44	TiO_2	0.16	0.06
Al_2O_3	5.86	9.02	Al_2O_3	22.22	22.83
FeO	8.39	13.37	FeO	13.18	12.57
MnO	0.08	0.44	MnO	0.12	0.21
MgO	17.93	14.17	MgO	0.06	0.11
CaO	11.54	10.70	CaO	22.89	22.99
Na_2O	2.09	1.66	Total	97.07	97.20
K_2O	0.54	0.47	Apfu	(12.5) O	
F	0.48	0.07	Si	3.290	3.267
Cl	0.14	0.05	Ti	0.010	0.004
Cr_2O_3	bdl	0.02	Al	2.241	2.286
Total	98.63	98.33	Fe	0.424	0.403
Apfu	(23) O		K2O	2.90	Mn
Si	6.953	6.663	Mg	0.008	0.014
Al iv	1.041	1.337	Ca	2.099	2.094
Al vi	0.085	0.182	X_{Fe}	15.92	15.01
Ti	0.166	0.155			
Cr	0.002	0.003			
Fe^{3+}	0.416	1.011			
Fe^{2+}	0.578	0.584			
Mn	0.009	0.053			
Mg	3.774	3.011			
Ca	1.749	1.636			
Na	0.568	0.459			
K	0.099	0.086			
F	0.248	0.056			
Cl	0.034	0.012			

4.6.1.7. Alunite supergroup minerals

Alunite group minerals (including aluminum phosphate-sulfate minerals/APS) , are the main minerals in the advanced argillic alteration zone, that is superimposed atop the Konos Hill porphyry system. Alunite supergroup minerals display a wide

compositional range corresponding to members of the alunite, beudantite, and plumbogummite subgroups. Alunite ss. Includes both K-, and Na-rich varieties (up to 9 wt% K_2O and 5.5 wt% NaO, respectively). Selected EPMA analyses of alunite/natroalunite solid solution members from the Konos Hill advanced argillic alteration zone are presented in the Appendix B7. For a detailed mineralogical/mineral-chemical descripition see Chapter 5.

4.6.1.8 Diaspore, zunyite, kaolinite, pyrophyllite

Zunyite, along with diaspore, kaolinite, and minor pyrophyllite, are together with quartz and alunite the mineralogical components of the advanced argillic alteration at Konos Hill. Diaspore presents almost stoichiometric composition, while zunyite is characterized by highly variable F and Cl content and may carry traces of other elements like REE (e.g., Nd_2O_3 was detected up to 0.21 wt %). For a detailed mineralogical/mineral-chemical descripition see Chapter 5.

4.6.2. Metallic (Ore) minerals

Table 4.5: Gold composition (at. %) from M-type, D-type, and E-type veins, associated with sodic/potassic-calcic, sericitic, and argillic alteration respectively, at the Pagoni Rachi prospect.

Alteration	**Sodic/potassic-calcic**			**Sericitic**			**Argillic**		
at. %	Au	Ag	Te	Au	Ag	Te	Au	Ag	Te
min	78.19	19.74	0.13	86.25	3.11	0.00	30.41	63.51	0.00
max	79.19	20.75	0.04	95.68	12.51	0.08	34.26	69.20	0.01
aver	78.88	20.28	0.02	88.73	10.08	0.02	31.72	66.40	0.00

4.6.2.1 Native elements

Native elements (Au, Ag) in the present study were identified only from the Pagoni Rachi prospect and occur in three forms. Early M-type and A-type veins associated with sodic/potassic-calcic alteration contain electrum with up to 0.79 at. Au (average 79 % at. Au). D-type veins, associated with sericitic alteration, carry almost pure native gold, up to 0.96 at. Au, with a small Ag content in some cases (average 89 % at. Au). Finally, epithermal-style (E-type) late quartz-carbonate veins contain Ag-Au alloy included in galena (average 32 % at. Au). Analytical data are summarized in Table 4.5 and graphically illustrated in Figure 4.14a-b, where it is clearly shown that the

evolution of the Pagoni Rachi systems records a fluctuation in the Au content. In a few cases, a minor tellurium content was identified in electrum from the M-type veins (up to 0.14 wt%). EPMA analyses of native elements are presented in the Appendix B8.

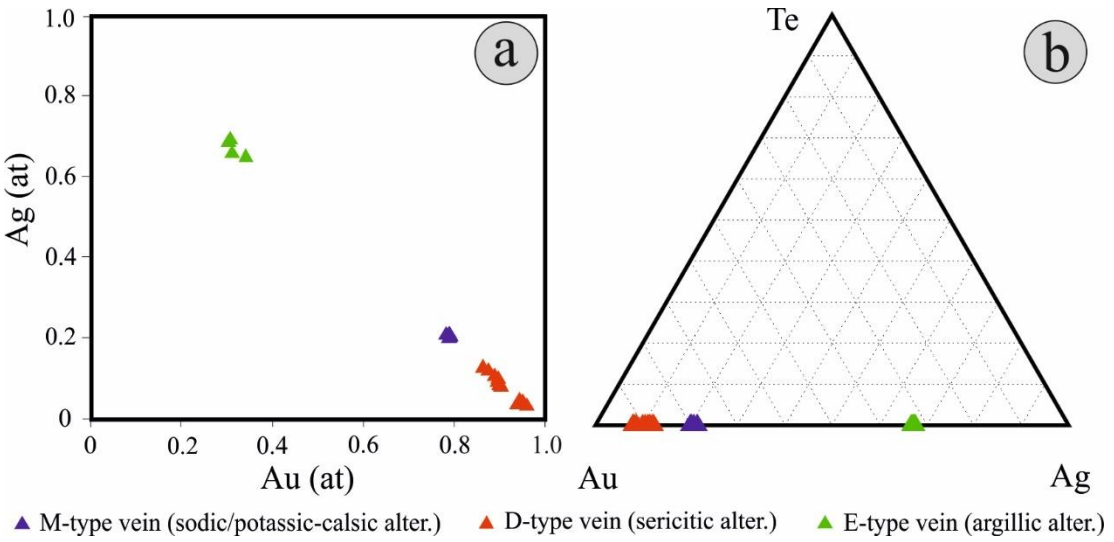

Figure 4.14: Compositional variation of native gold, electrum and Ag-Au alloy, from various mieralization stages at the Pagoni Rachi prospect. (a) Au versus Ag plot; Ternary Au-Ag-Te plot.

4.6.2.2. Molybdenite – Rheniite

Table 4.6. Summary of compositional data (in wt. %) from molyndenite at the Konos Hill and Pagoni Rachi porphyry prospects; bdl = below detection limit; n = number of analyses.

Alteration, prospect	**Sericitic, Konos Hill**			**Sodic-calcic/potassic, Pagoni Rachi**			**Sericitic, Pagoni Rachi**		
n =	74			14			46		
	min	max	aver	min	max	aver	min	max	aver
S	38.1	41.42	40.42	38.8	41.43	40.67	37.7	41.46	40.24
Cu	bdl	0.08	0.01	bdl	0.15	0.02	bdl	0.07	0.02
Re	bdl	1.96	0.49	0.22	1.72	0.65	0.04	3.15	1.09
Fe	bdl	0.57	0.04	0.04	2.21	0.70	bdl	1.85	0.40
Mo	57.5	61.49	59.99	55.9	61.37	59.90	53.5	61.93	59.52
Total	96.1	101.6	100.9	98.4	101.8	100.4	94.5	101.5	101.0

Molybdenite is a common mineral in the porphyry-style mineralization at both Konos Hill and Pagoni Rachi prospects. At Konos Hill, molybdenite occurs along with rheniite in B-type veins (which are always overprinted by D-type veins). It carries Re (average 0.57 wt% Re) in highly varying amounts, which range from 0.12 wt% to 1.96

wt%, corresponding up to 0.017 apfu in the structure of the mineral (Figure 4.15a). Rhenium is not evenly distributed in the molybdenite crystals and shows a sector zoning (Figure 4.15b,c).

At places, rheniite is associated with molybdenite, in small crystals which were too difficult to be analyzed, however, EDS spectra prove that it is pure Re-sulfide with no contribution of Mo (Figure 4.15e,f).

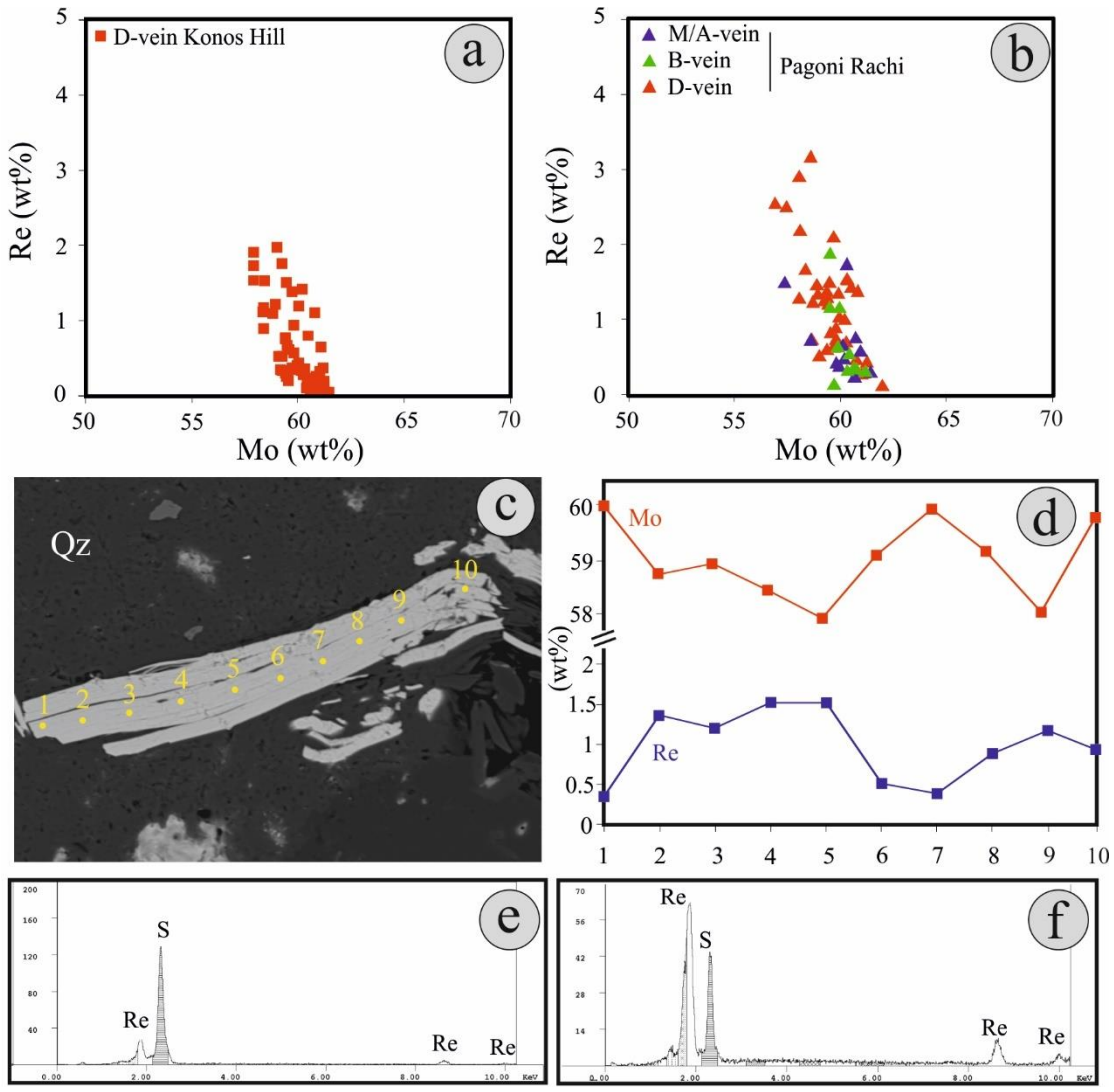

Figure 4.15: Re versus Mo plot for molybdenite from the Konos Hill (a) and the Pagoni Rachi (b) propects; (c) Back-scattered electron image of molybdenite cystal from D-type vein, Konos Hill prospect. Yellow dots represent EPM analyses; (d) Re and Mo content (in wt%) of the molybdenite crystal shown in (d). Numbers in the horizontal axis correspond to the analytical spots on (d); (e,f) EDS-spectra of rheniite from the Konos Hill prospect.

At the Pagoni Rachi prospect, molybdenite occurs in early M-, and A-type veins, in B-type veins and D-type veins and is associated with rheniite. It carries significant amounts of Re at all stages, but a prominent enrichment characterizes molybdenite from D-type veins (Table 4.6). Specifically, molybdenite from early M-, and A-type veins contains an average Re content of 0.67 wt%, while the maximum Re content reaches up to 1.99 wt% (corresponding to 0.017 apfu Re). In the B-type veins, the Re content reaches up to 1.78 wt% (corresponding to 0.014 apfu Re), while the average value is 0.68 wt% Re, roughly in the same level with the one from molybdenite in A-, and M-type veins. In the D-type veins, the maximum Re value is 3.15 wt% (corresponding to 0.027 apfu Re), and the average Re content is 1.18 wt%, almost double compared to the relevant value in molybdenite from A/M-, and B-type veins (Figure 4.15b). A summary of compositional data of molybdenite from the studied prospects is shown in Table 4.6.

Selected EPMA data of Re-rich molybdenite from the Konos Hill and the Pagoni Rachi prospects are presented in Appendix B.9.

4.6.2.3. Chalcopyrite

Chalcopyrite is widespread in both porphyry-, and epithermal-style mineralization. It is commonly associated with magnetite and/or pyrite in various generations of porphyry-style veins, or it can be intergrown with sphalerite (or included as tiny bleb-shaped crystals/chalcopyrite "disease"), galena, colusite, and tetrahedrite/tennantite group minerals. EPMA analyses (presented in Appendix B.10) revealed almost stoichiometric compositions.

4.6.2.4. Magnetite

Magnetite is present at the Pagoni Rachi prospect in the form of magmatic and hydrothermal magnetite. Magmatic magnetite occurs as euhedral crystals in fresh/propylitic altered granodiorite porphyry, while hydrothermal magnetite forms disseminations and/or veinlets (M-type), crosscutting sodic/potassic-calcic altered granodiorite porphyry, and is associated with a chalcopyrite, pyrite, molybdenite, and electrum. A series of trace elements are preferably enriched in hydrothermal magnetite, e.g., V, Pb, W, Mo, Ta, Zn, Cu, Nb, whereas Ti, Cr, Ni, and Sn display higher

concentration in its magmatic counterpart. EPMA data of magmatic and hydrothermal magnetite are presented in Appendix B.11, and LA-ICP-MS data in Appendix C.3. For a detailed description of magnetite chemistry refer to Chapter 6.

4.6.2.5. Pyrite

Pyrite is present in all the mineralizing events of the studied prospects. It is commonly anhedral, corroded and inclusion-bearing in the porphyry-style mineralization (in the M-, and D-type veins), while it forms idiomorphic, medium- to coarse-grained crystals in the late, epithermal style veins (E-type). Arsenic is the major impurity in the studied pyrite, commonly found in the late, epithermal-style pyrite (up to 1.48 wt%). Porphyry-style pyrite from both prospects is characterized by an enrichment in Co, Se, Cu, and minor Zn, and a depletion in other trace elements, while in the epithermal-style mineralization is enriched in As, Bi, Pb, Ni and Se. EPMA and LA-ICP-MS data of various pyrite generations are presented in Appendix B.1 and Appendix C.4, respectively. For a detailed description of pyrite chemistry refer to Chapter *7.*

4.6.2.6. Galena

Galena occurs both in porphyry-, and epithermal-style mineralization. In the first case, it forms microscopic, bleb-shaped crystals included in pyrite, of the D-type veins. Analytical results from such galena at the Pagoni Rachi prospect, revealed almost stoichiometric composition. In contrast, analyses of subhedral galena grains embedded in gypsum veins at the Konos Hill prospect, yielded elevated Se and Te contents, reaching up to 13.04 % Se, and 1.07 % Te (corresponding to 0.425 apfu Se and 0.022 apfu Te) respectively, and thus the mineral is characterized as galena-clausthalite solid solution (Figure 4.16a). EPMA data of galena from epithermal-style mineralization (E-type veins) at both areas, yielded small consentrations of Ag (up to 1.08 %) with only minor presence of Bi, up to 0.22 wt %. EPMA data of galena are presented in Appendix B.13.

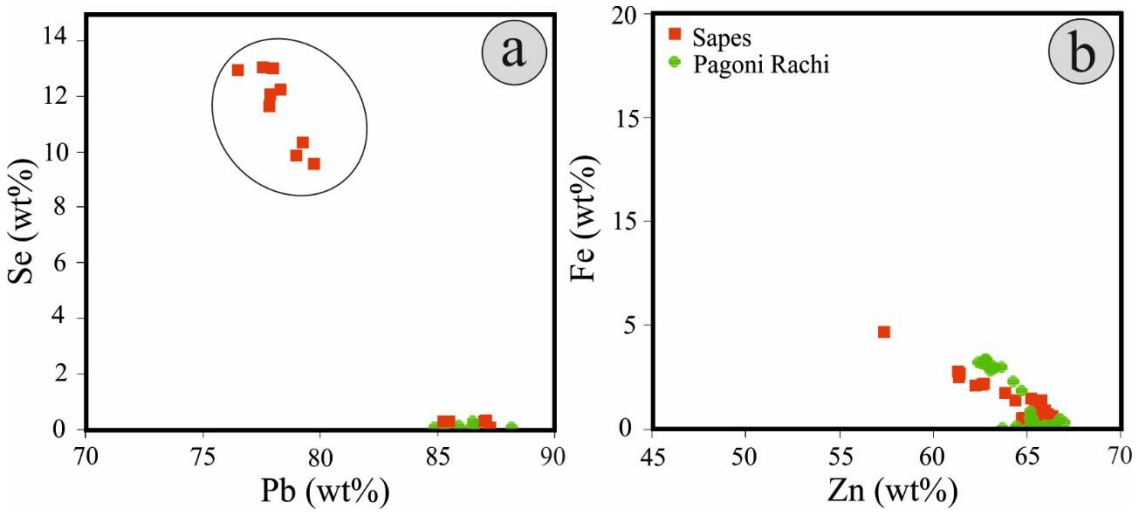

Figure 4.16: (a) Pb versus Se plot for galena. The samples inside the circle are Se-rich galena, hosted in gypsum veins at the Konos Hill prospect; (b) Zn versus Fe plot for sphalerite from Sapes and Pagoni Rachi areas.

4.6.2.7. Sphalerite

Sphalerite is common in the epithermal-style (E-type) veins throughout the study area. It forms euhedral zoned crystals in the majority of the cases, with zonation being related to its Fe-content. It is generally iron-poor (up to 5.89 % mol FeS, Figure 4.16b), but displays variation in its trace element content. LA-ICP-MS analyses are summarized in Table 4.7. Sphalerite from the Sapes area is Cd-rich, while Mn is characterizing galena from the Pagoni Rachi E-type veins. Sphalerite from both areas carries a significant amoun of Ga (up to 1852 ppm and 2043 ppm at Sapes and Pagoni Rachi, respectively), while Ge, despite present in sphalerite from both areas, shows a more significant enrichment in sphalerite from the Pagoni Rachi prospect. Indium exhibits important concentrations in sphalerite from Sapes, while a single spot analysis yielded 2049 ppm In, reflecting the presence of a submicroscopic In-bearing inclusion. EPMA data are presented in Appendix B.14, and LA-ICP-MS data in Appendix C.2.

Table 4.7: LA-ICP-MS analyses of sphalerite from E-type veins, at the Konos Hill and Pagoni Rachi porphyry/epithermal prospects. All values are reported in ppm.

	Konos Hill – Sapes (n = 10)				Pagoni Rachi (n = 10)			
Element	MIN	MAX	SD	AVRG	MIN	MAX	SD	AVRG
Mn	113	222	30	176	1014	2620	553	1460
Fe	2541	4363	531	3681	3010	4468	458	3798
Co	0.23	7.13	2.49	3.02	0.21	0.27	0.03	0.24

Ni	bdl	bdl	bdl	bdl	bdl	bdl	bdl	bdl
Cu	13	78	20	31	6.83	817	236	184
Ga	2.12	1852	719	356	2.00	2043	643	214
Ge	0.46	7.25	2.35	2.48	0.41	51.00	35.77	25.71
As	1.42	1.42	bdl	1.42	0.59	0.71	0.08	0.65
Se	bdl	bdl	bdl	bdl	1.87	2.90	0.35	2.34
Mo	0.04	0.26	0.08	0.11	0.03	0.12	0.03	0.08
Ag	0.44	1.28	0.29	0.88	0.83	4.05	1.10	2.07
Cd	12385	39434	8382	23635	3548	4577	335	4135
In	0.81	2049	876	540	0.02	9.14	3.16	1.33
Sn	2.43	21	5.17	8.01	0.22	49.07	16.14	17.04
Sb	0.07	3.00	1.32	1.22	0.06	0.46	0.20	0.31
W	bdl	0.01	bdl	bdl	bdl	0.01	bdl	bdl
Au	bdl	0.01	bdl	bdl	0.01	0.04	0.01	0.02
Tl	bdl	0.04	bdl	bdl	bdl	bdl	bdl	bdl
Pb	0.04	2.21	0.69	0.49	0.04	6.53	2.39	1.94
Bi	bdl	0.01	bdl	bdl	0.01	0.09	0.04	0.03

4.6.2.8. Enargite

Enargite is a rare mineralogical component in the study area, and occurs as inclusions in pyrite from the Konos Hill porphyry prospect. Mineral chemical analyses revealed mostly stoichiometric composition, but in some cases, a minor Fe content was remarked (up to 1.06 wt%).

EPMA data of enargite are presented in Appendix B.15.

4.6.2.9 Colusite

Colusite is found in the Konos Hill prospect (its presence at Konos Hill constitutes the second occurrence of this rare V-Sn sulfosalt in Greece), and and forms disseminated crystals commonly in association with chalcopyrite. EPM analyses revealed significant variations in its composition, mostly regarding its Sn (up tp 6.8 wt%), V (up to 3.29 wt%) and Sb (up to 6.52 wt%) content, which correspond to 0.796 apfu Sn, 0.880 apfu V, and up to 0.709 apfu Sb, respectively (Figure 4.17a). EPMA data of colusite are presented in Appendix B15. The majority of the analyzed compositions clearly plot in the field of colusite, however a few analyses are characterized by almost equal amounts of As, Sb and Sn, and thus plot close to the triple point between colusite, stibiocolusite and nekrasovite (Figure 4.17a).

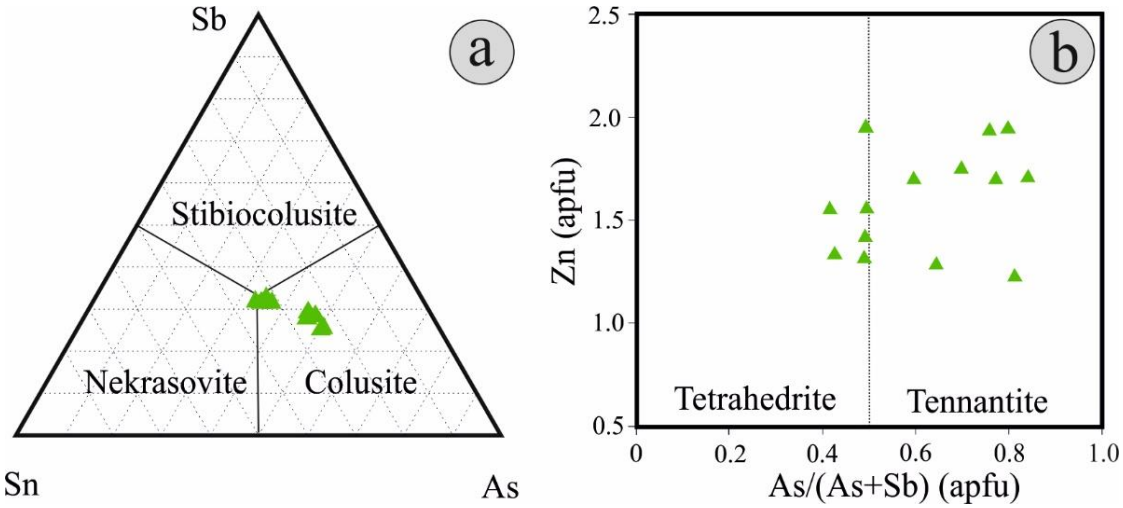

Figure 4.17: Chemical variation of (a) colusite and (b) tetrahedrite/tennantite group minerals.

4.6.2.10 Tetrahedrite/Tennantite group minerals

Tetrahedrite/tennantite group minerals are found mostly within E-type veins in both the Sapes and the Pagoni Rachi areas. Mineral-chemical analyses revealed significant variations in their As and Sb contents, which range between 8.31-16.38 wt%, and 5.03-17.92 wt%, respectively. In addition, Zn is always present in certain amounts in the structure of the minerals (up to 8 wt%), leading to the occurrence of zincian varieties of both tetrahedrite and tennantite in the study area (Figure 4.17b). EPMA data for tetrahedrite/tennantite group minerals are summarized in Appendix B17.

4.7. Bulk ore geochemistry

A total of 117 mineralized samples from porphyry and epithermal mineralization styles throughout the area were analyzed in order to determine their minor and trace element content. The results of 25 representative samples are presented in Table 4.8, and illustrated as multi-element correlation plots in figure 4.18 for the Sapes and figure 4.19 for the Pagoni Rachi area, respectively.

Porphyry-style mineralization in both Konos Hill and Pagoni Rachi displays enrichment in Mo, Re, Bi, Se and Te. However, this enrichment is significantly higher in samples from Pagoni Rachi compared to those from the Sapes area.

Binary correlation plots of selected trace elements from Sapes porphyry-style samples indicate a strong correlation between Mo and Re (R^2 = 0.72), with maximum values reaching up to 47 ppm and 0.67 ppm, respectively. Enrichment in those two elements can be found in all analyzed samples that have undergone a strong sericitic overprint, including those which are associated with relics of sodic alteration. Although moderately good correlations occur between Se and Au (R^2 = 0.59) and between Se and Te (R^2 = 0.41) correlations among other elements are poor (Figure 4.18a). It should be noted that the Au content in all analyzed samples is generally low (up to 0.14 ppm).

Mo and Re content in porphyry style mineralization from the Pagoni Rachi area, reaches values up to 164 and >1 ppm respectively (Figure 4.19a). The highest Mo and Re concentrations derived from samples of B-, and D-type veins associated with sodic/potassic, and sericitic-altered granodiorite. The Mo-Re plot clearly shows two different trends (Figure 4.19a): samples associated with sodic/potassic-calcic (M, A – type veins), sodic/potassic alteration (B-type veins) and sericitic alteration (D-type massive pyrite veins) show an excellent correlation. The rest of the samples, correspond to oxidized quartz porphyry stockwork veins and are characterized by very low values in both elements. Despite these two trends, a moderately good average correlation (R^2 = 0.50) occurs between these two elements, when taken as a whole. Se and Te display a similar pattern of enrichment with Mo and Re. The highest values (up to 56 and 6 ppm, respectively) are related to massive pyrite samples associated with sericitic alteration. The highest concentrations of Au are observed in massive pyrite D-type veins (up to 6.30 ppm; average = 3.68 ppm), whereas the Au content is lower in other types of alterations and associated porphyry mineralization. More specifically, the Au content of sodic/potassic-calcic and sodic/potassic alteration, and associated M/A-, and B-type of veinlets respectively, reaches up to 0.68 ppm (average = 0.15 ppm) and 0.29 ppm (average = 0.20 ppm), respectively. Finally, gold enrichment also occurs in some oxidized quartz stockwork samples, with values up to 1.12 ppm (average = 0.17 ppm). The average Au grade of the porphyry system at Pagoni Rachi, based on surface data, is 0.36 g/t. This content shows strong correlation with selenium and tellurium of R^2 = 0.94 and 0.85, respectively, indicating probably

contemporaneous introduction of these elements at the ore-forming system. However, the correlation between Au and Te is prominent mostly in the D-type veins.

Compared to the porphyry-style mineralization, samples from epithermal-style (E-type), HS and IS quartz-carbonate polymetallic veins from Sapes area have quite different trace element enrichment patterns (Figure 4.18b). Specifically, they are enriched in Bi (up to 14 ppm), Ga (up to 20 ppm), Se (up to 26 ppm), Te (up to 18 ppm) and V (up to 186 ppm). The Au and Ag content of these ores reach up to 0.9 and 3.4 ppm, respectively. Despite their relative enrichment, the above-mentioned elements do not show any positive correlations except for Ga and V (R^2 = 0.87), probably indicating their distribution in different minerals.

Epithermal-style IS mineralization from Pagoni Rachi area (including two samples from the Achla Tarla prospect as well) shares quite different features with those of Sapes (Table 4.8). Apart from the abundance of elements like Zn, Pb and As, several precious and critical metals are also enriched: Ag (up to 86 ppm), Bi (up to 19 ppm), Ga (up to 68 ppm), In (up to 12 ppm), Te (up to 7 ppm), and V (up to 87 ppm). The highest values come from the Achla Tarla deposit. Figure 4.19b shows clearly that very strong correlations occur between Ga and In (R^2 = 0.98), Ag and In (R^2 = 0.98) and Ag and Ga (R^2 = 0.95), indicating the likelihood of a mineral phase (e.g. a probable Ga and/or In analogue to argyrodite) that is common carrier of these elements in the ore. Note that strong to moderately strong correlations also occur between the following elements: Bi and Ag (R^2 = 0.84), Bi and In (R^2 = 0.78), Bi and Ga (R^2 = 0.68), Bi and Zn (R^2 = 0.66), Bi and Te (R^2 = 0.63), Ga and Te (R^2 = 0.76), In and Te (R^2 = 0.75), Zn and Te (R^2 = 0.59), and Se and V (R^2 = 0.58). The Au content in the epithermal type mineralization is significantly lower (0.8 ppm) compared to the porphyry-style ores in the same area.

Table 4.8: Trace element content of selected mineralized samples from Sapes (KMSPxx) and Pagoni Rachi (KMPRxx) areas. Samples KMSP63 and KMPR79 are epithermal-style veins, while the rest of the samples are from porphyry-style veins. See also Appendix E. Values in ppm; bdl = below detection limit.

Sample	As	Au	Ag	Cu	Bi	Sb	Pb	Zn	Ga	Mo	Re	Se	Te	V
KMSP4a	0.1	0.03	0.03	13	0.93	bdl	2.68	2.4	1	35	0.65	5.6	0.55	5
KMSP4b	1.9	0.05	0.04	20	1.19	bdl	2.71	2.6	1.1	6.99	0.03	11	0.62	6
KMSP17b	54	0.01	0.04	15	1.76	0.11	7.72	34	7.2	0.92	0.01	0.6	1.89	68
KMSP54	8.7	0.01	0.02	8.07	3.26	0.32	1.08	3.1	16	1.54	bdl	7	0.21	118
KMSP58	3.9	0.03	0.04	136	1.02	0.16	6.07	20	15	4.63	0.06	4.7	0.52	97
KMSP64	3.4	0.03	0.02	14	2.92	0.39	6.34	17	19	47	0.19	4.6	0.19	107
KMSP66	1.8	0.03	0.03	11	1.45	1.66	13	9.2	20	0.82	bdl	10.2	0.08	156
KMSP73	3.9	0.04	0.22	32	6.79	4.89	169	5.8	14	19	bdl	26.3	0.71	105
KMSP77	1.6	0.01	0.05	16	0.99	0.56	3.59	3.1	12	4.43	0.01	3.1	0.18	113
KMSP81	9.5	0.01	0.07	6.08	0.1	1.23	7.64	39	17	1.22	0.02	0.5	0.72	135
KMSP63	1121	0.92	3.4	31	3	31	603	790	5.47	127	0.02	2	18	80
KMPR16	7.2	0.22	0.32	207	1.25	0.03	14	20	6	24	0.01	2.7	0.26	58
KMPR28	28	1.12	0.06	168	1.24	0.15	16	5.3	3.1	58	0.01	1.1	0.57	31
KMPR52	1	0.46	0.12	122	0.48	bdl	7.53	30	7	4.93	0.07	0.7	0.05	87
KMPR60	2	0.04	0.14	163	0.03	0.05	8.91	42	4.3	0.81	bdl	bdl	bdl	71
KMPR61	1.5	0.03	0.15	89	0.1	bdl	5.01	47	5.3	1.61	bdl	bdl	0.02	70
KMPR66	409	6.30	1.73	208	1.8	0.39	16	48	0.9	35	0.57	56	5.53	14
KMPR68b	30	0.28	0.50	545	0.24	0.07	78	208	4.5	53	0.69	4.3	0.86	38
KMPR74	8.9	0.68	0.22	573	0.4	1.23	26	83	15	8.31	0.04	bdl	bdl	115
KMPR75a	29	0.16	0.18	283	0.21	0.81	16	57	7.79	67	0.96	2.8	1.02	61
KMPR75b	193	3.94	0.87	290	1.95	2.56	19	158	6.73	90	>1	28.7	5.68	87
KMPR79	2028	0.82	87	226	8.3	1166	>10000	5616	68	4.59	0.01	1.5	6.75	66

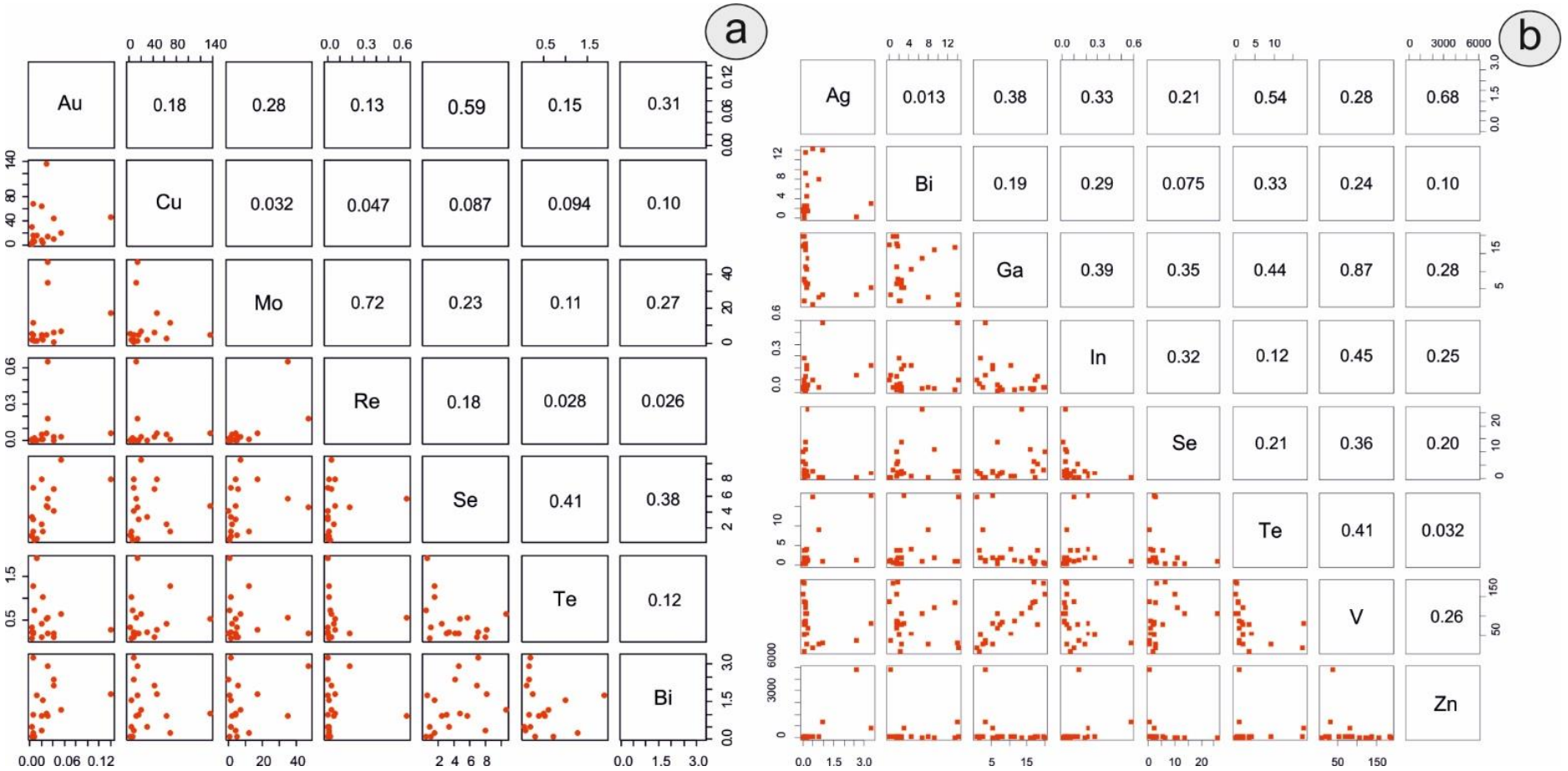

Figure 4.18: Multi-element correlation plot from porphyry-style (a) and epithermal-style mineralization (b), at Sapes area. Values in ppm. Numbers indicate correlation coefficient values between pairs of elements (R^2).

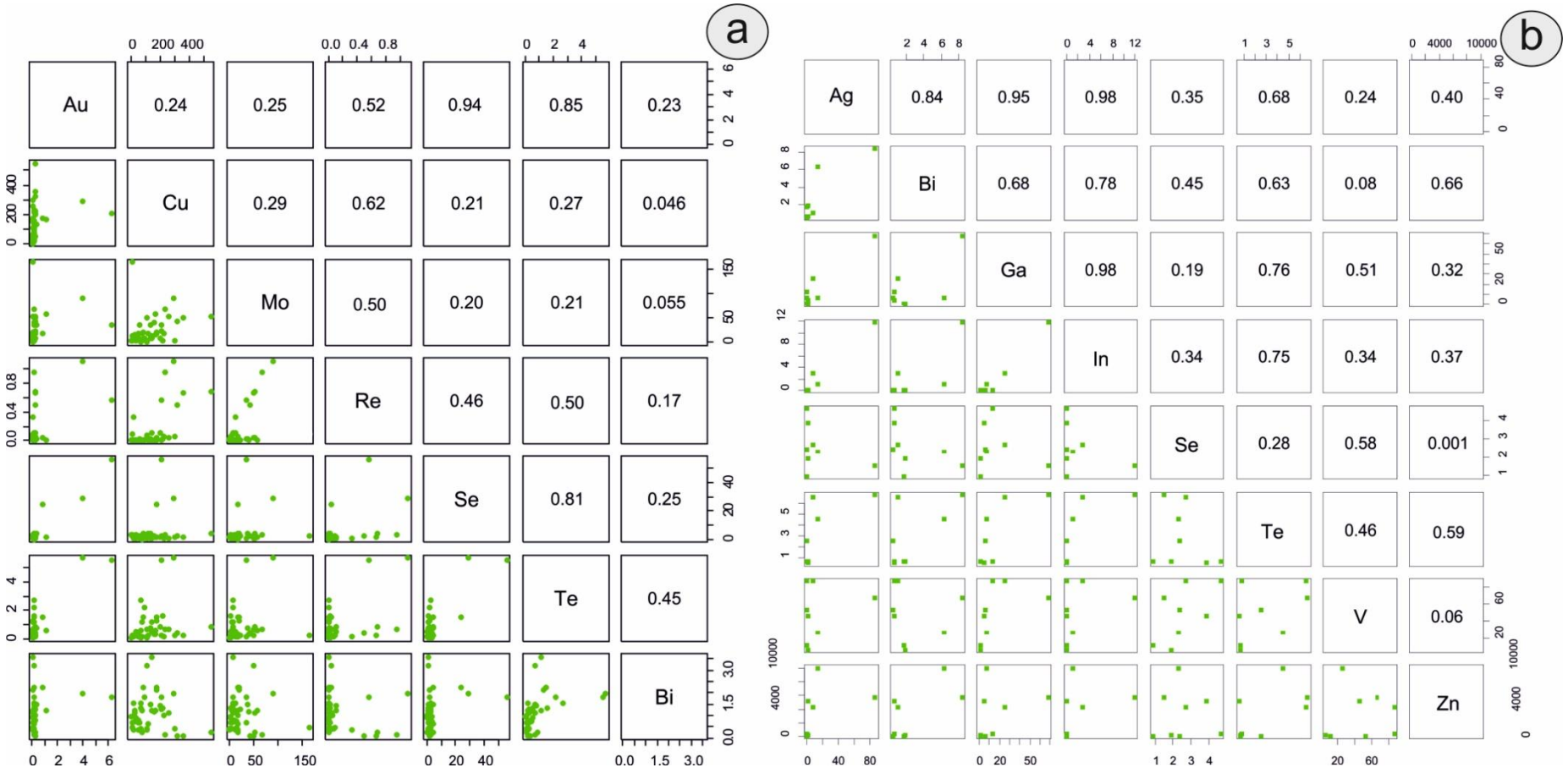

Figure 4.19: Multi-element correlation plot from porphyry-style (a) and epithermal-style mineralization (b), at Pagoni Rachi area. Values in ppm. Numbers indicate correlation coefficient values between pairs of elements (R^2).

4.8 Discussion

In the Sapes-Kirki area, granodiorite stocks that host the porphyry and associate epithermal-style mineralization have a post-collisional geochemical signature, since they are characterized by relatively low Y and Nb values. In addition, they display a relative enrichment in some LILEs (e.g., Ba, Rb, Sr), an observation made previously by Pe-Piper and Piper (2002), Christofides et al. (2004), and Perkins et al., (2018). Pb, Th, La and U are slightly enriched as well, whereas Ta and especially Nb and P are typically depleted. Elevated U and Th contents indicate significant crustal contribution (Kroll et al. 2002), whereas a depletion in Ta and Nb has been attributed to magmatic rocks that were affected by fluids derived from the dehydration of a subducted slab (Pearce and Peate 1995; Keppler 1996; Delibas et al 2016). The negative Nb anomaly has also been interpreted as typical signature of subduction-related calc-alkaline rocks (Eyal et al. 2010). On the other hand, enrichment in elements like La, is usually connected with mantle metasomatic processes by fluids that arise from subducted sediments (Plank 200; Delibas et al. 2016). According to Pearce et al. (1983), relatively variable Th:Yb ratios, that are in agreement with very low Ta:Yb ratios, may reflect an enrichment from a subduction zone, rather than within plate-related enrichment. The obtained wide variation in Ba values (278-1191 ppm) and the high Ba/La ratios (15.35-44.94) are indicative of the influence of aqueous solutions that originate from the mantle wedge and flow up to the sub-lithospheric mantle.

A notable feature from the analyzed lithologies, is that they follow more or less a linear fractionation trend: an increase of their SiO_2 content is consistent with an decrease of most compatible elements, e.g., MgO, FeO, TiO_2, as has recently been stated by Perkins et al. (2018), for the plutonic rocks in the so-called “Maronia magmatic corridor (including the study area plutonic rocks).

As stated by Voudouris et al. (2016a, 2019a), and based on geochemical and stable isotope data by Del Moro et al. (1988), Christofides et al. (1998), Pe-Piper and Piper (2002) and this study, post-subduction, post-collisional conditions characterizing magmatism within the Rhodope massif (i.e., arc-like magmas) were formed by remelting of previously subduction-modified (“fertilized”) upper plate lithosphere. (e.g. Richards 2009, 2011). Throughout the Oligocene and Miocene, magmatic activity

was derived from the mantle lithosphere, which had been intensely contaminated during the late Eocene and onwards, by oceanic and continental subduction (Ersoy and Palmer, 2013). Magma generation in the time interval 35-26 Ma, was related to delamination of sub-lithospheric mantle, which may have brought hot asthenosphere into contact with subduction-modified lithosphere and produced porphyry Cu-Au-Mo and epithermal high and intermediate sulfidation deposits in northern Greece, enriched in Au, Ag, Te, Se and Re (Marchev et al. 2005; Voudouris et al. 2013b, 2016, 2018a,b, 2019a,b).

A precise classification of the Oligocene Konos Hill and Pagoni Rachi porphyry deposits remains uncertain. As previously noted by Voudouris et al. (2016a,b), a common feature of Pagoni Rachi mineralization is the predominance of sodic-(potassic-calcic) alteration in the core of the system, its low Cu content (mean Cu/Au ≈0.104), an extreme Re-enrichment (both in molybdenite and due to the presence of rheniite), and the multistage introduction of gold during the evolution of the porphyry system (both associated with pyrite and with chalcopyrite), thus sharing some affinities to porphyry Au-only deposits (e.g. Kişladağ and Maricunga Belt porphyry Au deposits; Sillitoe 2000; Baker et al., 2016). According to Sillitoe (2000), porphyry Au-only deposits are characterized by a shallow level of emplacement of causative intrusions, an abundance of pyrite instead of chalcopyrite and bornite, the telescoped nature of the alteration systems, fine-grained free gold commonly associated with pyrite, and an exceptionally low Cu/Au ratio (≈ 0.03 at the Kişladağ, porphyry Au deposit, Turkey, Baker et al., 2016). Molybenite in gold-only porphyry deposits is extremely Re enriched as, for example, at the Kişladağ deposit (Baker et al. 2016). This fact holds true for the Pagoni Rachi and Konos Hill deposits: Mineral-chemical analyses yielded an average Re content of 0.48 wt% Re and 0.84 wt% Re for molybdenite at the Konos Hill and Pagoni Rachi, respectively. The presence of Re-enriched molybdenite, along with minor presence of rheniite leads to an important total Re content of the studied systems, with several samples yielding Re values >1ppm, and localizing at the cores of the porphyry systems of Konos and Pagoni Rachi areas. This fact comes in accordance with the findings of John and Taylor (2016), who stated that a higher Re content is usually expected along with the highest Cu-Mo-Au grades in the center of a porphyry system, associated with potassic-, chlorite-sericite- and sericite alteration.

The strong depletion of Re in samples that come from oxidized quartz stockwork in the higher topographic levels of the Pagoni Rachi system, indicates the mobility of the metal in the supergene environment (McCandless et al., 1993).

However, porphyry Au-only deposits (and also Cu-Au and Au-Cu deposits), are characterized by localization of the highest gold grades in the potassic alteration and not with sodic-calcic/potassic-, sodic/potassic- and sericitic alteration, as is the case for the Pagoni Rachi prospect, at least at the present level of exposure. At Pagoni Rachi, sodic/potassic-calcic- and sodic-enriched (i.e., albite-dominated) zones host high-density quartz stockworks and cannot be considered to be deep and distal parts of the Pagoni Rachi ore system, as commonly described for other porphyry systems elsewhere (e.g., Seedorf et al. 2005; Sillitoe 2010; Halley et al. 2015). Commonly, these types of alteration generally do not contain significant enrichments in metallic minerals. However at Pagoni Rachi, sodic/potassic-calcic and sodic/potassic altered rocks yielded the highest concentrations of gold and other critical elements, like Mo, Re, Te, V, Se and Ga instead of the K-rich silicate assemblages. Potassic alteration in the Pagoni Rachi system (mostly expressed by the presence of biotite and K-feldspar) is not abundant and is observed only as restricted, cm-sized laths in the sodic/calcic-altered areas that consist of the assemblage albite-epidote-amphibole-chlorite-titanite-calcite.

The presence of banded quartz veins, is another common characteristic of both the Konos Hill and the Pagoni Rachi porphyry-style mineralization. This is another important feature of porphyry Au/Au-Cu deposits, like the Biely Vrch deposit in Slovakia (Koděra et al., 2018), or the Pancho and Verde deposits, at the Maricunga belt, North Chille (e.g., Muntean 2000). This feature was recently described from other porphyry/epithemal mineralization in Greece, e.g., the Stypi prospect (Voudouris et al., 2019a,b), indicating that an Au-enriched zone of porphyry deposits may extend towards the south and comprise a continuous chain that links the Greek prospects with the Au-enriched deposits of the Afyon zone (e.g. the Kışladağ porphyry deposit, Baker et al., 2016).

A salient feature of the Pagoni Rachi prospect is that gold introduction took place during at least three episodes of mineralization. First, it is associated with chalcopyrite and bornite in early M-, and A-type veinlets that are related to sodic-calcic/potassic

alteration. In this case it occurs in the form of electrum (average Au content 79 % at. Au). Second, pyritic D-type veins associated with sericitic alteration carry native gold (average Au content 89% at. Au), and finally in the form of Ag-Au alloy (average Au content 32 % at. Au), hosted in E-type veins (epithermal style), associated with argillic alteration. The data suggest an increase of the gold purity in the porphyry system from early M/A type veins towards the D-type vein forming event, which also coincides with an increase of Au grade in bulk ore samples. This can probably be attributed to a remobilization and enrichment mechanism in late-stage porphyry-style events and has been previously descibed from porphyry deposits elsewhere (e.g., Kesler et al. 2002). An abrupt decrease of gold follows the transition from the porphyry to the epithermal environment, where Ag is preferably enriched in the mineralization, and gold occurs in the form of Ag-Au alloy.

At the Konos Hill porphyry Cu-Mo-Re prospect, several generations of porphyry quartz stockworks are overprinted by an extensive sericitic alteration that grades upwards into a high-temperature advanced argillic alteration lithocap consisting of pyrophyllite-diaspore- and alunite-zunyite-APS mineral-bearing lithologies (Voudouris et al. 2006; Ortelli et al. 2009; Voudouris 2014; this study). The porphyry mineralization consists mainly of pyrite±molybdenite±rheniite with trace amount of chalcopyrite, bornite, magnetite, enargite, colusite and zincian tetrahedrite-tennantite mostly included in pyrite, and represents a high-sulfidation epithermal mineralization genetically related to a porphyry system. Fluid inclusion microthermometric data of Ortelli et al. (2009) indicate early porphyry ore formation was associated with a boiling fluid at around 500 °C, such as that measured at Pagoni Rachi deposit by Voudouris et al. (2009). A later fluid, with salinities between 30 and 50 wt. % NaCl equiv, at around 240°C (Ortelli et al. 2009), could indicate the incursion of another magmatic fluid in the system, that may have partly contributed to the formation of sodic alteration at Konos Hill. It is hereby speculated, that the strong sericitic, and advanced argillic overprint associated within the Konos Hill porphyry prospect has probably resulted in redistribution of gold to the high-sulfidation epithermal environment and has lead to its deposition in neighboring epithermal Au-Ag-Cu deposit, like the St Demetrios and Viper deposits.

The widespread presence of sericite (term used to describe white micas, both muscovite and the K-deficient illite) in the study area, enhances the acid character of the hydrothermal fluids that caused the sericitic alteration. The solid-solution compositional changes in those minerals are of critical importance in exploring for porphyry deposits, as the compositional changes reflect the acidity of hydrothermal fluids from which they were precipitated (Thompson et al., 1999). Substitution of Al by Fe-Mg in the white micas results in phengitic compositions that indicate more neutral hydrothermal fluids and the wavelength absorption feature of the micas shifts from 2195 nm in muscovite towards 2200 nm in phengite. Measured spectra of sericitic-altered specimens from the study area display a relatively narrow variance between 2188 and 2206 nm, indicating a very minor phengite component. The abundance of muscovitic illite and illite in the sericitic-altered samples and the absence of phengite is a factor that favors low pH (acidic) hydrothermal fluids that affected the mineralized rocks during the late stages when epithermal-style ore was forming. High-to-intermediate sulfidation mineralization was accompanied by extensive sericitic alteration that produced a strong overprint on the porphyry-style alterations in the Sapes-Kirki area.

CHAPTER 5

The Konos Hill Lithocap: an epithermal high-sulfidation alteration assemblage superimposed on a porphyry system

Abstract: The Konos Hill prospect in NE Greece represents a telescoped Mo-Cu-Re-Au porphyry occurrence overprinted by deep-level high-sulfidation mineralization. Porphyry-style mineralization is exposed in the deeper parts of the system and comprises quartz stockwork veins hosted in subvolcanic intrusions of granodioritic composition. Ore minerals include pyrite, molybdenite, chalcopyrite, and rheniite. In the upper part of the system, intense hydrothermal alteration resulted in the formation of a silicified zone and the development of various advanced argillic alteration assemblages, which are spatially related to N–S, NNW–SSE, and E–W trending faults. More distal and downwards, advanced argillic alteration gradually evolves into sericitic assemblages dominated by quartz and sericite. Zunyite, along with various amounts of quartz, alunite, aluminum phosphate–sulfate minerals (APS), diaspore, kaolinite, and minor pyrophyllite, are the main minerals in the advanced argillic alteration. Mineral-chemical analyses reveal significant variance in the SiO_2, F, and Cl content of zunyite. Alunite supergroup minerals display a wide compositional range corresponding to members of the alunite, beudantite, and plumbogummite subgroups. Diaspore displays an almost stoichiometric composition. Mineralization in the lithocap consists of pyrite, enargite, tetrahedrite/tennantite, and colusite. Bulk ore analyses of mineralized samples show a relative enrichment in elements such as Se, Mo, and Bi, which supports a genetic link between the studied lithocap and the underlying Konos Hill porphyry-style mineralization. The occurrence of advanced argillic alteration assemblages along the N-, NNW-, and E-trending faults suggests that highly acidic hydrothermal fluids were ascending into the lithocap environment. Zunyite, along with diaspore, pyrophyllite, and Sr-, and Rare Earth Elements-bearing APS minerals, mark the proximity of the hypogene advanced argillic alteration zone to the porphyry environment.

Keywords: Zunyite; Alunite supergroup minerals; Lithocap; Porphyry-epithermal mineralization; Greece

5.1. Introduction

Porphyry deposits are characterized by a zonation of mineralization and associated types of hydrothermal alteration. In most deposits, this zonation comprises an inner, strongly mineralized part hosted by potassic alteration, which is outwardly replaced by sericitic and more distally by propylitic assemblages, the latter being commonly dominated by epidote and chlorite (Halley et al., 2015). This spatial succession of alteration types reflects the cooling of the hydrothermal fluids and, to some extent, their possible mixing with meteoric fluids (Heinrich et al., 2005; Gustafson and Hunt 1975.

In many cases, advanced argillic alteration zones, or "lithocaps" (Sillitoe, 1989), develop at shallow levels above porphyry Cu–Au deposits [e.g., Lepanto-Far Southeast, Philippines (Hedenquist et al. 1998); Maricunga, Chile (Muntean and Einaudi, 2001)]. Advanced argillic alteration mineral assemblages precipitate from SO2--, and HCl-rich magmatic vapor, which arises from an underlying intrusive source. The vapor condenses into near-surface fluids in a relatively shallow environment (Hedenquist and Lowenstern, 1994; Hedenquist and Taran, 2014), where leaching of the host rock by the most acidic condensate leaves residual silica that recrystallizes to quartz and forms the core of the alteration (Hedenquist and Taran, 2014). In cases where such fluids affect porphyritic magmatic rocks, commonly, the result is vuggy textures.

These lithocaps are favorable environments for exploration, as they can host high-sulfidation ores and can be located spatially adjacent to porphyry-style mineralization (Watanabe et al., 1997; Sillitoe, 1999). Commonly, they comprise various amounts of quartz, andalusite, pyrophyllite, topaz, kaolinite–dickite, diaspore, corundum, zunyite, tourmaline, alunite supergroup minerals, and dumortierite (e.g., Meyer and Hemley, 1967; Stoffregen and Alpers, 1987; Seedorf et al., 2005). Lithocaps are usually zoned. In the deep parts, quartz and pyrophyllite occur, commonly transitioning downwards

to porphyry-related sericitic alteration (Sillitoe, 2010), which hosts pyrite veinlets with silica–sericite selvedges (described also as “D-type” veins) [6,9]. In shallow levels, quartz and alunite predominate (Sillitoe 2010).

Advanced argillic alteration zones commonly overlie or overprint earlier alteration styles in many porphyry systems (Khashgerel et al., 2008). This telescoping has been attributed to rapid collapse of the isotherms, due to the retreat of the magma interface (Heinrich et al., 2004) or to the waning convection from the magmatic body at depth (Shinohara and Hedenquist, 1997), with exogenic factors such as rapid uplift and erosion or collapse of the volcanic edifice also playing important roles (Sillitoe, 1994). Advanced argillic alteration lithocaps have been described from a number of porphyry-epithermal deposits and prospects worldwide, and coupled with the occurrence of a transitional to sericitic alteration zone, they mark the change from the high-sulfidation epithermal to the porphyry environment. Examples include the Hugo Dummett deposit in Mongolia (Khashgerel et al., 2008), El Salvador in Chile (Watanabe et al., 1997), and Rosia Poieni in Romania (Milu et al., 2004).

In Greece, several advanced argillic alteration lithocaps have been identified (e.g., Melfos and Voudouris, 2017; Voudouris et al., 2018, 2019a). The best-known example is in the Kassiteres-Sapes district (Voudouris and Kyriakopoulos, 2003; Voudouris et al., 2006; Voudouris, 2014; Bissig et al., 2016), where advanced argillic alteration zones host significant, high-to-intermediate-sulfidation ores (e.g., the Viper Au–Cu–Ag–Te deposit, Kilias S.P. et al., 2013), which overprint or form laterally to porphyry-style mineralization (Voudouris, 2014; Ortelli et al., 2009; Voudouris et al., 2013b). Other examples include the Mavrokoryphi (Voudouris 2011) and Melitena (Voudouris and Melfos 2013) prospects in the Thrace district, northeastern Greece, as well as the Fakos and Stypsi prospects on Limnos and Lesvos islands, respectively (Voudouris et al., 2005, 2019a; Fornadel et al., 2012; Periferakis et al., 2017; 2018).

Zunyite is a relatively rare mineral in advanced argillic alteration assemblages. It is a F-, and Cl-bearing aluminosilicate [$Al_{13}Si_5O_{20}(OH, F)_{18}Cl$] that was originally described from and named after the Zuni mine at Anvil Mountain, Clorado, United States of America (Kloprogge and Frost, 1999). So far, the presence of zunyite in Greece is only documented from Kos Island (Papoulis et al., 2004), where it occurs in

advanced argillic-altered rhyolites, in association with kaolinite. Mavrogonatos et al., (2018) described the second occurrence of zunyite in Greece, and its only known occurrence (so far) in a lithocap that is superimposed on a porphyry system, namely the studied Mo-Cu-Re-Au Konos Hill porphyry/epithermal system.

This chapter presents further geological and mineralogical data regarding the Konos Hill lithocap and aims to expand previous knowledge on the mineralogy and mineral chemistry of advanced argillic alteration zones in the Sapes district. The study emphasizes in the mineral-chemical implications of phases such as zunyite and APS minerals (among them phases described for the first time in Greece, like the mineral florencite-Ce), because they may constitute an exploration tool for new mineralized centers in the adjacent areas and can be used to define the physicochemical conditions of the transition from the porphyry to the epithermal environment in the Konos Hill prospect.

5.2. Materials and Methods

Rock samples were collected from the advanced argillic-altered rocks of the Konos Hill area for petrographic, mineralogical, mineral-chemical, and geochemical studies. From these samples, sixteen polished-thin sections underwent detailed petrographic investigation using an Axio Scope.A1 (Zeiss) transmitted light microscope.

Powders from ten representative samples were analyzed by X-ray diffraction, using a Siemens/Bruker 5005 X-ray diffractometer at the Faculty of Geology and Geoenvironment, National and Kapodistrian University of Athens. Results were evaluated using the software package DIFFRACplus, EVA (version 10.0). Alteration assemblages in selected rock chips were also determined using short-wave infrared spectroscopy (SWIR) with a portable TerraSpec 4 Standard-Res mineral analyzer.

The chemical compositions of selected minerals (alunite–natroalunite, APS, diaspore, zunyite) were determined by electron probe microanalysis (EPMA) using a JEOL 8530F instrument at the Institute of Mineralogy, University of Münster, Germany. Analytical conditions included a 15-kV accelerating voltage, a 5-nA beam current, and counting times of 10 s for peaks and 5 s for the background signal. Natural (for Na, Mg, Al, Si, Mn, Fe, Sr, Cl, Ba, K, Ca, P, and S) and synthetic (for F, Ti, Cr, La, Ce,

Nd, and Pb) mineral standards were used for calibration prior to quantitative analyses. The phi-rho-z correction was applied to all data. Standard deviations of the major oxides are within 1–2%. Oxides and elements that were analyzed and their average (1σ) detection limits are: Na_2O (0.046 wt %), MgO (0.43 wt %), Al_2O_3 (0.038 wt %), SiO_2 (0.058 wt %), MnO (0.054 wt %), FeO (0.057 wt %), SrO (0.082 wt %), Cl (0.021 wt %), BaO (0.094 wt %), K_2O (0.032 wt %), CaO (0.038 wt %), P_2O_5 (0.049 wt %), SO_3 (0.063 wt %), F (0.14 wt %), TiO_2 (0.13 wt %), La_2O_3 (0.25 wt %), Ce_2O_3 (0.20 wt %), Nd_2O_3 (0.20 wt %), and PbO (0.047 wt %).

In addition, eight mineralized lithocap samples were analyzed commercially by inductively coupled plasma mass spectrometry (ICP-MS package AQ251) at ACME analytical laboratories in Vancouver, BC, Canada, in order to determine their metal concentrations.

5.3 The Konos Hill advanced argillic alteration zone

The Konos Hill area is part of a deeply eroded volcanic edifice built on the Eocene sedimentary deposits (Voudouris, 2014). This volcanic edifice comprises mostly subvolcanic intrusions of calc-alkaline to high-K calc-alkaline affinities, as well as lava domes, flows, and pyroclastic rocks. Both magmatic and pyroclastic rocks are characterized by intense hydrothermal alteration.

Konos Hill, its most prominent topographic feature, is located approximately 20 km N–NW of Alexandroupolis and consists of a hydrothermally altered granodiorite which intruded the volcanosedimentary rocks (Figure 5.1). Further to the ENE in the study area, a monzodioritic body intruded the volcanosedimentary rocks and the granodiorite. Available geochronological data for the monzodiorite yielded cooling ages of 31.9 ± 0.5 Ma (Rb/Sr on biotite Del Moro et al., 1988) and 32.6 ± 0.5 Ma ($^{40}Ar/^{39}Ar$ on biotite, Ortelli et al., 2010). Recently, Perkins et al., 2018, conducted a U–Pb zircon geochronological study on the Kassiteres magmatic suite, showing that magmatism occurred between 32.05 ± 0.02 and 32.93 ± 0.02 Ma. Previous studies in this area have shown that the granodiorite hosts the Konos Hill porphyry Mo–Cu–Re–Au porphyry prospect (Voudouris et al, 2006, 2013a; Ortelli et al., 2009).

Major faults in the Konos Hill area strike N-S, NNE-SSW, and E-W (Figure 5.1) and are usually high-angle faults (dipping between 60-80°). Zones of advanced argillic alteration mostly trend E-W and are related to the previously mentioned fault directions, indicating that magma emplacement, hydrothermal alteration, and associated mineralization were structurally controlled.

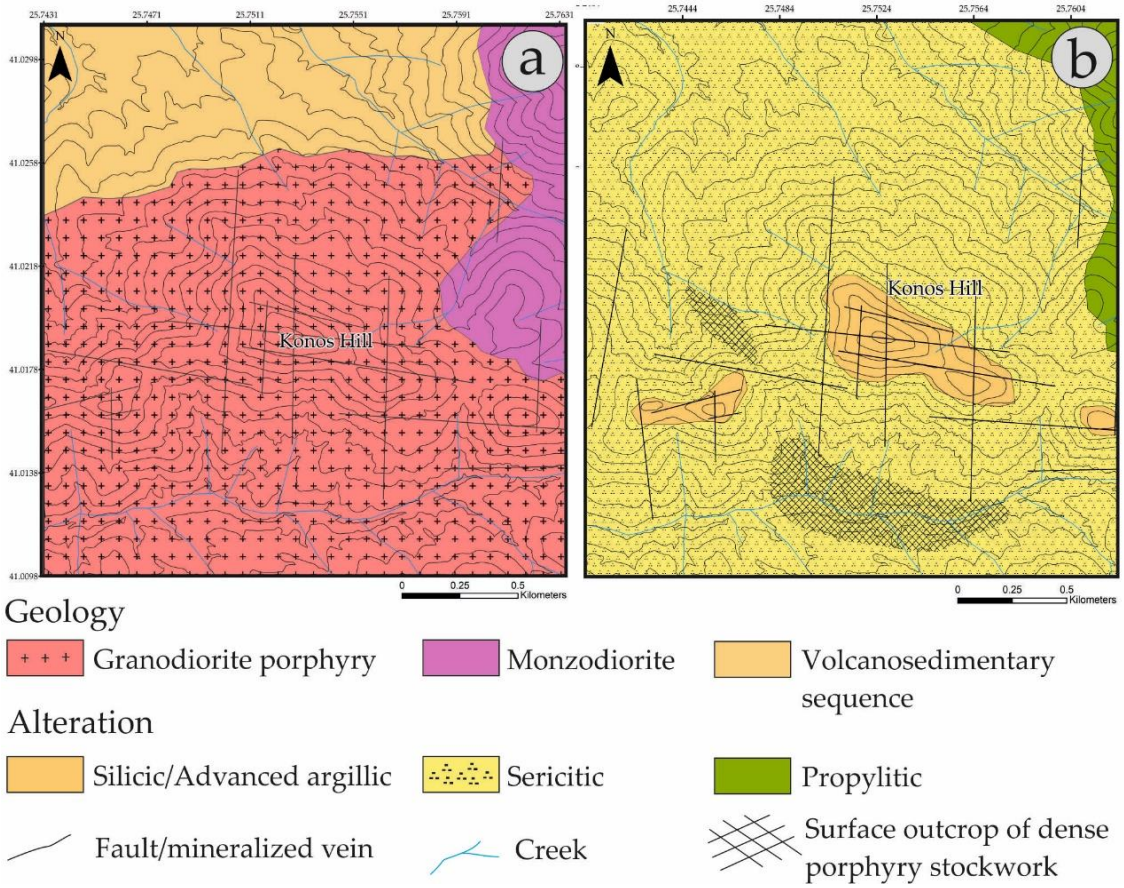

Figure 5.1. Geological (a) and alteration (b) map of the Konos Hill area, NE Greece.

5.4. Alteration and Mineralization

Hydrothermal alteration and mineralization occurring in the Kassiteres–Sapes district have been well-studied (e.g., Voudouris, 1993, 2014; Bridges et al., 1997; Ortelli et al., 2009; Kilias S.P. et al., 2013; Voudouris et al., 2013a; Bissig et al., 2016; Mavrogonatos et al., 2018a, b). Advanced argillic-altered lithocaps have been recognized at a number of sites (Voudouris and Kyriakopoylos, 2003; Voudouris,

2014). Among them, Konos Hill is located in the eastern part of the district and comprises the highest topographic level of the area.

Advanced argillic alteration at Konos Hill is related to E–W, N–S, and NNW–SSE trending fault lines (Figure 5.1). The latter direction is also related to porphyry-style stockwork outcrops, which are best exposed at lower elevation (Figure 5.2a). In the uppermost part, acidic leaching of the granodiorite resulted in a structurally controlled and spatially restricted zone, which comprises residual quartz with a vuggy texture. This zone grades outwards and downwards into alunite-rich assemblages (Figure 5.2b to e), which comprise alunite + APS minerals + quartz + zunyite ± pyrophyllite and quartz + alunite + APS minerals + diaspore + kaolinite ± pyrophyllite. Hematite pseudomorphs after pyrite accompany the abovementioned assemblages. The Konos Hill lithocap is deficient of any primary sulfides due to extensive supergene oxidation; however, it hosts a low-grade Au mineralization (see also Section 5.6). On the contrary, nearby lithocaps at Agios Demetrios, Scarp, Viper, and Agia Barbara host significant high-sulfidation epithermal, gold–enargite mineralization, which is generally found in the western part of the study area (e.g., Shaw and Consantinides, 2001; Michael, 2004; Voudouris et al., 2006, Voudouris, 2014; Bissig et al., 2016;). Advanced argillic alteration assemblages evolve downwards through a transitional zone of quartz + alunite + pyrophyllite + sericite into a typical sericite-rich assemblage, which is the most widespread type of hydrothermal alteration in the district. The latter hosts porphyry-style (A-, and banded) quartz stockwork (Figures 5.2f and 5.2i) and D-type quartz–sericite veins with a pyrite–molybdenite–chalcopyrite–rheniite mineralization (Voudouris et al., 2006, 2013a, 2019a; Ortelli et al., 2009; this study). Minor amounts of enargite, colusite, tetrahedrite–tennantite group minerals (fahlores), and galena occur both within the veins and as disseminations in the sericitic-altered granodiorite and comprise a high-sulfidation mineralization superimposed on the porphyry system.

Extensive sericitic alteration also affected outcrops of the volcanosedimentary succession as well as parts of the monzodiorite intrusion, especially along fault planes. It grades further outwards into propylitic alteration that is characterized by varying amounts of epidote, chlorite, carbonates (mainly calcite) and abundant pyrite.

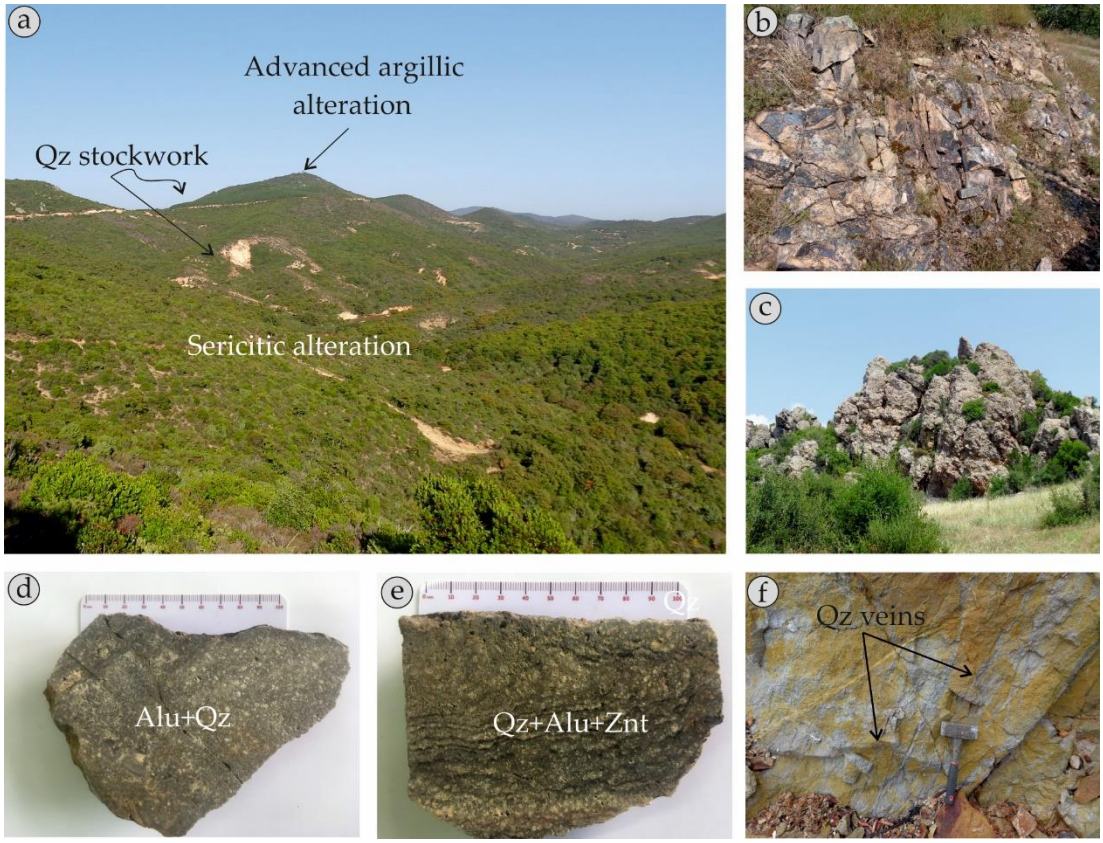

Figure 5.2. Field and hand-specimen photographs from Konos Hill, NE Greece. (a) Panoramic view of Konos Hill; (b) Quartz–alunite–zunyite-bearing rocks on top of Konos Hill; (c) Quartz–alunite–diaspore-bearing rocks in the NW slopes of Konos Hill; (d,e) Hand-specimens of quartz–alunite (Alu + Qz) and quartz–alunite–zunyite (Qz + Alu + Znt) assemblages, samples KMSP72 and KMSP71, respectively; (f) Quartz porphyry stockwork veins in sericitic-altered granodiorite from Saporema Creek.

5.5. Petrography and Mineral Chemistry

5.5.1. Zunyite

Zunyite forms euhedral crystals that are up to 300 μm in size (Figures 5.3a, b and 4.4a). They are commonly associated with quartz and tabular alunite–natroalunite crystals, with minor amounts of spheroidal hematite, which along with goethite, formed after pyrite (Figure 5.3a, b). In rare cases, zunyite contains submicroscopic APS inclusions (Figure 5.4b). Electron probe microanalyses show significant compositional variations (Table 5.1). The SiO_2 varies from 22.7 to 25.14 wt %, whereas the Al_2O_3 content clusters tightly at 54.97 to 55.81 wt %. Fluorine and chlorine contents range between 4.07 and 5.93 wt % and 2.72 to 2.97 wt %, respectively. In some cases, traces

of Na_2O, BaO, TiO_2, Na_2O, Ce_2O_3, and Nd_2O_3 were detected (up to 0.40, 0.26, 0.23, 0.34, and 0.21 wt %, respectively).

5.5.2. Diaspore

Diaspore is generally found as euhedral to subhedral crystals measuring up to 0.2 cm in size. Commonly, it forms isolated grains scattered in a fine-grained matrix of tabular alunite crystals and quartz (Figure 5.3c). Diaspore also forms aggregates of fine-grained subhedral crystals that replace earlier mineral phases of the silicified rock such as feldspars (Figures 5.3d and 5.4c). In some cases, diaspore crystals occur as euhedral grains in fissures or cracks in the matrix. Electron microprobe analyses reveal near stoichiometric compositions with traces of TiO_2, BaO, and REE, mostly Ce_2O_3 and Nd_2O_3 (up to 0.18, 0.98, 0.38, and 0.22 wt %, respectively; Table 5.1). Concentric zoning patterns occur in some crystals (Figure 5.3c), but are apparently not associated with chemical variations.

Table 5.1. Representative EPMA data of zunyite (1–6) and diaspore (7–10) from the advanced argillic alteration zone of the Konos Hill prospect, NE Greece.

wt %	1	2	3	4	5	6	7	8	9	10
SiO_2	25.14	22.96	23.66	24.35	22.70	24.58	bd	bd	bd	bd
TiO_2	bd	0.11	bd	0.26	bd	bd	0.18	bd	bd	bd
Al_2O_3	55.03	54.97	55.25	54.76	55.81	55.32	83.05	82.58	82.42	82.57
FeO	bd	0.05	0.04	0.16	bd	0.08	bd	bd	bd	bd
Na_2O	0.40	0.11	0.34	0.09	0.39	0.19	0.02	bd	0.02	0.01
BaO	0.11	bd	bd	bd	bd	0.23	0.98	bd	bd	bd
La_2O_3	bd	bd	bd	bd	bd	bd	bd	bd	bd	0.34
Ce_2O_3	bd	bd	bd	bd	bd	0.34	bd	0.38	0.24	bd
Nd_2O_3	bd	bd	0.21	bd	bd	bd	bd	0.30	0.16	0.22
P_2O_5	0.05	0.51	0.27	0.25	0.70	0.11	0.05	bd	0.05	bd
F	5.93	4.56	4.82	4.07	5.08	4.32	bd	0.11	bd	bd
Cl	2.90	2.82	2.97	2.91	2.72	2.75	bd	bd	0.01	bd
Total	89.63	86.16	87.60	86.92	87.47	88.04	84.42	83.37	82.90	83.23
apfu			29.5 (O)					1.5 (O)		
Si	5.013	4.679	4.787	4.895	4.596	4.920	0.000	0.000	0.000	0.000
Ti	0.005	0.017	0.000	0.039	0.000	0.000	0.001	0.000	0.000	0.000
Al	12.931	13.202	13.150	12.976	13.190	12.919	0.994	0.997	0.997	0.996
Fe	0.000	0.009	0.007	0.027	0.000	0.013	0.000	0.000	0.000	0.000
Na	0.016	0.043	0.134	0.033	0.154	0.072	0.000	0.000	0.000	0.000
Ba	0.001	0.005	0.002	0.001	0.000	0.018	0.004	0.000	0.000	0.000
La	0.002	0.000	0.000	0.000	0.000	0.002	0.000	0.000	0.000	0.002
Ce	0.000	0.011	0.002	0.003	0.000	0.027	0.000	0.000	0.001	0.001
Nd	0.000	0.000	0.015	0.000	0.000	0.000	0.001	0.001	0.001	0.001
P	0.008	0.089	0.046	0.043	0.120	0.019	0.000	0.000	0.001	0.000
F	3.224	2.956	2.704	2.305	2.837	2.431	0.000	0.004	0.000	0.000
Cl	0.844	0.860	0.891	0.884	0.817	0.830	0.000	0.000	0.000	0.000

bd: below detection; apfu: atoms per formula unit.

5.5.3. Alunite Supergroup Minerals

Alunite supergroup minerals consist of four major subgroups, each one containing a varying number of different members. These subgroups consist of the alunite (e.g., alunite, natroalunite), beudantite (e.g., woodhouseite, svanbergite), plumbogummite (e.g., crandalite, florencite), and dussertite groups (e.g., arsenocrandalite, segnitite) (Scott, 1987; Dill, 2001; Mills et al., 2009; Bayliss et al., 2010). Microscopic examinations together with EPMA data reveal a wide compositional range for alunite supergroup minerals in the Konos Hill area. Based on in the distribution of data in Figure 5.5a, analyzed compositions comprise members of the alunite, beudantite, and plumbogummite subgroups.

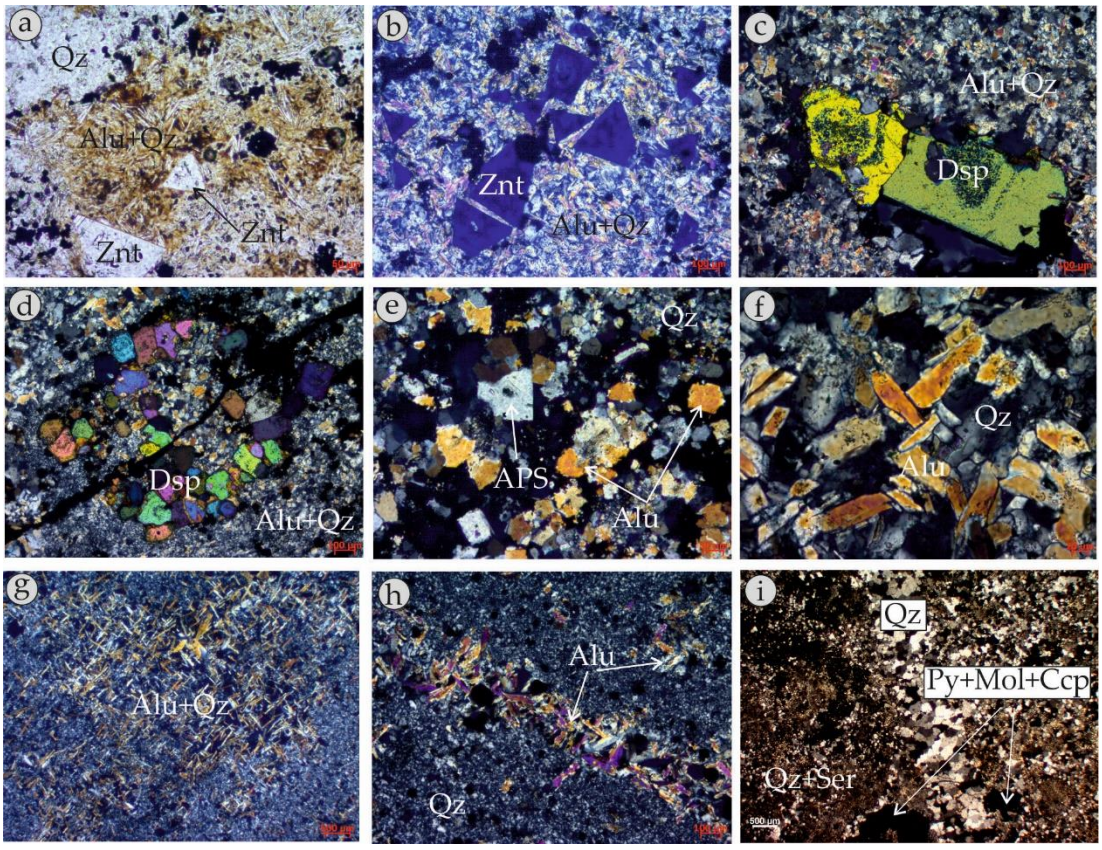

Figure 5.3. Transmitted light microphotographs of alteration assemblages from the Konos Hill area, NE Greece. (a,b) Euhedral zunyite (Znt) crystals in association with quartz and tabular alunite (Alu + Qz, plane-polarized and crossed-polarized light, respectively), sample KMSP71; (c) Subhedral diaspore (Dsp) crystals displaying concentric zonation patterns (crossed polarized light), sample KMSP73; (d) Subhedral diaspore (Dsp) crystals set in an alunite (Alu) and quartz (Qz) matrix of altered granodiorite (crossed-polarized light), sample KMSP71; (e) APS crystals form the core of pseudocubic alunite (crossed-polarized light), sample KMSP72; (f) Tabular alunite

crystals in association with quartz (Qz, crossed-polarized light), SAMPLE kmsp73; (g) Alunite (Alu) aggregate replacing a phenocryst in the granodiorite (crossed-polarized light) sample KMSP72; (h) Alunite (Alu) crystals forming veinlets in the quartz (Qz)-dominated matrix (crossed-polarized light), sample KMSP73; (i) Sugary quartz (Qz) crystals in porphyry-style vein hosting pyrite–molybdenite–chalcopyrite ore (Py + Mol + Ccp) in sericite-altered granodiorite (crossed-polarized light), sample KMSP77.

Aluminum phosphate–sulfate (APS) minerals occur mostly as euhedral pseudocubic inclusions in zoned natroalunite in all types of advanced argillic assemblages at Konos Hill (Figures 5.3e and 5.4d, e). EPMA data (Table 5.2) revealed varying amounts of CaO (up to 10.96 wt %), BaO (up to 3.60 wt %), SrO (up to 9.54 wt %), Ce_2O_3 (up to 11.06 wt %), La_2O_3 (up to 4.90 wt %), Nd_2O_3 (up to 4.72 wt %), and P2O5 (up to 29.55 wt %). In many cases, minor concentrations of K_2O and Na_2O were detected (up to 0.99 and 0.83 wt %, respectively). It is notable that all analyzed APS minerals contained small amounts of fluorine (up to 1 wt %). Chemical variations of the APS minerals are summarized in Table 5.2 and shown in Figure 5.5a to 5.5d. The most common compositions include woodhouseite and svanbergite. Crandallite and florencite are rare. Woodhouseite is the most common APS and it was present with near end-member compositions, although Ba- and Sr-rich varieties were also identified. The average compositions of woodhouseite and svanbergite correspond to the formulae $Ca_{0.63}Ba_{0.05}Na_{0.06}Sr_{0.20}Ce_{0.02}Al_{3.07}(SO_4)_{0.87}(PO4)_{1.17}$ and $Sr_{0.37}Ca_{0.20}Ba_{0.07}Ce_{0.03}Al_{3.08}(SO_4)_{0.87}(PO4)_{1.16}$, respectively. Crandallite is usually Sr-rich, whereas florencite-(Ce) was also identified for the first time in Greece (Table 5.2).

The APS minerals studied here comprise solid solution members of the beudantite and plumbogummite subgroups. They plot along the 1:1 line in Figure 5.5a and display a progressive substitution of PO_4^{3-} by SO_4^{2-}, coupled with a substitution of monovalent (K, Na) by divalent (Ca, Ba, Sr) cations in the D site. Compositions that plot further below this line display a significant variation in P, whereas compositional variations in the D site are limited. This points towards protonation of one of their trivalent anions to establish charge balance. Moreover, the APS minerals that are devoid of monovalent cations (P > 1 apfu) are also characterized by a 1:1 substitution in the monovalent-bearing D site by divalent cations (Figure 5.5b), whereas compositions that plot below this line indicate significant vacancies due to charge balance. In

addition, APS compositions that exhibit elevated phosphate contents are, according to Scott, 1987, consistent with the appearance of trivalent cations substituting in the A site of the minerals. This is mirrored by the presence of Ce-rich varieties such as florencite-(Ce) in Konos Hill. This substitution is in agreement with the findings of Voudouris, (2014) and Voudouris and Melfos, (2013), who studied the APS mineralogy of the Kassiteres–Sapes and Melitena prospects, respectively.

Alunite and natroalunite are the most common representatives of the supergroup and are found as minor constituents in the vuggy silica in both quartz + zunyite + kaolinite ± pyrophyllite and quartz + diaspore + kaolinite ± pyrophyllite assemblages, as well as in the transitional zone to the sericitic alteration. They are generally found in tabular-shaped or rhombohedral crystals that replaced earlier formed phenocrysts (e.g., feldspars, Figure 5.3g) or mafic minerals in the host rocks. However, pseudocubic shapes were also observed (Figures 5.3e to h, and 5.4). In other cases, tabular alunite forms in small veinlets crosscutting the silicified matrix. Many alunites are K-rich, with K_2O values reaching up to almost 9 wt % (Table 5.3). This corresponds to an average chemical formula of $K_{0.39}Na_{0.30}Ca_{0.01}Ba_{0.01}Al_{3.06}(SO_4)_{1.96}(PO_4)_{0.01}$. Sodium-rich alunite is more common and usually forms euhedral, tabular-shaped crystals with sizes up to 500 μm. In this case, the Na_2O content is higher than K_2O and reaches up to 5.51 wt %, corresponding to the average formula $Na_{0.61}K_{0.35}Ca_{0.01}Al_{3.01}(SO_4)_{1.98}(PO_4)_{0.01}$. Substitution between Na and K in the D sites of alunite is almost ideal, leading to complete substitution of K by Na (Figure 5.5c). However, the majority of the analyzed compositions deviate from the ideal 1:1 substitution, probably reflecting vacancies in the structure, as proposed by Scott, 1987, and in accordance with the findings of Voudouris, 2014. Moreover, a few analyses plot above the 1:1 line and probably reflect a partial excess of K or Na in the D sites. Many grains of alunite carry traces of CaO, FeO, SrO, BaO, La_2O_3, Ce_2O_3, and Nd_2O_3 (values up to 0.38, 0.46, 0.38, 0.75, 0.42, 0.36, and 0.33 wt %, respectively). In some cases, oscillatory zoning is present in alunite crystals, as shown by alternations of concentric K- and Na-rich bands in Figures 5.5e, f. Many alunite grains, especially the tabular-shaped, zoned natroalunite, include cores of APS minerals, mostly woodhouseite or svanbergite.

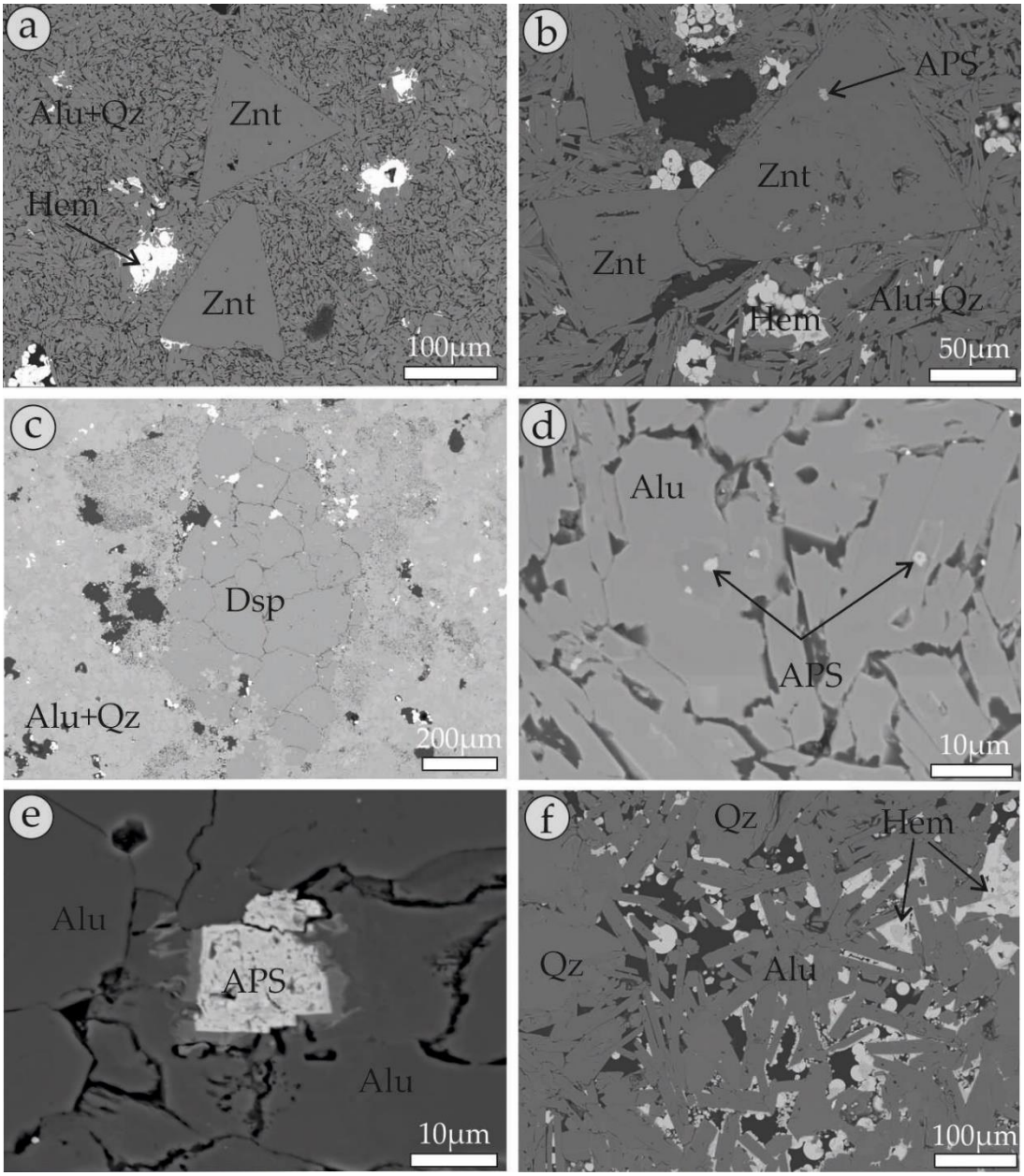

Figure 5.4. Back-scattered electron images of alteration minerals contained in samples from Konos Hill, NE Greece: (a) Euhedral zunyite (Znt) crystals in association with quartz, tabular alunite (Alu + Qz), and hematite (Hem), sample KMSP71; (b) APS included in euhedral zunyite (Znt), sample KMSP71; (c) Diaspore (Dsp) crystals included in an alunite and quartz (Alu + Qz)-dominated matrix sample KMSP73; (d, e) APS pseudocubic crystals in the core of tabular-shaped alunite, sample KMSP70; (f) Tabular alunite (Alu) in association with quartz (Qtz) and hematite (Hem), sample KMSP72.

5.5.4. Kaolinite–Pyrophyllite

Kaolinite and pyrophyllite are present as minor constituents and usually form small, acicular aggregates that accompany quartz–alunite–APS–diaspore and quartz–

alunite–zunyite–APS assemblages. Their presence, in addition to microscopic examination, was verified by X-ray diffraction and SWIR investigations (see appendices F and G, respectively) and Figure 5.6.

Table 5.2. Representative EPMA data of APS minerals from the advanced argillic alteration zone of the Konos Hill prospect, NE Greece. 1: Ba-rich woodhouseite; 2 to 4: Ca-rich svanbergite; 5: Ce-Ba-Ca-rich svanbergite; 3, 7 and 8: Sr-rich woodhouseite; 6: Ba-rich svanbergite; 9: Sr-rich crandalite; 10: florencite-(Ce).

wt %	1	2	3	4	5	6	7	8	9	10
Al_2O_3	33.59	34.10	34.22	35.41	36.67	34.88	34.48	38.09	32.79	32.31
FeO	0.09	0.06	bd	bd	0.10	bd	bd	bd	bd	0.07
CaO	10.96	3.36	7.11	3.93	2.11	0.97	5.86	5.91	5.94	0.66
Na_2O	0.61	0.28	0.08	0.31	0.48	0.27	0.36	0.83	0.12	bd
K_2O	0.48	0.37	0.21	0.59	0.99	0.78	0.74	0.89	0.43	0.11
BaO	1.47	1.52	0.87	1.61	2.10	3.60	1.09	1.06	0.97	3.92
La_2O_3	0.50	0.07	bd	0.19	0.43	0.91	bd	bd	bd	4.90
Ce_2O_3	1.42	0.32	bd	0.88	2.48	2.53	1.14	bd	bd	11.06
NdO_3	0.10	0.34	bd	0.10	1.45	3.48	0.30	bd	bd	4.72
SrO	0.83	9.54	7.63	8.41	7.45	6.33	5.37	4.54	7.82	3.30
PbO	bd	bd	bd	0.05	0.05	bd	bd	0.22	bd	bd
SO_3	15.33	14.35	11.81	15.95	14.98	14.32	13.63	20.31	3.19	3.63
P_2O_5	16.72	17.35	21.57	18.26	19.27	18.53	20.26	15.58	29.55	23.03
F	0.49	0.97	0.51	0.25	0.98	0.17	0.67	0.83	0.56	0.41
Total	82.59	82.63	84.10	85.94	89.54	86.83	83.92	88.35	81.41	88.12
apfu					11 (O)					
Al	3.022	3.034	3.037	3.098	3.067	3.139	3.060	3.180	2.996	3.076
Fe	0.007	0.004	0.000	0.000	0.006	0.000	0.001	0.000	0.000	0.005
Ca	0.858	0.282	0.574	0.313	0.161	0.080	0.473	0.445	0.488	0.057
Na	0.096	0.042	0.011	0.045	0.067	0.040	0.052	0.113	0.012	0.000
K	0.053	0.036	0.019	0.056	0.090	0.076	0.071	0.081	0.04	0.011
Ba	0.047	0.046	0.027	0.047	0.058	0.108	0.032	0.029	0.029	0.119
La	0.015	0.002	0.000	0.005	0.011	0.025	0.000	0.002	0.000	0.146
Ce	0.042	0.010	0.000	0.024	0.006	0.071	0.031	0.000	0.000	0.528
Nd	0.003	0.010	0.000	0.003	0.037	0.095	0.008	0.000	0.000	0.136
Sr	0.028	0.433	0.333	0.362	0.306	0.280	0.235	0.186	0.340	0.155
Pb	0.000	0.000	0.000	0.001	0.001	0.001	0.000	0.004	0.000	0.000
S	0.934	0.841	0.678	0.888	0.904	0.821	0.770	1.080	0.199	0.221
P	1.081	1.148	1.376	1.147	1.158	1.198	1.292	0.985	1.822	1.741
F	0.121	0.239	0.120	0.058	0.216	0.042	0.156	0.113	0.129	0.106

bd: below detection; apfu: atoms per formula unit.

Table 5.3. Representative EPMA data of members of the alunite–natroalunite solid solution from the advanced argillic alteration zone at the Konos Hill prospect, NE Greece.

wt %	1	2	3	4	5	6	7	8	9	10	11	12	13	14	15
Al_2O_3	37.90	37.66	39.47	36.54	37.19	37.40	37.65	36.80	36.96	38.08	42,41	36.95	38.24	40.44	39.95
FeO	0.46	0.30	0.23	0.12	0.28	0.17	0.02	0.10	0.07	bd	0.01	bd	bd	bd	0.12
CaO	0.01	0.02	0.05	0.38	0.03	0.07	0.02	bd	bd	0.09	0.10	0.01	0.05	0.00	0.05
Na_2O	4.63	5.12	2.57	3.07	4.58	5.01	2.79	1.78	1.97	5.51	5.31	1.97	1.64	1.33	2.18
K_2O	3.52	3.59	3.02	4.91	3.90	3.41	5.75	7.10	6.86	2.6	1.95	7.02	4.71	4.44	3.69
BaO	0.15	0.37	0.21	0.21	0.10	0.21	0.16	bd	0.12	0.11	0.17	0.46	0.75	0.30	0.38
SrO	bd	bd	0.28	0.38	0.12	bd	0.19	bd	bd	0.15	0.22	0.05	0.24	bd	0.07
La_2O_3	bd	bd	bd	bd	0.37	0.25	0.26	bd	bd	bd	0.19	0.25	bd	0.42	bd
Ce_2O_3	0.11	bd	0.35	bd	0.13	0.11	bd	bd	0.19	bd	bd	0.36	bd	bd	0.15
Nd_2O_3	bd	bd	bd	0.28	bd	bd	0.33	bd	bd	bd	bd	0.27	0.25	0.11	bd
SO_3	34.74	35.16	36.72	34.05	34.24	34.57	34.73	33.69	34.52	34.46	35.48	33.66	33.93	36.46	35.05
Total	81.61	82.32	82.90	79.97	80.94	81.28	81.90	79.49	80.69	81.00	85.81	81.01	79.89	83.52	81.64
apfu								11 (O)							
Al	3.218	3.177	3.238	3.106	3.198	3.190	3.218	3.231	3.302	3.241	3.391	3.229	3.223	3.309	3.391
Fe	0.028	0.018	0.014	0.01	0.017	0.01	0.000	0.006	0.004	0.000	0.000	0.000	0.000	0.000	0.007
Ca	0.001	0.001	0.004	0.029	0.002	0.005	0.001	0.000	0.000	0.007	0.007	0.001	0.004	0.000	0.004
Na	0.646	0.708	0.317	0.335	0.649	0.704	0.392	0.258	0.279	0.772	0.701	0.283	0.228	0.181	0.296
K	0.324	0.332	0.298	0.447	0.363	0.315	0.532	0.675	0.644	0.240	0.169	0.664	0.430	0.400	0.331
Ba	0.004	0.010	0.006	0.006	0.002	0.004	0.004	0.000	0.003	0.004	0.004	0.013	0.021	0.008	0.010
Sr	0.000	0.000	0.011	0.006	0.006	0.000	0.008	0.000	0.000	0.005	0.009	0.002	0.010	0.000	0.003
La	0.000	0.000	0.000	0.000	0.022	0.007	0.007	0.000	0.000	0.000	0.005	0.007	0.002	0.011	0.000
Ce	0.003	0.000	0.012	0.000	0.010	0.003	0.000	0.000	0.005	0.000	0.001	0.010	0.000	0.001	0.004
Nd	0.000	0.000	0.000	0.000	0.003	0.000	0.009	0.000	0.000	0.000	0.000	0.007	0.007	0.003	0.000
S	1.878	1.889	1.789	1.716	1.879	1.891	1.890	1.894	1.904	1.868	1.816	1.873	1.738	1.855	1.847

bd: below detection; apfu: atoms per formula unit.

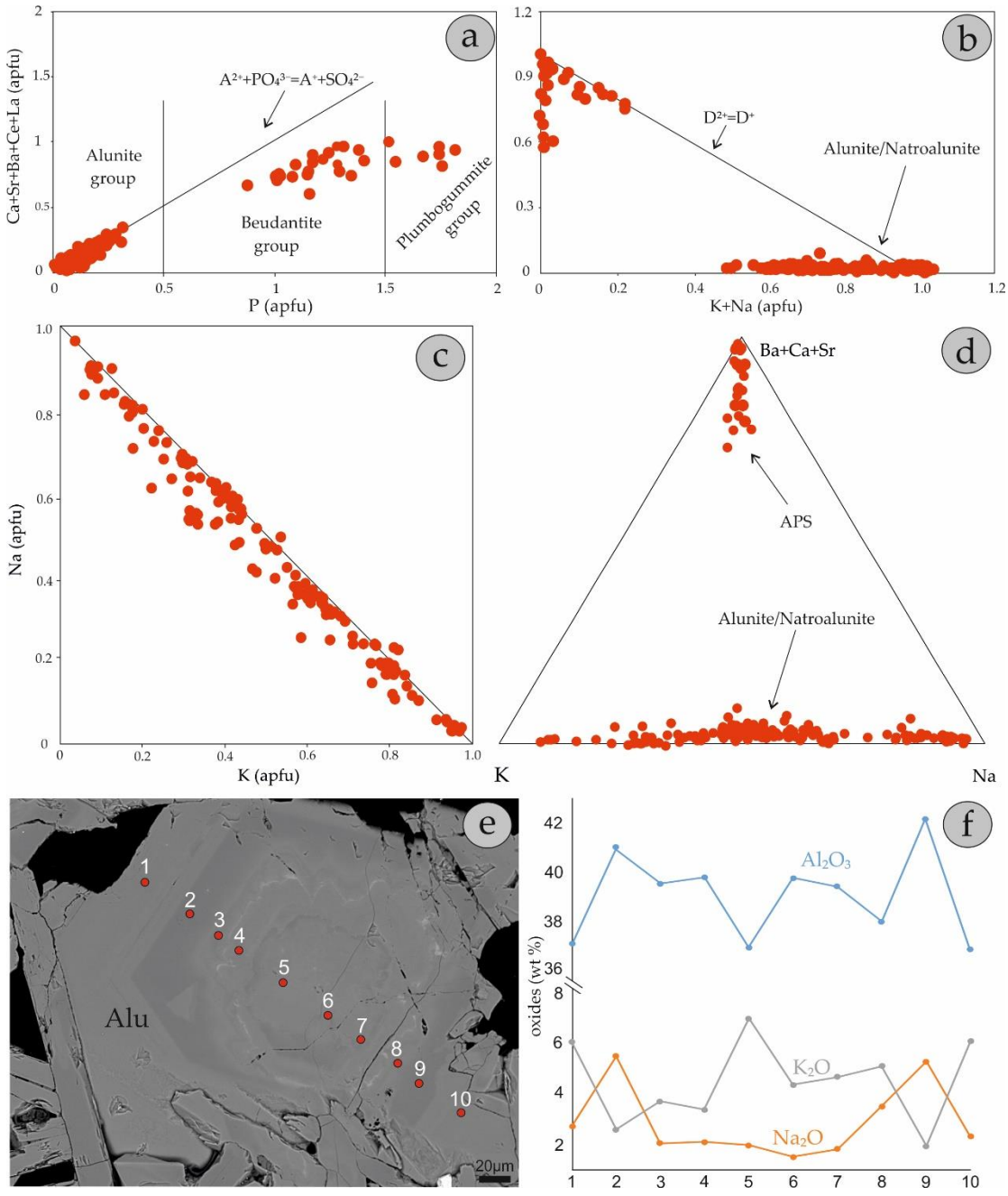

Figure 5.5. Chemical variation diagrams of alunite and APS minerals from the Konos Hill area, NE Greece. (a) Ca + Sr + Ba + Ce + La vs. P plot (the line represents the occupancy of divalent and trivalent cations in the A site relative to trivalent anions in the X site); (b) Ca + Sr + Ba + Ce + La vs. K + Na plot (the line represents the occupancy of monovalent relative to divalent cations in the D site); (c) Na vs. K in A sites; (d) Ternary K–Na–(Sr + Ba + Ca) plot of alunite supergroup minerals; (e) Back-scattered electron image showing a zoned alunite crystal, sample KMSP72. Numbers indicate EPMA spots; (f) Profile depicting the chemical variations of alunite in terms of Al_2O3, Na_2O, and K_2O (wt %). Numbers on the x axis represent the analyzed spots shown in (e).

5.6. Bulk Ore Geochemistry

Bulk analyses of advanced argillic-altered samples reveal (Table 5.4) low concentration values of Au and Ag, which reach up to 0.36 and 0.22 ppm, respectively. Pb concentration values reach up to 122 ppm, while a relative enrichment is also remarked in chalcophile elements such as Mo (up to 19 ppm), Bi (up to 13 ppm), and Se (up to 26 ppm), which mirrors the close genetic relation of the lithocap to the underlying porphyry-style mineralization. Finally, Ga and Sn are also enriched, with values up to 17 and 18 ppm, respectively.

Table 5.4. Metallic element concentrations of samples from the high-sulfidation mineralization at the Konos Hill prospect, NE Greece (values in ppm).

Sample	1	2	3	4	5	6	7	8
As	15	18	34	18	4	6	67	66
Ag	0.19	0.16	0.13	0.23	0.22	0.04	0.12	0.13
Au	0.04	0.02	0.36	0.19	0.04	0.03	bdl	0.05
Cu	10	7	7	5	32	9	14	13
Bi	2.03	2.97	2.42	2.08	6.79	1.79	13	9.22
Mo	3.56	2.36	2.37	3.76	19	5.95	1.30	4.55
Se	2.50	4.40	14	5.90	26	6.50	2.50	11
Te	0.23	0.12	0.16	0.21	0.71	0.16	0.78	1.83
Pb	110	116	122	93	169	59	93	87
Zn	4.40	2.50	2	4.30	5.80	7.40	12	6.60
Sb	5.07	1.88	1.93	5.34	4.89	0.56	4.91	7.35
Ga	5.12	4.22	6.72	11	14	17	17	16
Sn	3.70	2.10	2	1.60	4.60	18	1	2.50

bdl: below detection; Au detection limit: 0.02 ppm.

5.7. Discussion

5.7.1 Genetic implications

Advanced argillic lithocaps form in higher topographic levels from the condensation of magmatic vapors into surface waters, and slightly postdate the potassic alteration in the porphyry environment and the advanced argillic alteration in the high sulfidation environment (Hedenquist and Taran, 2013; Hikov et al., 2010). Field and mineralogical data from the Konos Hill area are consistent with the concept

of hypogene formation of the advanced argillic alteration. This is in agreement with the findings of Voudouris and Melfos, 2013 and Voudouris, 2014, who described similar assemblages from advanced argillic-altered rocks in the Kassiteres–Sapes and Melitena districts, respectively. The occurrence of both advanced argillic and transitional to sericitic alteration zones in the Konos Hill area is similar to other porphyry/epithermal transitional systems (e.g., Lepanto-Far Southeast, Philippines, Hedenquist et al.,1998; Asarel porphyry Cu deposit, Bulgaria, Reyes, 1991), and is the result of different degrees of hydrolytic alteration of the host rocks.

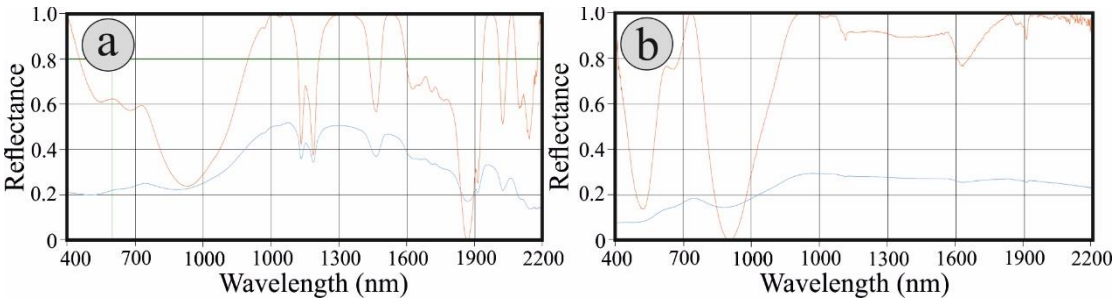

Figure 5.6. Short-wave infrared spectra of kaolinite (a) and Alunite-Na (b) from the Konos Hill advanced argillic alteration zone.

5.7.2 Conditions of formation of the Konos Hill Lithocap

The presence of zunyite in the Konos Hill lithocap (Mavrogonatos et al., 2018) reflects the availability of F and Cl in the hydrothermal fluid and can be used to constrain the conditions of formation of the studied assemblages. Estimations can be made based on similar advanced argillic alteration assemblages reported in the literature. A low-temperature limit is set by the coexistence of zunyite with pyrophyllite, which according to Reyes (1990, 1991) is not stabilized at temperatures below 200 °C. Based on isotopic and microthermometric data, Watanabe et al., 1997, reported formation temperatures of 260 to 350 °C for an assemblage of zunyite + topaz + diaspore + pyrophyllite in the Kobui area of Hokkaido, Japan. A similar temperature range (~250 to 380 °C) was reported for the assemblage of topaz + alunite + diaspore + APS + pyrophyllite from the Koryphes Hill area, where topaz, not

zunyite, is the F-carrier (Voudouris, 2014). Based on similarities between the studied occurrence and the Hugo Dummett porphyry Cu–Au deposit, a T range of 280–350 °C is likely, based on the data of Khasgherel et al., 2008. Further constraints can be made since alunite at Konos Hill contains APS minerals, which according to Hedenquist et al., 1998, are formed in a high-temperature environment at the margins of a magmatic intrusion, compared to APS-free alunite. Chemical zonation in the alunite supergroup minerals in the current study, according to Stoffregen and Alpers, 1987, reflects fast changes in the physicochemical variations in the hydrothermal fluid (decrease in pH and temperature). In addition, the widespread presence of Na-rich alunite versus its K-rich counterpart may suggest either higher temperatures of formation or a higher concentration of Na during the formation of the assemblages. This hypothesis is in accordance with the findings of Chang et al., 2011, who stated that high Na/(Na + K) ratios in alunites from the Mankayan area in the Philippines mark the proximity of the assemblage to the intrusive body. In addition, the chemical composition (e.g., Sr/Pb and La/Pb ratios) of alunite can be used as exploration tools, since Pb is highly soluble in higher temperatures and is preferably incorporated in the alunite structure in distal assemblages, where the hydrothermal fluid is cooler, as is the case for the Mankayan deposit (Chang et al., 2011). However, at the Melitena prospect, Pb-rich APS minerals are associated with the porphyry-style mineralization (Voudours and Melfos, 2013). The studied alunites from the Konos Hill prospect are Pb-free, similarly to alunites from the broader Kassiteres–Sapes district (Voudouris, 2014), thus precluding any application of Pb as an exploration tool, according to Chang et al., 2011. In contrast, the elevated concentrations of Sr and REE in the studied alunite supergroup minerals, as expressed by the presence of woodhouseite and REE-bearing APS minerals (e.g., florencite-Ce) suggest the proximity to the causative intrusion and could be used as an exploration tool in the study area.

Bulk ore analyses from lithocap samples yielded low concentrations of Au and Ag, but significant enrichment in chalcophile elements such as Mo, Se, Bi, and Pb, which were probably introduced after the early event of acid leaching. Similar element anomalies are also reported from the advanced argillic alteration lithocap of Agia Barbara, in the broader Kassiteres-Sapes district, by Voudouris, 2014.

The fact that advanced argillic zones in the Konos Hill area display a more-or-less E-W trend, which follows the major tectonic orientation of the granodiorite emplacement, suggests that the SO_2- and HCl-bearing magmatic vapor may have ascended through these fault planes.

Close to the paleosurface, it condensed into surficial water and formed the advanced argillic alteration assemblages in a typical HS environment, in accordance with the findings of Holley et al. 2017, who studied the Veladero Au–Ag HS epithermal mineralization. Moreover, the presence of the Konos Hill lithocap suggests that detailed mapping and mineralogical studies in hypogene advanced argillic alteration zones are critical, due to their common cogenetic and close spatial relations with porphyry-style mineralization in many prospects in Greece (Voudouris, 2014; Voudouris and Melfos 2013). The presence of F-bearing phases such as zunyite, alunite, APS minerals, diaspore, and pyrophyllite at Konos Hill provides a potential vector towards possible hidden intrusions that may host porphyry-style mineralization.

CHAPTER 6

Magmatic versus Hydrothermal magnetite: a case study from the Pagoni Rachi porphyry prospect

Abstract: Magnetite is a common accessory phase in various types of ore deposits. Its trace element content has proven to have critical implications regarding petrogenesis and as guides in the exploration for ore deposits in general. In this study we use LA-ICP-MS (laser ablation- inductively coupled plasma-mass spectrometry) analyses of trace elements to chemically characterize magnetite from the Pagoni Rachi Cu-Mo-Re-Au porphyry-style prospect, Thrace, northern Greece. Igneous magnetite mostly occurs as euhedral grains, which are commonly replaced by hematite in fresh to propylitic-altered granodiorite porphyry, whereas, hydrothermal magnetite forms narrow veinlets or is disseminated in sodic/potassic-calcic altered (albite + K-feldspar + actinolite + biotite +chlorite) granodiorite porphyry. Magnetite is commonly associated with chalcopyrite and pyrite and can locally exhibits martitization. Laser ablation ICP-MS analyses of hydrothermal magnetite yielded elevated concentrations in several trace elements (e.g., V, Pb, W, Mo, Ta, Zn, Cu, Nb) whereas Ti, Cr, Ni, and Sn display higher concentration in its magmatic counterpart. A noteworthy enrichment in Mo, Pb and Zn is an unusual feature of hydrothermal magnetite from Pagoni Rachi. High Si, Al and Ca values in a few analyses of hydrothermal magnetite imply the presence of submicroscopic or nano-inclusions (e.g., chlorite, titanite). The trace element patterns of the hydrothermal magnetite and especially the decrease in its Ti content reflect an evolution from the magmatic towards the hydrothermal conditions under decreasing temperatures, which is consistent with findings from analogous porphyry-style deposits elsewhere.

Keywords: Magnetite; Magmatic; Hydrothermal; Trace elements; LA-ICP-MS; Porphyry; Exploration; Greece

---

6.1 Introduction

Magnetite (Fe_3O_4), a mineral of the spinel group, is a common constituent in a wide variety of rock types and ore deposits. It forms under very different physicochemical conditions which may extend from crystallization of silicate and sulfide melts at high magmatic temperatures, up to precipitation from hydrothermal fluids in low temperature environments (Dare et al., 2014). Its chemistry is a function of various factors like sulfur and oxygen fugacity (fS_2, fO_2), temperature, cooling rate, silica activity and melt/fluid composition (e.g., Sack and Ghiorso, 1991; Roeder, 1994; Barns and Roeder, 2001; Nadoll et al., 2012; Dare et al., 2014). The sensitivity of magnetite to these parameters, results in variable concentrations of minor and trace elements including, Al, Ti, Mg, Mn, Zn, Cr, V, Ni, Co and Ga (Chen et al., 2019).

Analytical methods such as laser ablation-inductively coupled plasma-mass spectrometry (LA–ICP–MS), allow to analyze a wide range of trace elements in magnetite at very low detection limits (e.g., Dupuis and Beaudoin, 2011; Liu et al., 2008; Wijbrans et al., 2015). As magnetite is commonly found in many rocks and ore deposits, its trace elements content is of particular interest to geoscientists. Many studies revealed that certain enrichments and/or depletions in minor and trace elements reflect different mineralization styles and host rocks (Dupuis and Beaudoin, 2011; Nadoll et al., 2012; Müller et al., 2003; Carew et al., 2004; Dare et al., 2012; Nadoll et al., 2014, 2015; Canil et al., 2016; Huang et al., 2019). This fact favors the use of magnetite chemistry both as a promising petrogenetic indicator and as an exploration tool.

Statistical interpretation of the trace element geochemistry of magnetite from different styles of mineralization, coupled with petrographic interpretations and elemental ratios, allowed the establishment of discriminant diagrams: Dupuis and Beaudoin (2011), were among the first who correlated the composition of magnetite to its origin and formation conditions (e.g., magmatic vs. hydrothermal) and to different major deposit types (e.g. iron oxide copper-gold vs. porphyry deposits). They used the plots of Ca + Al + Mn versus Ti + V and of Ti + V versus Ni / (Cr + Mn), to distinguish the average composition of magnetite from iron oxide copper-gold (IOCG), Kiruna type iron oxide-apatite (IOA), skarn, banded iron formation (BIF), porphyry-Cu,

Fe-Ti-V and Ni-Cu-PGE deposits. These diagrams proved to be potentially useful in identifying magnetite of unknown origin, however it must be noted that magnetite can display a broad compositional variation, within a single deposit. In this context, Dare et al. (2012) used the Ti, Ni and Cr concentration of magnetite as a means to distinguish between hydrothermal and magmatic magnetite. By studying the composition of magnetite in porphyry-Cu and skarn deposits in the SW United States, Nadoll et al. (2014, 2015) suggested that the compositional boundary between the two types of deposits is highly transitional. More recently, Canil et al. (2016), used principal component analysis to suggest that the composition of magnetite from porphyry Cu-Au-Mo deposits in British Columbia is a function of temperature, oxygen fugacity and nature/composition of the hydrothermal fluids. Based on detailed textural characterization and high-resolution in situ compositional analyses, Wen et al. (2017), proposed that a V / Ti versus Fe diagram should be used to discriminate between pristine igneous magnetite, re-equilibrated magnetite, and hydrothermal magnetite. Finally, Pisiak et al. (2017), via the use of linear discriminant analysis, calculated discriminant factors based on the composition of magnetite in barren and ore-related igneous rocks as well as hydrothermal magnetite, suggesting that the method was a useful tool when exploring for ore-related, magnetite-bearing intrusions.

Porphyry-type deposits, are not generally exposed at the surface and so, one aspect of exploring for such deposits has used potential indicator minerals such as apatite, epidote, garnet, tourmaline as a guide (e.g., Averill, 2001; Kelley et al., 2011; Celis et al., 2013; Hashmi et al., 2015). However, the chemical composition of igneous and hydrothermal magnetite and its association with the porphyry deposit subtypes and the magmatic affinity of the host intrusive rocks remains poorly constrained. Recently Huang et al. (2019), have tried to establish the potential relationships among the composition of magnetite, the geochemical signature of the host rock, and the porphyry deposit sub-types.

Magnetite, despite being common in numerous geological environments in Greece, has been poorly studied to date. In this chapter, a first attempt is made, to evaluate the composition of magmatic and hydrothermal magnetite from a porphyry-style mineralization in Greece, namely the Pagoni Rachi Cu-Mo-Re-Au prospect. The

trace element composition of magnetite was used to monitor the physicochemical conditions of ore formation and to identify possible relations between the magnetite chemistry and the geochemical affinities of the host rock. Finally, the identification of possible chemical fingerprints in the hydrothermal magnetite, that could point towards ore-grade mineralized zones is investigtaed, in an attempt to establish a new exploration tool for porphyry-style deposits and prospects in Greece, and elsewhere.

6.2 Materials and methods

Ten polished thin sections of magnetite-bearing samples and host rocks were studied by optical and a JEOL JSM 5600 scanning electron microscope (SEM) equipped with back-scattered imaging capabilities, at the Department of Mineralogy and Petrology of the University of Athens, Greece. Major and minor elements quantitative analyses on magnetite from three representative samples were carried out at the "Eugen F. Stumpfl" Laboratory, University of Leoben, Austria, using a Jeol Superprobe JXA 8200 wavelength-dispersive electron microprobe (WDS). Analytical conditions were as follows: 20 kV accelerating voltage, 10 nA beam current, 1 μm beam diameter. Peak and backgrounds counting times were 20 and 10 s for major and 40 and 20 s for minor and trace elements, respectively. The MgKα, AlKα, SiKα, CaLα, TiKα, VKα, CrKα, FeKα, MnLα, NiLα, and ZnKα X-ray lines were used, with respect to the following standards: corundum for Al, wollastonite for Si and Ca, rutile for Ti, synthetic V for V, chromite for Mg and Cr, natural pyrite for Fe, rhodonite for Mn, NiS for Ni and natural sphalerite for Zn. Corrections were applied using the PAP online program (Pouchou and Pichoir, 1991).

Laser ablation ICP-MS analyses of the same samples were conducted at the Institute of Mineralogy, University of Münster, Germany, with a pulsed 193 nm ArF excimer laser (Analyte G2, Photon Machines). A repetition rate of 10 Hz and an energy of ~4 J/cm^2 were used throughout the entire session. The beam spot diameter was set to 35 μm. Trace element analysis has been carried out with an Element 2 mass spectrometer (ThermoFisher). Forward power was 1250 W and reflected power <1 W, gas flow rates were 1.2 L/min for He carrier gas, 0.9 L/m and 1.2 L/m for the Ar-auxiliary and sample gas, respectively. The argon cooling gas flow rate was set to 16

L/min. Before starting an analysis, the system was calibrated to a NIST 612 reference glass measuring ^{139}La, ^{232}Th and $^{232}Th^{16}O$ to get stable signals and high sensitivity, as well as low oxide rates ($^{232}Th^{16}O/^{232}Th < 0.1\%$) during ablation. A total of 26 elements (^{25}Mg, ^{27}Al, ^{29}Si, ^{43}Ca, ^{45}Sc, ^{49}Ti, ^{51}V, ^{53}Cr, ^{55}Mn, ^{59}Co, ^{60}Ni, ^{63}Cu, ^{66}Zn, ^{69}Ga, ^{85}Rb, ^{88}Sr, ^{89}Y, ^{90}Zr, ^{93}Nb, ^{95}Mo, ^{118}Sn, ^{137}Ba, ^{178}Hf, ^{181}Ta, ^{182}W and ^{208}Pb) were quantitatively analyzed using the NIST 612 glass as an external standard while stoichiometric Fe (97% wt.% FeO) was the internal standard, since total concentration of minor elements is <3 wt.% (cf. Milani et al., 2017). Run time of the single ablation pattern was 60 s (20 s for background, 40 s for peak after switching the laser on). Concentrations of measured elements were calculated using the Glitter software (van Achterbergh et al., 2001; Griffin et al., 2008). Standard reference glasses BHVO-2G and BIR1-G were analyzed in order to monitor for precision and accuracy during the course of this study. The results from these glasses match the published range of concentrations (standard deviation in the range of 5%), given in the GeoReM database (version 23, Jochum et al., 2011).

6.3 Alteration and mineralization

The Pagoni Rachi Cu-Mo-Re-Au porphyry was identified by Arikas (1991), and occurs in an Oligocene granodiorite porphyritic body, which intrudes a Tertiary volcanosedimentary sequence (Figure 6.1). This sequence consists of conglomerates, marls, sandstones and volcaniclastic material (e.g., tuffs) of Priambonian age. It is in turn overlain by volcanic (lava domes, flows) and/or pyroclastic rocks. The northern part of the study area is occupied by a large quartz monzodiorite intrusion which crosscuts both the volcano-sedimentary sequence and the granodiorite porphyry. The monzodiorite exhibits a medium-grained to porphyritic texture, consisting of plagioclase and various amounts of pyroxene, amphibole, biotite, quartz, and opaques. Radiometric dating for the monzodiorite yielded ages of 31.9±0.5 Ma (Rb/Sr on biotite, Del Moro et al., 1998) and 32.05±0.07 Ma (U-Pb on zircon, Perkins et al., 2018).

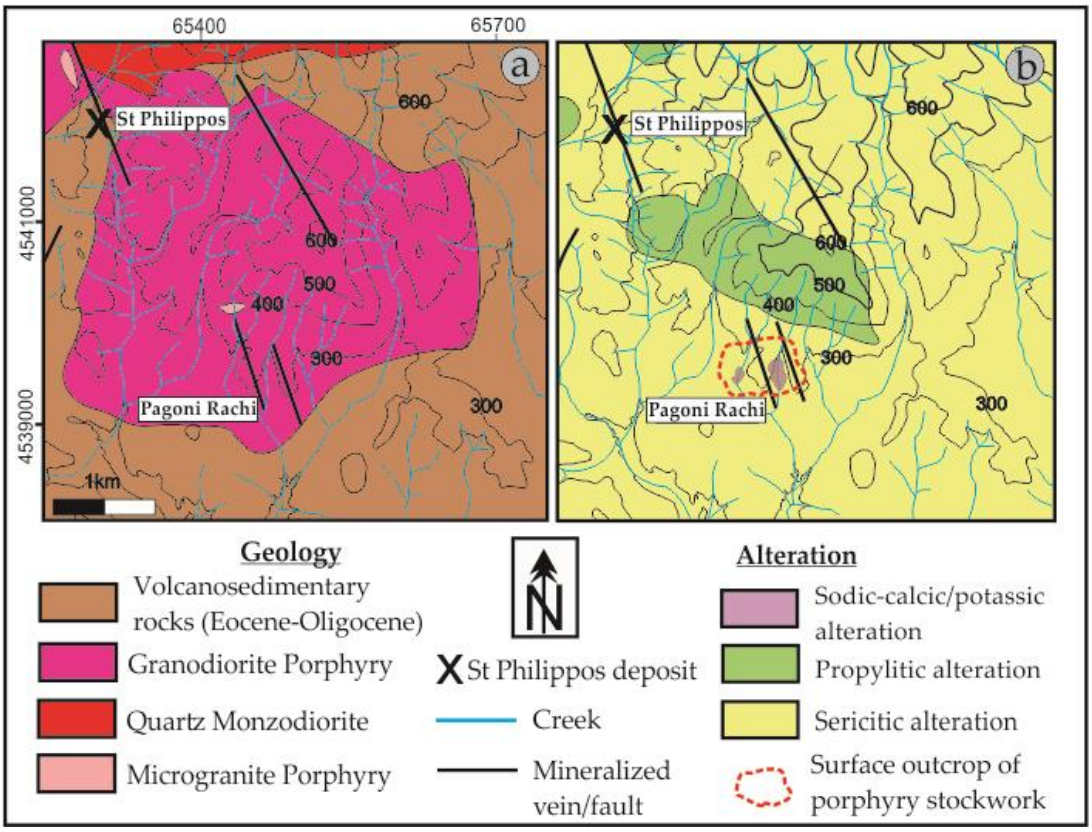

Figure 6.1: Geological (a) and alteration (b) map of the Pagoni Rachi prospect.

Late, NNW-, and E-trending microgranite porphyry dikes (Figure 6.1) crosscut the aforementioned magmatic rocks and comprise the final intrusive stage in the area (Voudouris et al., 2013b; this study). These dikes display a porphyritic texture and are composed of coarse-grained resorbed quartz and feldspar phenocrysts; the latter were commonly replaced by sericite, due to pervasive sericitic alteration.

The granodiorite porphyry that hosts the porphyry-style Cu-Mo-Re-Au mineralization is composed of plagioclase, amphibole, biotite, titanite and scarce resorbed quartz phenocrysts (quartz-eyes), set in a microlitic matrix of quartz, orthoclase, plagioclase and abundant opaque minerals, mainly magnetite. Mineralization occurs in a very dense quartz stockwork and is associated with extensive hydrothermal alteration of the granodiorite host (Figure 6.1b). Late-stage, N- and NW-trending epithermal-style veins crosscut the porphyry mineralization and are associated with argillic (quartz-sericite-carbonates), and, rarely, as advanced-argillic (quartz-kaolinite-sericite) alteration selvages, leading to partial telescoping of the porphyry system.

Figure 6.2: Field and hand-specimen photographs of magnetite-beatring rocks from the Pagoni Rachi prospect.

Porphyry-style mineralization (and alteration) has been attributed to four paragenetic stages (Voudouris et al., 2013b): (a) early sodic/potassic-calcic alteration associated with magnetite + bornite + chalcopyrite + molybdenite + native gold + quartz veins (M-type veins,) and contemporaneous, distal propylitic alteration; (b) sodic/potassic alteration with pyrite + chalcopyrite + molybdenite + quartz veins (B-type); (c) sericitic alteration with pyrite + chalcopyrite + molybdenite veins (D-type) that also contain native gold along with an important suite of Ag-, Bi-,Te-, and Se-bearing minerals; and (d) argillic alteration with base and precious metal epithermal-style veins (E-type) rich in Ag, Au and Te. Mineralogical similarities of these veins suggest that they may share a genetic relationship with the D-type veins. Bulk ore chemical analyses of surface samples showed that the system is significantly enriched in Cu (up to 0.5 wt.%), Mo (up to 2000 ppm), Au (up to 5 ppm) and Re (up to 20 ppm). The extreme rhenium enrichment of the Pagoni Rachi system, reflects the presence of the rare sulfide rheniite and Re-rich molybdenite (Voudouris et al., 2009, 2013b).

6.4 Modes of magnetite occurrence (petrography)

Following the textural and morphological criteria proposed by McQueen and Cross, (1999) and Nadoll et al. (2015), magnetite in the Pagoni Rachi porhyry-style mineralization occurs in two distinct types.

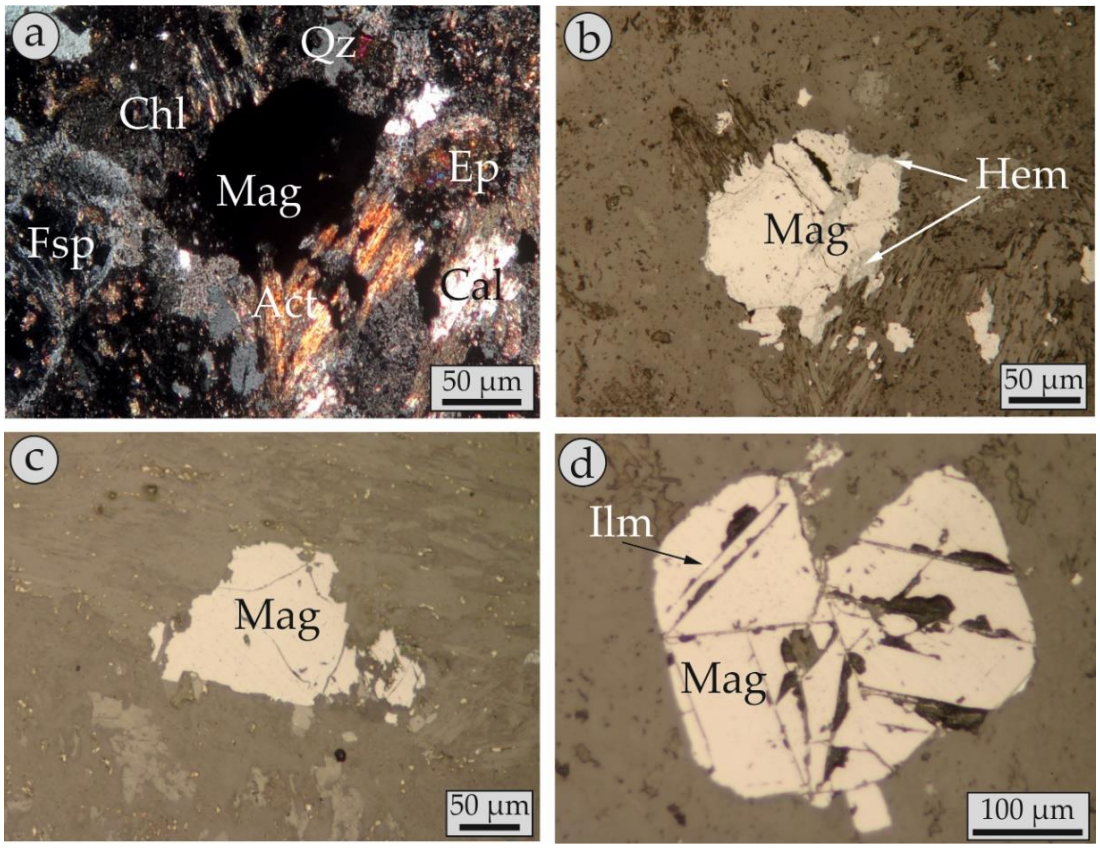

Figure 6.3: Transmitted (a) and reflected (b-d) light microphotographs of magmatic magnetite from fresh to propylitic-altered granodiorite porphyry (SAMPLE KMPR81): (a) magnetite (Mag) grain, set in a propylitic matrix consisting of plagioclase replacing feldspar (Fsp), actinolite (act), epidote (ep), quartz (Qz), calcite (Cal) and chlorite (chl), (crossed-polarized light); (b) the same grain as in (a). Note the partial replacement of magnetite by hematite (Hem); (c) subhedral magnetite grain; (d) euhedral magnetite grain showing minor exsolution lamellae of ilmenite (Ilm).

6.4.1 Magmatic magnetite

The first type, hereafter called as magmatic magnetite, occurs in fresh to propyliticaly-altered granodiorite porphyry (Figure 6.2a to c). Primary magnetite (Figure 6.3a to d) usually forms relatively large (up to a 0.2cm), euhedral to subhedral crystals (octahedral, cubo-octahedral habits), that are randomly scattered in the matrix of the rock, and which exhibit a characteristic porphyrytic texture (Figure 6.3).

It comprises the most abundant opaque accessory phase (approx. 5% modal) and is associated with the primary silicate minerals of the granodiorite. Commonly propylitic alteration is present; in this case magnetite is set in a matrix of relict primary minerals replaced by variable amounts of secondary epidote, albite, acinolite, chlorite and calcite (Figure 6.3a, b).

In such cases, magnetite is commonly replaced by hematite (martitization, Fig. 6.3b) in the periphery of the crystals or along fractures. Rare exsolution lamellae (trellis-type) of ilmenite, typical for magmatic magnetite (cf. Wen et al., 2017) were identified (Fig. 6.3d), at places also replaced by hematite.

6.4.2 Hydrothermal magnetite

The second type of magnetite is secondary (hereafter called “hydrothermal”) and (Figures 6.2c to e, and 6.4) is only found in the central part of the studied porphyry mineralization and is associated with sodic-potassic/calcic alteration. Its modal abundance (more than 10%) is significantly higher compared to its magmatic counterpart in the fresh to propylitic-altered granodiorite.

Hydrothermal magnetite forms a complex network of dark-colored veinlets set in a greenish to brown-colored matrix of secondary minerals. Moreover, magnetite may also be present in granular wavy to locally straight-sided quartz veins (A-type), that lack alteration selvages. Rarely, aggregates of magnetite occur in the sodic-potassic/calcic altered matrix.

This style of alteration (sodic-potassic/calcic) has totally obliterated the igneous porphyritic texture of the granodiorite and resulted in its complete recrystallization. It is composed of variable amounts of secondary albite, orthoclase, biotite, actinolite and chlorite. The veinlets (M-type) are commonly very narrow (less than 0.5cm), irregular in shape and discontinuous, but there are also cases where straight-sided veinlets were identified.

Magnetite in the veins is commonly anhedral, has a grain size that does not exceed a few tens of microns and may contain (sub-) microscopic inclusions of silicates (e.g., titanite) and/or sulfides (e.g., chalcopyrite). It is associated with variable amounts of orthoclase, biotite, albite, chlorite, actinolite and quartz (Figure 6.4a to b).

Minor chalcopyrite and pyrite accompany magnetite in the veins (Figure 6.4c to e) along with minor amounts of bornite, gold, and molybdenite. In places, replacement features occur (martitization) whereas exsolution lamellae are absent.

6.5 Chemical composition of magnetite

Analytical data from both magmatic and hydrothermal magnetite are shown in Tables 6.1 and 6.2 for the EPM and LA-ICP-MS analyses, respectively. Chemical differences between the two types of magnetite are displayed in covariation plots of Figure 6.5.

Electron probe micro-analyses of magmatic magnetite show that Ti is the major impurity, reaching up to 2.77 wt.% TiO_2 (average 1.41wt.%). Despite this relatively broad range, no zoned structure was observed. Silica (up to 0.52 wt.% SiO_2) and Ca (up to 0.34 wt.% CaO) are the next most abundant elements. The majority of other divalent (e.g., Mg, Mn) and trivalent (e.g., Al, Cr) cations that can be incorporated into the structure of magnetite, are mostly very close to, or below detection limits, with the exception of V, with values of up to 0.28 wt.% V_2O_3.

On the other hand, hydrothermal magnetite contains significantly less TiO2 (up to 0.78 wt.% and 1.13 wt.% in the two samples respectively) compared to the magmatic one, but has relatively elevated contents of Mg, Mn and V (values up to 0.88 wt.% MgO, 0.32 wt.% MnO, and 0.33 wt.% V_2O_3, respectively). Most of the other trace elements are close to or below the detection limit of the method (Table 6.1). Zonation features were not observed.

Laser ablation-inductively coupled plasma mass-spectrometry analyses yielded comparable results to those obtained through EPMA: Ti values in the two hydrothermal magnetite-bearing samples that reach up to 4852 ppm and 11517 ppm Ti (average values 3202 ppm and 2419 ppm respectively), and are much smaller compared to those in magmatic magnetite which contain up to 22545 ppm (average 9915 ppm).

Alumina, Si and Ca values are up to 7845 ppm (average 4112 ppm), 8521 ppm (average 991 ppm), and 4125 ppm (average 740 ppm) respectively. It must be noted that the maximum values in these elements correspond to the same analytical spots,

which may reflect the presence of sub-millimetric or nano-scale silicate inclusions at subsurface during ablation (cf. Deditius et al., 2018).

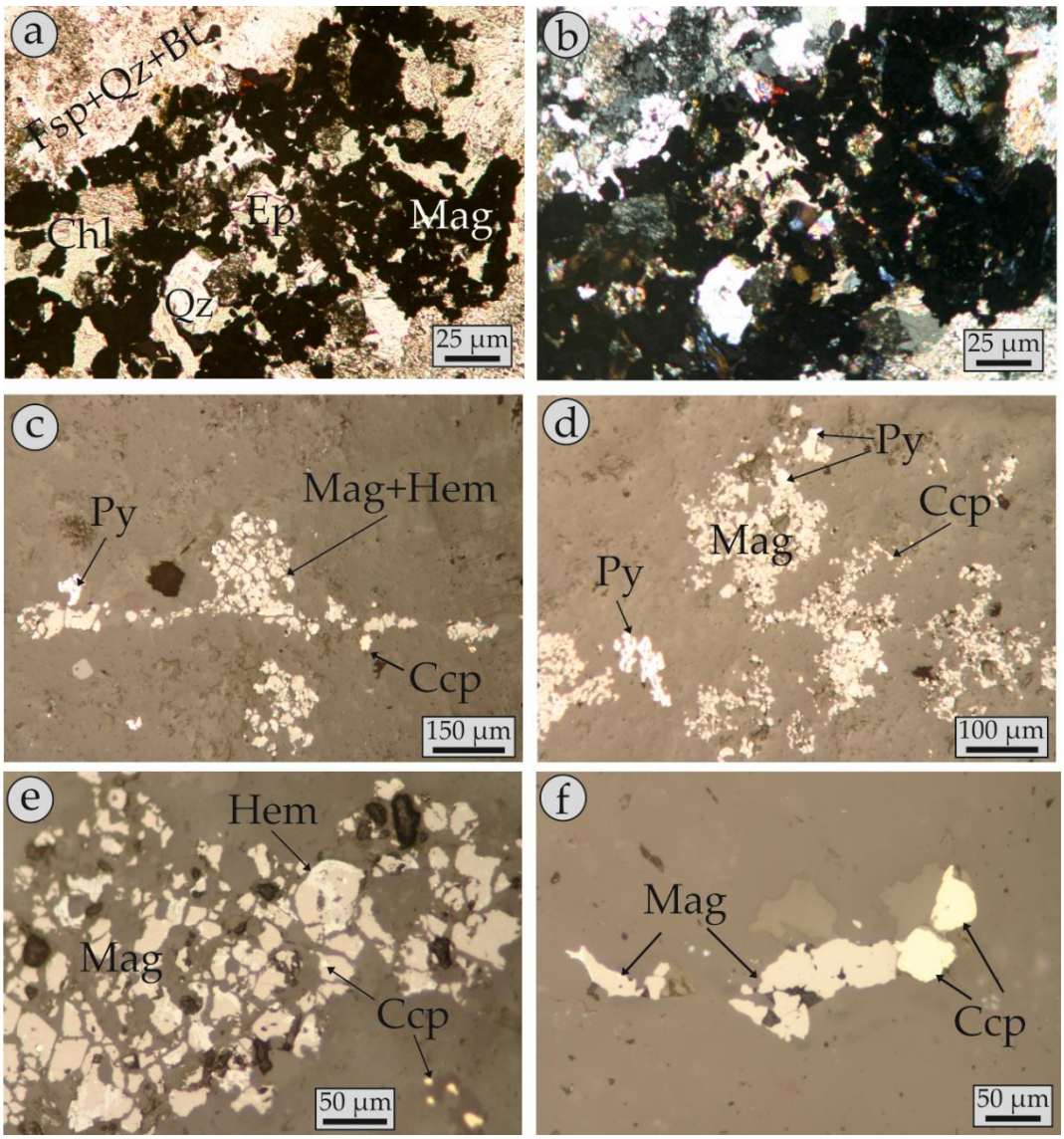

Figure 6.4: Transmitted (a,b) and reflected (c-f) light microphotographs of hydrothermal magnetite from M-type veinlets cross-cutting sodic-calcic/potassic altered granodiorite porphyry: (a, b) Subhedral to anhedral magnetite grains forming aggregates set in a matrix consisting of albite and orthoclase (Fsp), epidote (Ep), biotite (bt), chlorite (Chl) and quartz (Qz), (plane- and crossed-polarized light, respectively) sampleS KMPR68 and KMPR74. respectively; (c-e) Subhedral to anhedral magnetite associated with hematite (Hem), pyrite (Py) and chalcopyrite (Ccp). (c, d: sample KMPR68; e, f: Sample KMPR74)

The average Mg content of the two types of magnetite, is approximately the same (612 ppm for magmatic magnetite and 451 and 550 ppm for the two hydrothermal

magnetite samples. Maximum values are much higher (up to 2678 ppm in the magmatic sample and 6896 and 3613 ppm in the two hydrothermal samples.

Table 6.1. EPMA data of magmatic and hydrothermal magnetite from the Pagoni Rachi prospect.

Sample	**KMPR81**			**KMPR68**			**KMPR74**		
Type	Magmatic (n=15)			Hydrothermal (n=29)			Hydrothermal (n=30)		
(wt %)	aver	min	max	aver	min	max	aver	min	max
MgO	0.01	bdl	0.03	0.01	bdl	0.24	0.01	bdl	0.88
CaO	0.05	0.02	0.34	0.04	bdl	0.07	0.03	bdl	0.23
MnO	0.01	bdl	0.18	0.01	bdl	0.10	0.01	bdl	0.32
FeO_{tot}	97.10	95.44	98.69	97.94	96.88	98.40	98.11	97.03	99.19
TiO_2	1.41	1.05	2.77	0.39	0.20	0.78	0.47	0.11	1.13
Al_2O_3	0.04	bdl	0.58	0.16	0.22	0.46	0.05	bdl	0.17
SiO_2	0.06	bdl	0.52	0.07	bdl	0.30	0.05	bdl	0.18
Cr_2O	0.02	0.01	0.08	0.02	bdl	0.04	0.01	bdl	0.06
NiO	0.01	bdl	0.04	0.01	bdl	0.06	0.02	bdl	0.07
ZnO	0.01	bdl	0.05	0.04	0.03	0.18	0.01	bdl	0.03
V_2O	0.16	bdl	0.28	0.21	0.05	0.32	0.22	0.09	0.33
Total	97.70	98.04	99.13	98.87	97.01	99.41	98.85	94.71	99.28

n = number of analyses; aver = average value; min = minimum value; max = maximum value; bdl = below detection limit

Vanadium is enriched in the hydrothermal magnetite. Maximum values range between 1968 ppm (average 1622) and 3079 ppm (average 1077) in the two samples, whereas maximum values in the magmatic magnetite is 770 ppm (average 395 ppm).

A similar trend is the case for most trace elements (Table 6.2): hydrothermal magnetite is enriched in high-field strength elements (e.g., Nb, Hf, Ta, W) and metals (e.g., Cu, Zn, Mo).

On the other hand, some elements are preferably enriched in the magmatic magnetite: the Co of magmatic magnetite is slightly higher (up to 27 ppm) than that of the hydrothermal ones (up to 21 ppm). Other enriched elements are Cr (up to 454 ppm in magmatic; and up to 28 ppm in hydrothermal magnetite, respectively), Ni (up to 31 ppm in magmatic and up to 21 ppm in hydrothermal magnetite) and Sn (up to 99 ppm in magmatic and up to 41 ppm in hydrothermal magnetite).

Differences in the concentrations observed between EPM and LA-ICP-MS analyses for elements like Ti, Mg, Cr, Ca, and Si is attributed to the variation of the beam-size

of the two methods, especially when exsolved phases or micro-inclusions are present in the magnetite. Furthermore, elevated contents acquired by LA-ICP-MS analyses (e.g., values of Si, Ca, Ti, Al) may suggest that at least some of the very high concentrations is due to unavoidal submicroscopic or nano-scale inclusions of silicates.

Table 6.2. LA-ICP-MS data of magmatic and hydrothermal magnetite from the Pagoni Rachi prospect.

Sample	**KM81**			**KM68**			**KM74**		
Type	Magmatic (n=12)			Hydrothermal (n=15)			Hydrothermal (n=15)		
(ppm)	aver	min	max	aver	min	max	aver	min	max
Mg	1271	612	2678	2643	550	6896	2043	451	3613
Al	5679	4112	7845	5131	3354	5977	4676	2002	6808
Si	3120	991	8521	3376	1338	6247	4481	1982	6679
Ca	1755	740	4125	1386	980	2065	2749	910	4158
Sc	3	2	4	4	1	18	12	4	23
Ti	20179	9915	22545	3202	1200	4852	2419	1305	11517
V	561	395	770	1777	1622	1968	1784	1077	3079
Cr	329	221	454	20	16	25	23	14	28
Mn	316	224	412	1047	637	2199	954	412	2672
Co	22	19	27	12	3	21	7	4	14
Ni	23	19	31	16	12	21	16	14	19
Cu	5	2	8	56	bdl	156	21	bdl	152
Zn	51	33	79	189	1417	2163	2926	1860	4004
Ga	15	9	22	17	11	35	34	31	40
Rb	3	2	5	2	bdl	7	4	bld	19
Sr	6	4	8	11	2	30	18	bdl	72
Y	10	4	14	11	1	53	1	bdl	10
Zr	15	4	24	1	bdl	10	4	bdl	23
Nb	4	1	9	8	bdl	55	10	bdl	40
Mo	1	bdl	2	4	1	9	3	1	6
Sn	64	36	99	13	5	39	35	26	41
Ba	6	2	11	5	3	8	4	bdl	11
Hf	0.3	bdl	1.2	0.2	bdl	1	0.4	bdl	2
Ta	bd	bdl	1	1	bdl	7	1	bdl	3
W	2	1	4	6	bdl	44	3	bdl	9
Pb	21	12	36	49	10	128	6	bdl	20

n = number of analyses; aver = average value; min = minimum value; max = maximum value; bdl = below detection limit.

6.6 Discussion

Magnetite is a common mineral in porphyry deposits. Magnetite of magmatic origin is commonly disseminated in the unaltered intrusive rocks or partly as a relict in propylitic alteration that surrounds the mineralized center (Nadoll et al., 2015; Canil et al., 2016). The composition of magnetite seems to be a function of several factors including temperature, fS_2 and/or fO_2, cooling rate, melt composition and element partitioning between co-precipitating phases (e.g., Sack and Ghiorso, 1991; Frost and Lindsley, 1992; Dare et al., 2012, 2014; Nadoll et al., 2014; Hung et al., 2019). Available experimental data on igneous magnetite have shown that its composition depends mainly on the temperature of crystallization, the fS2 and fO2 conditions and buffering between melt and the host rock (Toplis and Corgne, 2002; Sievwright et al., 2017; Sossi et al., 2018). For instance, an increase in oxygen fugacity would reduce the solubility of Ti in magnetite and consequently cause oxy-exsolution of ilmenite (cf. Wen et al., 2017).

In contrast, hydrothermal magnetite is usually common in early, high-temperature stages associated with potassic alteration assemblages at the cores of the systems (Nadoll et al., 2014, 2015; Canil et al., 2016). Here, elemental availability in the hydrothermal fluid seems to be a critical component that determines its composition, combined with temperature, sulfur and oxygen fugacities and fluid-rock interaction (Nadoll et al., 2014). Although present in the majority of the porphyry-style deposits, there seems to be a greater abundance of magnetite in gold-rich deposits, a feature that could be attributed to the generation of such deposits by more oxidized magmas (Sillitoe, 1997; Sinclair, 2007). Iron in the porphyry environment is usually thought to be transported as a chloride complex in a magmatic vapor (FeCl2) and magnetite is considered to precipitate as a result of volatile exsolution at relatively high temperature and pressure conditions (Simon et al., 2004).

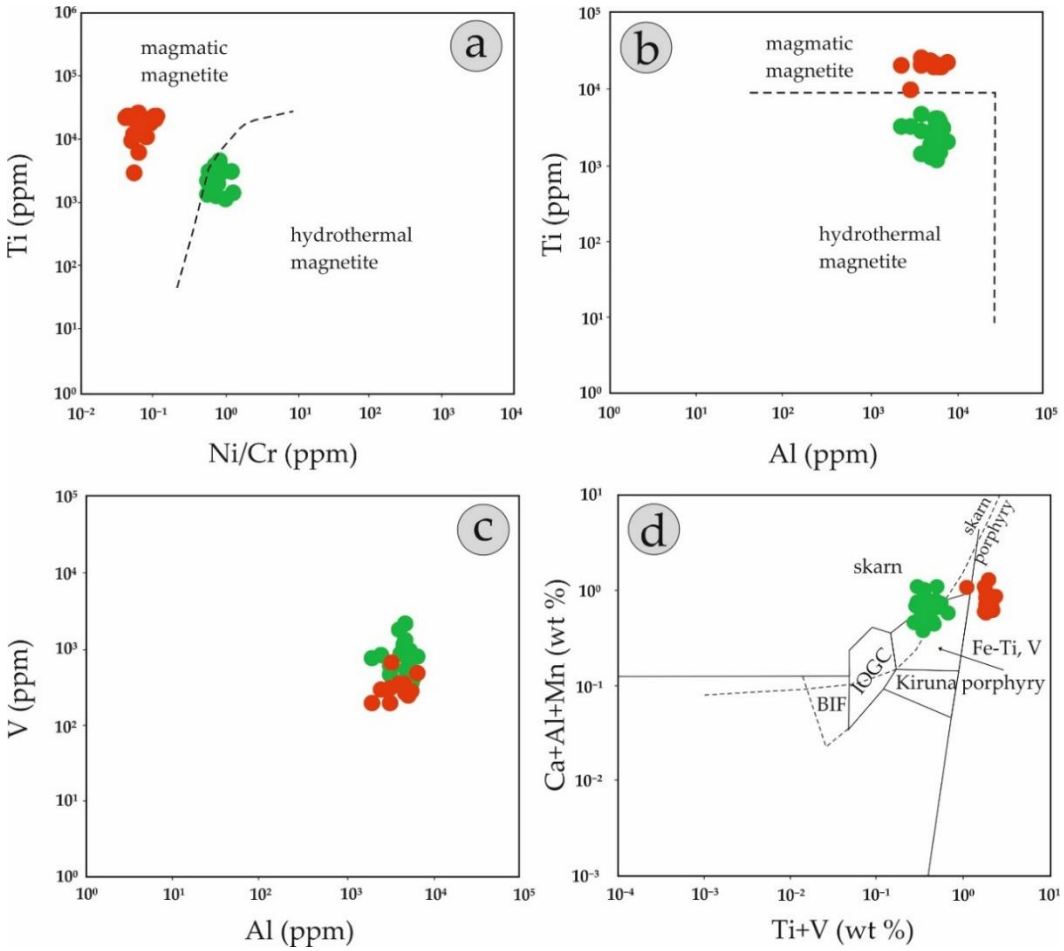

Figure 6.5: Covariation plots of magmatic (red symbols) and hydrothermal (green symbols) magnetite from the Pagoni Rachi porphyry prospect: (a) Ti versus Ni / Cr ratio (fields after Dare et al., 2014); (b) Ti versus Al (fields after Canil et al., 2016); (c) V versus Al; (d) Ca + Al + Mn versus Ti + V (fields after Dupuis and Beaudoin, 2011, and Nadoll and Koenig, 2011).

6.6.1 Fingerprinting magmatic and hydrothermal processes

The Ti versus Ni/Cr discrimination diagram of Dare et al., (2012), distinguishes the two types of magnetite in the Pagoni Rachi prospect (Figure 6.5a), as magmatic magnetite has high Ti and low Ni/Cr values compared to its hydrothermal counterpart. Furthermore, the Ti versus Al plot, proposed by Canil et al., (2016), also distinguishes the studied magnetite, but mostly based on Ti content, since their Al content is relatively constant (Figure 6.5b) in both magmatic and hydrothermal magnetite.

The significant enrichment of V in magnetite of the Pagoni Rachi prospect, is a feature previously described from other porphyry deposits elsewhere (e.g., Nadoll et

al., 2015; Canil et al., 2016). Vanadium in the Pagoni Rachi is present in both types of magnetite, but its concentration is higher in the hydrothermal grains (Figure 6.5c). Vanadium is characterized by significant mobility even in low temperature hydrothermal fluids (Oliver et al., 2004). Its presence, commonly is in the trivalent state, since it has a similar ionic radius to Fe3+ (Toplis and Corgne, 2002), is a function of oxygen fugacity of the hydrothermal fluid as well as of the presence of any other co-existing minerals with magnetite, that can also incorporate V3+ (e.g. ilmenite, biotite).

Since V is enriched in the hydrothermal type of magnetite from Pagoni Rachi, its availability in the hydrothermal fluid could be strengthened by dissolution of magmatic magnetite. This procedure could result in reprecipitation of newly-formed hydrothermal magnetite that has partly inherited features of its magmatic counterpart, as described by Wen et al., (2017).

The two types of magnetite in the Pagoni Rachi prospect are also partly discriminated in the plot of Ca + Al + Mn versus Ti + V plot (Figure 6.5d), although it should be noted here that composition of magnetite regardless of its origin in the prospect, overlaps the genetic fields defined by Dupuis and Beaudoin, (2011) and Nadoll and Koenig, (2011).

Figure 6.6 graphically represents the chemical composition of magmatic and hydrothermal magnetite analyzed during the present study. In Figure 6.6a, the average composition of the two varieties of magnetite from Pagoni Rachi, normalized to bulk composition of the continental crust, plot along with the compositional range of high-temperature hydrothermal magnetite of Dare et al., (2012). With the exception of Ti, Sn, and Cr, most elements are enriched in the hydrothermal magnetite. The concentrations of Si and Ca from both types of magnetite in the Pagoni Rachi prospect, are higher than those reported by Dare et al., (2014), for hydrothermal magnetite. In general, magmatic magnetite is depleted in both elements, since they are considered to be incompatible, when igneous magnetite crystallizes from silicate melts (Dare et al., 2012).

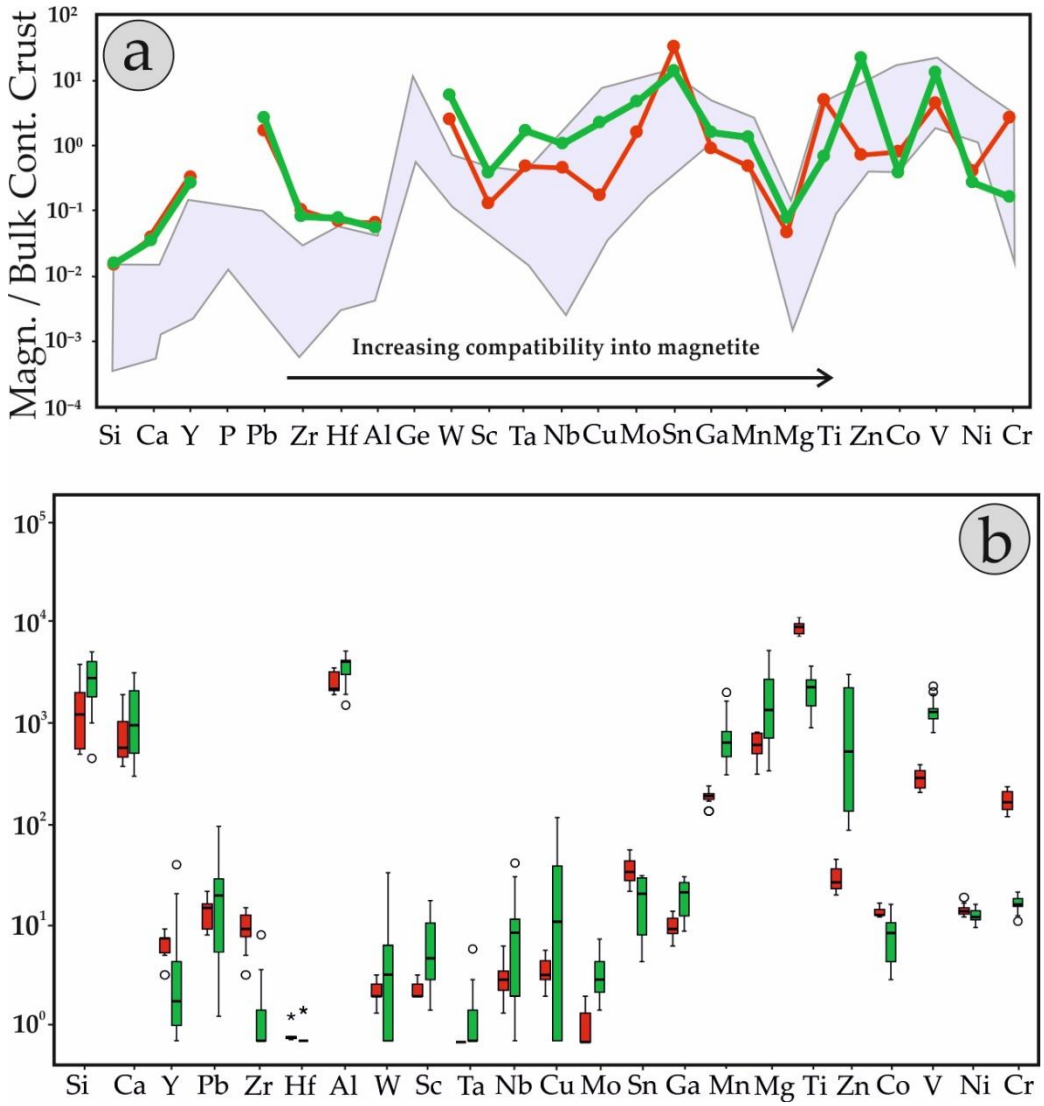

Figure 6.6: Chemical variation diagrams of magmatic (red symbols) and hydrothermal (green symbols) magnetite from the Pagoni Rachi porphyry/epithermal prospect (values in ppm): (a) Multi-element plot of average trace element composition of magmatic and hydrothermal magnetite, normalized to bulk continental crust (values after Rudnick and Gao, 2003) (grey field represents the compositional range of high-temperature hydrothermal magnetite, after Dare et al., 2012); (b) Box and whisker plot of various trace elements in magmatic (red boxes) and hydrothermal (green boxes) magnetite for the Pagoni Rachi porphyry prospect, analyzed by LA-ICP-MS. The upper and lower margins of the boxes represent the upper and lower 75% and lower 25% of the data, respectively. The whiskers represent upper and lower threshold values (95% of the data), while median values are shown as thick black lines inside the boxes. Open circles and stars represent extreme values. Maximum values of Si, Al, Mg and Ca attributed to inclusions have been excluded from this plot.

On the other hand, hydrothermal magnetite may carry significant amounts of Si and Ca, as both elements are highly mobile during hydrothermal alteration. Silicon-

and Ca-rich magnetite has been reported from several deposits, commonly skarns (e.g., Ciobanu and Cook, 2004). In the case of the Pagoni Rachi porphyry prospect, significant Si-Ca mobility during alteration has been well documented, as hydrothermal magnetite is accompanied by Ca-rich mineral assemblages (e.g. hydrothermal actinolite, Voudouris et al. 2009, 2013b). Moreover, very high values of these two elements, when they correlate along high Ti values (Figure 6.7) are likely due to the presence of nano-scale inclusions of titanite (cf. Deditius et al., 2018).

Magnesium and less commonly Mn can be enriched in hydrothermal magnetite, due to extensive fluid-rock interactions (Einaudi et al., 1981; Meinert et al., 20005). Such interactions enriched both elements in the studied magnetite and could easily be explained by the mafic component of the hosting granodioritic intrusion.

With the exception of Zr and Hf, which display relatively constant concentrations both in magmatic and hydrothermal magnetite, other high-field strength elements are preferably enriched in the hydrothermal magnetite (Figure 6.6b).

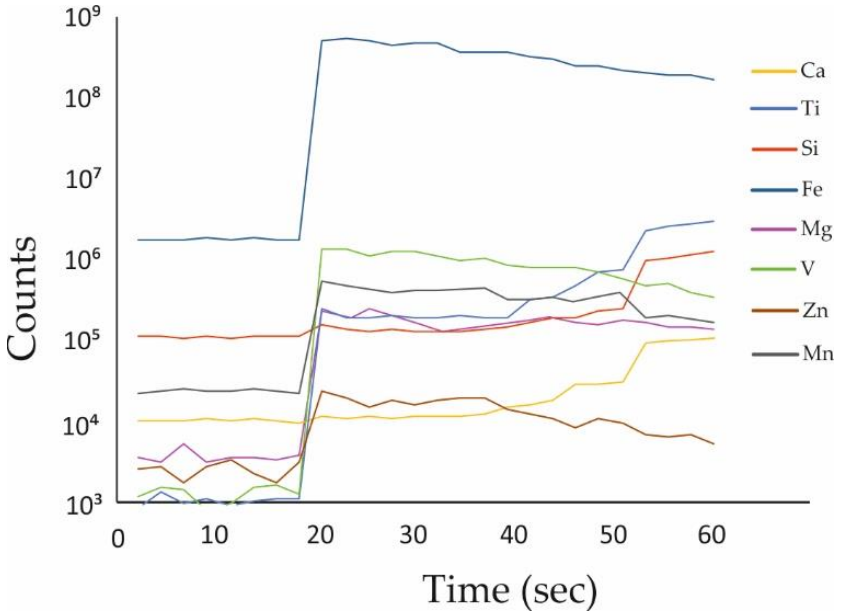

Figure 6.7: Time resolved analytical profile on a grain of hydrothermal magnetite. The increase of Si, Ca and Ti values implies the intersection of nano-scale titanite inclusion.

As most of these elements are incompatible in magnetite, they are relatively immobile and tend to be incorporated in late magmatic magnetite. Their solubility in hydrothermal fluids is restricted (Pearce and Cann, 1973; Floyd and Winchester, 1978; Middelburg et al., 1988). However, the enrichment of elements like W, Mo, Ta, and

Nb in the hydrothermal magnetite could indicate that it precipitated from a hydrothermal fluid that derived from a felsic intrusion and contained significant amount of such elements. Large variation in their concentration could imply that they were incorporated in the magnetite grains following an inhomogeneous distribution.

The copper content of magmatic magnetite is very low, but a significant enrichment is present in the hydrothermal variety. Copper-rich magnetite is common in many porphyry-style deposits, with extreme values of a few thousands of ppm (e.g., magnetite from Mt Polley porphyry deposit, (Pisiak et al., 2017), but its origin is still a matter of debate, as the presence of nano-scale inclusions of copper sulfides cannot be ruled out (e.g., Hough et al., 2008).

Lead enrichment is an important feature of magnetite from Pagoni Rachi. Minor amounts of Pb are present in the magmatic magnetite, and can be explained by its weakly compatible behavior (D_{Pb} = 1.4 in magmatic magnetite). The Pb content rises significantly in the hydrothermal type of magnetite: Given the fact that Pb is a chalcophile element, and is preferably incorporated in coexisting Fe-Cu sulfides (e.g., Dare et al., 2014), its presence in hydrothermal magnetite suggests enrichment of this element in the parental hydrothermal fluid, that is exsolved from a felsic magmatic source, as also described by Huang et al., (2019).

Another notable feature of the studied magnetite is their enrichment in Sn, which is obvious in both types of magnetite but is larger in the igneous magnetite. Analogous enrichment of Sn in porphyry-related magnetite was reported previously from the Endako porphyry-Mo deposit (Hough et al., 2008), which is hosted in granitoids which are notably more felsic compared to the granodiorite hosting the Pagoni Rachi prospect.

6.6.2 Genetic considerations – Implications for exploration

Although hosted in an intermediate magmatic body with high-K calc-alkaline affinity, the Pagoni Rachi porphyry prospect is characterized by a number of features that point towards a genetic relation to a more evolved, felsic intrusive phase. This inquiry has already been stated by Voudouris et al., (2013b), who discussed the

possibility of a genetic relationship between the porphyry system and a buried granitic intrusion similar to that exposed at the nearby St. Philippos deposit. Furthermore, the presence of fluorite as a gangue mineral in the quartz porphyry veins of the Pagoni Rachi (Voudouris et al., 2013b; this study), as well as the enrichment of F and Cl in secondary biotite (see also Chapter 4) from the sodic/potassic-calcic alteration of the system, also suggest a strong affinity with a halogen-enriched hydrothermal fluid derived from a felsic magma.

High-field strength elements, which are enriched in secondary magnetite, suggest elevated mobility during hydrothermal alteration. Such enrichment, has been described previously from fluoride-rich magmatic systems, especially of alkaline character (Whalen et al., 2001). Moreover, as has been shown by experimental studies, even the presence of a minor amount of base metals like Mn and Zn in hydrothermal magnetite, reflects an elevated concentration of these elements in chloride-rich hydrothermal fluids, which suggest an enrichment caused by fluid-rock interactions (Einaudi and Meinert, 1981; Ciobanu and Cook, 2004).

Significant porphyry-style mineralization hosted in microgranite, has already been described from the Thrace metallogenic district, thus documenting a genetic link between porphyry-style prospects and the microgranitic magmatism. Characteristic examples are the Maronia porphyry Cu-Mo-Re-Au (Melfos et al., 2002; 2020), and the Aisymi-Leptokarya porphyry Mo (Galanopoulos et al., 2018; Voudouris et al., 2019a) systems. The existence of microgranitic bodies in the Pagoni Rachi area, as well as the presence of F-rich phases in advanced argillic alteration assemblages in epithermal-style mineralization (see also Chapter 5), locally superimposed on the porphyry-style ores in the broad area (Voudouris, 2014; Mavrogonatos et al., 2018a,b), is also compatible with a deep, large-scale microgranitic intrusion, that could (at least partly) control the alteration styles and contribute to the metal endowment of the Pagoni Rachi porphyry prospect.

Further studies of trace elements in magnetite from other deposits and prospects in the district will increase our knowledge concerning their distribution during ore formation and will help to determine a trace element pattern that could be used as a vector towards ore-grade mineralized centers in the Thrace metallogenic district.

Chapter 7

Trace element distribution in different pyrite generations from the Konos Hill and Pagoni Rachi porphyry/epithermal prospects

Abstract: The Konos Hill and Pagoni Rachi porphyry-epithermal prospects in NE Greece are characterized by abundant pyrite that displays significant textural and geochemical variations between the various ore stages. It is commonly fine-grained and anhedral in the porphyry-related mineralization (M- and D-type veins), while it forms idiomorphic, medium- to coarse-grained crystals in the late, epithermal style veins (E-type). Porphyry-style pyrite from both prospects is characterized by an enrichment in Co, Se, Cu, and minor Zn, and a depletion in other trace elements, like Bi., Mo, Ag, etc. Pyrite in epithermal-style mineralization is mostly characterized by the presence of As, Bi, Pb, Ni and Se. Gold in pyrite from all mineralization stages, occur as a non-stoichiometric substituting element, and its abundance correlates with As content. Arsenic in pyrite from Konos Hill records an increase from the porphyry stage to the epithermal stage (along with gold), however, at Pagoni Rachi, the highest Au and As contents are recorded in D-type pyrite and in the epithermal stage.

The composition of the studied pyrite, marks changes in the physico-chemical conditions of the ore-forming fluids and generally follows the geochemical trends from other porphyry-epithermal systems elsewhere. However, a notable enrichment of Se in the porphyry-style pyrite here is a prominent feature compared to other deposits and can be considered as an exploration tool towards Au-enriched mineralized areas.

Keywords: Pyrite; Trace elements; LA-ICP-MS; Critical metals; Porphyry-epithermal; Exploration; Greece

---

7.1 Introduction

Pyrite is the most common sulfide mineral in the Earth's crust, and is generally common in most ore deposit types (e.g., Abraitis et al., 2004; Cook et al., 2009a;

Deditius et al., 2014; Keith et al., 2016a). Its ideal chemical composition, as expressed by the formula FeS_2, is not common in nature, as natural pyrites always contain small quantities of various elements beyond the essential Fe and S (Abraitis et al., 2004). Thus pyrite has attracted attention regarding its utilization as a potential vector towards fertile ore zones, as it may contain a significant budget of trace elements including Au, Ag, Cu, Pb, Zn, Co, Ni, As, Sb, Se, Te, Hg, Tl, Bi, and PGE, some of which, can reach concentrations of up to a few weight-percent (e.g., Cook and Chryssoulis, 1990; Cook et al., 2009a; Deditius et al., 2014; Reich et al., 2013; Keith et al., 2016a, b). In such cases, pyrite may represent an economically exploitable source for these metals (Reich et al., 2005; Kesler et al., 2007; Keith et al., 2018).

Trace elements may be present in pyrite, as nano-sized inclusions (or nanoparticles, e.g., Emsbo et al., 2003; Deditius et al., 2011) or as non-stoichiometric substitutions in its structure (Cook and Chryssoulis, 1990; Huston et al., 1995; Deditius et al., 2008). Arsenic is one of the most commonly incorporated elements into pyrite, reaching significant concentrations (almost up to 10 wt. %, e.g., Reich and Becker, 2006; Blanchard et al., 2007) and is commonly associated with gold-enrichment (Emsbo et al., 2003; Morey et al., 2008; Deditius et al., 2008, 2014).

The composition of pyrite has emerged as an indicator of ore-forming processes, including knowledge on the transport and depositional mechanisms of precious and critical elements in most hydrothermal systems (Reich et al., 2013; Deditius et al., 2014; Wohlgemuth-Ueberwasser et al., 2015; Francini et al., 2015; Sykora et al., 2018; Keith et al., 2016a, b, 2018). The chemistry of pyrite is highly dependent on the hydrothermal processes responsible for its deposition, which may fractionate trace elements between the vapor, liquid, and solid phases (e.g., Goldfarb et al., 2005; Seedorff et al., 2005; Simmons et al., 2005). This means that its composition is mainly a function of the physicochemical features of the precipitating fluid including pH, temperature, redox, and the availability of complex-forming ligands (Huston et al., 1995; Deditius et al., 2014; Revan et al., 2014; Keith et al., 2016a, b, 2018). Fluid-wall rock interaction, the composition of the host rocks, and phase separation also affects the chemical signature of pyrite (Foustoukos and Seyfried, 2007; Wohlgemuth-Ueberwasser et al., 2015; Keith et al., 2016a, b, 2018). However, elements enriched in

the host rocks are not necessarily leached by the associated hydrothermal fluids (e.g., Schmidt et al., 2007).

In deposits where pyrite is a major Au carrier (e.g., orogenic-Au and Carlin-style deposits), the trace elements content of pyrite has been well studied, owing to its economic significance. This has provided significant constraints on the mineral/fluid partitioning of such elements, and the saturation state of the parental hydrothermal solutions (e.g., Cook et al., 2009a, b; Ciobanu et al., 2009). However, this is not the case with porphyry deposits, where only a relatively small number of studies have been conducted (e.g., Deditius et al., 2009,2014; Maydagán et al., 2013; Reich et al., 2013; Gregory et al., 2013; Zwahlen et al., 2014; Francini et al., 2015; Alford et al., 2020). The trace element geochemistry of pyrite in the transition from the porphyry to epithermal environment remains poorly constrained (Francini et al., 2015; Sykora et al., 2018).

Pyrite, is a common mineralogical constituent in numerous ore deposits and prospects in Greece, however its trace element geochemistry remains poorly constrained. This chapter constitutes the first documentation of the trace element content in various generations of pyrite from porphyry/epithermal mineralization in Greece.

In this chapter, laser ablation-inductively coupled plasma-mass spectrometry (LA-ICP-MS) analyses are used to evaluate the composition of various pyrite stages in two neighboring porphyry-epithermal systems in NE Greece, namely the Konos Hill and Pagoni Rachi prospects. The trace element composition of pyrite was used to identify possible relations between the metal endowment of the hydrothermal fluids, from which pyrite precipitated, and to elucidate any changes in the physico-chemical conditions, as the ore forming system evolved. Finally, a comparison to analogous porphyry/epithermal deposits elsewhere is made, in an attempt to recognize any possible chemical fingerprints in the various generations of pyrite, that could point towards ore-grade mineralized events and/or zones. This comparison proves that the trace element content of pyrite carries potential as an important exploration tool for other similar deposits and prospects in Greece, similarly to other analogous mineralization elsewhere, in which pyrite chemistry has emerged as an important vector towards high-grade Au zones.

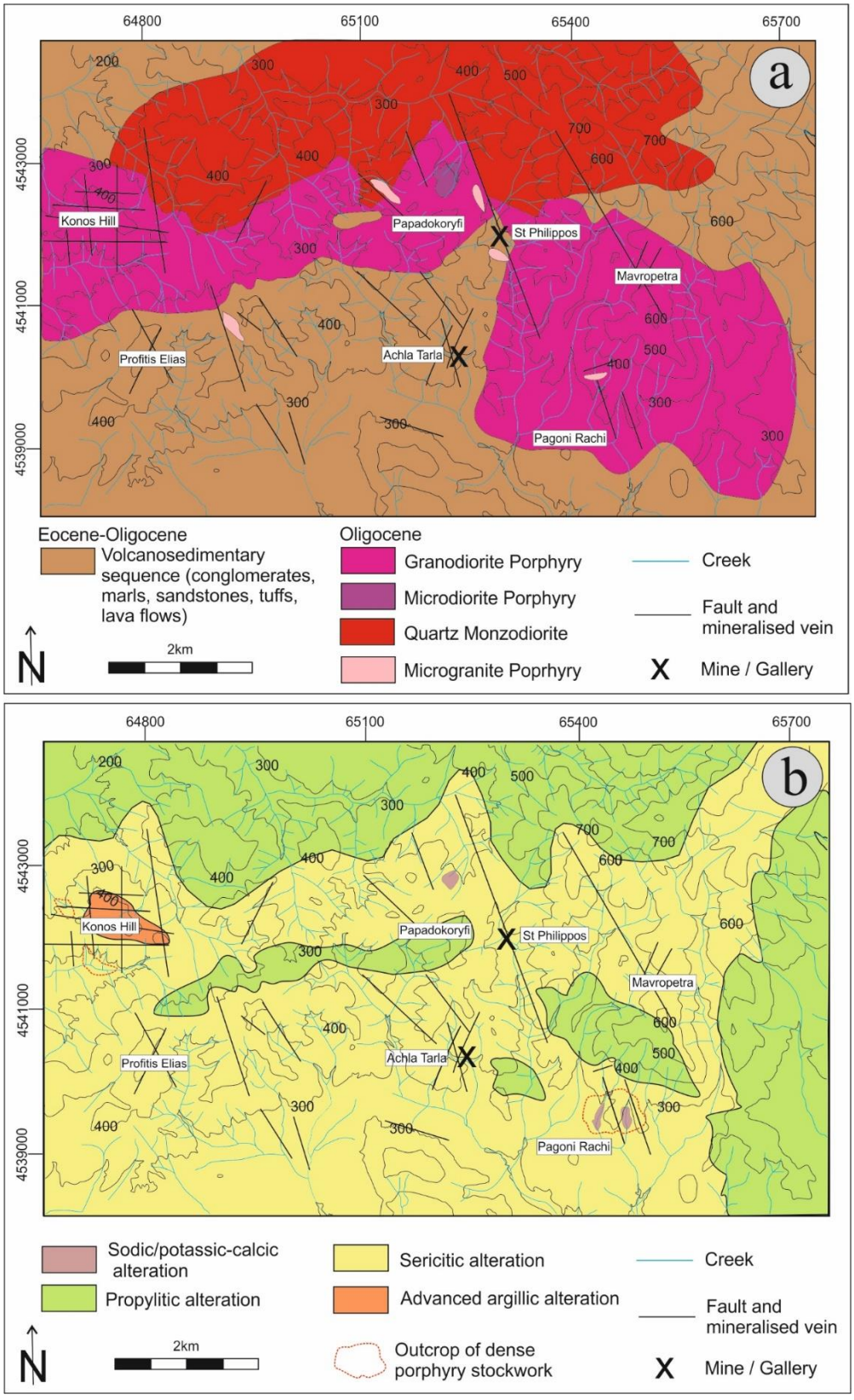

Figure 7.1: Geological (a) and alteration (b) map showing the location of the Konos Hill and Pagoni Rachi porphyry-epithermal prospects, among other mineralization occurring in the Sapes-Kirki area.

7.2 Materials and methods

Forty-five polished sections of sulfide mineralization were studied with an optical microscope and a JEOL JSM 5600 scanning electron microscope equipped with back-scattered imaging capabilities, at the Department of Mineralogy and Petrology, University of Athens, Greece. The chemical composition of sulfides from selected sections was carried out using a JEOL JXA 8200 Superprobe electron-microprobe at the "Eugen F. Stumpfl" Laboratory, Leoben University, Austria. The operating conditions were: accelerating voltage 20 kV, beam current 10 nA, beam size ≈ 1 μm. Counting times were 20 s on the peak and 10 s on the backgrounds for major elements. The counting times were increased to 60 s and 30 s for peak and backgrounds, respectively, when analyzing the trace elements. The following X-ray lines were used: AsLα, AuLα SeLα, CuKα, FeKα, PbMα, SKα, SbLα, NiKα, CoKα and ZnKa. Standards were: synthetic GaAs for As (detection limit 350 ppm), synthetic electrum for Au (detection limit 100 ppm), synthetic $AgBiSe_2$ for Se (detection limit 200 ppm), natural chalcopyrite for Cu (detection limit 150 ppm), natural pyrite for S and Fe (detection limit 150 ppm), natural galena for Pb (detection limit 700 ppm), natural stibnite for Sb (detection limit 350 ppm), natural skutterudite for Co (detection limit 150 ppm), natural millerite for Ni (detection limit 150 ppm), and natural sphalerite for Zn (detection limit 400 ppm).

Laser ablation-ICP-MS analyses of the same samples were conducted at the Institute of Mineralogy, University of Münster, Germany, with a pulsed 193 nm ArF excimer laser (Analyte G2, Photon Machines). Pre-defined areas of the polished sections were ablated using a 35 μm-sized spot diameter. A repetition rate of 10 Hz and an energy of ~4 J/cm^2 were used throughout the session. The laser system was coupled to an Element 2 mass spectrometer (ThermoFisher). Forward power was 1250 W and reflected power <1 W, gas flow rates were 1.2 L/m for He carrier gas, 0.9 L/m and 1.2 L/m for the Ar-auxiliary and sample gas, respectively. The argon cooling gas flow rate was set to 16 L/min. Before starting an analysis, the system was calibrated to a NIST 612 reference glass measuring ^{139}La, ^{232}Th and $^{232}Th^{16}O$ to get stable signals and high sensitivity, as well as low oxide rates ($^{232}Th^{16}O/^{232}Th < 0.1\%$) during ablation. A total of 20 elements (^{55}Mn, ^{59}Co, ^{60}Ni, ^{63}Cu, ^{66}Zn, ^{69}Ga, ^{73}Ge, ^{75}As, ^{77}Se, ^{95}Mo, ^{107}Ag,

^{111}Cd, ^{115}In, ^{118}Sn, ^{121}Sb, ^{182}W, ^{197}Au, ^{205}Tl, ^{208}Pb, and ^{209}Bi) were quantitatively analyzed using the NIST 612 glass as an external standard. Sulfur, previously determined by EPM analyses, was used as the internal standard. Run time of the single ablation pattern was 60 s (20 s for background, 40 s for peak after switching the laser on). Concentrations of measured elements were calculated using the Glitter software (van Achterbergh et al., 2001; Griffin et al., 2008). Standard reference glasses BHVO-2G and BIR1-G were analyzed in order to monitor for precision and accuracy. The results obtained from these glasses matched the published range of concentrations (standard deviation in the range of 5%), given in the GeoReM database (version 23, Jochum et al., 2005). Average detection limits for the analyzed elements are as follows (in ppm): Mn = 0.8, Co = 0.3, Ni = 4, Cu = 0.5, Zn = 4, Ga = 0.2, Ge = 1.3, As = 1.9, Se = 5.6, Mo = 0.15, Ag = 0.8, Cd = 0.8, In = 0.06, Sn = 0.3, Sb = 0.19, W = 0.04, Au = 0.04, Tl = 0.02, Pb = 0.06, Bi = 0.03.

7.3 Alteration and mineralization

At the central part of the West Thrace metallogenic province, lies the Sapes-Kirki area, which mainly comprises conglomerates, marls, sandstones and volcaniclastic material (e.g., tuffs) of Priabonian age (Figure 7.1). The sequence is intruded by four types of subvolcanic rocks with subalkaline to alkaline affinities that form stocks and dikes (Arikas and Voudouris, 1998). These rocks are, (from the oldest to the youngest, based on cross-cutting relations; Ortelli et al., 2010; Voudouris, 2014) hornblende-biotite granodiorite porphyry, pyroxene-biotite microdiorite porphyry, quartz monzodiorite, and microgranite porphyry. Available radiometric ages for the granodiorite porphyry are 32.6±0.5 Ma (^{40}Ar/^{39}Ar on biotite, Ortelli et al., 2010), and for the monzodiorite, 31.9±0.5 Ma (Rb/Sr on biotite, Del Moro et al., 1988) and 32.05±0.07 (U-Pb zircon, Perkins et al., 2018). The hornblende-biotite granodiorite porphyry occupies the major part of the study area, and forms an E-trending elongated stock that hosts both the Konos Hill and the Pagoni Rachi porphyry-epithermal prospects (Figure 7.1).

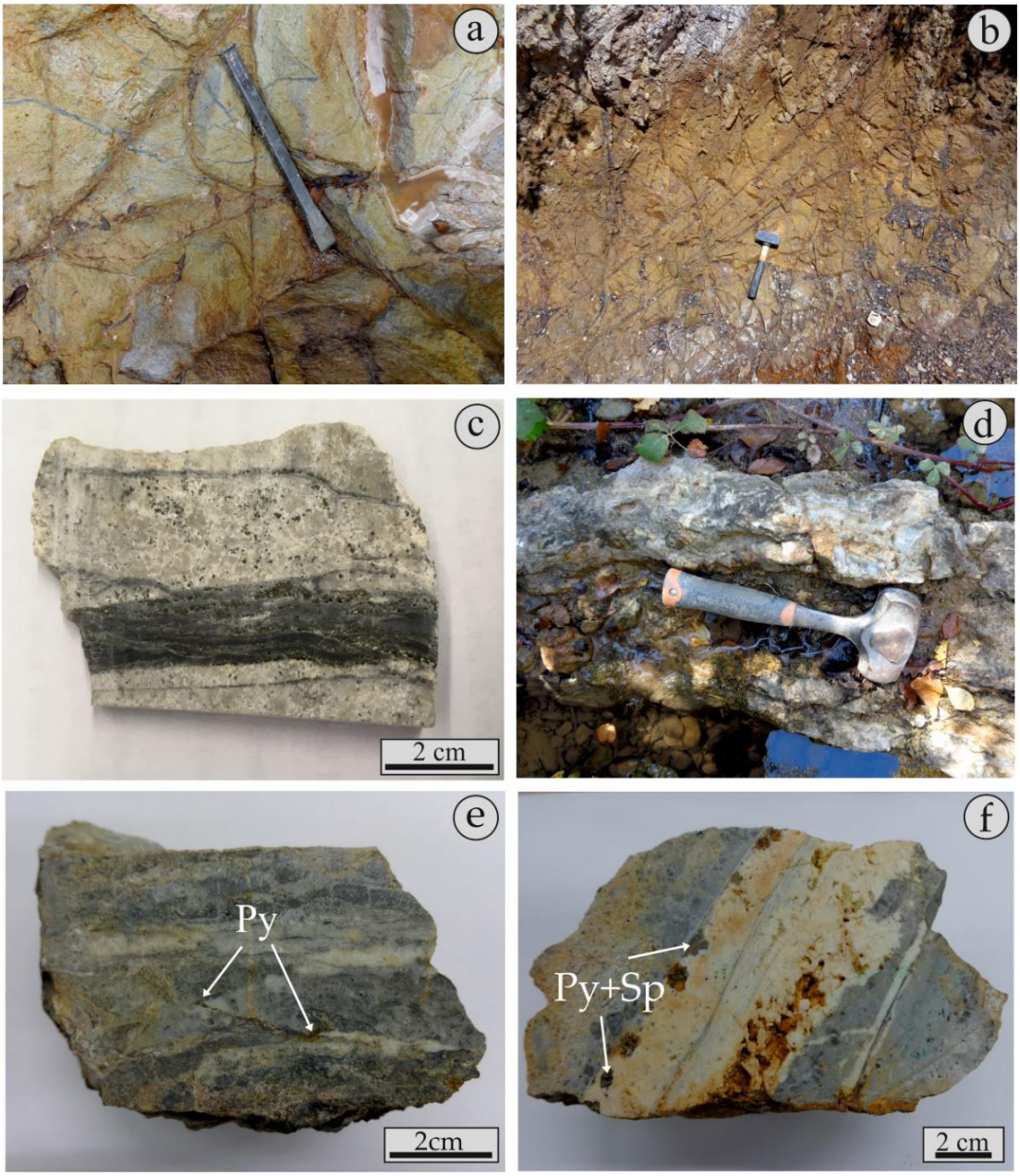

Figure 7.2: Field and hand-specimen photographs of pyrite-bearing ores from the Konos Hill porphyry-epithermal prospect: (a) Oxidized D-type veins crosscutting sericitic-altered granodiorite porphyry; (b, c) Surface outcrop of quartz stockwork veins crosscutting sericitic-altered granodiorite porphyry. Note in c that pyrite is mostly deposited along center lines of the quartz veins (sample KMSP64); (d) NNE-trending, epithermal-style, milky quartz-calcite vein (E-type) associated with quartz-sericite-calcite alteration of the host granodiorite porphyry; (e) Hand specimen with pyrite (Py) from the quartz-calcite vein shown in (d) (sample KMSP48); (f) Epithermal-style, quartz-calcite (E-type) vein with pyrite (Py) and sphalerite (Sp), (sample KMSP78).

The northernmost part of the area is dominated by quartz monzodiorite, while a small body of pyroxene-biotite microdiorite occurs north of the Papadokoryphi Hill.

Table 7.1: Typology and alteration characteristics of pyrite-bearing mineralization stages analysed in the present study, from the Konos Hill and Pagoni Rachi porphyry/epithermal prospects.

Prospect	Vein type	Vein assemblage	Alteration assemblage	Form, texture, zonation
Konos Hill	D-type	Qz + Py + Ccp ± Mol + Bn + Po + Hem + Ser	Ser + Qz ± Py ± Cal ("Sericitic")	Continuous quartz-pyrite veins / pyrite-chalcopyrite-molybdenite veins reopening and overprinting earlier quartz veins
	"Epithermal" (E-type)	Qz + Cal + Sp + Gn + Py + Ccp ± Tnt/Ttr ± Eng ± Ag-Au	Qz + Cal + Ser ± Kln ("Argillic")	Continuous straight-sided, up to 15 cm wide, quartz-carbonate veins with sharp parallel walls
Pagoni Rachi	M-type	Mag + Ccp + Hem + Py + Bn + Or/Ab + Bt + Act + Ep + Mol + Au	Qz + Or/Ab + Act + Ep + Bt + Chl + Cal + Mag ("Sodic/Potassic-Calcic")	Narrow (width less than 0.5 cm), irregular in shape and discontinuous and/or straight-sided veinlets
	D-type	Py + Ccp ± Mol + Po + Hem + Ser ± Qz ± Au + Cal ± Rhn ± Bn ± Gn	Qz + Ser + Py ± Cal ("Sericitic")	Continuous, up to 10cm wide, massive pyrite veins / pyrite-molybdenite-chalcopyrite veins, reopening and overprinting eralier quartz veins
	"Epithermal" (E-type)	Qz + Cal + Sp + Gn + Ccp + Py ± Tnt/Ttr ± Eng ± Ag-Au ± Tell ± Ser ± Kln	Qz + Cal + Ser ± Kln (Argillic")	Continuous straight-sided, up to 20 cm wide, quartz-carbonate veins with sharp parallel walls

Abbreviations: Act = actinolite, Ab = albite, Ag-Au = gold-silver alloy, Au = native gold, Bn = bornite, Bt = biotite, Cal = calcite, Chl = chlorite, Ccp = chalcopyrite, Ep = epidote, Gn = galena, Hem = hematite, Kln = kaolinite, Mag = magnetite, Mol = molybdenite, Or = orthoclase, Py = pyrite, Po = pyrrhotite, Rhn = Rheniite, Qz= quartz, Ser= sericite, Sp= sphalerite, Tell = tellurides, Tnt= tennantite, Ttr=tetrahedrite.

Small bodies of microgranite porphyry are scattered in the area, emplaced mainly along NNW-trending fault zones. The majority of the rocks underwent intense

hydrothermal alteration (Figure 7.1b) (e.g., Voudouris 2014; Voudouris et al., 2006, 2013a, b, 2016a, b; 2019; Mavrogonatos et al., 2018a, b, c, 2019).

The tectonic regime in the area comprises four major fault directions: N-S, E-W, ENE-WSW and NNW-SSE, with the last being associated with major ore-bearing structures, which, for example, hosts the St Philippos polymetallic deposit (e.g., Voudouris et al., 2013b).

The Konos Hill porphyry-epithermal prospect comprises quartz porphyry stockworks, hosted in the intensively-altered granodiorite porphyry, set in a NNW-trending direction (Figure 7.1), (Voudouris, 2014; Mavrogonatos et al., 2018b, c). The veins are sinuous to planar and banded, a feature that was recently found to characterize quartz veins from several porphyry Cu-Mo-Re-Au systems in northeastern Greece (Voudouris et al., 2019a, b).

The main metallic minerals are pyrite, molybdenite, rheniite, chalcopyrite along with minor amounts of bornite, enargite, colusite and tetrahedrite/tennantite (Ortelli et al., 2009; Voudouris et al., 2006, 2013a, 2016a, b, 2019a; Mavrogonatos et al. 2018b, c), and are associated with sodic/potassic alteration of the host granodiorite. Pyrite veins, usually form stockworks (now mostly oxidized), but also fill the center-lines of early quartz veins, thus overprinting the quartz stockwork. These pyrite veins are associated with widespread sericitic alteration, which dominates over the sodic/potassic alteration assemblages.

At the higher topographic levels of the system (on top of Konos Hill), advanced argillic alteration assemblages occur mostly along N- and E-trending faults, leading to partial telescoping of the porphyry system (see chapter 5). They comprise pyrophyllite, diaspore, zunyite, alunite, and aluminum-phosphates-sulfates (APS), associated with oxidized mineralization (Ortelli et al., 2009; Voudouris, 2014; Mavrogonatos et al., 2018b, c,). Peripheral to the system, quartz-calcite veins (E-type) with base metals and epithermal affinities occur.

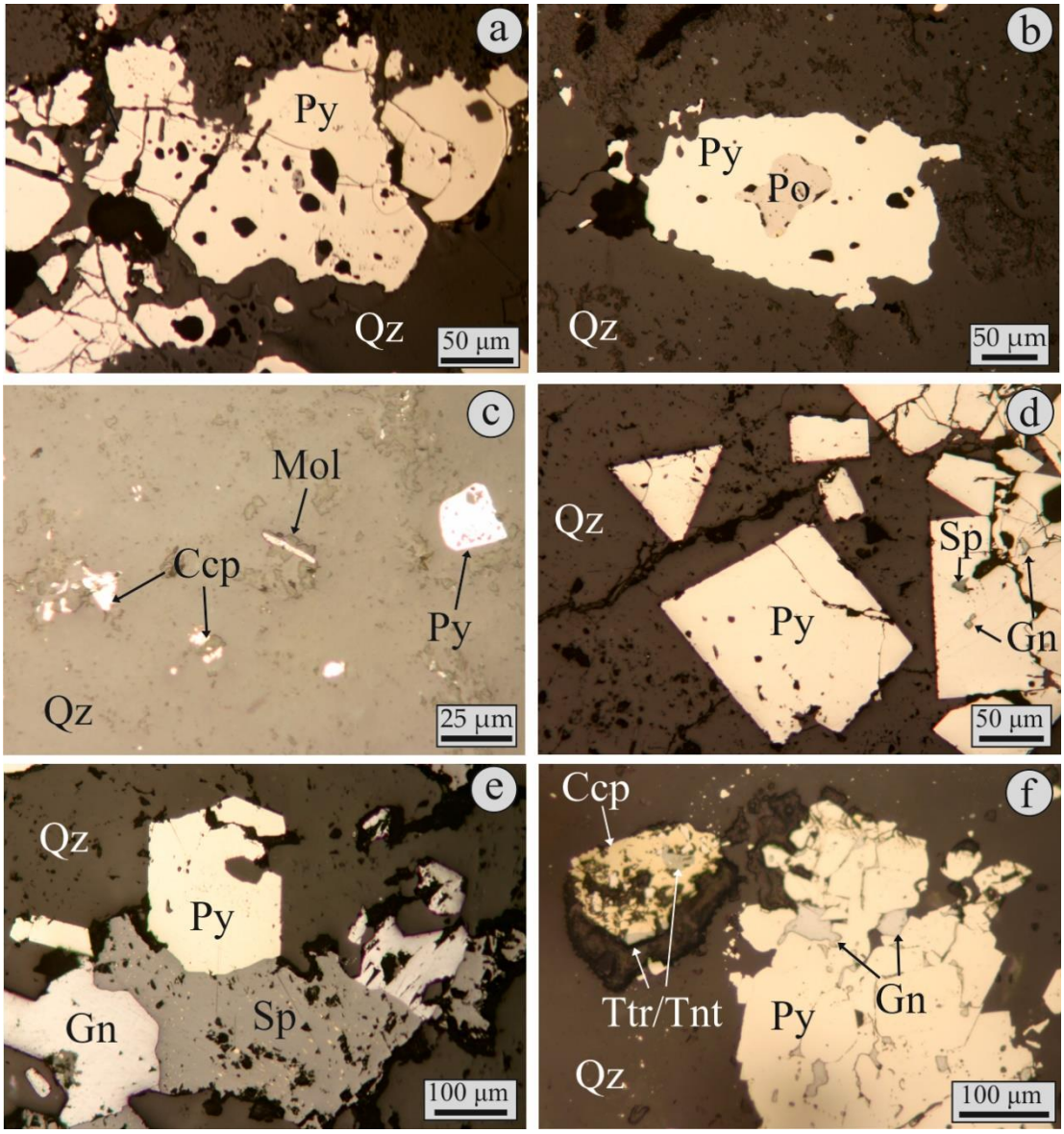

Figure 7.3. Reflected light photomicrographs of pyrite and associated opaque minerals from different stages mineralization in the Konos Hill porphyry-epithermal prospect. (a) Anhedral, "corroded" pyrite (py) grains in quartz (Qz), from a D-type vein (Sample KMSP64); (b) Anhedral, "corroded" pyrite grain including pyrrhotite (Po), D-type vein (Sample KMSP64; (c) Disseminated molybdenite (Mol) in association with chalcopyrite (Ccp) and pyrite (Py) in quartz (Qz), D-type vein, (Sample KMSP64); (d) Euhedral pyrite (py) in quartz (Qz) that includes blebs of sphalerite (Sp) and galena (Gn), epithermal-style vein, (sample KMSP48); (e) Euhedral pyrite (py) associated with galena (Gn) and sphalerite (Sp), the latter displaying "chalcopyrite disease", within quartz (Qz), E-type vein (KMSP48); (f) Euhedral pyrite rimmed by and including galena (Gn), in association with an intergrowth of chalcopyrite (Ccp) and tetrahedrite-tennantite group mineral (Ttr/Tnt), included in quartz (Qz), E-type vein (KMSP48).

They are associated with lateral sericitic (and minor argillic) alteration, dominated by quartz, sericite, calcite (± kaolinite) and comprise mostly pyrite, sphalerite, galena, and tetrahedrite/tennantite group minerals.

The Pagoni Rachi telescoped porphyry-epithermal prospect is hosted in a similar granodiorite porphyry stock like that at Konos Hill. The mineralization occurs as a very dense quartz stockwork, associated with extensive hydrothermal alteration (Voudouris et al., 2009; 2013b; Mavrogonatos et al., 2018a, 2019). The Pagoni Rachi system exhibits an unusual enrichment in Re, expressed by high concentrations of Re in molybdenite and by the presence of the rare sulfide rheniite (Voudouris et al., 2009; 2013a, b). The core of the system is dominated by sodic/potassic-calcic alteration associated with magnetite and quartz veins, as well as sodic/potassic alteration related to banded, quartz-molybdenite veins. Massive pyrite veins associated with sericite-carbonate alteration overprint earlier alteration and mineralization. Epithermal-style veins (E-type) commonly set in a N- and NW-trending direction, locally overprint the porphyry mineralization. They are related to argillic alteration assemblages and carry base metal sulfides (pyrite, sphalerite galena) as well as precious metals (Ag-Au alloy) and a suite of sulfosalts and tellurides (Voudouris et al., 2013b, 2019a). For a detailed description of alteration and mineralization see Chapter 4.

7.4 Occurrence and textural features of pyrite (petrography)

Vein terminology used thereafter, is based on Arancibia and Clark (1996) for M-type veins, Gustafson and Hunt (1975) and Seedorff et al. (2005) for A-, D-type veins, and Masterman et al. (2005), Voudouris et al. (2013b), Monecke et al. (2018) for E-type veins. The vein characteristics, as well as their mineralogical and textural features are summarized in Table 7.1.

Pyrite is a common constituent of the Konos Hill prospect, where M-type veins are absent. It is the dominant mineral in D-type veins, which form stockworks, and is associated with sericitic alteration of the host granodiorite porphyry (Figure 7.2a to c).

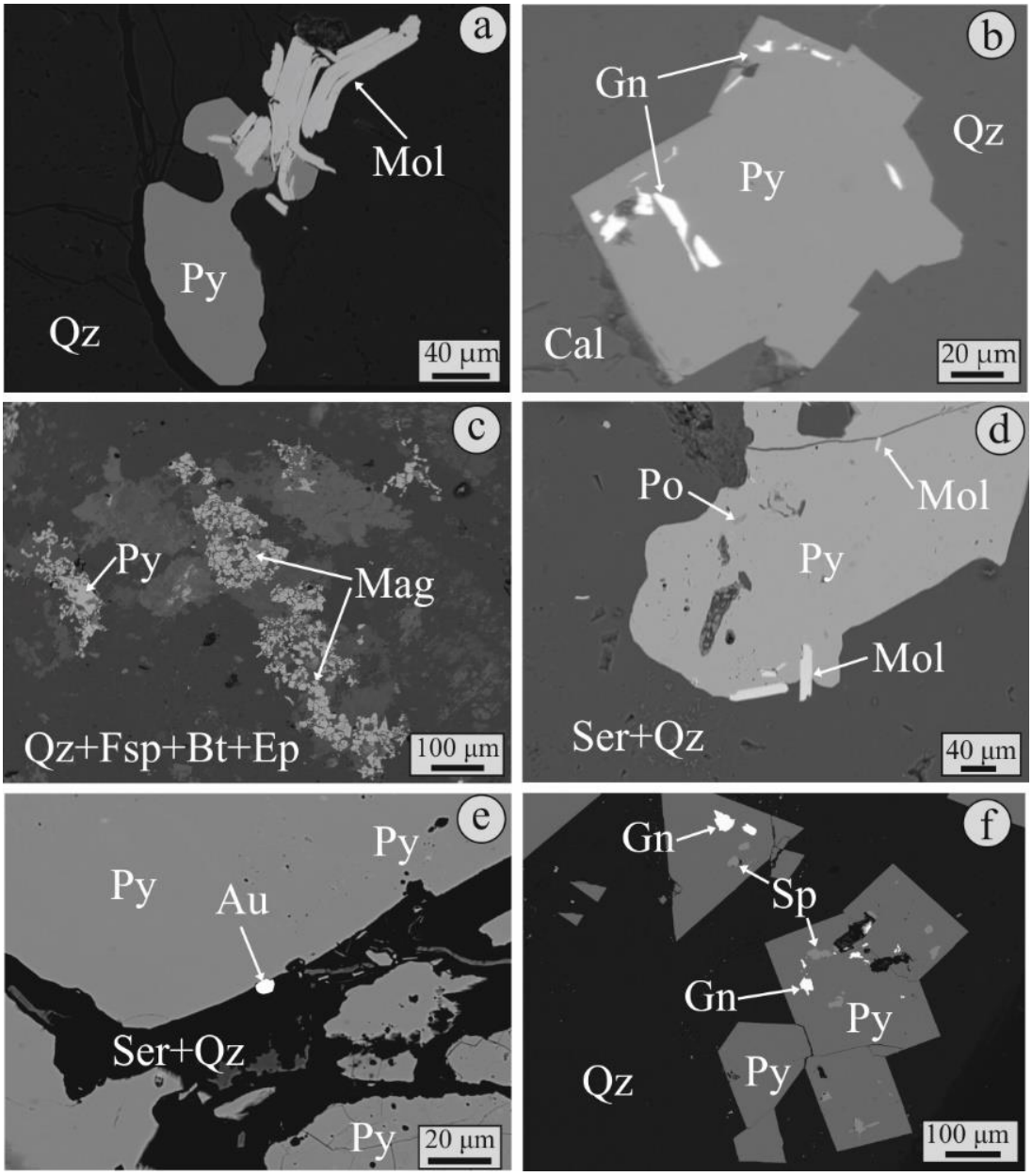

Figure 7.4: SEM back-scattered electron images of pyrite-bearing assemblages. (a) Intergrowth of pyrite (Py) and molybdenite (Mol) in quartz (Qz), D-type vein, Konos Hill prospect (sample KMSP64); (b) Euhedral pyrite (Py) that includes galena (Gn) in quartz (Qz) and calcite (Cal), epithermal style vein, Konos Hill prospect (sample KMSP48); (c) Magnetite (Mag) with pyrite (Py) associated with quartz (Qz) – feldspar (Fsp, orthoclase and/or albite) – biotite (Bt) – epidote (Ep) altered granodiorite porphyry, M-type vein, Pagoni Rachi prospect (sample KMPR74); (d) Pyrite (Py) including minor pyrrhotite and associated with molybdenite (Mol), in sericite (Ser) and quartz (Qz) altered granodiorite porphyry, D-type vein, Pagoni Rachi prospect (sample KMPR66); (e) Native gold (Au) in association with pyrite (Py)in a sericite (Ser) and quartz (Qz) matrix, D-type vein, Pagoni Rachi prospect (sample KMPR66); (f) Euhedral pyrite (Py) crystals in quartz (Qz) and including galena (Gn) and sphalerite (Sp), E-type vein, Pagoni Rachi prospect (sample KMPR53).

Sericitic (or “phyllic”) alteration is the most widespread type in the area and caused pervasive obliteration of pre-existing, sodic±potassic alteration assemblages (e.g., albite, K-feldspar, biotite, chlorite). The D-type pyritic veins are mostly oxidized, and their width ranges from a few mm up to 5 cm. Commonly, pyrite from this stage, fills center-lines that are associated with reopening of A-type, quartz-stockwork veins (Figure 7.1b, c). Pyrite in D-type veins is usually fine- to medium-grained (from a few μm, up to 0.5 cm) and is characterized by a porous texture. Its grain shape is anhedral, and displays a characteristic “corroded” rim (Figure 7.3a to c). Pyrrhotite (Figure 7.4d), and less commonly chalcopyrite, occurs as inclusions. Molybdenite is in places associated with chalcopyrite and pyrite, disseminated in the sericitic-altered granodiorite or in the quartz veins (Figure 7.3c). In addition, molybdenite forms fine-grained aggregates (up to 100μm in length) that develop in the grain boundaries of pyrite (Figure 7.4a). Bornite, magnetite, enargite, and colusite also accompany pyrite, but occur in trace amounts (see also Voudouris et al., 2006, 2013b; Ortelli et al., 2009; Mavrogonatos et al. 2018b, c).

Pyrite is also widespread in epithermal-style (E-type) veins that crosscut/overprint the porphyry-style mineralization. These veins, most of which occur along NNW-, and E-trending directions, are composed of quartz and calcite (Figure 7.2d to f) and display minor banding. The veins are of high- to intermediate-sulfidation affinities (Mavrogonatos et al., 2018b,c; Voudouris et al., 2019a) and are associated with argillic (and less commonly advanced argillic) alteration. In these veins, pyrite forms euhedral crystals that are up to 1 cm in size. The crystals are commonly isolated, included in quartz and/or calcite, or they form as aggregates. They are commonly associated with Fe-poor sphalerite, galena, chalcopyrite, and tetrahedrite-tennantite group minerals (Figure 7.3d to e). Galena forms euhedral to subhedral grains, spatially associated with sphalerite and pyrite (Figure 7.3e), or it occurs interstitially between pyrite grains (Figure 7.3f). It can also form swarms of inclusions that commonly occur along growth zones of the host pyrite crystal (Figure 7.4b).

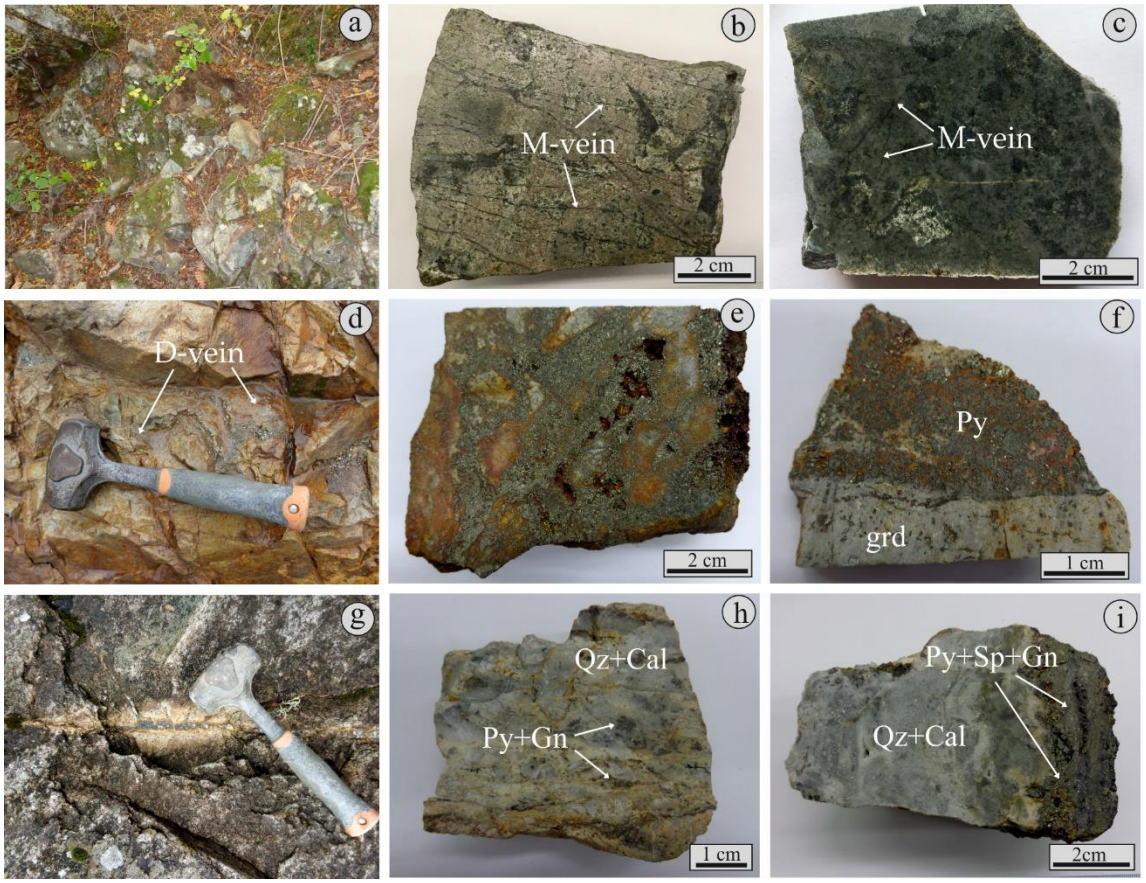

Figure 7.5: Field and hand-specimens photographs of pyrite-bearing rocks from the Pagoni Rachi porphyry/epithermal prospect: (a) Sodic/potassic-calcic altered granodiorite porphyry crosscut by magnetite veinlets; (b, c) Magnetite (M-type) veins crosscutting sodic/potassic-calcic altered granodiorite (samples KMPR74 and KMPR68, respectively); (d) D-type pyrite (py) vein crosscutting sericitic-altered granodiorite porphyry; (e-f) Massive pyrite vein (D-type), cementing fragments of sericite altered granodiorite porphyry (sample KMPR66); (g) Epithermal-style vein with sphalerite and pyrite, crosscutting sericitic-altered (sericite and calcite) granodiorite porphyry; (h, i) Hand specimens of epithermal-style, clear to milky quartz (Qz) - calcite (Cal) veins (E-type) with pyrite (Py), sphalerite (Sp) and galena (Gn) (samples KMPR53 and KMPR83, respectively).

Sphalerite usually contains tiny inclusions of chalcopyrite (chalcopyrite “disease”). These inclusions appear commonly as rounded and/or bleb-shaped grains, randomly distributed in the host-sphalerite crystal, and their size ranges between a few micrometers up to 0.1 millimeters (Figure 7.3e).

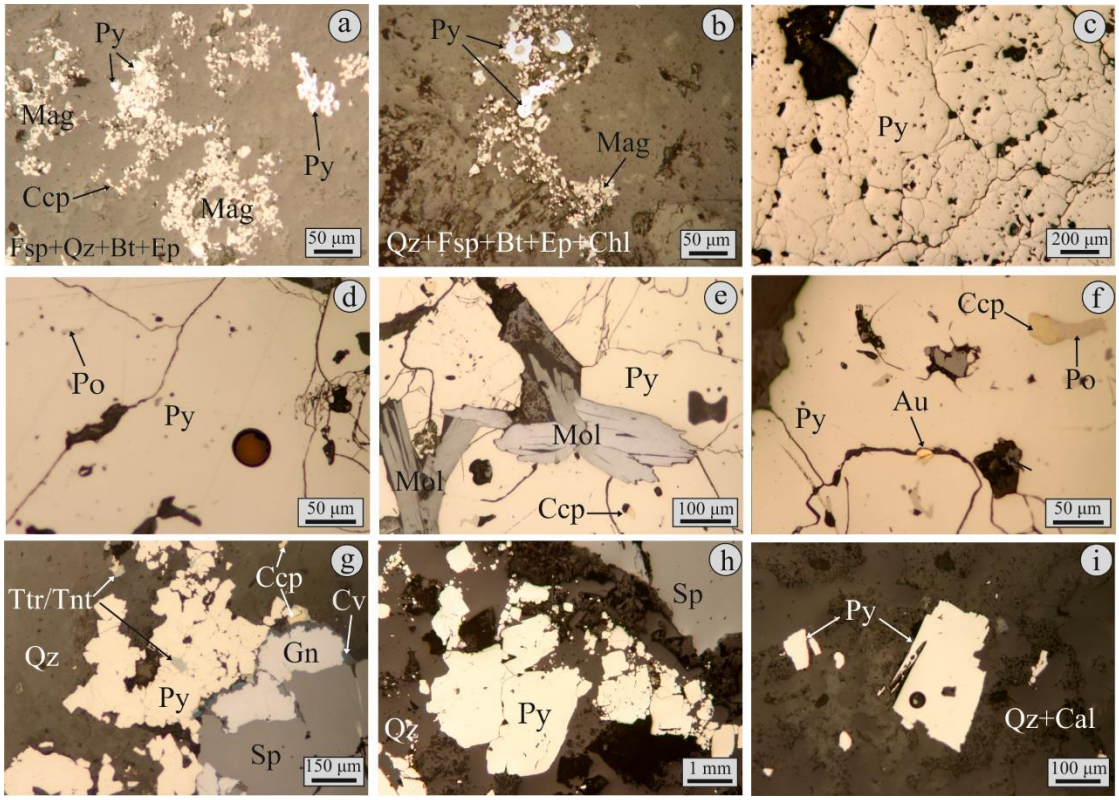

Figure 7.6: Reflected light photomicrographs of pyrite and associated opaque minerals from different mineralization events in the Pagoni Rachi prospect. (a) Fine grained magnetite (Mag) in association with pyrite (Py) and chalcopyrite (Ccp), in calcic/potassic matrix dominated by feldspar (Fsp, orthoclase and/or albite), quartz (Qz), feldspar (Fsp, orthoclase and/or albite) biotite (Bt) and epidote (Ep), M-type vein (sample KMPR74); (b) Magnetite (Mag) along with pyrite (Py) in sodic/potassic-calcic altered granodiorite porphyry, consisting of quartz (Qz), feldspar (Fsp, albite and/or orthoclase), biotite (Bt), epidote (Ep) and chlorite (Chl), M-type vein, (sample KMPR68); (c, d) Massive, subhedral to anhedral pyrite (Py), including minor pyrrhotite (Po), D-type vein, (sample KMPR66). Note in (d) the black circle indicates the laser-ablation ICP-MS analysis spot; (e) Subhedral pyrite (Py) intergrown with molybdenite (Mol) and including minor chalcopyrite (Ccp), D-type vein (sample KMPR66); (f) Native gold (Au) associated with pyrite (Py), which includes pyrrhotite (Po) and chalcopyrite (Ccp), D-type vein (sample KMPR66); (g) Euhedral pyrite (Py) in association with galena (Gn), sphalerite (Sp), covellite (Cv), and fahlores (Ttr/Tnt), in quartz (Qz), E-type vein (sample KMPR53); (h) Coarse-grained, euhedral pyrite (Py) and sphalerite (Sp) in quartz (Qz), epithermal-style vein (sample KMPR53); (i) Pyrite grain included in a quartz (Qz) and calcite (Cal) dominated matrix. The black circle marks the laser-ablation ICP-MS analysis spot, E-type vein (sample KMPR53).

In the Pagoni Rachi mineralization, pyrite is widespread and occurs throughout the paragenetic sequence (Voudouris et al., 2013b). Three different pyrite generations

are found in: (i) early magnetite veins (M-type), (ii) D-type veins, and (iii) epithermal (E-type) veins.

Pyrite is a minor constituent of the early M-type veins. They are irregular in shape and discontinuous and are associated with sodic/potassic-calcic alteration of the granodiorite porphyry (Figure 7.5a to c). They form a stockwork of veinlets up to 0.5 cm wide (Figure 7.5b, c) associated with variable amounts of secondary albite, orthoclase, biotite, actinolite, and chlorite. The M-type veinlets are commonly very narrow (less than 0.5cm), and are dominated by very fine-grained, anhedral magnetite. The pyrite grains are also fine-grained (reaching sizes up to 100 μm) and are commonly anhedral in shape. They coexist with magnetite, chalcopyrite (Figures 7.6a, b, and 7.7c), and minor amounts of bornite, gold, and molybdenite.

The transitional porphyry to epithermal, D-type veins are very well developed in the Pagoni Rachi system, and are the major carrier of Au in the system (Voudouris et al., 2013b). They form disrupted, planar to curvy veins, that are up to 15 cm wide (Figure 7.5d to f). Pyrite occupies more than 90 % of the vein, and is associated with strong sericitic (sericite, quartz, and calcite) alteration of the host rock, that obliterates earlier alteration assemblages. Pyrite in D-type veins (Figure 7.6c to f) is massive, and forms anhedral grains up to 0.5 cm in size. Some brecciation is evident, and locally, pyrite grains are characterized by suture-like grain boundaries (Figure 7.6c). They commonly contain numerous, minute inclusions of pyrrhotite and/or chalcopyrite (Figures 7.6d to f, and 7.7d). Pyrite is also spatially associated with molybdenite (Figures 7.6e, and 7.7d). In such cases, molybdenite forms fine- to medium-grained aggregates composed of elongated crystals, and fills interstices (Figure 7.6e), or can be included in pyrite (Figure 7.7d). Fine-grained native gold (up to 15μm in size) occurs in fractures of pyrite crystals (Figure 7.6f), or along their margins (Figure 7.7e).

Base and precious metal-bearing, epithermal-style veins (E-type) occur laterally and/or crosscut the porphyry-style mineralization. They are composed mainly of alternating bands of quartz and calcite (Figure 7.5h, i). In these veins, pyrite forms medium-, to coarse-grained (up to 1 cm) crystals, that occur either as isolated grains in the quartz and calcite-dominated matrix, or as aggregates with other sulfides. They exhibit idiomorphic, commonly cubic, shapes (Figures 7.6g to i, and 7.7f).

Pyrite in the E-type veins is associated with galena, sphalerite, chalcopyrite, covellite, and tetrahedrite-tennantite group minerals (Fig. 7.6g to i). The other sulfides as well as the fahlores, develop as rims on /or as inclusions in pyrite crystals, or in fractures, thus postdating the pyrite deposition.

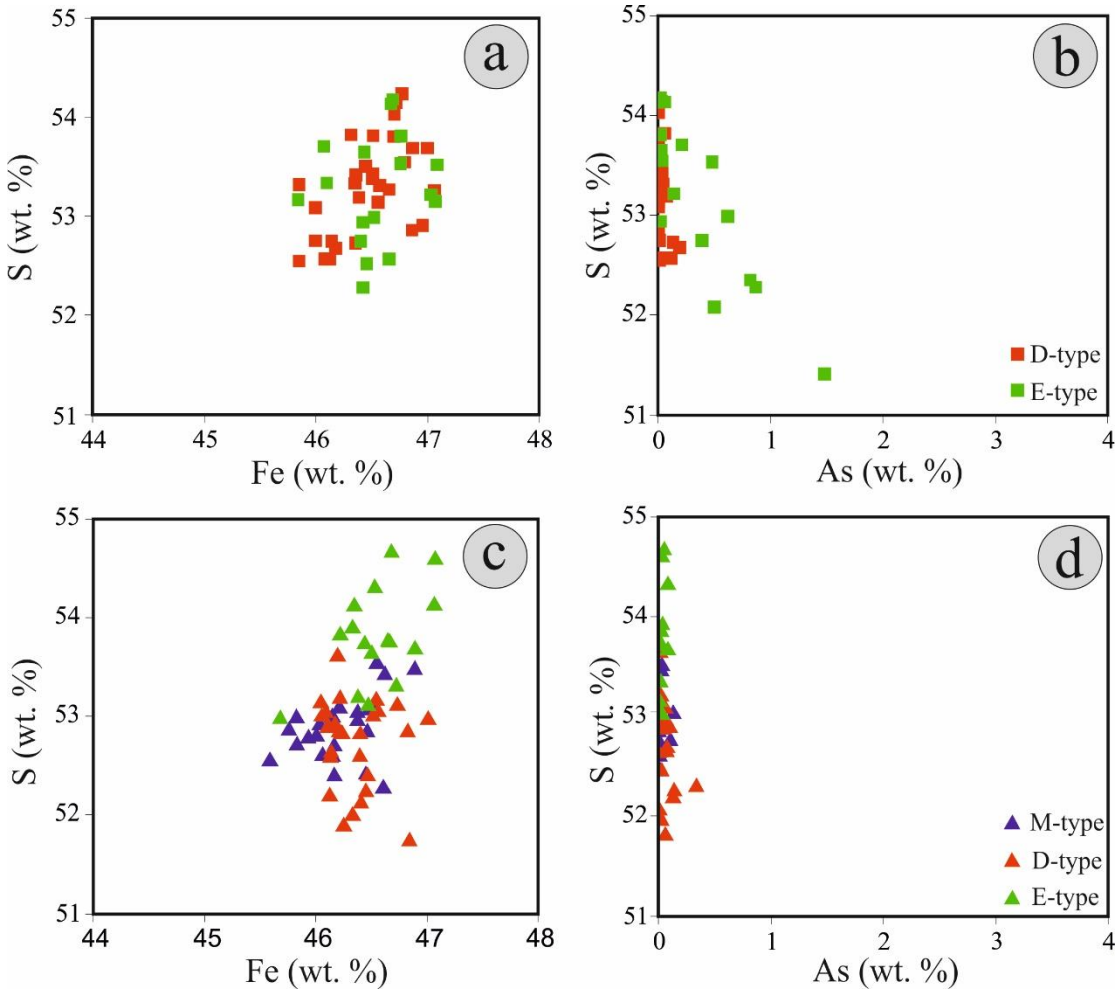

Figure 7.7: Concentration of S versus Fe and As (in wt. %) in pyrite from different mineralization events at the Konos Hill (a and b, respectively) and the Pagoni Rachi (c and d, respectively) porphyry-epithermal prospects.

7.5 Major and trace element geochemistry of pyrite

Electron probe micro-analyses (EPMA) of various generations of pyrite are summarized in Table 7.2 and plotted in Figure 7.7. Results of the LA-ICP-MS analyses of pyrite from the Konos Hill and the Pagoni Rachi prospect are shown in Tables 7.3 and 7.4, respectively. Chemical differences between the various generations of pyrite

from both prospects, based on their trace element content, are illustrated in Figures 7.8, 7.9, 7.10, and 7.11. Correlation coefficients between the most important trace elements impurities are summarized for the Konos Hill prospect and the Pagoni Rachi prospect in Tables 7.5 and 7.6, respectively.

7.5.1 EPM analyses

The Fe and S content of pyrite form the Konos Hill prospect varies significantly in the two mineralization stages (Table 7.2). Specifically, the Fe content of pyrite from the D-type veins ranges between 45.85 wt.% and 47.06 wt. %, while the S content is in the range of 52.55 wt.% - 54.24 wt.%. In the E-type veins, the compositional variation is wider for both elements: Fe ranges between 45.84 wt.% and 48.37 wt. %, and S, between 51.41 wt. % and 54.18 wt.% (Figure 7.7a). These variations probably reflect the presence of trace element impurities, that substitute for both Fe and S, in the structure of pyrite (e.g., Fouquer et al., 1998; Reich et al., 2013; Keith et al., 2016). Arsenic in pyrite from D-type veins is in the range of minor elements, reaching values of up to 0.19 wt. % and thus, it does not display any systematic relation to the content of sulfur. However, in the E-type veins, As is a major impurity and reaches values of up to 1.48 wt. %. The negative correlation between the two elements indicates a relatively restricted substitution of S by As (Figure 7.7b).

In the Pagoni Rachi prospect, pyrite from the early, magnetite-rich (M-type) veins is characterized by Fe and S values that are relatively homogenous, and range from 45.59 to 46.89 wt.% and 52.27 and 53.70 wt. %, respectively (Figure 7.7c). Compared to pyrite from these veins, pyrite from the D-type veins is characterized by slightly higher Fe values, that are in the range 46.05 wt. % - 47.01 wt. %, and by slightly lower S values, that vary from 51.74 wt. to 53.61 wt. %. The higher values for both elements, are recorded in pyrite from the E-type veins.

Table 7.2: EPM analyses of various pyrite generations from the Konos Hill and Pagoni Rachi porphyry/epithermal prospects. All values are reported in wt. %.

Konos Hill prospect								
Type	D - type (n = 29)				E - type (n = 17)			
Element	min	max	sd	aver	min	max	sd	aver
As	0.04	0.19	0.04	0.03	0.11	1.48	0.41	0.32
Fe	45.85	47.06	0.34	46.47	45.84	48.37	0.58	46.70
Cu	bdl	0.05	0.01	0.01	bdl	0.23	0.06	0.04
Ni	bdl	bdl	-	-	bdl	bdl	-	-
Co	0.05	0.14	0.02	0.08	bdl	0.03	0.03	002
Au	bdl	0.08	0.03	0.02	bdl	0.07	0.01	0.00
Se	bdl	0.06	-	-	bdl	bdl	-	-
S	52.55	54.24	0.48	53.29	51.41	54.18	0.74	53.14
Total	98.56	101.13	0.71	99.91	99.58	100.77	0.58	100.17

Pagoni Rachi prospect												
Type	M - type (n = 22)				D - type (n = 26)				E - type (n = 15)			
Element	min	max	sd	aver	min	max	sd	aver	min	max	sd	aver
As	bdl	0.14	0.03	0.02	bdl	0.34	0.07	0.05	bdl	0.09	0.03	0.02
Fe	45.59	46.89	0.32	46.23	46.05	47.01	0.26	46.35	45.68	47.07	0.34	46.54
Cu	bdl	bdl	0.02	0.01	bdl	0.04	0.01	0.01	bdl	0.05	0.02	0.01
Ni	bdl	bdl	0.01	0.00	bdl	0.20	0.04	0.01	bdl	bdl	-	-
Co	bdl	bdl	0.14	0.13	0.08	0.30	0.06	0.07	bdl	0.01	-	-
Au	bdl	bdl	0.04	0.02	bdl	0.16	0.04	0.04	bdl	0.06	-	-
Se	bdl	bdl	-	-	bdl	0.10	0.02	0.04	bdl	bdl	-	-
S	52.27	53.70	0.35	52.88	51.74	53.61	0.45	52.73	52.98	54.66	0.49	53.79
Total	98.69	100.55	0.53	99.29	98.73	100.23	0.49	99.26	98.70	101.31	0.75	100.09

n = number of analyses; min = minimum value; max = maximum value; sd = standard deviation; aver = average value; bdl = below detection limit.

In these grains of pyrite, Fe ranges between 45.68 wt. % and 47.07 wt. %, and S between 52.98 wt. % and 54.66 wt. % (Figure 7.7c). Arsenic is within the range of trace concentrations of up to 0.14 wt. %, 0.34 wt. %, and 0.09 wt. %, that is observed in pyrite from the M-, D-, and E-type veins, respectively (Fig. 7.7d). The majority of the other elements are mostly below the detection limits (Table 7.2).

7.5.2 LA – ICP – MS analyses

The trace elements concentration of pyrite varies significantly between the two stages of mineralization at the Konos Hill prospect (Table 7.3). The most abundant trace element is As, which reaches values up to 1577 ppm in pyrite from the D-type veins, and up to 16429 ppm in pyrite from the E-type veins. Pyrite from both stages is characterized by relatively low Au content, which contains only values of up to 0.06 ppm and 1.10 ppm, respectively. The Ag content reflects a preferable enrichment in the late stage of the mineralization (up to 19 ppm in the E-type veins), relative to the D-type veins, where its concentration never exceeds the detection limit. Regarding the rest of the trace elements, pyrite from the D-type veins is depleted in all elements except for Co (up to 1395 ppm) and Se (up to 233 ppm) in contrast to pyrite from the E-type veins, which is characterized by much less Co (up to 457 ppm) and is depleted in Se (below the detection limit).

Nickel and Cd have an opposite behavior to Co, being enriched in pyrite from the E-type veins (up to 628 ppm and 41 ppm, respectively), relative to pyrite from the D-type veins (up to 46 ppm and 0.50 ppm, respectively). Other notable concentrations in pyrite from the E-type veins that are generally well above detection limits are Pb (up to 898 ppm), Cu (351 ppm), Sb (up to 292 ppm), Bi (up to 42 ppm). Molybdenum is characterized be very low concentrations in the D-type pyrite, but reaches values of up to 15 ppm in pyrite from the late, E-type veins. Traces of Ga and Ge occur both in the D-, and E-type pyrite, however the average values for both elements are higher in the epithermal stage (average values for Ga and Ge are 0.27 ppm and 1.15ppm at Konos Hill, and 0.85 ppm and 1.29 ppm at Pagoni Rachi, respectively.

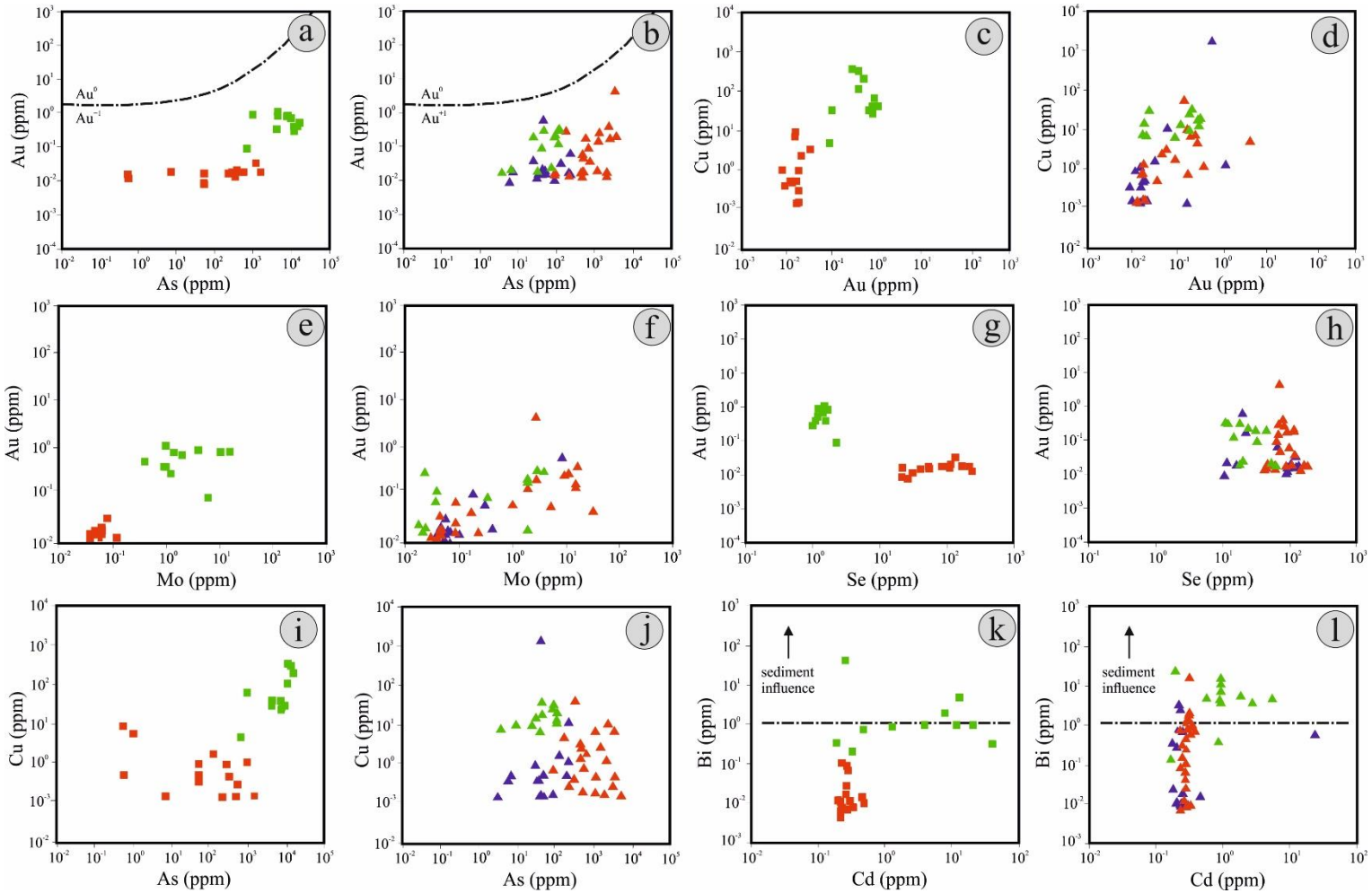

Figure 7.8: Trace elements variation plots of pyrite from different mineralization events at the Konos Hill (a, c, e, g, i, and k) and the Pagoni Rachi (b, d, f, h, j, and k) porphyry-epithermal prospects (same symbols as in Figure 8; values in ppm). (continuation in the next page).

(Figure 7.8, continuation): (a, b) As versus Au. The black, dash-dotted curve represents the solubility limit of Au as a function of As concentration (Reich et al., 2005); (c, d) Au versus Cu; (e, f) Mo versus Au; (g, h) Se versus Au; (i, j) As versus Cu; (k, l) Bi versus Cd. The black, dash-dotted line marks elevated Bi contents in pyrite due to addition of a sedimentary component to the hydrothermal system (Keith et al., 2016b). The maximum Bi value of 7451 ppm, attributed to Bi-bearing inclusion, has been excluded from the plot in 9f.

In the Pagoni Rachi prospect, the LA-ICP-MS analyses reveal a large variation in the concentration of trace elements among the various generations of pyrite (Table 7.4). Pyrite from the early magnetite veins (M-type) is characterized by very low contents of Au and Ag (up to 0.61 ppm and 2 ppm, respectively), and elevated concentrations of Zn and Cu, which reach values of up to 2751 ppm and 1659 ppm, respectively. The concentration of As content is relatively low (maximum value is 233 ppm), but it is relatively enriched in Se, which reaches values up to 137 ppm. Other elements that exhibit low concentrations are Ni (up to 77 ppm), Cd (up to 27 ppm), Co (up to 13 ppm) and Mo (up to 9 ppm), while the rest of the elements analyzed are generally below 5 ppm.

Pyrite in D-type veins are enriched in several elements: The Cu content is as high as 9824 ppm, while the concentration of As varies between 91 ppm and 3745 ppm. Cobalt, Se and Ni display relatively high concentrations of up to 576 ppm, 187 ppm, and 113 ppm, respectively. Molybdenum is as high as 33 ppm, while Au and Ag reach concentrations of up to 4 ppm and 0.6 ppm, respectively. The rest of the elements are characterized by very low concentrations (generally below 5 ppm) with the exception of Pb and Bi, which both reach values of up to 18 ppm.

Pyrite in E-type veins contains Bi and Zn with up to 7451 ppm and 2012 ppm, respectively with the latter being comparable to the Zn content of in pyrite in M-type veins. Other elements that are significantly enriched in pyrite from E-type veins include Pb (up to 220 ppm), Co (up to 198 ppm), As (up to 121 ppm) and Se (11-63 ppm). Copper (up to 31 ppm) is depleted in pyrite in E-type veins compared to that in other previous stages of the mineralization. Moreover, the concentrations of Au (up to 0.33 ppm) and Ag (up to 2 ppm) are also depleted.

Table 7.3: LA-ICP-MS analyses of various pyrite generations from the Konos Hill porphyry/epithermal prospect. All values are reported in ppm.

	D - type (n = 15)				E - type (n = 12)			
Element	min	max	sd	aver	min	max	sd	ver
Mn	0.57	1.12	0.19	0.75	0.42	13	4.90	6.55
Co	0.56	1395	378	254	0.30	457	156	101
Ni	3.50	46	15	18	1.96	628	196	102
Cu	0.30	9.12	2.99	2.33	4.78	351	124	111
Zn	2.11	3.35	0.47	2.75	3.99	49	15	18
Ga	0.13	0.56	0.25	0.27	0.17	2.00	0.53	0.85
Ge	1.03	1.22	0.09	1.15	0.75	2.20	0.52	1.29
As	7.22	1577	485	436	688	16429	5207	8203
Se	21	233	69	93	bdl	bdl	-	-
Mo	0.12	0.12	-	0.12	0.41	15	4.85	4.00
Ag	bdl	bd	-	-	0.92	19	6.38	8.76
Cd	0.47	0.50	0.02	0.49	0.49	41	13	13
In	bdl	bdl	-	-	0.04	0.25	0.08	0.09
Sn	0.16	0.21	0.04	0.19	0.29	9	3.18	1.81
Sb	0.10	0.11	0.01	0.10	1.98	292	99	131
W	0.04	0.04	-	0.04	0.01	0.40	0.13	0.18
Au	0.02	0.06	0.01	0.03	0.09	1.10	0.30	0.62
Tl	0.00	0.01	0.00	0.01	0.05	18	6.31	11
Pb	0.05	0.48	0.13	0.27	34	898	277	401
Bi	0.02	0.11	0.04	0.06	0.21	42	12	4.55

n = number of analyses; min = minimum value; max = maximum value; sd = standard deviation; aver = average value; bdl = below detection limit.

Additionally, minor amounts of Ga and Ge were measured: The Ga content ranges from 1 ppm to 4 ppm, and the Ge content is almost identical, ranging from 1 ppm to 3.2 ppm. For both elements, their average values (2.37 ppm and 1.64 ppm, respectively) are higher compared to those in pyrite from the M-, and D-veins (Table 7.4).

7.6 Discussion

7.6.1 Distribution of trace elements in porphyry-style pyrite

Pyrite from the early stages of porphyry-style deposits is commonly characterized by a poor budget of trace elements.

Table 7.4: LA-ICP-MS analyses of various pyrite generations from the Pagoni Rachi porphyry/epithermal prospect. All values are reported in ppm.

	M - type (n = 16)				D - type (n = 22)				E - type (n = 12)			
Element	min	max	sd	aver	min	max	sd	aver	min	max	sd	aver
Mn	0.53	9.10	2.64	2.74	0.59	5.83	1.35	1.87	0.92	264	80	58
Co	0.49	13	3.63	3.67	0.28	576	169	97	1.24	198	49	55
Ni	2.88	77	22	20	3.27	113	25	22	4.38	52	17	28
Cu	0.54	1659	524	168	0.49	9824	2530	678	6.22	31	8.52	16
Zn	2.04	2751	734	199	3.02	3.55	0.22	3.39	3	2012	669	326
Ga	0.15	0.16	0.01	0.15	0.12	0.70	0.26	0.37	1	4	1.25	2.37
Ge	1.09	1.22	0.07	1.16	1.09	1.59	0.18	1.27	1.1	3	0.65	1.64
As	3.20	233	80	78	91	3745	1084	1166	3.77	121	43	63
Se	11	137	45	77	42	187	39	91	11	63	17	29
Mo	0.11	8.69	4.20	2.39	0.09	33	9.98	11	0.36	4	1.22	2.23
Ag	bdl	2.10	-	2.10	0.56	0.56	-	0.56	0.56	2	0.49	1.32
Cd	bdl	27	18	14	bdl	bdl	-	-	0.61	6	1.65	1.75
In	bdl	0.20	0.10	0.09	0.03	0.04	0.01	0.03	0.09	0.10	0.01	0.10
Sn	bdl	0.17	-	0.17	0.13	0.19	0.04	0.16	0.12	0.20	0.03	0.18
Sb	0.07	1.08	0.44	0.50	0.13	0.57	0.20	0.33	0.17	1.77	0.46	0.53
W	bdl	0.24	-	0.24	0.03	0.23	0.09	0.08	0.01	0.11	0.04	0.06
Au	0.02	0.61	0.25	0.18	0.04	4.35	1.21	0.52	0.09	0.33	0.09	0.22
Tl	0.01	0.02	0.00	0.01	0.01	0.01	-	-	0.06	0.21	0.05	0.15
Pb	0.04	129	43	24	0.05	18	5.09	3.43	34	620	166	134
Bi	0.02	4.85	1.76	1.07	0.03	18	4.06	3.04	0.14	7451	628	2148

n = number of analyses; min = minimum value; max = maximum value; sd = standard deviation; aver = average value; bdl = below detection limit.

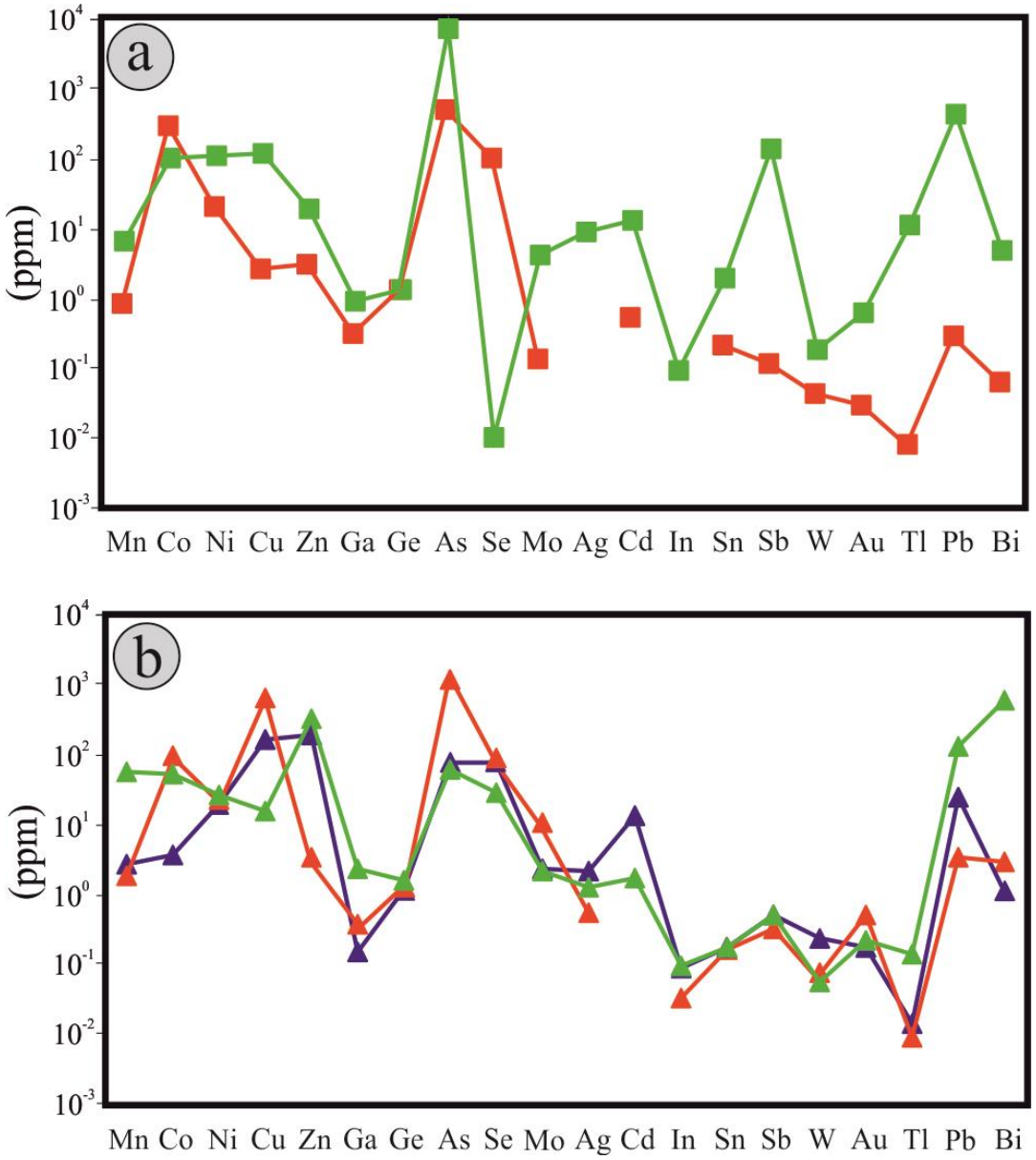

Figure 7.9: Multi-element variation plots of pyrite from different vein types at the Konos Hill (a) and the Pagoni Rachi (b) porphyry-epithermal prospect (symbols as in Figure 8; mean values in ppm). Porphyry-style pyrite follows a relatively homogeneous path, with an enrichment of Cu and Au being the prominent features of the Pagoni Rachi porphyry-style pyrite. Note the difference between the epithermal stages in the two areas: The depletion in Se, and the enrichment in Ag, Cd and Sb being the dominant features of epithermal-style pyrite from the Konos Hill prospect, in contrast to the Pagoni Rachi prospect, where it is characterized by elevated Bi content.

This fact that has already been recognized from other porphyry deposits and prospects (e.g., Reich et al., 2013; Maydagán et al., 2013; Francini et al., 2015). The gold content of pyrite in the Konos Hill and the Pagoni Rachi systems is relatively low. The only exception is pyrite from the D-type veins in the Pagoni Rachi prospect, where Au values reach up to 4.35 ppm. This is consistent with the findings of Voudouris et al., (2013b), who stated that major introduction of gold in the system was achieved during the D-event. Since the speciation of gold in pyrite is highly dependent on its arsenic content (Reich et al., 2005), it is evident from the plots in Figure 7.8a and 7.8b, that the gold concentration of pyrite from Konos Hill and Pagoni Rachi never exceeds the solubility limit of Au as a function of As. Thus, no gold nanoparticles (Au^0) are present, meaning that gold is incorporated as a non-stoichiometric substituting element (Au^{+1}) in the structure of pyrite. However, a positive correlation between Au and As is evident (Tables 7.5 and 7.6). Regarding its relation to Cu, Au displays a notable correlation in pyrite from M-type veins at Pagoni Rachi, but this is not the case for D-veins pyrite, where no systematic correlation is observed (Figure 7.8c, d).

Given the absence of an early M-type event in the Konos Hill prospect, the hypothesis of the deficiency of pyrite in trace elements during the early stages of the porphyry mineralization, can only be tested for the Pagoni Rachi prospect, where magnetite-veins constitute the first ore stage (Voudouris et al., 2013b; Mavrogonatos et al., 2019). Pyrite from the M-type veins is generally depleted in trace elements, but there are a few exceptions; a notable enrichment Cu, Zn and, Se and minor Cd, is evident. Values that characterize the majority of these elements are higher in the Pagoni Rachi prospect, compared to those described from mineralization related to sodic-potassic and potassic alteration in other deposits, for example, the Pebble porphyry Cu-Mo-Au deposit (Gregory et al., 2013). The abundance of chalcopyrite in association with pyrite and magnetite in the M-veins suggests elevated availability of Cu during this event, and probably indicates the presence of Cu^{2+} as solid solution in pyrite. A similar abundance in the precipitating fluid can be inferred for Zn, as it presents constantly elevated values.

Table 7.5: Correlation coefficient (R) between the most important trace elements of different pyrite generations at the Konos Hill porphyry/epithermal prospect.

D - type vein									
Element	Au	Ag	Cu	As	Co	Ni	Se	Mo	Bi
Au	-								
Ag	0.24	-							
Cu	0.13	0.21	-						
As	0.60	0.18	0.19	-					
Co	0.14	0.10	0.26	0.19	-				
Ni	0.24	0.49	0.21	0.32	0.29	-			
Se	0.36	0.13	0.19	0.23	0.62	0.04	-		
Mo	0.64	0.26	0.02	0.24	0.67	0.12	0.71	-	
Bi	0.06	0.34	0.08	0.30	0.18	0.04	0.50	0.20	-
E - type vein									
Element	Au	Ag	Cu	As	Co	Ni	Se	Mo	Bi
Au	-								
Ag	0.38	-							
Cu	0.47	0.81	-						
As	0.30	0.53	0.71	-					
Co	0.24	0.59	0.52	0.55	-				
Ni	0.44	0.38	0.42	0.54	0.93	-			
Se	0.17	0.53	0.72	0.60	0.86	0.87	-		
Mo	0.21	0.69	0.46	0.39	0.70	0.46	0.49	-	
Bi	0.20	0.39	0.21	0.24	0.25	0.06	0.17	0.43	-

These findings from M-type related pyrite, fit with those of Mavrogonatos et al., (2019), (see Chapter 6) who described elevated content of Cu and Zn in hydrothermal magnetite, at the Pagoni Rachi prospect, thus strengthening the hypothesis of elevated content of Cu and Zn in the precipitating fluid. Given the highly-saline nature of the fluid that precipitated A-type quartz veins, that formed at the same time as M-type veins (38.9 wt. % - 69.9 wt. % NaCl equiv., Voudouris et al., 2013b), the Zn (and possibly Cu) enrichment in the brine during this stage is further supported by the assumption of Ding and Seyfried (1992), Bazarkina et al. (2010), and Pokrovski et al. (2013), who suggested that metals with a chloride affinity like Zn, are fixed in dense, highly saline brines.

The Mo values of pyrite from the porphyry stages at both prospects are low (up to 15 ppm at Konos Hill, and up to 10 ppm at Pagoni Rachi), and reflect the widespread presence of molybdenite in the porphyry-style mineralization (Figure 7.8e, f). This suggests that Mo is preferably precipitating as a metal sulfide, rather than substituting in the structure of pyrite. The high correlation coefficient between Mo and Au in pyrite from the D-type veins at Pagoni Rachi (Table 7.6), is strong evidence of

contemporaneous introduction of these elements during this mineralization stage. A similar hypothesis can be made for Au, Ag, and Mo in the early magnetite veins, since their correlation coefficients are very high, (R ranging between 0.96 and 0.98, Table 6).

Table 7.6: Correlation coefficient (R) between the most important trace elements of different pyrite generations at the Pagoni Rachi porphyry/epithermal prospect.

M - type vein									
Element	Au	Ag	Cu	As	Co	Ni	Se	Mo	Bi
Au	-								
Ag	0.96	-							
Cu	0.97	0.98	-						
As	0.13	0.12	0.11	-					
Co	0.12	0.02	0.02	0.36	-				
Ni	0.42	0.47	0.47	0.01	0.23	-			
Se	0.41	0.34	0.33	0.42	0.56	0.12	-		
Mo	0.97	0.98	0.98	0.01	0.02	0.5	0.33	-	
Bi	0.01	0.01	0.01	0.45	0.32	0.05	0.29	0.01	-
D - type vein									
Element	Au	Ag	Cu	As	Co	Ni	Se	Mo	Bi
Au	-								
Ag	0.05	-							
Cu	0.03	0.14	-						
As	0.51	0.18	0.15	-					
Co	0.04	0.63	0.04	0.10	-				
Ni	0.10	0.22	0.21	0.10	0.23	-			
Se	0.13	0.21	0.14	0.20	0.20	0.13	-		
Mo	0.77	0.16	0.36	0.07	0.03	0.09	0.20	-	
Bi	0.18	0.10	0.06	0.19	0.48	0.10	0.16	0.01	-
E - type vein									
Element	Au	Ag	Cu	As	Co	Ni	Se	Mo	Bi
Au	-								
Ag	0.46	-							
Cu	0.24	0.22	-						
As	0.62	0.12	0.55	-					
Co	0.14	0.33	0.04	0.31	-				
Ni	0.36	0.14	0.54	0.21	0.35	-			
Se	0.53	0.17	0.37	0.64	0.45	0.12	-		
Mo	0.57	0.02	0.04	0.43	0.11	0.27	0.45	-	
Bi	0.15	0.44	0.1	0.35	0.41	0.23	0.30	0.03	-

Selenium enrichment in D-type pyrite from both prospects as well as in pyrite from M-type veins at the Pagoni Rachi prospect is notable. According to Huston et al. (1995) and Layton-Matthews et al. (2008), who conducted thermodynamic modelling

on the chemistry of selenium, the Se content of pyrite is solely a function of the ΣSe/S ratio of the precipitating fluid, and thus it reflects its availability in the precipitating hydrothermal fluids of studied systems. There is no systematic relationship between Se and the Au content of pyrite (Figure 7.8g and h). This may be indicative of the absence or the rarity of Au-Se inclusions in pyrite (Keith et al., 2018). The correlation of Se with other trace elements, like Co and/or Ni (in some porphyry and the epithermal stages of the studied prospects, Tables 7.5 and 7.6), could reflect the presence of selenides that incorporate such elements (e.g., like the mineral tyrrellite [$Cu(Co,Ni)_2Se_4$], Keith et al., 2018). This speculation is in agreement with the findings of Voudouris et al., 2013b, who reported the presence of two unnamed, Se-bearing inclusions in pyrite. However, the obtained ablation patterns do not clearly show the presence of such inclusions and rather speak for a homogeneous distribution of these elements in pyrite.

7.6.2 Distribution of trace elements in epithermal-style pyrite

The compositional variation between pyrite from the M-, D- and E-type veins in the studied prospects (Figure 7.9), is most likely due to variation in the composition of the precipitating fluid. For example, this can result from the mixing between magmatic vapors and hydrothermal fluids, a common and repeated process during the evolution of porphyry systems (e.g., Kesler et al., 2002; Pokrovski et al., 2002, 2005; William-Jones and Heinrich, 2005; Klemm et al., 2007; Simon et al., 2007; Deditius et al. 2009). However, a roughly common trend can be remarked regarding the metal endowment of the two studied systems (Figure 7.9).

Voudouris et al. (2013b) stated that the base and precious metal bearing epithermal-style veins (E-type) may represent the root zones of high-sulfidation veins at higher topographic levels of a given ore system, which seems to be the case for the higher levels of the Konos Hill prospect, where advanced argillic alteration assemblages have been described in association with (mostly oxidized) high-sulfidation mineralization (Voudouris 2014; Mavrogonatos et al., 2018b, c). However, it remains speculative whether such a lithocap once overprinted the Pagoni Rachi system. Mineralogical similarities between D- and E-type veins (e.g., presence of

molybdenite, tellurides, Voudouris et al. 2013b) record the transition from the porphyry to the epithermal environment, and is reflected in the changes in the trace element content of pyrite.

As indicated by their very low correlation coefficients, As and Cu display a decoupling behavior (Figure 7.8i, j) in all porphyry-style stages of mineralization, both in the Konos Hill and the Pagoni Rachi prospect (Tables 7.5 and 7.6, respectively). This is in accordance with the findings of Reich et al. (2013), who studied the trace elements distribution in pyrite from the Dexing porphyry Cu-Mo-Au deposit (China) and demonstrated that Cu is geochemically decoupled from As. This further suggests that this selective partitioning of metals into pyrite probably reflects compositional variations of the hydrothermal fluid (Reich et al., 2013). The presence of micrometer-scaled chalcopyrite inclusions in the D-type veins from the Pagoni Rachi prospect, likely indicates Cu-saturated conditions derived from cooling of high temperature pyrite forming fluids as the hydrothermal system evolved with time (Monecke et al. 2018). Chalcopyrite inclusions in pyrite from D-type veins at Pagoni Rachi are indicated by the LA-ICP-MS profile (Figure 7.10a) where, a spot analysis yielded a very high value (9824 ppm) of Cu.

This decoupling behavior is not characterizing the epithermal-style pyrite, indicating a more homogeneous introduction of Cu and As, as indicated by their higher correlation coefficients for pyrite in the epithermal stages (E-type veins) of both prospects. Regardless, the As content of pyrite from the epithermal stage of both prospects is relatively low, when compared to other epithermal gold deposits (e.g., Yanacocha, Peru, Deditius et al. 2009), thus indicating a restricted activity of As in the late hydrothermal fluids (Francini et al., 2015) and/or its preferable incorporation into other As-carrying phases (e.g., enargite, tennantite/tetrahedrite group minerals).

Another distinctive feature of pyrite from the late E-type veins, is their Pb content. Generally, Pb displays high concentrations in the epithermal-style veins (up to 898 ppm and 620 ppm at Konos Hill and Pagoni Rachi, respectively) rather than in the porphyry mineralization. These values are likely Pb substituting for Fe in the structure of pyrite, despite the much larger size of the Pb ion, as indicated by the flat LA-ICP-MS Pb-patterns (Figure 7.10).

The transition between the porphyry and epithermal stages is also supported by the presence of Se in pyrite throughout the depositional history of both systems, thus indicating that Se was present during the evolution of the porphyry to epithermal stages.

A distinctive feature of pyrite from the E-type event in the Konos Hill and Pagoni Rachi prospects (Figure 7.8k and l, respectively), is their relative enrichment in Bi, compared to pyrite from the other stages of mineralization. The majority of the analytical spots yielded values >1 ppm Bi, similar to other epithermal pyrite elsewhere, while the extreme Bi value of 7451 ppm, is indicative of intersection of a Bi-bearing phase (bismuthinite?) during the ablation procedure, as reflected by the spiky peak of Bi in Figure 7.10b. The presence of Bi along with Te and Au in the mineralization, in the form of Bi-tellurides/sulfosalts or Bi-bearing galena, appears to be diagnostic of the proximity to a magmatic center (Voudouris et al., 2018a,b, 2019a).

This assumption holds true for both the Konos Hill and the Pagoni Rachi epithermal style veins, as they occur laterally, or overprint the porphyry-stage mineralization. Thus, Bi which was transported by magmatic volatiles that was derived from the causative intrusion into the hydrothermal fluids, could have at least partly been incorporated in the structure of pyrite as well as forming Bi sulfosalts and tellurides in the E-type veins (Voudouris et al. 2013b). However, the low correlation coefficient between Au and Bi in pyrite raises the question as to whether Bi could have had an alternative origin. Bismuth-enriched pyrite has been recently attributed to reflect a sedimentary contribution to the hydrothermal system, and was described for pyrite from hydrothermal vents (Keith et al., 2016).

This hypothesis seems to be a possibility for pyrite from the E-type veins studied here. Voudouris et al. (2013b) suggested that E-type mineralization in Pagoni Rachi precipitated from dilute (<3 wt.% NaCl equiv.), late-stage magmatic fluids that probably mixed with sulfur-bearing, non-magmatic, aqueous fluids of meteoric or seawater origin at shallow levels. Given the abundance of hydrothermally-altered sediments in close proximity to the gold mineralization, circulation of meteoric and/or seawater-dominated hydrothermal fluids through such rocks could partly contribute to the introduction of Bi in the ore-forming system by leaching of the sediments.

Finally, traces of Ge and Ga that occur in pyrite from the E-type veins, is a feature that is also found in the porphyry-related stages of mineralization. However, their higher average values in pyrite from the epithermal stage at both prospects, could be related to the presence of sphalerite as is commonly described from low-temperature deposits (e.g., Cook et al., 2009c; Frenzel et al., 2016).

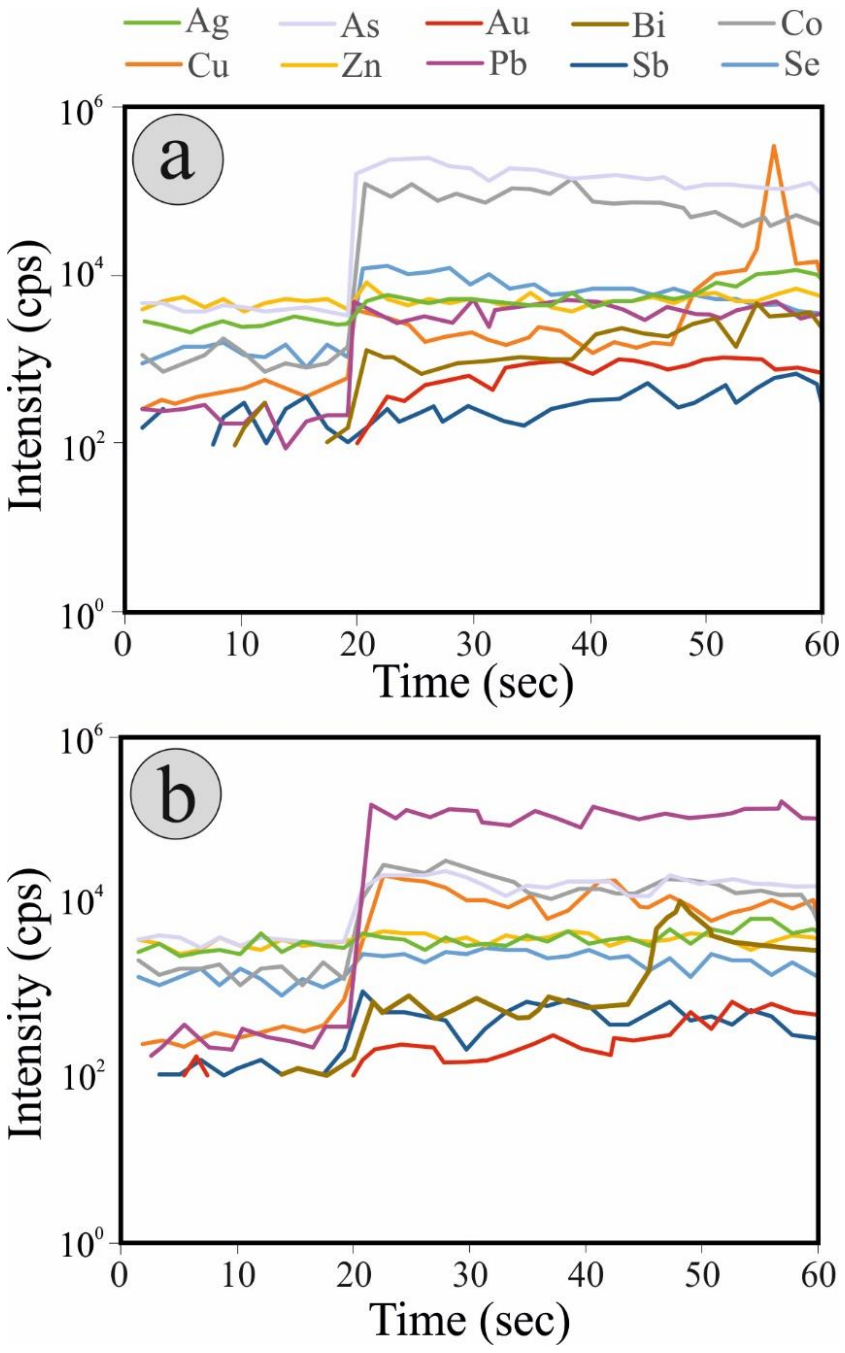

Figure 7.10: Time-resolved laser ablation ICP-MS depth profiles of Ag, As, Au, Bi, Co, Cu, Zn, Pb, Sb, and Se in pyrite. (a) D-type vein, (sample KMPR66). The majority of the elements are characterized by homogeneous distribution, as expressed by their flat

concentration patterns. The spiky patterns of Cu and to a lesser extent of Zn indicate the presence of submicroscopic inclusions (chalcopyrite); (b) E-type vein, (sample KMPR53). All elements but Bi show homogeneous distribution in pyrite. The spiky pattern of Bi is indicative of the presence of a submicroscopic, Bi-bearing phase (bismuthinite?).

7.5.3 *Fingerprinting the transition from the porphyry to the epithermal environment - Comparison to other porphyry/epithermal systems*

The composition of pyrite is already known to roughly reflect the metal endowment of the precipitating fluid in many hydrothermal systems, with the porphyry-epithermal association being, among others, a prominent example (Deditius et al., 2014). Despite the relatively restricted availability of compositional data of pyrites from porphyry systems worldwide, the chemical composition of pyrite from both the Konos Hill and the Pagoni Rachi porphyry/epithermal systems seems to follow the general trend of other deposits, however, it displays some notable differences.

The gold content of the studied porphyry pyrite is generally in the range of values that commonly characterize pyrite from porphyry-deposits, which is characterized by low values and homogeneous distribution. As indicated by the gold concentration in pyrite as a function of its As content (Figure 7.8a, b), the pyrite precipitating fluids at both deposits remained constantly undersaturated in Au (cf. Reich et al., 2013). At the Konos Hill prospect, the gold content of pyrite increases from the D-, towards the E-type veins (average values from 0.03 ppm to 0.62 ppm, respectively), in accordance with an increase to the As content. Similar behavior has been described from other porphyry/epithermal deposits and prospects, like the Agua Rica porphyry/high sulfidation deposit (Francini et al., 2015) and the Lienetz porphyry-related epithermal system (Sykora et al., 2018). This fact has been attributed to the preferable scavenging of Au by the hydrothermal fluid in the high-temperature porphyry environment, in contrast to the shallow epithermal conditions, which favor precipitation of gold, thus explaining the much higher Au grades in the epithermal deposits (Deditius et al., 2014; Keith et al., 2016). However, at the Pagoni Rachi system, early pyrite from M-type veins, as well as late pyrite from the epithermal stage, are characterized by gold contents (mean Au values of 0.18 ppm and 0.22 ppm, respectively), which are

significantly lower compared to pyrite from D-type veins (average 0.52 ppm Au). The As content follows the same trend: the maximum As values correlate with gold, and originate from D-vein pyrite. The late-stage epithermal pyrite is characterized by significantly lower As (and Au) content, fact that comes in contrast with other analogous porphyry/epithermal systems, where the transition from the porphyry to the epithermal environment is marked by significant increase of the Au and As content of pyrite.

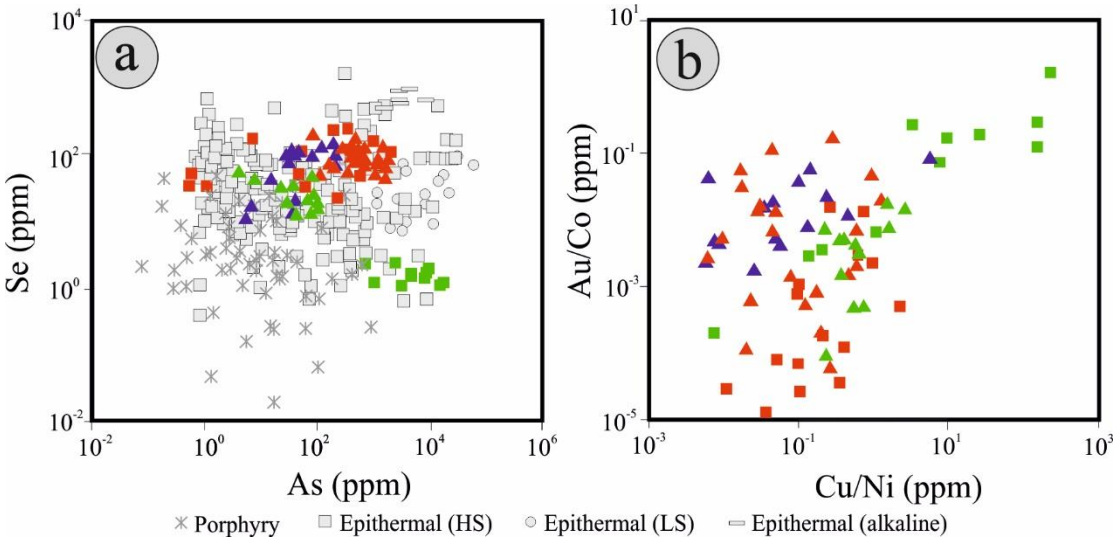

Figure 7.11: (a) Variation of As versus Se in pyrite from the present study compared to pyrites from orogenic Au, Carlin-type, high-sulfidation (HS) epithermal, low-sulfidation (LS) epithermal, alkaline rock-hosted epithermal and porphyry Cu deposits. Adopted from Keith et al., 2018; (b) As versus Au plot showing the composition of pyrite from the present study (symbols as in Figure 8) in respect to the compositional fields of pyrite from other porphyry and epithermal deposits worldwide (data from Deditius et al., 2014; Francini et al., 2015). The black, dash-dotted curve represents the solubility limit of Au as a function of As concentration (Reich et al., 2005).

Another distinctive feature of early, porphyry-style pyrite worldwide, is their enrichment in Co, Se (and Ni, Cu) (Gregory et al., 2013; Reich et al., 2013, Sykora et al., 2018). Early M-vein hosted pyrite at the Pagoni Rachi system, confirms this assumption, and moreover, the enrichment in Co, Se and Cu, grows larger towards the D-event. This fact characterizes D-vein hosted pyrite from both the Konos Hill and the Pagoni Rachi systems. The relative enrichment is obvious in Figure 7.11a, where, compared to other porphyry-style pyrites, those from the studied prospects display

higher Se concentrations, being roughly comparable to the highest concentrations of Se in (high-sulfidation) epithermal-style pyrite. As far as the Ni is concerned, at the Konos Hill prospect, it is preferably found in late, E-type pyrite (average value 102 ppm), contrary to other deposits, where Ni is usually found in early, porphyry-style pyrites (e.g, Franchini et al. 2015; Sykora et al., 2018; Alford et al., 2020). No significant Ni variation was recorded at the Pagoni Rachi system.

Only recently, Alford et al., 2020, proposed that a positive correlation between the Cu/Ni and Au/Co ratios, successfully records the transition from the porphyry to the epithermal conditions in the Lienetz mineralization, Lihir deposit. This assumption holds true for the studied pyrite: Owing mostly to their larger Co values, and their generally low Au content, porphyry-style samples commonly plot in the lower part of the diagram (Figure 7.11b), as is the case for pyrite from the studied prospects as well. This is clearer in the case of pyrite from the Konos Hill Deposit. Regarding the Pagoni Rachi prospect, pyrite generally records a similar trend, but the high Au content of pyrite from the D-type veins, as well as the higher Cu in M-, and D-vein pyrite, leads to significant overlapping with pyrite of the late, epithermal stage. These similarities imply, that late-stage hydrothermal fluids at the Pagoni Rachi record an evolution of a genetically-linked parental magmatic fluid, and finally its mixing with non-magmatic fluids, which lead to the formation of the epithermal-style mineralization. This is further supported by fluid inclusion studies of (Voudouris et al., 2013b), who suggested that formation of the porphyry/epithermal association at the Pagoni Rachi prospect is the result of the evolution of a hydrothermal fluid under constantly dropping pressure and temperature conditions.

Many trace elements (including Pb, Zn, Sb, Bi, Ag) are enriched in the late E-type pyrite at both studied prospects, compared to their porphyry-style counterparts. An analogous remark at the Agua Rica deposit, led Franchini et al., 2015 to propose that, enrichment in this chalcophile group of trace elements in the epithermal pyrite, could partly be the result of leaching and remobilization from earlier (porphyry-style) pyrite. This hypothesis could be true in the studied prospects and could be the mechanism that contributed (at least partly) to the metal budget of the epithermal-style pyrite. Especially at the Pagoni Rachi, the presence of Se in the late stage (epithermal) pyrite

holds evidence for a common genetical evolution of the ore-forming system from the deep porphyry to the shallow epithermal conditions.

Based on the studies of Voudouris et al. (2013a, b; 2018, 2019a), the Konos Hill and the Pagoni Rachi porphyry-epithermal prospects contain a variety of minerals that reflect the trace elements that are also enriched in pyrite that is observed here (e.g., Au, Bi, Se). Their presence adds a new perspective to the economic significance of these deposits. The current study complements recent studies by Voudouris et al. (2007, 2018a,b, 2019a), Melfos and Voudouris (2017) and Mavrogonatos et al. (2019) that identified potential mineralogical vectors useful in the exploration for precious and critical metals in porphyry/epithermal systems in Greece.

The LA-ICP-MS studies of pyrite here revealed that gold in pyrite is preferably into its structure rather than as nano-, or micro- inclusions. Furthermore, the high correlation between Au and Cu in pyrite from the M-type veins, and the high Se content of pyrite in the D-type veins of both studied prospects, should be further tested as an exploration tool in other porphyry-epithermal prospects in the nearby area, as an indication of Au-bearing ore. In terms of exploration and exploitation, this means that pyrite should be considered in the future as a potential target, owing to its trace element budget, because some of these elements could be recovered as by-products in addition to the main commodities (e.g., Hofstra and Cline, 2000; Reich et al., 2013; Deditius et al., 2014). The collection of more data regarding the trace element geochemistry of pyrite in other neighboring deposits/prospects in NE Greece, could further help on establishing the pyrite chemistry as a tool for exploration, in the very promising, but yet unexplored metallogenic province of Thrace.

Chapter 8

Concluding remarks

The Sapes-Kirki area hosts porphyry Cu+Mo±Au±Re style mineralization, high/intermediate sulfidation Au-Ag-Bi-Te epithermal systems, and polymetallic base metal veins. Mineralization is hosted within intermediate-to-acidic, high-K alkaline and calc-alkaline intrusive rocks, which have post-collisional geochemical signatures, as indicated by strong negative Eu, Nb and P and positive LILE (e.g. Sr, Ba) Pb, La, Th, U anomalies. Widespread hydrothermal alteration resulted to distinct alteration zones. The cores of the porphyry systems are associated with sodic (Sapes), potassic, potassic-calcic and sodic (Koryfes), potassic/calcic (Papadokoryphi) and sodic/potassic-calcic (Pagoni Rachi) alteration assemblages, that grade outwards into propylitic-altered rocks. A sericitic overprint is widespread, but in the higher topographic levels of the Konos Hill area advanced argillic assemblages are also present.

Albite/orthoclase, along with F-rich phlogopite are the main secondary silicates in the cores of the porphyry systems, and are accompanied by various amounts of epidote, actinolite, chlorite and calcite, thus forming, sodic-, potassic/calcic-, and sodic/potassic-calcic alteration asemblages.

Porphyry-style mineralization develops in the form of stockworks and disseminations. At the Konos Hill porphyry system, A-, and B-type banded quartz veins, accompany sodic alteration of the granodiorite porphyry. They are overprinted by D-type veins, mostly expressed as pyritic centerlines in the earlier quartz veins, and associate sericitic alteration, which almost completely overprints earlier alteration. At the Pagoni Rachi prospect, early magnetite veins and A-type banded quartz veins, are associated with sodic/potassic-calcic alteration. They are locally crosscut by B-type veins, associated with sodic/potassic alteration, and finally by massive pyrite veins (D-type), with pervasive sericitic alteration.

Porphyry-style mineralization at both prospects is locally crosscut by late, commonly N-S to NW-SE trending epithermal-style (E-type) veins. The veins are composed of quartz and calcite, are associated with argillic (quartz, sericite,

carbonates) alteration of the wall rocks, and comprise mineralization of pyrite, galena, sphalerite, Ag-Au alloy, tetrahedrite/tennantite.

Porphyry-style mineralization in the study area is characterized by enrichment in a series of precious and/or critical metals like Au, Re, Mo, Se, Te, while epithermal-style ores display an analogous enrichment but in different elements, e.g., Ag, Bi, Te, Sn, In, Se, and Ga. Especially for Re in the porphyry systems, its extreme enrichment is both due to the presence of Re-rich molybdenite (average Re content 0.48 wt%, and 0.84 wt% Re at Konos Hill and Pagoni Rachi, respectively) and rheniite.

Although the studied porphyry systems, and especially the Pagoni Rachi system, share some common characteristics with porphyry-Au systems elsewhere, they differ because precious and critical metals are enriched in sodic and sodic/potassic-calcic alteration zones rather than in potassic alteration zones, which are locally present but not dominant. Moreover, another strong similarity of the studied systems to the Au-porphyries, is the presence of banded quartz veins, and the dominant presence of pyrite over the Cu-sulfides (chalcopyrite/bornite) in the hypogene ores.

Gold in the Pagoni Rachi porphyry/epithermal system was introduced in consecutive episodes, as suggested by its presence in distinct ore-forming evets associated with sodic/potassic-calcic, sericitic, and argillic alteration. It is present with three distinct froms: as electrum (aver. 79 % at. Au), in the early M-, and A-type veins, as native gold (aver. 89 % at. Au) in the D-type veins, associated with the sericitic alteration, and finally as Ag-Au alloy (aver. 32 % at. Au) in E-type veins, associated with argillic alteration of the host granodiorite.

Telescoping of the studied porphyry systems is a common characteristic, but especially in the case of Konos Hill, the system records a very well exposed transition from a deep porphyry mineralization, to a shallow level high-sulfidation epithermal environment. The Konos Hill lithocap comprises vuggy silica zones, grading to quartz-alunite-APS-diaspore-kaolinite ± pyrophyllite and quartz-alunite-APS-zunyite-kaolinite ± pyrophyllite assemblages, while transitional zones are typified by the presence of sericite. A wide chemical variety of alunite group minerals was remarked, belonging to the alunite, beudantite and plumbogummite subgroups. The lithocap hosts mineralization enriched in chalcophile elements, like Bi, Mo, and Se, thus supporting

the hypothesis of the spatial and temporal connection between the lithocap and the underlying porphyry-style mineralization.

The chemistry of magnetite at the Pagoni Rachi prospect (magmatic versus hydrothermal varieties) is examined as a potential mineral-chemical vector towards ore-grade zones/mineralization. Beyond distinct textural features between the two types of magnetite, LA-ICP-MS analyses revealed different geochemical trends: Magmatic-type magnetite, from fresh to propylitic-altered granodiorite porphyry, is enriched in Ti, Cr, Ni and Sn, similar to magmatic magnetite from intrusions related to ore deposits elsewhere. On the other hand, hydrothermal magnetite, which forms disseminations and M-type veinlets associated with sodic/potassic-calcic alteration of the host rock, is enriched in high-field strength elements and metals. An enrichment of hydrothermal magnetite in Zn, Pb, W, Ta, and Mo is a distinctive feature of the Pagoni Rachi system, and can be further evaluated as an exploration tool towards ore-grade mineralization.

Furthermore, as pyrite is a dominant sulfide trhougout all the stages of mineralization in both Konos Hill and the Pagoni Rachi prospects, LA-ICP-MS analyses were used to evaluate its geochemical signature. At the Konos Hill prospect, D-type veins carry pyrite enriched in Se, Cu, Co and minor Zn, but depleted in other trace elements. Pyrite in late, epithermal-style (E-type) calcite-quartz veins, associated with argillic alteration at the same area, is enriched in As, Pb, Ni, Sb, Bi and minor Ag. In contrast, at the Pagoni Rachi prospect, pyrite in M-type veins associated with sodic/potassic-calcic alteration is enriched in Cu, Zn, Se and minor Cd, but depleted in other trace elements, as commonly described for early stages of porphyry-style mineralization elsewhere. The D-type veins host Au-rich pyrite that is also characterized by high concentrations of Cu (partly attributed to nano-inclusions), Co and Se. In the late E-type veins, pyrite is characterized by the abundance of Bi (also present as submicroscopic inclusions), Pb and Zn, with minor amounts of Se, and traces of Ga and Ge.

Gold, throughout the evolution of the mineralization at both prospects, remains in the form of a non-stoichiometric substituting element in the structure of pyrite (Au^{+1}) and not as nanoparticles (Au^{0}), as a function of its As content. A critical feature of porphyry-style pyrite from both prospects, is a strong enrichment in Se, probably

higher compared to other porphyry-style pyrite from elsewhere. This fact arises as an important exploration tool, since Se at both prospects correlates with the highest amoun of gold grades in the mineralization.

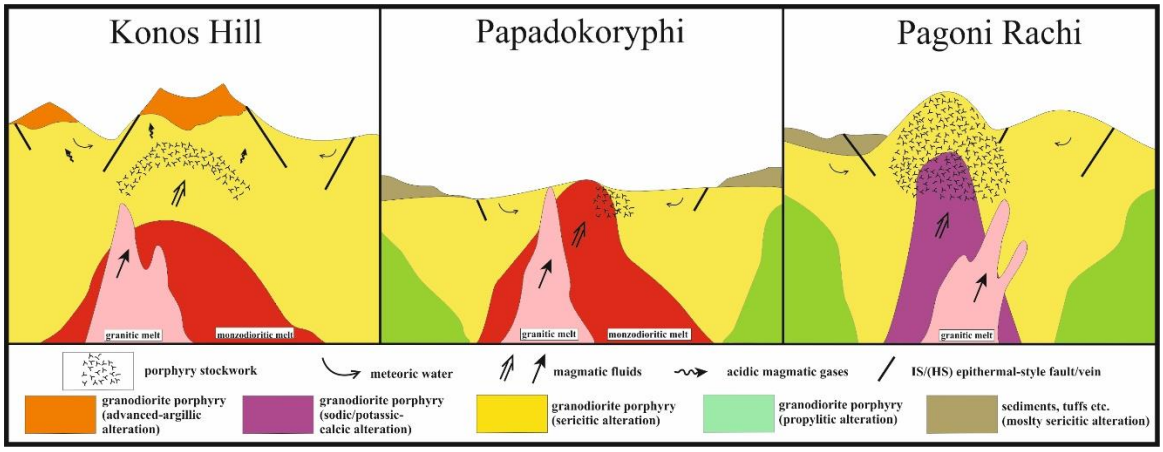

Figure 8.1: Conceptualized sketch depicting alteration and mineralization distribution in the (a) Konos Hill, (b) Papadokoryphi, and (c) Pagoni Rachi prospects. Dimentions not to scale.

The studied porphyry/epithermal prospects record a multi-stage evolution from the deep/magmatic-hydrothermal to the shallow/epithermal conditions. As evident by the presence of F-rich phases in different styles of hydrothermal alteration, there is a high possibility that, the late microgranite porphyry dykes which are widespread in the area, have (at least partly) contributed to the mineralization and alteration assemblages of the porphyry/epithermal prospects. F- enriched mineral phases like zunyite (from the advanced-argillic alteration at the Konos Hill prospect), or F-rich secondary biotite from both Sapes area (namely the Koryphes prospect close to Konos Hill) and the Pagoni Rachi, and the occurrence of fluorite as a gangue mineral in the porphyry-style veins, support this hypothesis.

In addition, enrichment of hydrothermal magnetite in elements like Sn and V, which are also enriched in various mineralization stages, are also compatible with a felsic magmatic source. This means that the porphyry/epithermal mineralization in the study area is probably the result of the accumulation of distinct magmatic hydrothermal pulses, related to the different intrusive phases that occur in the broad area. As graphically depicted in Figure 8.1, mineralization carries evidence for a

genetic link with both the granodiorite porphyry, which are also the host rocks of the mineralization, as well as the microgranite porphyries dykes.

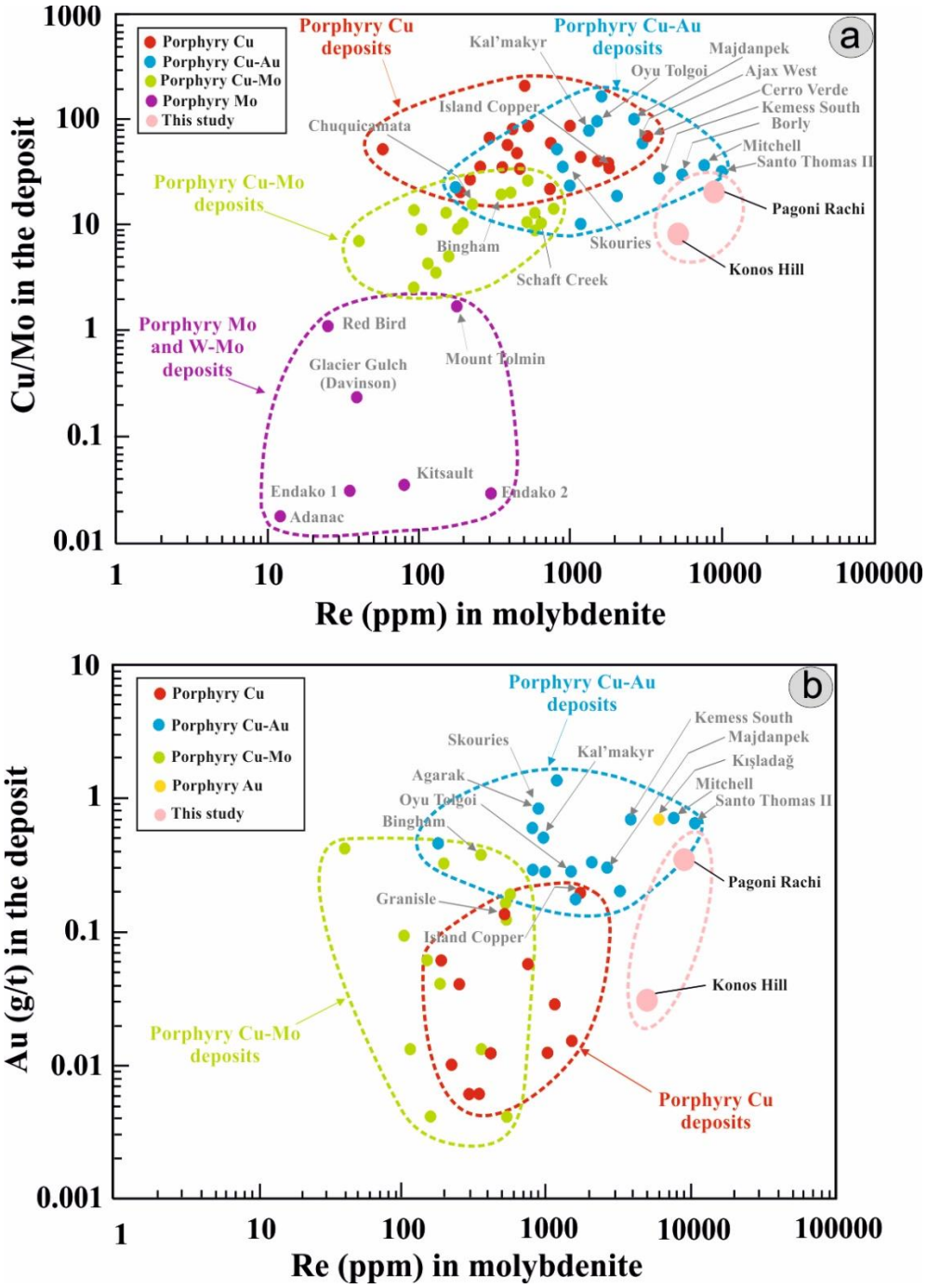

Figure 8.2: Comparison of the studied porphyry prospects with other porphyry deposits worldwide: (a) Re content of molybdenite versus Cu/Mo ratio in the deposit; (b) Re content of molybdenite versus gold grade of the deposit. An extreme enrichment of Re in the molybdenite from both Konos Hill and Pagoni Rachi prospects is obvious (modified after Voudouris et al., 2013b).

A secure classification of the studied porphyry systems, remains up to date problematic. The critical metal that mostly characterizes both the Konos Hill and Pagoni Rachi prospects is Re, for which geochemical analyses revealed extreme high values, compared to any other porphyry deposit from which Re is currently recovered (e.g., the Chuquicamata deposit; Wanheinan et al. 2015). Rhenium, Se and Te are generally not mined exclusively in ore deposits but are important by-products of porphyry Cu±Mo deposits. Such deposits will likely become the primary source of these metals in the near future (John and Taylor 2016).

Table 8.1: Comparison of the Konos Hill and Pagoni Rachi porphyry prospects to selected major porphyry systems worldwide (compilation of data from Cooke et al., 2005; Sun et al. 2015, Armstrong et al., 2011; Baker et al., 2016; John et al., 2017)

Deposit/prospect	Type	Location	Re (g/t)	Au (g/t)	Cu (%)	Mo (%)
Bingham	Cu-Mo-Au	USA	0.22	0.50	0.88	0.02
Oyu Tolgoi	Cu-Au	Mongolia	-	0.32	0.83	-
Rosario	Cu-Mo	Chile	-	0.01	0.82	0.02
Cerro Colorado	Cu	Panama	-	0.11	0.45	-
Lepanto Far Southeast	Cu-Au	Philippines	-	1.42	0.80	-
Snowfield	Au	Canada	0.48	0.82	0.09	0.008
El Teniente	Cu-Mo	Chile	0.13	0.04	0.92	0.02
Grasberg	Cu-Au	Indonesia	-	1.07	1.12	-
Kışladağ	Au	Turkey	-	0.73	-	-
Chuquicamata	Cu-Mo	Chile	0.18	0.013	0.59	0.04
Butte	Cu-Mo	USA	0.11	0.04	0.67	0.03
Henderson	Mo	USA	-	-	-	0.17
Pagoni Rachi	**Au-Re (?)**	**Greece**	**0.34**	**0.36**	**0.01**	**0.002**
Konos Hill	**(?)**	**Greece**	**0.03**	**0.03**	**0.03**	**0.001**

Based solely on surficial data (on the absence of any drilling projects for porphyry-style mineralization in the area), both porphyry systems, are characterized by extremely low Cu contents, thus excluding any potential relation to the class of porphyry-Cu deposits (Table 8.1).

The Pagoni Rachi prospect has an average Au content of 0.36 g/t and is characterized by a very low Cu/Au ratio, which is close to 0.11, and can be stated that it resembles the class of porphyry-Au deposits, like the Kışladağ porphyry Au in Turkey (which, however, is characterized by an extremely low Cu/Au ratio, ≈0.03; Baker et al.,

2016). Furthermore, the extreme enrichment of the Pagoni Rachi prospect in Re (which has an average value of 0.34ppm in the prospect), seems to be a unique feature, uncommon to other porphyry deposits elsewhere. In Figure 8.2, it is clear that the Pagoni Rachi prospect coincides with the lowest limit of the porphyry Cu-Au deposits, in both terms of the Cu/Mo ratio (Figure 8.2a) and the Au content (Figure 8.2b) of the prospect. However, its Re content is higher compared to vast majority of other kinds of porphyry deposits (cf. Sincler et al., 2016). This means that the broad area shoulb be explored for other possible Re-enriched mineralization.

The presence of up to 20 ppb Pd in samples from Pagoni Rachi area (Voudouris et al. 2013b; this study) is an indication that the Pagoni Rachi prospect may hosts minor amounts of PGE, which are known to be occasionally enriched in porphyry-style mineralization hosted in alkaline rocks (e.g. Skouries deposit; Eliopoulos and Economou-Eliopoulos 1991; Kroll et al. 2002; McFall et al., 2016).

For the case of the Konos Hill prospect, average grades of Au, Mo, and Cu do not allow any specific characterization to the prospect. Especially for the Au, there is a high possibility that it has been leached and redistributed in nearby epithermal-style prospects (e.g. Viper), at the stage of subsequent overprinting by widespread sericitic and advanced-argillic alteration.

Further work on the porphyry/epithermal mineralization is required in the study area, in order to fully understand its metallogenetic context. Detailed field investigation will probably result to further new discoveries in NE Greece. Furthermore, thorough investigation of fluid and melt inclusions in ore-bearing veins, coupled with trace elements geochemistry studies on both ore and alteration minerals from other deposits and prospects in the area, will help to define the conditions of ore formation and to better undesratnd why there is such a prominent enrichment of precious and critical metals in mineralization at NE Greece, which, especially for Re, is considered to be among the most promising districts worldwide.

References

Abraitis, P.K.; Pattrick, R.A.D.; Vaughan, D.J. Variations in the compositional, textural and electrical properties of natural pyrite: a review. International Journal of Mineral Processing 2004, Volume 74, pages 41–59.

Alford, L.; Gysi, A.P.; Hurtig, N.C.; Monecke, T.; Pfaff K. Porphyry-related polymetallic Au-Ag vein deposit in the Central City district, Colorado: Mineral paragenesis and pyrite trace element chemistry. Ore Geology Reviews 2020, Volume 119, page 103295.

Anders, B.; Reischmann, T.; Kostopoulos, D. The oldest rocks of Greece: first evidence for a Precambrian terrane within Pelagonian Zone. Geological Magazine 2006, Volume 143, pages 41-58.

Arancibia, O.N.; Clark, A.H. Early magnetite–amphibole–plagioclase alteration-mineralization in the Island Copper porphyry copper–gold–molybdenum deposit, British Columbia. Economic Geology 1996, Volume 91, pages 402–438.

Arikas, K.; Voudouris, P. Hydrothermal alterations and mineralizations of magmatic rocks in the southern Rhodope Massif. Acta Volcanologica 1998, Volume 10, pages 353–365.

Arikas, K. The porphyry Mo occurrence at Panoni Rachi (NE Kirki) and the mineralogy of hydrothermally altered subvolcanic rocks at Kirki–Esymi area. Bullin of the Geological Society of Greece 1991, Volume 25, pages 259-274 (in Greek).

Armstrong, T.; Brown, F.; Puritch, E. Technical report and updated resource estimate on the Snowfield property, Skeena Mining Division, British Columbia, Canada. Report prepared for Pretium Resources Inc., 2011. 90p.

Audétat, A., Pettke, T., Heinrich, C.A., and Bodnar, R.J., 2008, The composition of magmatic-hydrothermal fluids in barren and mineralized intrusions. Economic Geology, Volume 103, pages 877−908.

Averill, S.A. The application of heavy indicator mineralogy in mineral exploration with emphasis on base metal indicators in glaciated metamorphic and plutonic terrains. In: McClenaghan, M.B.; Bobrowsky, P.T.; Hall, G.E.M.; Cook, S.J. (Eds.), Drift Exploration in Glaciated Terrane. Geological Society of London Special Publications 2001, Volume 185, pages 69–81. http://dx.doi.org/10.1144/GSL.SP.2001.185.01.04.

Baker, T.; Bickford, D.; Juras, S.; Lewis, P.; Oztas, Y.; Ross, K.; Tukac, A.; Rabayrol, F.; Miskovic, A.; Friedman, R., Creaser R.A.; Spikings, R. The geology of the Kişladağ porphyry gold deposit, Turkey. Sociey of Economic Geologists Spec. Publ. 2016, Volume 19, pages 57-83.

Barnes, S.J.; Roeder, P.L. The range of spinel compositions in terrestrial mafic and ultramafic rocks: Journal of Petrology 2001, Volume 42, pages 2279–2302.

Bauer, C.; Rubatto, D.; Krenn, K.; Proyer, A.; Hoinkes, G. A zircon study from the Rhodope metamorphic complex, N-Greece: Time record of a multistage evolution. Lithos 2007, Volume 99(3-4), pages 207–228, doi:10.1016/j.lithos.2007.05.003.

Bayliss, P.; Kolitsch, U.; Nickel, E.H.; Pring, A. Alunite supergroup: Recommended nomenclature. Mineralogical Magazin 2010, Volume 74, pages 919–927.

Bazarkina, E.F.; Pokrovski, G.S.; Zotov, A.V.; Hazemann, J.-L. Structure and stability of cadmium chloride complexes in hydrothermal fluids. Chemical Geology 2010, Volume 276, pages 1–17.

Beane, R.E.; Titley, S.R. Porphyry copper deposits. Part II. Hydrothermal alteration and mineralization: Economic Geology 1981, 75TH anniversary Volume, pages 235−269.

Bissig, T.; Cooke, D. Introduction to the Special Issue Devoted to Alkalic Porphyry Cu-Au and Epithermal Au Deposits. Economic Geology 2014, Volume 109(3), pages 819–825.

Bissig, T.; Monecke, T.; Holley, E.A.; Leroux, G.; Voudouris, P.; Miškovic, A. Geochemical and quartz mineralogical vectors to epithermal ore in lithocaps in the TV Tower district, Biga peninsula, Turkey and Kassiteres-Sapes district, Greece. In Proceedings of the SEG-MJD Conference, Cesme, Turkey, 25–28 September 2016.

Blanchard, M.; Alfredsson, M.; Brodholt, J.; Wright, K.; Catlow, C.R.A. Arsenic incorporation into FeS2 pyrite and its influence on dissolution: A DFT study. Geochimica et Cosmochimica Acta 2007, Volume 71(3), pages 624–630.

Bonev, N.; Burg, J.P.; Ivanov, Z. Mesozoic–Tertiary structural evolution of an extensional gneiss dome-the Kesebir–Kardamos dome, eastern Rhodope (Bulgaria–Greece). Internatonal Journal of Earth Sciences, 2006, Volume 95(2), pages 318-340, doi:10.1007/s00531-005-0025-y.

Bonev, N.; Dilek, Y.; Hanchar, J.M.; Bogdanov, K.; Klain, L. Nd–Sr–Pb isotopic composition and mantle sources of Triassic rift units in the Serbo-Macedonian and the western Rhodope massifs (Bulgaria–Greece). Geological Magazine 2012, Volume 149, pages 146-152.

Bonev, N.; Marchev, P.; Moritz, R.; Collings, D. Jurassic subduction zone tectonics of the Rhodope Massif in the Thrace region (NE Greece) as revealed by new U–Pb and 40Ar/39Ar geochronology of the Evros ophiolite and high-grade basement rocks. Gondwana Research 2015, Volume 27, pages 760–775.

Bridges, P.S.; Gordon, M.J.; Michael, C.; Ampatzioglou, M. Gold mineralization at Sappes, northern Greece. In Europe's Major Gold Deposits; Harvey, S., Ed.; Irish Association for Economic Geology, Dublin, Ireland: 1997; pp. 95–107.

Brun, J.P.; Faccenna, C. Exhumation of high-pressure rocks driven by slab rollback. Earth and Planetary Science Letters 2008, Volume 272, pages 1–7, doi:10.1016/j.epsl.2008.02.038.

Brun, J.P. Sokoutis, D. Kinematics of the southern Rhodope core complex (North Greece). Interntional Journal of Earth Sciences 20007, Volume 96/6, pages 1079-1099.

Brun, J.P.; Sokoutis, D. Core complex segmentation in North Aegean, a dynamic view. Tectonics 2018, Volume 37, pages 1797–1830.

Burg, J.P.; Ricou, L.E.; Ivano, Z.; Godfriaux, I.; Dimov, D.; Klain, L. Syn-metamorphic nappe complex in the Rhodope Massif. Structure and kinematics. Terra Nova 1996, Volume 8(1), pages 6–15, doi:10.1111/j.1365-3121.1996.tb00720.x.

Burg, J.-P., 2012. Rhodope: from Mesozoic convergence to Cenozoic extension. Review of petro-structural data in the geochronological frame. Journal of the Virtual Explorer Volume 42, 44, paper 1.

Canil, D.; Grondahl, C.; Lacourse, T.; Pisiak, L.K. Trace elements in magnetite from porphyry Cu-Mo-Au deposits in British Columbia, Canada. Ore Geology Reviews 2016, Volume 72, pages 1116–1128.

Cannell, J.; Cooke, D.R.; Walshe, J.L.; Stein, H. Geology, mineralization, alteration, and structural evolution of the El Teniente porphyry Cu-Mo deposit: ECONOMIC GEOLOGY 2005, Volume 100, pages 979−1003.

Carew, M.J. Controls on Cu–Au Mineralisation and Fe-oxide metasomatism in the Eastern Fold Belt, NW Queensland, Australia. PhD thesis, James Cook University, Townsville, Australia, 2004.

Celis, M.A.; Bouzari, F.; Bissig, T.; Hart, C.J.R.; Ferbey, T. Petrographic characteristics of porphyry indicator minerals from alkalic porphyry copper-gold deposits in south-central British Columbia (NTS 092, 093): Geoscience BC, Summary of Activities 2013, Report 2014-1, pages 53–62.

Chang, Z.; Hedenquist, J.W.; White, N.C.; Cooke, D.R.; Roach, M.; Deyell, C.; Garcia, J., Jr.; Gemmell, J.B.; Mcknight, S.; Cuisone, A.L. Exploration Tools for Linked Porphyry and Epithermal Deposits: Example from the Mankayan Intrusion-Centered Cu-Au District, Luzon, Philippines. Economic Geology. 2011, Volume 106, pages 1365–1398.

Chen, J.; Xu, J.; Wang, B.; Yang, Z.; Ren, J.; Yu, H.; Liu, H.; Feng, Y. Geochemical differences between subduction-and collision-related copper-bearing porphyries and implications for metallogenesis. Ore Geology Reviews 2015, Volume 70, pages 424–437.

Chen W, Ying Y.C., Bai T., Zhang J.J., Jiang S.Y., Zhao K.D., Shin D., Kynicky, J. In situ major and trace element analysis of magnetite from carbonatite-related complexes: Implications for petrogenesis and ore genesis. Ore Geology Reviews 2019, Volume 107, pages 30-40, https://doi.org/10.1016/j.oregeorev.2019.01.029.

Christofides, G.; Pecksay, Z.; Eleftheriadis, G.; Soldatos, T.; Koroneos, A. The Tertiary Evros volcanic rocks (Thrace, Northeastern Greece): Petrology and K/Ar geochronology. Geologica Carpathica 2004, Volume 55(5), pages 397-409.

Cioacă, M.E.; Munteanu, M.; Qi, L.; Costin, G. Trace element concentrations in porphyry copper deposits from Metaliferi Mountains, Romania: A reconnaissance study. Ore Geology Reviews 2014, Volume 63, pages 22–39. doi:10.1016/j.oregeorev.2014.04.01

Ciobanu, C.L.; Cook, N.J. Skarn textures and a case study: The Ocna de Fier-Dognecea orefield, Banat, Romania: Ore Geology Reviews 2004, Volume 24, pages 315–370.

Ciobanu, C.L.; Cook, N.J.; Pring, A.; Brugger, J.; Danyushevsky, L.V.; Shimizu, M. 'Invisible gold' in bismuth chalcogenides. Geochimica et Cosmochica. Acta 2009, Volume 73, pages 1970–1999.

Cloos, M. Bubbling magma chambers, cupolas, and porphyry copper deposits International Geology Review 2001, Volume 43(4), pages 285–311. https://doi.org/10.1080/00206810109465015.

Cook, N.J.; Chryssoulis, S.L. Concentrations of invisible gold in the common sulfides. The Canadian Mineralogist. 1990, Volume 28, pages 1–16.

Cooke, D.R.; Hollings, P.; Walshe, J.L. Giant porphyry deposits: Characteristics, distribution, and tectonic controls. Economic Geology 2005, Volume 100(5), pages 801–818.

Cook, N.J.; Ciobanu, C.L.; Mao, J.W. Textural control on gold distribution in As-free pyrite from the Dongping, Huangtuliang, and Hougou gold deposits, North China craton (Hebei Province, China): Chemical Geology 2009a, Volume 264, pages 101–121.

Cook, N.J.; Ciobanu, C.L.; Spry P.G.; Voudouris P. Understanding gold-(silver)-telluride-(selenide) mineral deposits. Episodes 2009b, Volume 32, pages 249–263.

Cook, N.J.; Ciobanu, C.L.; Pring, A.; Skinner, W.; Shimizu, M.; Danyushevsky, L.; Saini-Eidukat, B.; Melcher, F. Trace and minor elements in sphalerite: A LA-ICPMS study. Geochimica et Cosmochimica Acta 2009c, Volume 73, pages 4761–4791.

Core, D.P.; Kesler, S.E.; Essene, E.J. Unusually Cu-rich magmas associated with giant porphyry copper deposits: Evidence from Bingham, Utah. Geology, 2006, Volume 34(1), pages 41–44.

Cox, K.G.; Bell, J.D.; Pankhurst, R.J. The Interpretation of Igneous Rocks. George, Allen and Unwin, London, 1979, 450pp.

Dare, S.A.S.; Barnes, S.-J., Beaudoin, G., 2012. Variation in trace element content of magnetite crystallized from a fractionating sulfide liquid, Sudbury, Canada: implications for provenance discrimination. Geochimica et Cosmochimica Acta 2012, Volume 88, pages 27–50.

Dare, S.A.S.; Barnes, S.-J.; Beaudoin, G.; Méric, J.; Boutroy, E.; Potvin-Doucet, C. Trace elements in magnetite as petrogenetic indicators: Mineralium Deposita 2014, Volume 49, pages 785–796.

Deditius, A.P.; Utsunomiya, S.; Renock, D.; Ewing, R.C.; Ramana, C.V.; Becker, U.; Kesler, S.E. A proposed new type of arsenian pyrite: Composition, nanostructure and geological significance. Geochimica et Cosmochimica Acta 2008, Volume 72, pages 2919–2933.

Deditius, A.P.; Utsunomiya, S.; Ewing, R.C.; Chryssoulis, S.L.; Venter, D.; Kesler, S.E. Decoupled geochemical behaviour of As and Cu in hydrothermal systems. Geology 2009, Volume 37, pages 707–710.

Deditius, A.P., Utsunomiya, S., Reich, M., Kesler, S.E., Ewing, R.C., Hough, R., Walshe, J. Trace metal nanoparticles in pyrite. Ore Geology Reviews 2011, Volume 42, pages 32–46.

Deditius, A.P.; Reich, M.; Kesler, S.E.; Utsunomiya, S.; Chryssoulis, S.L.; Walshe, J.; Ewing, R.C. The coupled geochemistry of Au and As in pyrite from hydrothermal ore deposits. Geochhimica et Cosmochimica Acta 2014, Volume 140, pages 644–670.

Deditius, A.P.; Reich, M.; Simon, A.C.; Suvorova, A.; Knipping, I.; Roberts, M.P.; Rubanov, S.; ·Dodd, A.; Saunders, M. Nanogeochemistry of hydrothermal magnetite. Contr. Mineralogy and Petrology 2018, Volume 173, 46, https://doi.org/10.1007/s00410-018-1474-1.

Deer, W.A.; Howie, R.A.; Zussman, J. An introduction to the rock-forming minerals.LongmanGroup Limited, 1992, 696 p.

Delibaş, O.; Moritz, R.; Ulianov, A.; Chiaradia, M.; Saraç, C.; Revan, K.M.; Göç, D. Cretaceous Subduction-Related Magmatism and Associated Porphyry-Type Cu-Mo Prospects in the Eastern Pontides, Turkey: New Constraints from Geochronology and Geochemistry. Lithos 2016, Volume 248 pages 121-137, doi: 10.1016/j.lithos.2016.01.020

Del Moro, A.; Innocenti, F.; Kyriakopoulos, C.; Manetti, P.; Papadopoulos, P. Tertiary granitoids from Thrace (Northern Greece): Sr isotopic and petrochemical data. Neues Jahrbuch für Mineralogie 1988, Volume 159, pages 113–135.

Dill, H.G. The geology of aluminium phosphates and sulfates of the alunite group minerals: A review. Earth Science Reviews 2001, Volume 53, pages 35–93.

Dilles, J.H.; Solomon, G.C.; Taylor, H.P.Jr.; Einaudi, M.T. Oxygen and hydrogen isotope characteristics of hydrothermal alteration at the Ann-Mason porphyry copper deposit, Yerington, Nevada: Economic Geology 1992, Volume 87, pages 44−63.

Dilles, J.H.; Einaudi, M.T. Wall-rock alteration and hydrothermal flow paths about the Ann-Mason porphyry copper deposit, Nevada - a 6-km vertical reconstruction. Economic Geology 1992, Volume 87, pages 1963−2001.

Dilles, J.H.; Farmer, G.L.; Field, C.W. Sodium-calcium alteration by non-magmatic saline fluids in porphyry copper deposits: Results from Yerington, Nevada: Mineralogical Association of Canada Short Course Series, 1995, Volume 23, pages 309−338.

Dimou, E. A correlative mineralogical study of Achla Tarla and St. Philippos mineralization, Kirki area (NE Greece). Bulletin of the Geological Society of Greece 1993, Volume 28, pages 37–54 (in Greek).

Ding, K.; Seyfried, W.E. Determination of Fe–Cl complexing in the low pressure supercritical region (NaCl fluid): iron solubility constraints on pH of subseafloor hydrothermal fluids. Geochimica et Cosmochimica Acta 1992, Volume 56, pages 3681–3692.

Dinter, D.A.; Macfarlane, A.; Hames, W.; Isachsen, C.; Bowring, S.; Royden, L. 1995. U-Pb and $^{40}Ar/^{39}Ar$ geochronology of the Symvolon granodiorite: implications for the thermal and structural evolution of the Rhodope metamorphic core complex, northeastern Greece. Tectonics 1995, Volume 14, pages 886–908.

Dinter, D.A. Late Cenozoic extension of the Alpine collisional orogen, northeastern Greece: Origin of the north Aegean basin. Geological Society of America Bulletin 1998, Volume 110(9), pages 1208–1230.

Dreyer, B.M.; Morris, J.D.; Gill, J.B. Incorporation of subducted slab-derived sediment and fluid in arc magmas: B–Be–10Be–εNd systematics of the Kurile convergent margin, Russia. Journal of Petrology 2010, Volume 51(8), pages 1761–1782.

Dupuis, C.; Beaudoin, G. Discriminant diagrams for iron oxide trace element fingerprinting of mineral deposit types. Miner. Deposita 2011, 46, 319–335.

Einaudi, M.T.; Meinert, L.D.; Newberry, R.J. Skarn deposits: Economic Geology 1981, 75th Anniv. Volume, pages 317–391.

Eliopoulos, D.G.; Economou-Eliopoulos, M. Platinum-Group Element and Gold Contents in the Skouries Porphyry Copper Deposit, Chalkidiki Peninsula, Northern Greece. Economic Geology 1991, Volume 86 pages 740-749.

Emsbo, P.; Hofstra, A.H.; Lauha, E.A.; Griffin, G.L.; Hutchinson, R.W.; John, D.A.; Theodore, T.G. Origin of high- grade gold ore, source of ore fluid components, and genesis of the Meikle and neighboring Carlin-type deposits, northern Carlin Trend, Nevada. Economic Geology 2003, Volume 98, pages 1069–1105.

Ersoy, E.Y.; Palmer, M.R. Eocene-Quaternary magmatic activity in the Aegean: Implications for mantle metasomatism and magma genesis in an evolving orogeny. Lithos 2013, Volume 180–181, pages 5–24.

Eyal, M.; Litvinovsky, B.; Jahn, B.M.; Zanvilevich, A.; Katzir, Y. Origin and evolution of post-collisional magmatism: Coeval Neoproterozoic calc-alkaline and alkaline suites of the Sinai Peninsula. Chemical Geology 2010, Volume 269 pages 153-179.

Farmer, G.L.; Depaolo, D.J. Origin of Mesozoic and Tertiary granite in the western United States and implications for Pre-Mesozoic crustal structure: 2. Nd and Sr isotopic studies of unmineralized and Cu-and Mo-mineralized granite in the Precambrian Craton. Journal of Geophysical Research. Solid Earth 1984, Volume 89(B12), pages 10141–10160.

Floyd, P.A.; Winchester, J.A. (1978) Identification and discrimination of altered and metamorphosed volcanic rocks using immobile elements. Chemical Geology 1978, Volume 21, pages 291–306.

Fornadel, A.P.; Voudouris, P.; Spry, P.G.; Melfos, V. Mineralogical, stable isotope and fluid inclusion studies of spatially related porphyry Cu-Mo and epithermal Au-Te mineralization, Fakos Peninsula, Limnos Island, Greece. Mineralogy and Perology 2012, Volume 105, pages 85–111.

Foustoukos, D.I.; Seyfried, W.E. Fluid Phase Separation Processes in Submarine Hydrothermal Systems. In: Liebscher, A.; Christoph, C.A. (Eds.). Fluid–Fluid Interactions, Reviews in Mineralogy and Geochemistry. Mineralogical Society of America, 2007, Volume 65, pages 213–233.

Fouquet, Y.; Henry, K.; Knott, R.; Cambon, P. Geochemical Section of the TAG Hydrothermal Mound. In: Proceedings of the Ocean Drilling Program, Scientific

Results, 1998; Herzig, P.M., Humphris, S.E., Miller, D.J., Zierenberg, R.A. (Eds.); 158, pages 363–387.

Franchini M.; McFarlane, C.; Maydagán L.; Reich, M.; Lentz, D.R.; Meinert, L.; Bouhier, V. Trace metals in pyrite and marcasite from the Agua Rica porphyry-high sulfidation epithermal deposit, Catamarca, Argentina: Textural features and metal zoning at the porphyry to epithermal transition. Ore Geology Reviews 2015, Volume 66, pages 366–387.

Frenzel, M.; Hirsch, T.; Gutzmer, J. Gallium, germanium, indium and other minor and trace elements in sphalerite as a function of deposit type – A meta-analysis. Ore Geology Reviews. 2016, Volume 76, pages 52-78.

Frost, B.R.; Lindsley, D.H. Equilibria among Fe-Ti oxides, pyroxenes, olivine, and quartz: Part II. Application. American Mineralogist 1992, Volume 77, pages 1004–1020.

Galanopoulos, E.; Voudouris, P.; Mavrogonatos, C.; Spry, P.G.; Hart, C.; Melfos, V.; Zaccarini, F.; Alfieris, D.A. New porphyry Mo mineralization at Aisymi-Leptokarya, South-Eastern Rhodope, North-East Greece: geological and mineralogical constraints. Geosciences 2018, Volume 8, 435.

Giggenbach, W.F. Magma degassing and mineral deposition in hydrothermal systems along convergent plate boundaries: Economic Geology 1992, Volume 87, pages 1927-1944.

Gilg, H.A.; Frei, R. Chronology of magmatism and mineralization in the Kassandra mining area, Greece: The potentials and limitations of dating hydrothermal illites. Geochimica Cosmochimica Acta 1994, Volue 58, pages 2107–2122.

Goldfarb, R.J.; Baker, T.; Dubé, B.; Groves, D.I.; Hart, C.J.R.; Gosselin, P. Distribution, character and genesis of gold deposits in metamorphic terranes. Economic Geology 2005, Volume 100, pages 407–450.

Gregory, M.J.; Lang, J.R.; Gilbert, S.; Hoal, K.O. Geometallurgy of the pebble porphyry copper–gold–molybdenum deposit, Alaska: implications for gold distribution and paragenesis. Economic Geology 2013, Volume 108, pages 463–482.

Griffin, W.L.; Powell, W.J.; Pearson, N.J.; O'Reilly, S.Y. GLITTER: data reduction software for laser ablation ICP-MS, in Sylvester, P.; ed., Laser Ablation ICP-MS in the Earth Sciences: Current Practices and Outstanding Issues, Mineralogical Association of Canada. Short Course Series 40, 2008, 308-311.

Gustafson, L.B.; Hunt, J.P. The porphyry copper deposit at El Salvador, Chile. Economic Geology 1975, Volume 70, pages 857–912.

Gustafson, L.B.; Quiroga, J. 1995, Patterns of mineralization and alteration below the porphyry copper orebody at El Salvador, Chile. Economic Geology 1995, Volume 90, pages 2−16.

Halley, S.; Dilles, J.H.; Tosdal, R. Footprints: The Hydrothermal Alteration and Geochemical Dispersion around Porphyry Copper Deposits; SEG News Letter No. 100; Society of Economic Geologists (SEG): Littleton, Colorado, United States of America, 2015.

Hashmi, S.; Ward, B.C.; Plouffe, A.; Leybourne, M.I.; Ferbey, T. Geochemical and mineralogical dispersal in till from the Mount Polley Cu-Au porphyry deposit, central British Columbia, Canada. Geochemistry: Exploration, Environment, Analysis 2015, Volume 15, pages 234–249.

Hattori, K.H.; Keith, J.D. Contribution of mafic melt to porphyry copper mineralization: Evidence from Mount Pinatubo, Philippines, and Bingham Canyon, Utah, USA. Mineralium Deposita 2001, Volume 36(8), pages .799–806.

Hedenquist, J.W.; Lowenstern, J.B. The role of magmas in the formation of hydrothermal ore deposits. Nature 1994, Volume 370, pages 519–527.

Hedenquist, J.W.; Arribas, A.; Reynolds, T.J. Evolution of an intrusion-centered hydrothermal system: Far Southeast-Lepanto porphyry and epithermal Cu–Au deposis, Philippines. Economic Geology 1998, Volume 93, pages 373–404.

Hedenquist, J.W.; Taran, Y.A. Modeling the formation of advanced argillic lithocaps: Volcanic vapor condensation above porphyry intrusions. Economic Geology 2013, Volume 108, pages 1523–1540.

Heinrich, C.A.; Driesner, T.; Stefansson, A.; Seward, T.M. Magmatic vapor contraction and the transport of gold from porphyry to epithermal ore deposits. Geology 2004, Volume 32, pages 761–764, doi:10.1130/G20629.1

Heinrich, C. The physical and chemical evolution of low-salinity magmatic fluids at the porphyry to epithermal transition: A thermodynamic study. Mineralium Deposita 2005, Volume 39, pages 864–889, doi:10.1007/s00126-004-0461-9.

Hey, M.H. A new review of the chlorites. Mineralogical Magazine 1954, Volume 30, pages 277-292.

Hikov, A.; Lerouge, C.; Velinova, N. Geochemistry of alunite group minerals in advanced argillic altered rocks from the Asarel porphyry copper deposit, Central Srednogorie. Review of the. Bulgaian Geological Society 2010, Volume 71, pages 133–148.

Himmerkus, F.; Reischmann, T.; Kostopoulos, D. Late Proterozoic and Silurian basement units within the Serbo-Macedonian Massif, northern Greece: the significance of terrane accretion in the Hellenides. Geological Society of London, Special Publication 2006, Volume 260, pages 35-50.

Himmerkus, F.; Reischmann, T.; Kostopoulos, D.K. Serbo-Macedonian revisited: a Silurian basement terrane from the northern Gondwana in the Internal Hellenides, Greece. Tectonophysics 2009, Volume 473, pages 20-35.

Hofstra, A.H.; Cline, J.S. Characteristics and models for Carlin-type gold deposits. Rev. Economic Geology 2000, Volume 13, pages 163–220.

Holley, E.A.; Monecke, T.; Bissig, T.; Reynolds, T.J. Evolution of High-Level Magmatic-Hydrothermal Systems: New Insights from Ore Paragenesis of the Veladero High-Sulfidation Epithermal Au-Ag Deposit, El Indio-Pascua Belt, Argentina. Economic Geology 2017, Volume 112, pages 1747–1771, doi:10.5382/econgeo.2017.4528.

Holliday, J.R.; Cooke, D.R. Advances in geological models and exploration methods for copper ± gold porphyry deposits. In: Milkereit, B. (ed.), Proceedings of Exploration 07: Fifth Decennial International Conference on Mineral Exploration, 2007, Toronto,

Hough, R.M.; Noble, R.R.P.; Hitchen, G.J.; Hart, R.; Reddy, S.M.; Saunders, M.; Clode, P.; Vaughan, D.; Lowe, J.; Anand, R.R.; Butt, C.R.M.; Verrall, M. Naturally occurring gold nanoparticles and nanoplates. Geology 2008, Volume 36, pages 571–574.

Huang, X.W.; Sappin, A.A.; Boutroy, E.; Beaudoin, G.; Makvandi S. Trace Element Composition of Igneous and Hydrothermal Magnetite from Porphyry Deposits: Relationship to Deposit Subtypes and Magmatic Affinity. Economic Geology 2019, Volume 114/5, pages 917–952.

Huston, D.L.; Sie, S.H.; Suter, G.F.; Cooke, D.R.; Both, R.A. Trace elements in sulfide minerals from Eastern Australian volcanic-hosted massive sulfide deposits: Part I. Proton microprobe analyses of pyrite, chalcopyrite and sphalerite, and part II. Selenium levels in pyrite: Comparison with $d^{34}S$ values and implications for the source of sulfur in volcanogenic hydrothermal systems. Economic Geology 1995, Volume 90, pages 1167–1196.

Irvine, T.N.; Baragar, W.R.A. A guide to the chemical classification of the common rocks. Canadian Journal of Earth Sciences 1971, Volume 8, pages 523–548.

Ishihara, S. The granitoid series and mineralization. Economic Geology 1981, 75th annivers. Volume, pages 458−484.

Jambor, J.L. Nomenclature of the alunite supergroup. Can. Mineral. 1999, 37, 1323–1341.

Jenner, F.E.; O'Neill, H.S.C.; Arculus, R.J.; Mavrogenes, J.A. The magnetite crisis in the evolution of arc-related magmas and the initial concentration of Au, Ag and Cu. Journal of Petrology 2010, Volume 51(12), pages 2445–2464.

Jochum, K.P.; Weis, U.; Stoll, B.; Kuzmin, D.; Yang, Q.; Raczek, I.; Jacob, D.E.; Stracke, A.; Birbaum, K.; Frick, D.A.; Günther, D.; Enzweiler, J. Determinationof reference values for NIST SRM 610–617 glasses following ISO guidelines. Geostandards and Geoanalytical Research 2011, Volume 35, pages 397–429.

John, D.A.; Taylor, R.D. By-products of porphyry Copper and Molybdenum systems. Reviews in Economic Geology 2016, Volume 18, pages 137-164.

John, D.A.; Seal, R.R.,II; Polyak, D.E. Rhenium, chap. P of Schulz, K.J.; DeYoung, J.H.Jr.; Seal, R.R., II; Bradley, D.C. (eds.). Critical mineral resources of the United States—Economic and environmental geology and prospects for future supply: U.S. Geological Survey Professional Paper 1802, 2017, p. P1–P49, https:/doi.org/10.3133/pp1802P.

Jolivet, L.; Brunn, J.P. Cenozoic geodynamic evolution of the Aegean Region. International Journal of Earth Sciences 2010, Volume 99, pages 109–138.

Jolivet, L.; Faccenna, C.; Huet, B.; Labrousse, L.; Le Pourhiet, L.; Lacombe, O.; Lecomte, E.; Burov, E.; Denèle, Y.; Brun, J.-P.; Philippon, M.; Paul, A.; Salaün, G.; Karabulut, H., Piromallo, C.; Monié, P.; Gueydan, F.; Okay, A.I.; Oberhänsli, R.; Pourteau, A.; Augier,

R.; Gadenne, L.; Driussi, O. Aegean tectonics: strain localization, slab tearing and trench retreat. Tectonophysics 2013, Volume 597, pages 1–33.

Kaiser-Rohrmeier, M., von Quadt, A., Driesner, T., Heinrich, C.A., Handler, R., Ovtcharova, M., Ivanov, Z., Petrov, P., Sarov, S., Peytcheva, I., 2013. Post-orogenic extension and hydrothermal ore formation: high precision geochronology of the Central Rhodopian metamorphic core complex (Bulgaria-Greece). Economic Geology 2013, Volume 108, pages 691-718.

Keith, M.; Haase, K.M.; Klemd, R.; Krumm, S.; Strauss, S. Systematic variations of trace element and sulfur isotope compositions in pyrite with stratigraphic depth in the Skouriotissa volcanic-hosted massive sulfide deposit, Troodos ophiolite, Cyprus. Chemical Geology 2016a, Volume 423, pages 7–18.

Keith, M.; Häckel, F.; Haase, K.M.; Schwarz-Schampera, U.; Klemd, R. Trace element systematics of pyrite from submarine hydrothermal vents. Ore Geology Reviews 2016b, Volume 72, pages 728–745.

Keith, M.; Smith, D.J.; Jenkin, G.R.T.; Holwell, D.A.; Dye, M.D. A review of Te and Se systematics in hydrothermal pyrite from precious metal deposits: insights into ore forming processes. Ore Geology Reviews 2018, Volume 96, pages 269–282.

Kelley, K.D.; Eppinger, R.G.; Lang, J.; Smith, S.M.; Fey, D.L. Porphyry copper indicator minerals (PCIMs) in glacial till samples as an exploration tool: example from the giant Pebble porphyry Cu-Au-Mo deposit. Geochemistry: Exploration, Environnment, Analysis 2011, Volume 11, pages 321–334.

Kelley, K.D.; Spry, P.G. Critical metals associated with alkaline-rock related epithermal gold deposits. Reviews in Economic Geology 2016, Volume 18, pages 195-216.

Keppler, H. Constraints from partitioning experiments on the composition of subdustion zone fluids. Nature 1996, Volume 380, pages 237-240.

Kesler, S.E.; Chryssoulis, S.L.; Simon, G. Gold in porphyry copper deposits: its abundance and fate. Ore Geology Reviews 2002, Volume 21, pages 103–124.

Kesler, S.E.; Deditius, A.P.; Chryssoulis, S. Geochemistry of Se and Te in arsenian pyrite: new evidence for the role of Se and Te hydrothermal complexes in Carlin and epithermal-type deposits. In: Au–Ag–Te–Se deposits: Espo, Finnland (Kojonen, K.K.; Cook, N.J.; Ojala, V.J., Eds.); Proceedings of the 2007 Field Workshop, Geological Survey of Finland 53, 85–95.

Khashgerel, B.; Kavalieris, I.; Ken-Ichiro, H. Mineralogy, textures and whole-rock geochemistry of advanced argillic alteration: Hugo Dumett porphyry Cu–Au deposit, Oyu Tolgoi mineal district, Mongolia. Economic Geology 2008, Volume 71, pages 849–863, doi:10.2113/gsecongeo.71.5.849.

Kilias, S.P.; Naden, J.; Paktsevanoglou, M.; Giampouras, M.; Stavropoulou, A.; Apeiranthiti, D.; Mitsis, I.; Koutles, T.; Michael, K.; Christidis, C. Multistage alteration, mineralization and ore–forming fluid properties at the Viper (Sappes) Au–Cu–Ag–Te ore body, W. Thrace, Greece. Bulletin of the Geological Society of Greece 2013, Volume 47, pages 1635–1644, doi:10.12681/bgsg.11007.

Kilias, A.; Falalakis, G.; Sfeikos, A.; Papadimitriou, E.; Vamvaka, A.; Gkarlaouni, C. The Thrace basin in the Rhodope province of NE Greece—A Tertiary supra-detachment basin and its geodynamic implications. Tectonophysics 2013, Volume 595–596, pages 90–105.

Kirchenbaur, M.; Pleuger, J.; Jahn-Awe, S.; Nagel, T.J.; Froitzheim, N.; Fonseca, R.O.C.; Münker, C. Timing of high-pressure metamorphic events in the Bulgarian Rhodopes from Lu-Hf garnet geochronology. Contribution to Mineralogy and Petrology 2012, Volume 163, pages 897-921.

Klemm, L.M.; Pettke, T.; Heinrich, C.A.; Campos, E. Hydrothermal evolution of the El Teniente deposit, Chile: porphyry Cu–Mo ore deposition from low-salinity magmatic fluids. Economic Geology 2007, Volume 102, pages 1021–1045.

Kloprogge, J.T.; Frost, R.L. Raman and infrared microscopy study of zunyite, a natural Al13 silicate. Spectrochim. Acta Part A Mol. Biomol. Spectrosc. 1999, 55, 1505–1513.

Koděra, P., Kozák, J., Brčeková, J. et al. Distribution and composition of gold in porphyry gold systems: example from the Biely Vrch deposit, Slovakia. Mineralium Deposita 2018, Volume 53, pages 1193–1212. https://doi.org/10.1007/s00126-018-0798-0.

Kósaka H.; Wakita K. Some geologic features of the Mamut porphyry copper deposit, Sabah, Malaysia. Economic Geology 1978, Volume 73, pages 618-627.

Kouzmanov, K.; Bogdanov, K.; Ramboz, C. Te- and Bi-bearing assemblages in the Elshitsa and Radka epithermal deposits, Central Srednogorie, Bulgaria: Mineralogy and genetical features. Bulg Acd Science Geochemistry, Mineralogy, Petrology 2005, Volume 43, pages 108-112.

Kouzmanov, K.; Pokrovski, G.S. Hydrothermal Controls on Metal Distribution in Porphyry Cu (-Mo-Au) Systems. Special Publication of the Society of Economic Geologists. 2012, pages 573–618.

Kroll, T.; Muller, D.; Seifert, T.; Herzig, P.M.; Schneider, A. Petrology and geochemistry of the shoshonite-hosted Skouries porphyry Cu-Au deposit, Chalkidiki, Greece. Mineralium Deposita 2002, Volume 37, pages 137-144.

Kydonakis, K.; Brunn, J.-P.; Sokoutis, D. North Aegean core complexes, the gravity spreading of a thrust wedge. J. Geophys. Res. Solid Earth 2015a, Volume 120, pages 595–616, doi:10.1002/2014JB011601.

Kydonakis, K.; Moulas, E.; Chatzitheodoridis, E.; Brunn, J.-P.; Kostopoulos, D. First-report on Mesozoic eclogite-facies metamorphism preceding Barrovian overprint from the western Rhodope (Chalkidiki, northern Greece). Lithos 2015b, Volume 220–223, pages 147–163, doi:10.1016/j.lithos.2015.02.007.

Landtwing, M.R.; Furrer, C.; Redmond, P.B.; Pettke, T.; Guillong, M.; Heinrich, C.A. The Bingham Canyon porphyry Cu-Mo-Au deposit. III. Zoned copper-gold ore deposition by magmatic vapor expansion. Economic Geology 2010, Volume 105(1), pages 91–118.

Lang, J.R.; Stanley, C.R.; Thompson, J.F.H., , Porphyry copper-gold deposits related to alkalic igneous rocks in the Triassic-Jurassic arc terranes of British Columbia. Arizona Geological Society Digest 1995, Volume 20, pages 219-236.

Layton-Matthews, D.; Peter, J.M.; Scott, S.D.; Leybourne, M. Distribution, mineralogy, and geochemistry of selenium in felsic volcanic-hosted massive sulfide deposits of the Finlayson Lake district, Yukon Territory, Canada. Economic Geology 2008, Volume 103, pages 61–88.

Leake, B.E.; Bernard, E.; Wolley, A.R.; Charles, E.S.; Birch, W.D.; Gilbert, C.M. 1997. Nomenclature of amphiboles: Report of the subcommitee on amphiboles of the International Mineralogical Association, commision on new minerals and mineral names. The Canadian Mineralogist 1997, Volume 35, pages 219 -246

Lee, C.-T.; Luffi, P.; Chin, E.; Bouchet, R.; Dasgupta, R.; Morton, D.; Le Roux, V.; Yin, Q.; Jin, D. Copper systematics in arc magmas and implications for crust–mantle differentiation. Science 2012, Volume 336, pages 64–68.

Lescuyer, J.L.; Bailly, L.; Cassard, D.; Lips, A.L.W.; Piantone, P.; McAlister, M. Sediment-hosted gold in south-eastern Europe: the epithermal deposit of Perama, Thrace, Greece. In: Eliopoulos, D.G. (Ed.), Mineral exploration and sustainable development. Millpress, Rotterdam, 2003, pages 499–502.

Liati, A.; Gebauer, D.; Wysoczanski, R. U–Pb SHRIMP-dating of zircon domains from UH garnet-rich mafic rock and late pegmatoids in the Rhodope zone (N Greece): evidence for Early Cretaceous crystallization and Late Cretaceous metamorphism. Chemical Geology 2002, Volume 184, pages 281–299.

Lilov, P.; Yanev, Y.; Marchev, P. K/Ar dating of the Eastern Rhodopes Paleogene magmatism. Geologica Balcanica 1987, Volume 17,pages 49-58.

Liu, Y.S.; Hu, Z.C.; Gao, S.; Günther, D.; Xu, J.; Gao, C.G. 2008. In situ analysis of major and trace elements of anhydrous minerals by LA-ICP-MS without applying an internal standard. Chemical Geology 2008, Volume 257, pages 34–43.

Lowell, J.D; Guilbert, J.M. Lateral and vertical alteration-mineralization zoning in porphyry ore deposits. Economic Geology 1970, Volume 65, pages 373−408.

Magganas, A.; Sideris, C.; Kokkinakis, A. Marginal basin-volcanic arc origin of metabasic rocks of the Circum-Rhodope Belt, Thrace, Greece. Mineralogy and Petrology 1991, Volume 44, pages 235-252.

Magganas, A.C. Constraints on the petrogenesis of Evros ophiolite extrusives, NE Greece. Lithos 2002, Volume 65, pages 165-182.

Marchev, P.; Singer, B.; Jelev, D.; Hasson, H.; Moritz, R.; Bonev, N. The Ada Tepe deposit: a sediment-hosted, detachment fault-controlled, low-sulfidation gold deposit in the Eastern Rhodopes, SE Bulgaria. Swiss Bulletim of Mineralogy and Petrology 2004, Volume 84(1-2), pages 59-78.

Marchev, P.; Kaiser-Rohrmeier, B.; Heinrich, C.; Ovtcharova, M.; von Quadt, A.; Raicheva, R. Hydrothermal ore deposits related to post-orogenic extensional magmatism and

core complex formation: The Rhodope Massif of Bulgaria and Greece. Ore Geology Reviews. 2005, Volume 27, pages 53–89.

Masterman, G.J.; Cooke, D.R.; Berry, R.F.; Walshe, J.L.; Lee, A.W.; Clark, A.H. Fluid chemistry, structural setting, and emplacement history of the Rosario Cu-Mo porphyry and Cu-Ag-Au epithermal veins, Collahuasi district, northern Chile: Economic Geology 2005, Volume 100, pages 835-862.

Mavrogonatos, C.; Voudouris, P.; Spry, P.G.; Melfos, V.; Klemme, S.; Berndt, J.; Periferakis, A. Biotite Chemistry from Porphyry-Style Mineralization in Western Thrace, Greece. In Proceedings of the 8th Geochemistry Symposium, Antalya, Turkey, 2–6 May 2018a.

Mavrogonatos, C.; Voudouris, P.; Spry, P.G.; Melfos, V.; Klemme, S.; Berndt, J.; Moritz, R.; Kanellopoulos, C. First zunyite-bearing lithocap in Greece: The case of Konos Hill Mo-Re-Cu-Au porphyry system. In Proceedings of the 1st International Electronic Conference on Mineral Science, Sciforum, 16–31 July 2018b; MDPI AG: Basel, Switzerland, 2018; Volume 1, doi:10.3390/IECMS2018-05450.

Mavrogonatos, C.; Voudouris, P.; Spry, P.G.; Melfos, V.; Klemme, S.; Berndt, J.; Baker, T.; Moritz, R.; Bissig, T.; Monecke, T.; Zaccarini, F. Mineralogical Study of the Advanced Argillic Alteration Zone at the Konos Hill Mo–Cu–Re–Au Porphyry Prospect, NE Greece. Minerals 2018c, Volume 8(11), 479.

Mavrogonatos, C.; Voudouris, P.; Berndt, J.; Klemme, S.; Zaccarini, F.; Spry, P.G.; Melfos, V.; Tarantola, A.; Keith, M.; Klemd, R.; Haase, K. Trace Elements in Magnetite from the Pagoni Rachi Porphyry Prospect, NE Greece: Implications for Ore Genesis and Exploration. Minerals 2019, Volume 9(12), 725, https://doi.org/10.3390/min9120725.

Maydagán, L.; Franchini, M.B.; Lentz, D.; Pons, J.; McFarlane, C. Sulfide composition and isotopic signature of the Altar Cu–Au deposit, Argentina: constraints on the evolution of the porphyry–epithermal system. The Canadian Mineralogist 2013, Volume 51, pages 813–840.

McCandless, T.; Ruiz, J.; Campbell, R. Rhenium behavior in molybdenite in hypogene and near-surface environments: Implications for Re-Os geochronometry. Geochimica et Cosmochimica Acta 1993, Volume 57, pages 889-905.

McFall, K.A.; Naden, J.; Roberts, S.; Baker, T.; Spratt, J.; McDonald, I. Platinum-group minerals in the Skouries Cu-Au (Pd, Pt, Te) porphyry deposit. Ore Geology Reviews 2018, Volume 99. Pages 344-364. https://doi.org/10.1016/j.oregeorev.2018.06.014.

McQueen, K.G.; Cross, A.J. Magnetite as a geochemical sampling medium: application to skarn deposits. In: Eggleton, R.A. (Ed.), The State of the Regolith. Geological Society of Australia, 1998, Brisbane, pages 194–199.

Meinert, L.D., Dipple, G.M., and Nicolescu, S. World skarn deposits: Economic Geology 2005, 100th Anniversary Volume, pages 299–336.

Meinhold, G.; Kostopoulos, D.K. The Circum-Rhodope Belt, northern Greece: Age, provenance, and tectonic setting: Tectonophysics 2013, Volume 595–596, pages 55–68, https:// doi .org/10 .1016 /j.tecto .2012 .03 .034.

Melfos, V.; Vavelidis, M.; Christofides, G.; Seidel, E. Origin and evolution of the Tertiary Maronia porphyry copper-molybdenum deposit, Thrace, Greece. Mineralium Deposita 2002, Volume 37, pages 648–668.

Melfos, V.; Voudouris, P. Geological, mineralogical and geochemical aspects for critical and rare metals in Greece. Minerals 2012, Volume 2, pages 300-317.

Melfos, V.; Voudouris, P. Cenozoic metallogeny of Greece and potential for precious, critical and rare metals exploration. Ore Geology Reviews 2017, Volume 59, pages 1030–1057.

Melfos, V.; Voudouris, P.; Melfou, M.; Sánchez, M.G.; Papadopoulou, L.; Filippidis, A.; Spry, P.G.; Schaarschmidt, A.; Klemd, R.; Haase, K.M.; Tarantola, A.; Mavrogonatos. C. Mineralogical constraints on the potassic and sodic-calcic hydrothermal alteration and vein-type mineralization of the Maronia porphyry Cu-Mo ± Re ± Au deposit in NE Greece. Minerals 2020, Volume 10(2), 182, https://doi.org/10.3390/min10020182.

Menant, A.; Jolivet, L.; Vrielynck, B. 2016. Kinematic reconstruction and magmatic evolution illuminating crystal and mantle dynamics of the eastern Mediterranean region since the late Cretaceous. Tectonophysics 2016, Volume 675, pages 103–140.

Meyer, C.; Hemley, J.J. Wall rock alteration. In Geochemistry of Hydrothermal Ore Deposits; Barnes, H.L., Ed.; Rinehart and Winston Holt: New York, United States of America, 1967; pages 166–235.

Michael, C. Geology and Geochemistry of Epithermal Gold Deposit in Konos Area; Internal Report; IGME Xanthi: Madrid, Spain, 1993; Volume 75, page 77.

Michael, C. Epithermal systems and gold mineralization in Western Thrace, (North Greece). Bulletin of the Geological Society of Greece 2004, Volume 36, pages 416–423.

Michailidis, K.; Filippidis, A.; Vavelidis, M.; Evangelou. E. Chemical composition of some ore minerals from St. Philippos (Kirki) polymetallic deposit. Geologica Rhodopica 1989, Volume 1, pages 389-395.

Micko, J. The geology and genesis of the Central zone alkali copper-gold porphyry deposit, Galore Creek district, northwestern British Columbia, Canada. PhD thesis, Vancouver, Univ. of British Columbia,2010, 359p.

MiddelburgJ.J.; van der Weijden, C.H.; Woittiez, J.R.W. Chemical processes affecting the mobility of major, minor and trace elements during weathering of granitic rocks Chemical Geology 1988, Volume 68(3-4), pages 253-273, doi: 10.1016/0009-2541(88)90025-3.

Milani, L.; Bolhar, R.; Cawthorn, R.G.; Frei, D. In situ LA-ICP-MS and EPMA trace element characterization of Fe-Ti oxides from the phoscorite-carbonatite association at Phalaborwa, South Africa. Mineralium Deposita 2017, Volume 52, pages 747–768.

Mills, S.J.; Harter, F.; Nickel, E.H.; Ferraris, G. The standardization of mineral group hierarchies: Application to recent nomenclature proposals. European ournl of. Mineralogy 2009, Volume 21, pages 1073–1080.

Milu, V.; Milesi, J.-P.; Leroy, J.L. Rosia Poieni copper deposit, Apuseni Mountains, Romania-advanced argillic overprint of a porphyry system. Mineralium Deposita 2004, Volume 39, pages 173–188.

Moëlo, Y.; Oudin, E.; Makovicky, E.; Karup-Møller, S.; Pillard, F.; Bornuat, M.; Evanghelou, E. La kirkiite, Pb10Bi3As3S19, une nouvelle espece minerale homologue de la jordanite. Bull. Mineral. 1985, Volume 108, pages 667–677.

Monecke, T.; Monecke, J.; Reynolds, T.J.; Tsuruoka, S.; Bennett, M.M.; Skewes, W.B.; Palin, R.M. Quartz Solubility in the H2O-NaCl System: A Framework for Understanding Vein Formation in Porphyry Copper Deposits. Economic Geology 2018, Volume 113, pages 1007–1046, doi:10.5382/econgeo.2018.4580.

Morey, A.A.; Tomkins, A.G.; Bierlin, F.P.; Wienberg, R.F.; Davidson, G.J. Bimodal distribution of gold in pyrite and arsenopyrite: examples from the Archean Boorara and Bardoc shear systems, Yilgarn craton, Western Australia. Economic Geology 2008, Volume 103, pages 599–614.

Moritz, R.; Márton, I.; Ortelli, M.; Marchev, P.; Voudouris, P.; Bonev, N.; Spikings, R.; Cosca, M. A review of age constraints of epithermal precious and base metal deposits of the Tertiary Eastern Rhodopes: Coincidence with Late Eocene-Early Oligocene tectonic plate reorganization along the Tethys. In: Proceedings of the XIX Congress Carpathian-Balkan Geological Association, Thessaloniki, Greece, 2010; Christofides, G., Kantiranis, N.; Kostopoulos, D.S.; Chatzipetros, A. Eds.; Scientific Annals of the School of Geology, Aristotle University of Thessaloniki, Greece, 2010; Volume 100, pages 351–358.

Moritz, R.; Rezeau, H.; Ovtcharova, M.; Tayan, R.; Melkonyan, R.; Hovakimyan, S.; Ramazanov, V.; Selby, D.; Ulianov, A.; Chiaradia, M.; Putlitz, B. Long-lived, stationary magmatism and pulsed porphyry systems during Tethyan subduction to post-collision evolution in the southernmost Lesser Caucasus, Armenia and Nakhitchevan. Gondwana Research 2016, Volume 37, pages 465–503.

Mountrakis, D. Tertiary and Quaternary tectonics of Greece, in Dilek, Y.; Pavlides, S., (eds) Postcollisional Tectonics and Magmatism in the Mediterranean Region and Asia: Geological Society of America Special Paper, 2006, Volume 409, pages 125–136, https:// doi .org /10 .1130 /2006.2409 (07).

Müller, B.; Axelsson, M.D.; Ohlander, B. Trace elements in magnetite from Kiruna, northern Sweden, as determined by LA-ICP-MS. GFF (Journal of the Geological Society of Sweden) 2003, Volume 125:1, pages 1-5, DOI: 10.1080/11035890301251001

Muntean, J.L. Porphyry Gold Deposits of the Refugio District, Maricunga Belt, Northern Chile. Economic Geology 2000, Volume 95(7), pages 1445-1472, doi: 10.2113/95.7.1445

Muntean, J.L; Einaudi, M.T. Porphyry-epithermal transition: Maricunga Belt, Northern Chile. Economic Geology 2001, Volume 96, pages 743–772.

Nadeau, O.; Williams-Jones, A.E.; Stix, J. Sulfide magma as a source of metals in arc-related magmatic hydrothermal ore fluids. Nature Geoscience 2010, Volume 3(7), pages 501–505.

Nadoll, P.; Koenig, A.E. LA-ICP-MS of magnetite: methods and reference materials. Journal of Analytical Atomic Spectrometry 2011, Volume 26, pages 1872–1877.

Nadoll, P.; Mauk, J.L.; Hayes, T.S.; Koenig, A.E.; Box, S.E. Geochemistry of magnetite from hydrothermal ore deposits and host rocks of the Mesoproterozoic Belt Supergroup, United States: Economic Geology 2012, Volume 107, pages 1275–1292.

Nadoll, P.; Angerer, T.; Mauk, J.L.; French, D.; Walshe, J. The chemistry of hydrothermal magnetite: a review. Ore Geology Reviews 2014, Volume 61, pages 1–32.

Nadoll, P.; Mauk, J.L.; Leveille, R.A.; Koenig, A.E. Geochemistry of magnetite from porphyry Cu and skarn deposits in the southwestern United States. Mineralium Deposita 2015, Volume 50, pages 493–515.

Okay, A.I.; Zattin, M.; Cavazza, W. Apatite fission-track data for Miocene Arabia-Eurasia collision. Geology 2010, Volume 38, pages 35-38.

Oliver N.H.; Cleverley J.S.; Mark G.; Pollard P.J.; Fu B.; Marshall L.J.; Rubenach M.J.; Williams P.J.; Baker T. Modeling the role of sodic alteration in the genesis of iron oxide-copper-gold deposits, Eastern Mount Isa block, Australia. Economic Geoogy. 2004, Volume 99, pages 1145–1176.

Ortelli, M.; Moritz, R.; Voudouris, P.; Spangenberg, J. Tertiary porphyry and epithermal association of the Sapes-Kassiteres district, Eastern Rhodopes, Greece. In Proceedings of the 10th Biennial SGA Meeting, Townsville, Australia, 17–20 August 2009; pages 536–538.

Ortelli, M.; Moritz, R.; Voudouris, P.; Cosca, M.; Spangenberg, J. Tertiary porphyry and epithermal association of the Sapes-Kassiteres district, Eastern Rhodopes, Greece. In Proceedings of the 8th Swiss Geiscience meeting, Fribourg, Switzerland, 2010.

Ossandòn, C.G.; Fréraut, C.R.; Gustafson, L.B.; Lindsay, D.D.; Zentilli, M. Geology of the Chuquicamata mine: A progress report. Economic Geology 2001, Volume 96, pages 249-270.

Ottens, B.; Voudouris, P. Griechenland: Mineralien-Fundorte-Lagerstätten; Christian Weise Verlag, Munchen, Germany, 2018, 480p.

Papoulis, D.; Tsolis-Katagas, P.; Katagas, C. New find of zunyite in advanced argillic alteration of rhyolites, Kos Island, South Aegean volcanic arc, Greece. Bulletin of the Geological Society of Greece 2004, Volume 36, pages 474–480.

Pearce, J.A.; Cann, J. 1973, Tectonic setting of basic volcanic rocks determined using trace element analyses: Earth and Planetary Science Letters 1973, Volume 19, pages 290–300.

Pearce, J.A.; Harris, N.B.W.; Tindle, A.J. Trace element discrimination diagrams for the tectonic interpretation of granitic rocks. Journal of Petrology 1984, Volume 25, pages 956-83.

Pearce, J.A.; Peate, D.W. Tectonic Implications of the Composition of Volcanic ARC Magmas. Annual Review of Earth and Planetary Sciences 1995, Volume 23, pages 251-285.

Peccerilo, A.; Taylor, S.R. Geochemistry of Eocene calc-alkaline volcanic rocks from the Kastamonu area, Northern Turkey. Contributions to Mineralogy and Petrology 1976, Volume 58, pages 63-81.

Pe-Piper, G.; Piper, D.J.W. The Igneous Rocks of Greece. The Anatomy of an Orogen; Beiträge der regionalen Geologie der Erde: Berlin, Germany, 2002; 573p.

Perelló, J.; Neyra, C.; Posso, H.; Zárate, A.; Ramos, P.; Caballero, A.; Martini, R.; Fuster, N.; Muhr, R. Cotabambas: Late Eocene porphyry copper-gold mineralization southwest of Cuzco, Peru. Society of Economic Geologists Special Publication 11, 2004 pages 213−230.

Periferakis, A.; Voudouris, P.; Melfos, V.; Mavrogonatos, C.; Alfieris, D. The Stypsi-Megala Therma porphyry-epithermal mineralization, Lesvos Island, Greece: New mineralogical and geochemical data. In: Geophysical Research Abstracts, Proceedings of the EGU General Assembly, Vienna, Austria, 23–28 April 2017; EGU2017-12950; EGU: Vienna, Austria, 2017; Volume 19.

Periferakis, A.; Voudouris, P.; Melfos, V.; Kolodziejczyk, J.; Mavrogonatos, C.; Alfieris, D. New Mineralogical Data and Geochemical Constraints on the Stypsi-Megala Therma Porphyry-Epithermal Mineralisation, Lesvos Island, Greece. In: Uysal I. (Ed.), 8th Geochemistry Symposium Abstracts Book, 2018, Trabzon, Turkey, pp. 189.

Perkins, R. Post-Collisional Magmatism and Porphyry - Epithermal Style Mineralisation along the Maronia Magmatic Corridor, northeastern Greece. PhD Thesis, University of Bristol, 270pp.

Perkins, R.; Copper, F.J.; Condon, D.J.; Tattitsch, B.; Naden, J. Post-collisional Cenozoic extension in the northern Aegean: The high-K to shoshonitic intrusive rocks of the Maronia Magmatic Corridor, northeastern Greece. Lithosphere 2018, Volume 10, pages 582–601, doi:10.1130/L730.1.

Pisiak, L.K.; Canil, D.; Lacourse, T.; Plouffe, A.; Ferbey, T. Magnetite as an indicator mineral in the exploration of porphyry deposits: A case study in till near the Mount Polley Cu-Au deposit, British Columbia, Canada. Economic Geology 2017, Volume 112, pages 919–940.

Plank, T. Constraints from thorium/lanthanum on sediment recycling at subduction zones and the evolution of continents. Journal of Petrology 2005, Volume 46, pages 921-944.

Pokrovski, G.S.; Zakirov, I.V.; Roux, J.; Testemale, D.; Hazemann, J.L.; Bychkov, A.V.; Golikova, G.V. Experimental study of arsenic speciation in vapor phase to 500 °C: implications for As transport and fractionation in low-density crustal fluids and volcanic gases. Geochimica et Cosmochimica Acta 2002, Volume 66, pages 3453-3480.

Pokrovski, G.S.; Roux, J.; Harrichoury, J.C. Fluid density control on vapor–liquid partitioning of metals in hydrothermal systems. Geology 2005, Volume 33, pages 657–660.

Pokrovski, G.S.; Borisova, A.Y.; Bychkov, A.Y. Speciation and Transport of Metals and Metalloids in Geological Vapors. In: Thermodynamics of Geothermal Fluids, Reviews in Mineralogy and Geochemistry. Mineralogical Society of America, Stefánsson, A.; Driesner, T.; Bénézeth, P. (Eds.), 2013, Volume 76, pages 165–218.

Pollard, P.J.; Taylor, R.G. Paragenesis of the Grasberg Cu-Au deposit, Irian Jaya, Indonesia: Results from logging section 13. Mineralium Deposita 2002, Volume 37, pages 117−136.

Pouchou, J.L. Pichoir, F. Quantitative analysis of homogeneous or stratified microvolumes applying the model ‘‘PAP’’. In: Heinrich, K.F.J.; Newbury, D.E. (eds) Electron probe quantitation. Plenum Press, 1991, New York, United States of America, pages 31–75.

Redmond, P.B.; Landtwing, M.R.; Einaudi, M.T., 2001, Cycles of porphyry dike emplacement, veining, alteration and mineralization in the Bingham porphyry Cu-Au-Mo deposit, Utah. In: Piestrzyński., A., et al., eds., Mineral deposits at the beginning of the 21st century: Joint Biennial SGA-SEG Meeting, 6th, Kraków, Poland, 2001, Proceedings, pages 473−476.

Reich, M.; Kesler, S.E.; Utsunomiya, S.; Palenik, C.S.; Chryssoulis, S.L.; Ewing, R.C. Solubility of gold in arsenian pyrite. Geochimica et Cosmochimica Acta 2005, Volume 69, pages 2781–2796.

Reich, M.; Becker, U. First-principles calculations of the thermodynamic mixing properties of arsenic incorporation into pyrite and marcasite. Chemical Geology 2006a, Volume 225(3–4), pages 278-290, doi: 10.1016/j.chemgeo.2005.08.021

Reich, M.; Utsunomiya, S.; Kesler, S.E.; Wang, L.M.; Ewing, R.C.; Becker, U. Thermal behavior of metal nanoparticles in geologic materials. Geology 2006b, Volume 34, pages 1033–1036.

Reich, M.; Deditius, A.; Chryssoulis, S.; Li, J.-W.; Ma, C.-Q.; Parada, M.A.; Barra, F.; Mittermayr, F. Pyrite as a record of hydrothermal fluid evolution in a porphyry copper system: a SIMS/EMPA trace element study. Geochimica et Cosmochimica. Acta 2013, Volume 104, pages 42–62.

Reischmann, T.; Kostopoulos, D. Terrane accretion in the internal Hellenides. Geophys. Res. Abstracts 2007, 9, 05337.

Repstock, A.; Voudouris, P.; Kolitsch, U. New occurrences of watanabeite, colusite, “arsenosulvanite” and Cu-excess tetrahedrite-tennantite at the Pefka high-sulfidation epithermal deposit, northeastern Greece. Neues Jahrbuch für Mineralogie. 2015, Volume 192, pages 135–149.

Repstock, A.; Voudouris, P.; Zeug, M.; Melfos, V.; Zhai, M.; Li, H.; Kartal, T.; Matuszczak, J. 2016. Chemical composition and varieties of fahlore-group minerals from Oligocene mineralization in the Rhodope area, southern Bulgaria and northern Greece. Mineralogy and Petrology 2016, Volume 110, pages 103–123.

Reyes, A.G. Petrology of Philippine geothermal systems and the application of alteration mineralogy to their assessment. Journal of Volcanology and Geothermal Research 1990, Volume 43, pages 279–309.

Reyes, A.G. Mineralogy, distribution and origin of acid alteration in Philippine geothermal systems; Geological Survey of Japan Report; Geological Survey of Japan: Tsukuba, Japan, 1991.

Revan, M.K.; Genç, Y.; Maslennikov, V.V.; Maslennikov, S.P.; Large, R.R.; Danyushevsky, L.V. Mineralogy and trace-element geochemistry of sulfide minerals in hydrothermal chimneys from the Upper-Cretaceous VMS deposits of the eastern Pontide orogenic belt (NE Turkey). Ore Geology Reviews 2014, Volume 63, pages 129–149.

Richards, J.P. Postsubduction porphyry Cu-Au and epithermal Au deposits. Products of remelting of subduction-modified lithosphere. Geology 2009, Volume 37(3), pages 247–250.

Richards, J.P. Magmatic to hydrothermal metal fluxes in convergent and collided margins. Ore Geology Reviews 2011, Volume 40(1), pages 1–26.

Ricou, L.E.; Burg, J.P.; Godfriaux, I.; Ivanov, Z. Rhodope and Vardari the metamorphic and the olistostromic paired belts related to the Cretaceous subduction under Europe. Geodinynamica Acta 1998, Volume 11, pages 285–309.

Ring, U.; Glodny, J.; Will, T.; Thomson, S. The Hellenic subduction system: High pressure metamorphism, exhumation, normal faulting, and large-scale extension. Annu. Rev. Earth and Planetary Science Letters 2010, Volume 38, pages 45–76.

Robertson, A.H. Overview of the genesis and emplacement of Mesozoic ophiolites in the Eastern Mediterranean Tethyan region. Lithos 2002, Volume 65, pages 1–67.

Robertson, A.H.; Trivić, B.; Derić, N.; Bucurc, I.I. Tectonic development of the Vardar ocean and its margins: evidence from the Republic of Macedonia and Greek Macedonia. Tectonophysics 2013, Volume 595-596, pages 25–54.

Roeder, P.L. Chromite: From the fiery rain of chondrules to the Kilauea Iki lava lake: The Canadian Mineralogist 1994, Volume 32, pages 729–746.

Rose, A.W.; Burt, D.M. Hydrotherm.al alteration. In: Barnes, H.L. (ed), Geochemistry of hydrothermal ore deposits, 2nd ed., John Wiley, New York, 1979, pages 173–235.

Rudnick, R.L.; Gao, S. Composition of the continental crust. In: Holland, H.D.; Turekian, K.K. (eds.) Treatise on geochemistry, v. 3. The crust: Oxford, Elsevier-Pergaman, 2003, 1–64.

Rusk, B.G.; Reed, M.H.; Dilles, J.H. Fluid inclusion evidence for magmatic-hydrothermal fluid evolution in the porphyry copper-molybdenum deposit at Butte, Montana: Economic Geology 2008a, Volume 103, pages 307−334.

Rusk, B.G.; Miller, B.J.; Reed, M.H. Fluid-inclusion evidence for the formation of Main Stage polymetallic base-metal veins, Butte, Montana, USA. Arizona Geological Society Digest 2008b Volume 22, pages 573−581.

Sack, R.O.; Ghiorso, M.S. Chromian spinels as petrogenetic indicators: Thermodynamics and petrological applications: American Mineralogist 1991, Volume 76, pages 827–847.

Schmid, S.M.; Bernoulli, D.; Fügenschuh, B.; Matenco, L.; Schefer, S.; Schuster, R.; Tischler, M.; Ustaszewski, K. The Alpine-Carpathian-Dinaridic orogenic system: correlation and evolution of tectonic units. Swiss Journal of Geosciences 2008, Volume 101, pages 139-183.

Schmid, S.M.; Fügenschuh, B.; Kounov, A.; Matenco, L.; Nievergelt, P.; Oberhänsli, R.; Pleuger L.; Schefer, S.; Schuster, R.; Tomljenović, B.; Ustaszewski, K.; van Hinsbergen D.J.J. Tectonic units of the Alpine collision zone between Eastern Alps and western Turkey. Gondwana Research 2020, Volume 78, pages 308-374, doi: 10.1016/j.gr.2019.07.005

Schmidt, K.; Koschinsky, A.; Garbe-Schönberg, D.; de Carvalho, L.M.; Seifert, R. Geochemistry of hydrothermal fluids from the ultramafic-hosted Logatchev hydrothermal field, 15°N on the Mid-Atlantic Ridge: temporal and spatial investigation. Chemical Geology 2007, Volume 242, pages 1–21.

Scott, K.M. Solid solution in, and classification of, gossan-derived members of the alunite-jarosite family, northwest Queensland, Australia. Am. Mineral. 1987, 72, 178–187.

Seedorff, E.; Dilles, J.H.; Proffett, J.M.; Einaudi, M.T.; Zurcher, L.; Stavast, W.J.A.; Johnson, D.A; Barton, M.D. Porphyry deposits: Characteristics and origin of hypogene features. In 100th Year Anniversary Issue; Hedenquist, J.W., Thompson, J.F.G., Goldfarb, R.J., Richards, J.P., Eds.; Economic Geology; GeoScienceWorld: McLean, VA, United States of America, 2005, Volume 100, pages 251–298.

Shand, S.J. The Eruptive Rocks, 2nd ed. New York, John Wiley, 1943. 444pp.

Shawh, A.J.; Constantinides, D.C. The Sappes gold project. Bulletin of the Geological Society of Greece 2001, Volume 34, pages 1073–1080.

Shinohara, H.; Hedenquist, J. Constraints on magma degassing beneath the Far Southeast porphyry Cu–Au deposit, Philippines. Journal of Petrology 1997, Volume 38, pages 1741–1752.

Sievwright, R.H.; Wilkinson, J.J.; O'Neill, H.S.C.; Berry, A.J. Thermodynamic controls on element partitioning between titanomagnetite and andesitic-dacitic silicate melts. Contributions to Mineralogy and Petrology 2017, Volume 172, pages 1–33.

Sillitoe, R.H. Gold deposits in Western Pacific island arc: The magmatic connection. In The Geology of Gold Deposits: The Perspective in 1988; Keays, R., Ramsay, R., Groves, D., Eds.; Economic Geology Monograph Series; GeoScienceWorld: McLean, VA, United States of America, 1989; Volume 6, pages 251–298.

Sillitoe, R. Erosion and collapse of volcanoes: Causes of telescoping in intrusion-centered ore deposits. Geology 1994, Volume 22, pages 945–948, doi:10.1130/0091-7613(1994)022<0945:EACOVC>2.3.CO;2.

Sillitoe, R.H. Exploration of porphyry copper lithocaps, in Proceedings Pacific Rim Congress 1995, (Eds: Mauck, J.L. and George, J.D.St.), pp 527-532 (The Australasian Institute of Mining and Metallurgy: Melbourne).

Sillitoe, R.H. Characteristics and controls of the largest porphyry copper-gold and epithermal gold deposits in the circum-Pacific region. Australian Journal of Earth Sences. 1997, Volume 44, pages 373–388.

Sillitoe, R.H. Styles of high-sulfidation gold, silver and copper mineralization in the porphyry and epithermal environments. In Proceedings of the PACRIM'99 Congress, Bali, Indonesia, 10–13 October 1999; Weber, G., Ed.; Australasian Institute of Mining and Metallurgy: Parkville, VIC, Australia, 1999; pages 29–44.

Sillitoe, R.H. Gold-rich porphyry deposits: descrip¬tive and genetic models and their role in exploration and discovery. Reviews in Economic Geology 2000, Volume 13 pages 315–345.

Sillitoe, R.H. Porpyry copper systems. Economic Geology 2010, Volume 105, pages 3–41, doi:10.2113 /gsecongeo.105.1.3.

Simon, G.; Huang, H.; Penner-Hahn, J.E.; Kesler, S.E.; Kao, L.S. Oxidation state of gold and arsenic in gold-bearing arsenian pyrite. American Mineralogist 1999, Volume 84, pages 1071–1079.

Simon, A.C.; Pettke, T.; Candela, P.A.; Piccoli, P.M.; Heinrich, C.A. Magnetite solubility and iron transport in magmatic-hydrothermal environments. Geochimica et Cosmochimica Acta 2004, Volume 68, pages 4905–4914.

Simon, A.C.; Pettke, T.; Candela, P.A.; Piccoli, P.M.; Heinrich, C.A. The partitioning behaviour of As and Au in S-free and S-bearing magmatic assemblages. Geochimica et Cosmochimica Acta 2007, Volume 71, pages 1764–1782.

Simmons, S.F.; White, N.C.; John, D.A. Geological characteristics of epithermal precious and base metal deposits. Economic. Geology 2005, Volume 100, pages 485–522.

Sinclair, D.W. Porphyry Deposits. In: Goodfellow, W.D., Ed., Mineral Deposits of Canada: A Synthesis of Major Deposit-Types, District Metallogeny, the Evolution of Geological Provinces, and Exploration Methods, Geological Association of Canada, Mineral Deposits Division, Special Publication 5, 2007, Canada, Newfoundland, pages 223-243.

Sinclair, D.W.; Jonasson, I.R.; Kirham, R.V.; Soregaroli, A.E. Rhenium and other Platinum-group metals in porphyry deposits. Geological Survey of Canada open file, 6181, 2009.

Sinclair, W.D.; Jonasson, I.R.; Kirkham, R.V.; Soregaroli, A.E. Rhenium in Canadian mineral deposits. Geological Survey of Canada, Open File 7780, 2016, 62 pages, https://doi.org/10.4095/299202.

Singer, D.A.; Berger, V.I.; Menzie, W.D.; Berger, B.R. Porphyry copper deposit density. Economic Geology 2005, Volume 100(3), pages 491–514.

Siron, C.R.; Thompson, J.F.H.; Baker, T.; Friedman, R.; Tsitsanis, P.; Russell, S.; Randall, S.; Mortensen, J. Chapter 2: Magmatic and Metallogenic Framework of Au-Cu Porphyry

and Polymetallic Carbonate- Hosted Replacement Deposits of the Kassandra Mining District , Northern Greece. Economic Geology Special Publication, 19, 2016, pages 29–55.

Skarpelis, N. The Aghios Filippos ore deposit, Kirki (Western Thrace). A base-metal part of a high-sulfidation epithermal system. Bulletin of the Geological Sociey of Greece 1999, Volume 33, pages 51–60.

Sossi, P.A.; Prytulak, J.; O'Neill, H.S.C. Experimental calibration of vanadium partitioning and stable isotope fractionation between hydrous granitic melt and magnetite at 800°C and 0.5 GPa: Contributions to Mineralogy and Petrology 2018, Volume 173, 27, https://doi.org/10.1007/s00410-018-1451-8.

Stergiou, C.L.; Melfos, V.; Voudouris, P. A review on the critical and rare metals distribution throughout the Vertiskos Unit, N. Greece. Proceedings of the 1st International Electronic Conference on Mineral Science, 16-31 July 2018, 8 pp. (https://sciforum.net/paper/view/conference/5453).

Stoffregen, R.E.; Alpers, C.N. Woodhouseite and svanbergite in hydrothermal ore deposits: Products of apatite destruction during advanced argillic alteration. The Canadian Mineralogist 1987, Volume 25, pages 201–211.

Sun, S.S.; McDonough, W.F Chemical and isotopic systematics of oceanic basalts; implications for mantle composition and processes. In: Magmatism in the ocean basins. Saunders, A.D.; Norry, M.J. (eds), Geological Society of London 1989, Volume 42, pages 313-345.

Sun, W.; Arculus, R.J.; Kamenetsky, V.S.; Binns, R. Release of gold-bearing fluids in convergent margin magmas prompted by magnetite crystallization. Nature 2004, Volume 431, pages 975–978.

Sykora, S.; Cooke, D.R.; Meffre, S.; Stephanov, A.S.; Gardner, K.; Scott, R.; Selley, D.; Harris, A.C. Evolution of pyrite trace element compositions from porphyry-style and epithermal conditions at the Lihir gold deposit: implications for ore genesis and mineral processing. Economic Geology 2018, Volume 113, pages 193–208.

Tarkian, M.; Stribrny, B. Platinum-group elements in porphyry copper deposits: A reconnaissance study. Mineralogy and Petrology 1999, Volume 65, pages 161−183.

Thompson, A.J.B.; Hauff, P.L.; Robitaille, A.J. Alteration mapping in exploration: application of short-wave infrared spectroscopy. SEG Newsletter 1999, Volume 39, pages 1-13.

Tooth, B.; Brugger, J.; Ciobanu, C.; Liu, W. Modeling of gold scavenging by bismuth melts coexisting with hydrothermal fluids. Geology 2008, Volume 36(10), pages 815–818.

Toplis, M.J.; Corgne, A. An experimental study of element partitioning between magnetite, clinopyroxene and iron-bearing silicate liquids with particular emphasis on vanadium. Contributions to Mineralogy and Petrology 2002, Volume 144, pages 22–37.

Tsirambides, A.; Filippidis, A. Metallic mineral resources of Greece. Central European Journal of Geosciences 2012, Volume 4, pages 641–650.

Tsirambides, A.; Filippidis, A. Sb- Bi-Bearing Metallogeny of the SerboMacedonian-Rhodope Metallogenic Belt (SRMB). Bulletin of the Geological Society of Greece 2019, Volume 55(1), pages 34-64.

Turpaud, P.; Reischmann, T. Characterisation of igneous terranes by zircon dating: implications for UHP occurrences and suture identification in the Central Rhodope, northern Greece. International. Journal of Earth Sciences 2010, Volume 99, pages 567–591.

van Achterbergh, E.; Ryan, C. G.; Jackson, S. E.; Griffin, W. L. Data reduction software for LA-ICP-MS: appendix. In: P. J. Sylvester (Ed.), Laser Ablation-ICP Mass Spectrometry in the Earth Sciences: Principles and Applications (volume 29, pages 239-243). Ottawa. Mineralog. Assoc. Canada (MAC) Short Course Series, 2001.

Vavelidis, M.; Filippidis, A.; Michailidis, K.; Evangelou, E. The polymetallic ore mineralization of the Kirki area, Alexandroupolis district, Northeastern Greece. Geologica Rhodopica 1989, Volume 1, pages 350–365.

von Quadt. A.; Moritz, R.; Peytcheva, I.; Heinrich, C. Geohronology and geodynamics of late Cretaceous magmatism and Cu-Au mineralization at the Panagyuristhe region of the Apuseni-Banat-Timok-Srednogorie belt, Bulgarioa. Ore Geology Reviews 2005, Volume 27, pages 95-126.

Voudouris, P. Mineralogical, Geochemical and Fluid Inclusion Studies on Epithermal Vein Type Gold/Silver Mineralizations at Kassiteres/Sapes, (NE-Greece). Ph.D. Thesis, University of Hamburg, Hamburg, Germany, 1993.

Voudouris, P.; Arikas, K. Epithermal Au-Ag-Mineralization at Kassiteres/Sape, NE-Greece: Geological, Mineralogical and Microthermometric studies. Bulletin of the Geoogical Society of Greece, 1994, Volume 30, pages 427-443 (in Greek).

Voudouris, P.; Skarpelis, N. Epithermal gold-silver mineralization at Perama (Thrace) and Lemnos Island. Bulletin of the Geological Society of Greece 1998, Volume 32, pages 125–135.

Voudouris, P.; Kyriakopoulos K. Magma degassing in a Tertiary vocanic edifice: Mineralogy, petrology and depositional environment of lithocaps related to a porphyry-Cu occurrence (Kassiteres/W. Thrace, Greece). In: Eliopoulos et al. (eds) Mineral exploration and sustainable development. Millpress, Rotterdam, 2003, pages 415-418.

Voudouris, P.; Alfieris, D. New porphyry-Cu ± Mo occurrences in northeastern Aegean/Greece: Ore mineralogy and transition to epithermal environment. In Mineral Deposit Research: Meeting the Global Challenge; Mao, J., Bierlein, F.P., Eds.; Springer: Berlin, Germany, 2005; pages 473–476.

Voudouris, P.; Papavassiliou, K.; Melfos, V. (2005) Silver mineralogy of St Philippos deposit (northeastern Greece) and its relationship to a Te-bearing porphyry-Cu-Mo mineralization. In: N. Cook and I. Bonev (eds): Au-Ag-Te-Se deposits, Geochemistry, Mineralogy and Petrology 2005, Volume 43, pages 155-160.

Voudouris, P.; Tarkian, M.; Arikas, K. Mineralogy of telluride-bearing epithermal ores in Kassiteres-Sappes area, western Thrace, Greece. Mineralpgy and Petrology 2006, Volume 87, pages 31–52.

Voudouris, P. A comparative mineralogical study of Te-rich magmatic-hydrothermal systems in northeastern Greece. Minerogy and Petrology 2006, Volume 87, pages 241-275.

Voudouris, P.; Spry, P.G.; Melfos, V.; Alfieris, D. Tellurides and bismuth sulfosalts in gold occurrences of Greece: mineralogy and genetic considerations. Geol. Survey of Finland Guide 2007, Volume 53, pages 85-94

Voudouris, P.; Melfos, V.; Spry, P.G.; Bindi, L.; Kartal, T.; Arikas, K.; Moritz, R.; Ortelli, M. Rhenium-rich molybdenite and rheniite (ReS_2) in the Pagoni Rachi-Kirki Mo-Cu-Te-Ag-Au deposit, Northern Greece. implications for the rhenium geochemistry of porphyry style Cu-Mo and Mo mineralization. The Canadian. Mineralogist 2009, 47, 1013–1036.

Voudouris, P.; Melfos, V.; Moritz, R.; Spry, P.G.; Ortelli, M.; Kartal, T. 2010. Molybdenite occurrences in Greece: mineralogy, geochemistry and depositional environment. In: Christofides, G. (Ed.), Proceedings of the XIX Congress of the Carpathian-Balkan Geological Association, Thessaloniki. Scientific Annals of the School of Geology A.U.Th. Volume 100, pages 369–378.

Voudouris, P. Conditions of formation of the Mavrokoryphi high-sulfidation epithermal Cu-Ag-Au-Te deposit (Petrota Graben, NE Greece). Mineralogy and. Petrology 2011, Volume 101, pages 97–113.

Voudouris, P.; Melfos, V.; Spry, P.G.; Moritz, R.; Papavasiliou, C.; Falalakis, G. Mineralogy and geochemical environment of formation of the Perama Hill high sulfidation epithermal Au-Ag-Te-Se deposit, Petrota graben, NE Greece. Mineralogy and Petrology 2011, Volume 103, pages 79–100.

Voudouris, P.; Melfos, V.; Spry, P.G.; Bindi, L.; Moritz, R.; Ortelli, M.; Kartal, T. Extremely Re-rich molybdenite from porphyry Cu-Mo-Au prospects in northeastern Greece: Mode of occurrence, causes of enrichment, and implications for gold exploration. Minerals 2013, Volume 3, pages 165–191.

Voudouris, P.; Melfos, V.; Spry, P.G.; Kartal, T.; Schleicher, H.; Moritz, R.; Ortelli, M. The Pagoni Rachi/Kirki Cu-Mo-Re-Au-Ag-Te deposit, northern Greece: mineralogical and fluid inclusion constraints on the evolution of a telescoped porphyry-epithermal system. The Canadian Mineralogist. 2013, Volume 51, pages 411–442.

Voudouris, P.; Melfos, V. Aluminum-phosphate-sulfate (APS) minerals in the sericitic-advanced argillic alteration zone of the Melitena porphyry-epithermal Mo-Cu- ± Au ± Re prospect, western Thrace, Greece. Neues Jahrbuch für Mineralogie 2013, Volume 190, pages 11–27.

Voudouris, P. Hydrothermal corundum, topaz, diaspore and alunite supergroup minerals in the advanced argillic alteration lithocap of the Kassiteres-Sapes porphyry-

epithermal system, western Thrace, Greece. Neues Jahrbuch für Mineralogie 2014, Volume 191, pages 117–136.

Voudouris, P., Melfos, V., Spry, P.G., Baker, T. Cenozoic Porphyry-Epithermal and Other Intrusion-Related Deposits in Northeastern Greece: Geological, Mineralogical and Geochemical Constraints. SEG Guidebook Series, 2016a; Voudouris, P.; Siron, C.R.; Márton, I. (Eds), 54, 43-82.

Voudouris, P.; Melfos, V.; Baker, T.; Spry, P.G., Diverse Styles of Oligocene-Miocene Magmatic-Hydrothermal Deposits in Northeastern Greece: Relationships between Tectonic-, Magmatic Activity, Alteration and Au-Ag Mineralization. In: SEG Guidebook Series, 2016b; Voudouris, P.; Siron, C.R.; Márton, I. (Eds), 54, 83-112.

Voudouris, P.; Spry, P.G.; Melfos, V.; Alfieris, D.; Mavrogonatos, C.; Repstock, A.; Djiba, A.; Stergiou, C.; Periferakis, A.; Melfou, M. Porphyry and Epithermal Deposits in Greece: A Review and New Discoveries. In Proceedings of the 8th Geochemistry Symposium, Antalya, Turkey, 2–6 May 2018.

Voudouris, P.; Spry, P.G.; Melfos, V.; Haase, K.; Klemd, R.; Mavrogonatos, C.; Repstock A.; Alfieris, D. Gold deposits in Greece: Hypogene ore mineralogy as a guide for precious and critical metal exploration. In: Proc. 1st Int. Electr. Conf. Mineral Science, 2018, pp. 13, doi: 10.3390/IECMS2018-05452.

Voudouris, P.; Mavrogonatos, C.; Spry, P.G.; Baker, T.; Melfos, V.; Klemd, R.; Haase, K.; Repstock, A.; Djiba, A.; Bismayer, U.; Tarantola, A.; Scheffer, C.; Moritz, R.; Kouzmanov, K.; Alfieris, D.; Papavassiliou, K.; Schaarschmidt, A.; Galanopoulos, E.; Galanos, E.; Kołodziejczyk, J. Stergiou, C.; Melfou, M. Porphyry and epithermal deposits in Greece: An overview, new discoveries, and mineralogical constraints on their genesis. Ore Geology Reviews 2019a, Volume 107, pages 654-691, https://doi.org/10.1016/j.oregeorev.2019.03.019.

Voudouris,P.; Mavrogonatos, C.; Melfos, V.; Spry, P.G.; Magganas, A.; Alfieris, D.; Soukis, K.; Tarantola,A.; Periferakis, A.; Kołodziejczyk,J.; Scheffer, C.; Repstock, A.; Zeug, M. The geology and mineralogy of the Stypsi porphyry Cu-Mo-Au-Re prospect, Lesvos Island, Aegean Sea, Greece. Ore Geology Reviews 2019b, Volume 112, 2019, 103023, https://doi.org/10.1016/j.oregeorev.2019.103023.

Watanabe, Y.; Aoki, M.; Yamamoto, K. Geology, age and style of the advanced argillic alteration in the Kobui area, Southwesterm Hokkaido, Japan. Resource Geology 1997, Volume 47, pages 263–281.

Watanabe, Y.; Hedenquist, J.W. Mineralogical and stable isotope zonation at the surface over the El Salvador porphyry copper deposit, Chile. Econ Geol 2001, Volume 96, pages 1775-1797.

Whalen, J.B.; Anderson, R.G.; Struik, L.C.; Villeneuve, M.E. Gochemistry and Nd isotopes of the François Lake plutonic suite, Endako batholith: host and progenitor to the Endako molybdenum camp, central British Columbia. Canadian Journal of Earth Sciences 2001, Volume 38(4), pages 603-618, https://doi.org/10.1139/e00-080.

Wen, G.; Li, J.W.; Hofstra, A.H.; Koenig, A.E.; Lowers, H.A.; Adams, D. Hydrothermal reequilibration of igneous magnetite in altered granitic plutons and its implications for magnetite classification schemes: Insights from the Handan-Xingtai iron district, North China Craton Guang. Geochimica et Cosmochima Acta 2017, Volume 213, pages 255–270.

White, N.C.; Hedenquist J.W. Epithermal gold deposits: styles, characteristics and exploration. Society of Economic Geologists Newsletter, 1995, Volume 23, pages. 1, 9-13.

Whitney, D.; Evans, B.W. Abbreviations for Names of Rock-Forming Minerals. American Mineralogist 2010, Volume 95(1), pages 185-187, doi:10.2138/am.2010.3371.

Wijbrans, C.H.; Klemme, S.; Berndt, J.; Vollmer, C. Experimental determination of trace element partition coefficients between spinel and silicate melt: The influence of chemical composition and oxygen fugacity. Contributions to Mineralogy and Petrology 2015, Volume 69(4), pages 45-77. doi: 10.1007/s00410-015-1128-5.

Wilkinson, J.J. Triggers for the formation of porphyry ore deposits in magmatic arcs. Nature Geoscience 2013, Volume 6(11), pages 917–925.

Williams-Jones, A.E.; Heinrich, C.A. Vapor transport of metals and the formation of magmatic-hydrothermal ore deposits. Economic Geology 2005, Volume 100, pages 1287–1312.

Wilson, A.J. The geology, genesis and exploration context of the Cadia gold-copper porphyry deposits, NSW, Australia. Unpublished Ph.D. thesis, University of Tasmania, 2003, 335 pp.

Wohlgemuth-Ueberwasser, C.C.; Viljoen, F.; Petersen, S.; Vorster, C. Distribution and solubility limits of trace elements in hydrothermal black smoker sulfides: an insitu LA-ICP-MS study. Geochimica et Cosmochimica Acta 2015, Volume 159, pages 16–41.

Wortel, M.J.R.; Spakman, W. Subduction and slab detachment in the Mediterranean-Carpathian region: Science 2000, Volume 290, pages 1910-1917.

Wuthrich, E. Low Temperature Thermochronology of the North Aegean Rhodope Massif. Ph.D. Thesis, Swiss Federal Institute of Technology, Zurich, Switzerland, 2009.

Yang, X.-M.; Lentz, D.R.; McCutcheon, S.R. Petrochemical evolution of subvolcanic granitoid intrusions within the Late Devonian Mount Pleasant caldera, southwestern New Brunswick, Canada: Comparison of Au versus Sn-W-Mo-polymetallic mineralization systems. Atlantic Geology 2003, Volume 39, pages 97–121.

Zwahlen, C.; Cioldi, S.; Wagner, T.; Rey, R.; Heinrich, C. The porphyry Cu–(Mo–Au) deposit at Altar (Argentina): tracing gold distribution by vein mapping and LA–ICPMS mineral analysis. Economic Geology 2014,Volume 109, pages 1341–1358.

Appendix A – Sample Inventory

Table A1. Code, sampling season/date, coordinates (Greek Grid/ΕΓΣΑ '87) analytical technique employed for every sample. Abbreviations: MA = magmatic rock; MI = mineralized magmatic rock; SE = mineralized sedimentary rock. KMSP series = broad area of Sapes; KMPR series = broad area of Pagoni Rachi.

No.	Sample code	Date	Rock type	XRD	SWIR	ICP-MS	XRF	THIN/POL	POL
1	KMSP-1	10/8/2013	MI	-	✓	✓	-	✓	✓
2	KMSP-2	10/8/2013	MI	✓	✓	-	-	✓	✓
3	KMSP-3	10/8/2013	MI	✓	✓	✓	-	✓	✓
4	KMSP-4a	10/8/2013	MI	-	✓	✓	-	✓	-
5	KMSP-4b	10/8/2013	MI	✓	✓	✓	-	-	✓
6	KMSP-5	10/8/2013	MI	✓	-	-	-	✓	-
7	KMSP-6	10/8/2013	MI	✓	-	-	-	-	-
8	KMSP-7	12/8/2013	MI	-	-	-	-	-	✓
9	KMSP-8	12/8/2013	MI	✓	-	-	-	-	-
10	KMSP-9	18/8/2013	MI	-	✓	-	-	-	-
11	KMSP-10	18/8/2013	MI	-	✓	-	-	-	-
12	KMSP-11	18/8/2013	MI	-	✓	-	-	✓	✓
13	KMSP-12	18/8/2013	MI	-	✓	-	-	✓	✓
14	KMSP-13	18/8/2013	MI	-	✓	-	-	-	✓
15	KMSP-14	18/8/2013	MA	-	✓	-	-	✓	-
16	KMSP-15	18/8/2013	SE	-	✓	-	-	✓	-
17	KMSP-16	18/8/2013	MA	✓	-	✓-	✓	✓	-
18	KMSP-17a	18/8/2013	MI	-	-	-	-	-	-
19	KMSP-17b	18/8/2013	MI	-	-	✓	-	-	-
20	KMSP-18	18/8/2013	MI	-	✓	-	-	-	-

21	KMSP-19	18/8/2013	MI	-	✓	-	-	-	-
22	KMSP-20	18/8/2013	MI	-	✓	-	-	-	-
23	KMSP-21	18/8/2013	MI	-	✓	-	-	-	-
24	KMSP-22a	19/8/2013	MI	-	-	-	-	-	-
25	KMSP-22b	19/8/2013	MA	-	-	✓	✓	-	-
26	KMSP-23	19/8/2013	MI	✓	✓	-	-	✓	✓
27	KMSP-24	19/8/2013	MI	-	✓	-	-	✓	-
28	KMSP-25	19/8/2013	MA	-	-	✓	✓	✓	-
29	KMSP-26a	19/8/2013	MI	✓	-	-	-	✓	-
30	KMSP-26b	19/8/2013	MI	✓	-	-	-	-	-
31	KMSP-26c	19/8/2013	MI	✓	-	-	-	✓	✓
32	KMSP-26d	19/8/2013	MI	✓	-	-	-	-	✓
33	KMSP-27	19/8/2013	MI	✓	✓	-	-	✓	✓
34	KMSP-28	19/8/2013	MI	✓	✓	-	-	✓	-
35	KMSP-29	19/8/2013	MI	-	✓	-	-	-	-
36	KMSP-30	19/8/2013	MI	✓	✓	-	-	✓	-
37	KMSP-31	19/8/2013	MI	✓	✓	-	-	✓	-
38	KMSP-32	20/8/2013	MI	-	-	-	-	-	-
39	KMSP-33	23/8/2013	MA	-	✓	✓	✓	✓	-
40	KMSP-34	24/8/2013	MA	-	-	✓	✓	✓	-
41	KMSP-35	28/8/2013	MI	-	-	✓	-	✓	-
42	KMSP-36	28/8/2013	MI	-	-	✓	-	✓	-
43	KMSP-37	28/8/2013	MI	-	-	✓	-	✓	✓
44	KMSP-38	10/10/2013	MA	-	-	✓	✓	✓	-
45	KMSP-39	10/10/2013	MA	-	-	✓	✓	✓	-
46	KMSP-40	10/10/2013	MI	-	-	-	-	-	-
47	KMSP-41	10/10/2013	MI	-	-	-	-	-	-

48	KMSP-42	-10/10/2013	MI	-	-	-	-	-	✓
49	KMSP-43	26/6/2014	MI	✓	✓	✓	-	✓	-
50	KSMP-44	26/6/2014	MI	-	-	✓	-	-	-
51	KMSP-45	27/6/2014	MI	-	-	✓	-	✓	✓
52	KMSP-46	28/6/2014	SE	-	-	✓	-	-	-
53	KMSP-47	28/6/2014	SE	-	-	✓	-	-	-
54	KMSP-48	28/6/2014	SE	-	-	✓	-	-	✓
55	KMSP-49	28/6/2014	MI	-	-	✓	-	✓	✓
56	KMSP-50	30/6/2014	MI	✓	✓	✓	-	✓	-
57	KMSP-51	30/6/2014	MI	✓	✓	✓	-	✓	-
58	KMSP-52	1/7/2014	MA	-	-	✓	✓	✓	-
59	KMSP-53	1/7/2014	MA	-	-	-	-	✓	-
60	KMSP-54	1/7/2014	MI	-	-	✓	-	-	-
61	KMSP-55	2/7/2014	MA	-	-	✓	✓	✓	-
62	KMSP-56	2/7/2014	MA	-	-	-	-	✓	-
63	KMSP-57	2/7/2014	MA	-	✓	✓	✓	✓	-
64	KMSP-58	7/7/2014	MI	-	✓	✓	-	-	-
65	KMSP-59	10/7/2014	MI	-	-	✓	-	-	-
66	KMSP-60	10/7/2014	MI	-	-	✓	-	-	-
67	KMSP-61	13/7/2014	MI	✓	✓	✓	-	✓	-
68	KMSP-62	13/7/2014	MI	-	-	✓	-	✓	✓
69	KMSP-62b	13/7/2014	MA	-	-	-	-	✓	-
70	KMSP-63	13/7/2014	MI	-	-	✓	-	-	-
71	KMSP-64	15/7/2014	MI	✓	✓	✓	-	-	✓
72	KMSP-65	15/7/2014	MI	✓	✓	✓	-	✓	✓
73	KMSP-66	15/7/2014	MI	-	-	✓	-	-	-
74	KMSP-67	16/7/2014	MI	✓	✓	✓	-	✓	✓

75	KMSP-68	17/7/2014	MI	-	-	✓	-	✓	-
76	KMSP-69	18/7/2014	MI	✓	✓	✓	-	✓	-
77	KMSP-70	18/7/2014	MI	✓	-	✓	-	✓	-
78	KMSP-71	18/7/2014	MI	-	-	✓	-	✓	-
79	KMSP-72	18/7/2014	MI	-	-	✓	-	✓	-
80	KMSP-73	18/7/2014	MI	-	-	✓	-	✓	-
81	KMSP-74	18/7/2014	MI	✓	✓	✓	-	✓	-
82	KMSP-75	18/7/2014	MI	✓	-	✓	-	✓	-
83	KMSP-76	18/7/2014	MI	✓	-	✓	-	✓	-
84	KMSP-77	19/7/2014	MI	✓	✓	✓	-	✓	✓
85	KMSP-78	9/10/2014	MI	-	-	✓	-	-	✓
86	KMSP-79	10/10/2014	MI	-	-	✓	-	-	✓
87	KMSP-80a	10/10/2014	MI	-	✓	✓	✓	✓	-
88	KMSP-80b	10/10/2014	MI	✓	-	✓	-	✓	-
89	KMSP-81	10/10/2014	MA	✓	✓	-	-	✓	✓
90	KMSP-82	10/10/2014	MI	✓	-	-	-	✓	-
91	KMSP-83	11/10/2014	MI	-	-	✓	-	-	-
92	KMSP-84	11/10/2014	MI	-	-	✓	-	✓	✓
93	KMSP-85	11/10/2014	MI	-	-	✓	-	-	-
94	KMSP-86	11/10/2014	MI	-	-	✓	-	-	-
95	KMSP-87	11/10/2014	MA	-	✓	✓	✓	✓	-
96	KMSP-88	12/10/2014	MA	-	-	-	-	✓	-
97	KMSP-89	12/10/2014	MA	-	✓	-	-	✓	-
98	KMSP-90	13/10/2014	MI	-	✓	✓	-	✓	-
99	KMPR-1	30/9/2013	MI	-	-	-	-	✓	-
100	KMPR-2	30/9/2013	MI	-	-	-	-	✓	-
101	KMPR-2b	30/9/2013	MI	-	-	-	-	✓	-

102	KMPR-3	30/9/2013	MI	✓	✓	✓	-	✓	✓
103	KMPR-4	30/9/2013	MI	✓	-	✓	-	✓	-
104	KMPR-5	30/9/2013	MI	-	-	✓	-	✓	-
105	KMPR-6	30/9/2013	MI	✓	✓	✓	-	-	✓
106	KMPR-7	2/10/2013	MI	-	-	✓	-	-	-
107	KMPR-8	2/10/2013	MI	✓	-	✓	-	✓	-
108	KMPR-9	2/10/2013	MI	-	-	✓	-	-	-
109	KMPR-10	2/10/2013	MI	-	-	✓	-	-	-
110	KMPR-11	2/10/2013	MI	-	-	✓	-	-	-
111	KMPR-12	2/10/2013	MI	-	-	✓	-	-	-
112	KMPR-13	2/10/2013	MI	-	-	✓	-	-	-
113	KMPR-14	2/10/2013	MI	-	-	✓	-	-	-
114	KMPR-15	2/10/2013	MI	-	✓	✓	-	-	✓
115	KMPR-16	2/10/2013	MI	-	-	✓	-	✓	-
116	KMPR-17	2/10/2013	MI	-	-	✓	-	✓	-
117	KMPR-18	2/10/2013	MI	-	-	✓	-	-	-
118	KMPR-19	3/10/2013	MI	-	✓	✓	-	-	-
119	KMPR-20	3/10/2013	MI	-	-	-	-	-	-
120	KMPR-21	3/10/2013	MI	✓	-	✓	-	✓	✓
121	KMPR-22	3/10/2013	MI	-	-	✓	-	-	-
122	KMPR-23	3/10/2013	MI	-	-	✓	-	-	-
123	KMPR-24	3/10/2013	MI	-	-	✓	-	-	-
124	KMPR-25	3/10/2013	MI	-	✓	✓	-	-	-
125	KMPR-26	3/10/2013	MI	-	-	✓	-	-	-
126	KMPR-27	3/10/2013	MI	-	-	✓	-	-	-
127	KMPR-28	3/10/2013	MI	-	-	✓	-	-	✓
128	KMPR-29	3/10/2013	MI	-	-	-	-	-	✓

129	KMPR-30	3/10/2013	MI	-	-	-	-	✓	-
130	KMPR-31	4/10/2013	MI	-	✓	-	-	✓	-
131	KMPR-32	4/10/2013	MI	-	-	✓	-	✓	-
132	KMPR-33	6/10/2013	MI	-	-	✓	-	-	✓
133	KMPR-34	6/10/2013	MI	✓	✓	✓	-	✓	✓
134	KMPR-35	6/10/2013	MI	-	-	-	-	-	-
135	KMPR-36	6/10/2013	MI	-	-	✓	-	✓	-
136	KMPR-37	6/10/2013	MI	-	✓	✓	-	✓	✓
137	KMPR-38	6/10/2013	MI		✓	-	-	✓	✓
138	KMPR-39	6/10/2013	MI		-	-	-	-	✓
139	KMPR-40	6/10/2013	MI		-	✓	-	✓	-
140	KMPR-41	6/10/2013	MI	✓	✓	✓	-	✓	-
141	KMPR-42	6/10/2013	MI		-	-	-	✓	✓
142	KMPR-43	6/10/2013	MI	-	-	✓	-	✓	✓
143	KMPR-44	6/10/2013	MI	-	-	✓	-	✓	✓
144	KMPR-45	7/10/2013	MI	-	-	-	-	-	-
145	KMPR-46	7/10/2013	MI	-	-	-	-	-	-
146	KMPR-47	7/10/2013	MI	-	-	✓	-	✓	-
147	KMPR-48	7/10/2013	MI	✓	-	-	-	-	✓
148	KMPR-49	7/10/2013	MI	✓	✓	-	-	-	-
149	KMPR-50	7/10/2013	MI	-	✓	-	-	-	-
150	KMPR-51	7/10/2013	MA	✓	-	✓	-	-	✓
151	KMPR-52	7/10/2013	MI	-	✓	✓	-	-	-
152	KMPR-53	7/10/2013	MI	-	✓	-	-	-	✓
153	KMPR-54	7/10/2013	MI	-	-	-	-	✓	✓
154	KMPR-55	7/10/2013	MI	-	-	✓	-	✓	✓
155	KMPR-56	8/10/2013	MI	-	-	✓	-	-	✓

156	KMPR-57	8/10/2013	MI	-	✓	✓	-	-	-
157	KMPR-58	8/10/2013	MI	-	-	✓	-	-	-
158	KMPR-59	8/10/2013	MI	-	-	✓	-	-	-
159	KMPR-60	8/10/2013	MI	-	-	✓	-	✓	-
160	KMPR-61	8/10/2013	MI	-	-	✓	-	✓	-
161	KMPR-62	8/10/2013	MI	-	-	✓	-	-	-
162	KMPR-63	8/10/2013	MI	-	-	✓	-	-	-
163	KMPR-64	9/10/2013	MI	✓	✓	✓	-	✓	-
164	KMPR-65	9/10/2013	MI	-	-	-	-	✓	✓
165	KMPR-66	9/10/2013	MI	-	-	✓	-	-	✓
166	KMPR-67	9/10/2013	MI	✓	✓	✓	-	✓	✓
167	KMPR-68	9/10/2013	MI	-	✓	✓	-	✓	✓
168	KMPR-68b	9/10/2013	MI	-	✓	✓	-	✓	✓
169	KMPR-69	11/10/2013	MI	-	-	✓	-	-	-
170	KMPR-70	11/10/2013	MI	-	-	✓	-	-	-
171	KMPR-71	11/10/2013	MI	-	-	✓	-	-	-
172	KMPR-72	3/7/2014	MI	-	✓	-	-	✓	✓
173	KMPR-73	19/8/2014	MI	-	-	✓	-	-	✓
174	KMPR-74	19/8/2014	MI	✓	✓	✓	-	✓	-
175	KMPR-75a	19/8/2014	MI	-	✓	✓	-	✓	✓
176	KMPR75b	19/8/2014	MI	-	-	✓	-	-	-
177	KMPR76	22/8/2014	MI	-	-	✓	-	-	-
178	KMPR-77a	22/8/2014	MI	✓	✓	✓	-	✓	✓
179	KMPR-77b	22/8/2014	MI	-	-	✓	-	-	-
180	KMPR-78	6/10/2014	MI	-	-	✓	-	-	
181	KMPR-79	6/10/2014	MI	-	-	✓	-	-	✓
182	KMPR-80	6/10/2014	MA	-	✓	✓	✓	✓	-

183	KMPR-81	6/10/2014	MA	-	✓	✓	✓	✓	-
184	KMPR-82	7/10/2014	MA	-	✓	✓	✓	✓	-
185	KMPR-83	8/10/2014	MI	-	✓	-	-	-	✓
186	KMPR-84	8/10/2014	MI	-	✓	✓	-	✓	-
187	KMPR-85	8/10/2014	MA	-	-	✓	✓	✓	-
188	KMPR-86	8/10/2014	MA	-	-	-	-	✓	-
189	KMPR-87	12/10/2014	SE	✓	✓	✓	-	-	✓
190	KMPR-88	12/10/2014	MA	-	✓	✓	✓	✓	-
191	KMPR-89	12/10/2014	MI	-	-	✓	-	-	-
192	KMPR-90	12/10/2014	MI	-	-	✓	-	-	-
194	KMPR-91	12/10/2014	MI	-	-	✓	-	-	-
195	KMPR-92	13/10/2014	SE	-	-	✓	-	-	✓
196	KMPR-93	14/10/2014	MI	-	-	✓	-	-	✓
197	KMPR-94	15/10/2014	MI	-	-	✓	-	-	-
198	KMPR-95	6/10/2018	MA	-	-	✓	✓	✓	-

Appendix B – EPMA data from alteration and ore minerals.

Table B.1. Selected EPMA data of magmatic biotite (sample KMPR88); bd: below detection; apfu: atoms per formula unit.

analysis	1	2	3	4	5	6	7	8	9	10	11	12	13	14	15
SiO_2	37.44	37.23	38.01	37.71	37.26	37.41	37.99	37.86	37.89	37.65	37.91	38.02	38.11	37.96	37.78
TiO_2	3.62	3.56	3.84	3.51	3.90	4.08	3.88	4.41	4.31	4.01	4.12	3.98	3.36	4.12	4.09
Al_2O_3	14.16	14.15	14.25	14.25	14.57	14.61	14.44	14.32	14.46	14.32	14.25	14.36	14.35	14.22	14.17
FeO	13.89	14.08	13.20	13.70	13.54	13.78	14.62	13.48	13.46	13.42	13.56	13.49	13.72	13.56	13.71
MnO	0.18	0.13	0.18	0.13	0.06	0.15	0.15	0.15	0.09	0.12	0.11	0.09	0.15	0.17	0.18
MgO	15.97	16.17	16.09	15.80	15.95	15.82	15.69	16.26	16.21	15.89	15.75	15.93	15.95	16.12	16.11
CaO	0.01	0.06	0.06	bdl	0.12	0.08	0.07	0.08	0.08	bdl	0.01	0.06	bdl	bdl	0.12
Na_2O	0.45	0.38	0.35	0.32	0.38	0.34	0.38	0.40	0.25	0.29	0.41	0.36	0.23	0.41	0.38
K_2O	8.66	8.31	8.64	8.98	8.49	9.03	8.82	8.45	8.78	8.45	8.65	8.45	8.75	8.69	8.56
BaO	0.62	0.63	0.50	0.58	0.63	0.50	0.45	0.59	0.45	0.61	0.45	0.63	0.59	0.48	0.61
F	0.76	0.65	0.48	0.07	0.76	bdl	0.22	0.48	0.21	0.13	0.22	0.14	0.19	0.22	0.24
Cl	0.10	0.19	0.09	0.17	0.03	0.08	0.07	0.13	0.10	0.12	0.11	0.14	0.06	0.08	0.12
Subt	99.54	99.18	99.54	99.16	99.38	99.90	100.74	100.43	100.28	99.00	99.51	99.69	99.50	99.96	99.99
O=F,Cl	0.34	0.32	0.22	0.07	0.33	0.02	0.11	0.23	0.11	0.08	0.12	0.09	0.09	0.11	0.13
Total	99.19	98.86	99.32	99.09	99.05	99.88	100.63	100.20	100.17	98.92	99.39	99.60	99.99	99.85	99.86
apfu								22(O)							
Si	6.159	6.006	6.065	6.038	6.045	6.102	6.017	6.078	5.994	6.035	6.094	6.093	6.099	6.133	5.937
Al iv	1.740	1.896	1.832	1.856	1.854	1.819	1.888	1.807	1.904	1.856	1.827	1.793	1.784	1.778	1.929
Al vi	0.000	0.000	0.000	0.000	0.000	0.000	0.000	0.000	0.000	0.000	0.000	0.000	0.000	0.000	0.000
Ti	0.248	0.249	0.291	0.259	0.244	0.228	0.263	0.280	0.249	0.232	0.201	0.264	0.256	0.216	0.301
Fe	0.174	0.165	0.200	0.184	0.195	0.170	0.181	0.185	0.193	0.153	0.143	0.158	0.173	0.141	0.131
Mn	0.000	0.006	0.003	0.004	0.006	0.006	0.000	0.004	0.000	0.009	0.000	0.000	0.000	0.003	0.004
Mg	5.515	5.552	5.414	5.510	5.470	5.519	5.458	5.465	5.502	5.583	5.586	5.505	5.471	5.550	5.546
Ca	0.002	0.000	0.002	0.001	0.000	0.000	0.000	0.004	0.000	0.000	0.000	0.000	0.000	0.005	0.000
Na	0.096	0.119	0.148	0.127	0.144	0.182	0.141	0.146	0.160	0.164	0.139	0.154	0.152	0.135	0.156
K	1.673	1.701	1.669	1.717	1.766	1.628	1.774	1.661	1.764	1.708	1.717	1.706	1.776	1.715	1.728
Sr	0.000	0.000	0.000	0.000	0.000	0.000	0.000	0.000	0.000	0.000	0.000	0.000	0.000	0.000	0.000

Ba	0.000	0.010	0.003	0.003	0.010	0.008	0.012	0.012	0.001	0.000	0.009	0.003	0.002	0.005	0.008
OH	2.343	1.688	1.989	2.141	2.268	2.040	2.110	1.487	1.801	1.526	1.972	1.593	1.902	1.769	1.763
F	1.639	2.288	1.994	1.833	1.729	1.954	1.873	2.493	2.176	2.452	2.001	2.376	2.076	2.209	2.215
Cl	0.017	0.024	0.017	0.026	0.003	0.005	0.017	0.020	0.023	0.021	0.027	0.031	0.022	0.023	0.022
XTi	0.042	0.042	0.049	0.043	0.041	0.038	0.045	0.047	0.042	0.039	0.034	0.044	0.043	0.037	0.050
XMg	0.969	0.971	0.964	0.968	0.966	0.970	0.968	0.967	0.966	0.973	0.975	0.972	0.969	0.975	0.977

Table B.1. Selected EPMA data of hydrothermal biotite (sample B26); bd: below detection; apfu: atoms per formula unit.

analysis	1	2	3	4	5	6	7	8	9	10	11	12	13	14	15
SiO_2	41.32	40.93	41.47	42.34	42.23	41.74	43.38	40.72	4094	42.96	43.73	40.79	41.67	40.61	40.73
TiO_2	2.37	2.37	2.77	2.47	2.32	2.17	2.52	2.68	2.37	2.20	1.92	2.52	2.44	2.09	2.88
Al_2O_3	10.62	11.50	11.14	11.30	11.25	11.06	11.55	11.03	11.57	11.21	11.12	10.93	10.84	10.97	11.78
FeO	1.50	1.41	1.71	1.58	1.67	1.46	1.56	1.59	1.65	1.30	1.23	1.36	1.48	1.23	1.13
MnO	bdl	0.05	0.03	0.03	0.05	0.05	bdl	0.04	bdl	0.08	bdl	bdl	bdl	0.03	0.03
MgO	26.62	26.62	26.03	26.53	26.24	26.54	26.40	26.37	26.44	26.66	26.89	26.54	26.28	27.08	26.78
CaO	0.01	bdl	0.01	bdl	bdl	bdl	bdl	0.02	bdl	bdl	bdl	bdl	bdl	0.04	bdl
Na_2O	0.36	0.44	0.55	0.47	0.53	0.67	0.52	0.54	0.59	0.60	0.51	0.57	0.56	0.51	0.58
K_2O	9.44	9.53	9.38	9.66	9.90	9.15	10.03	9.37	9.91	9.53	9.66	9.61	9.97	9.78	9.75
BaO	bdl	0.19	0.06	0.06	0.18	0.15	0.23	0.21	0.02	bdl	0.16	0.05	0.04	0.10	0.14
F	3.73	5.17	4.52	4.16	3.91	4.43	4.27	5.67	4.93	5.52	4.54	5.40	4.70	5.08	5.04
Cl	0.07	0.10	0.07	0.11	0.01	0.02	0.07	0.09	0.10	0.09	0.11	0.13	0.09	0.10	0.09
Subt	99.58	100.12	99.94	99.02	99.76	101.67	99.81	99.94	99.46	99.78	99.02	100.63	99.13	99.56	99.84
O=F,Cl	1.59	2.20	1.92	1.78	1.65	1.87	1.81	2.41	2.10	2.34	1.94	2.30	2.00	2.16	2.14
Total	100.99	100.92	101.02	100.96	100.83	99.80	101.80	101.53	101.36	101.44	100.99	101.32	101.13	101.40	101.69
apfu								22(O)							
Si	6.059	6.006	6.065	6.038	6.045	6.102	6.017	6.078	5.994	6.035	6.094	6.093	6.099	6.133	5.937
Al iv	1.740	1.896	1.832	1.856	1.854	1.819	1.888	1.807	1.904	1.856	1.827	1.793	1.784	1.778	1.929
Al vi	0.000	0.000	0.000	0.000	0.000	0.000	0.000	0.000	0.000	0.000	0.000	0.000	0.000	0.000	0.000
Ti	0.248	0.249	0.291	0.259	0.244	0.228	0.263	0.280	0.249	0.232	0.201	0.264	0.256	0.216	0.301
Fe	0.174	0.165	0.200	0.184	0.195	0.170	0.181	0.185	0.193	0.153	0.143	0.158	0.173	0.141	0.131

Mn	0.000	0.006	0.003	0.004	0.006	0.006	0.000	0.004	0.000	0.009	0.000	0.000	0.000	0.003	0.004
Mg	5.515	5.552	5.414	5.510	5.470	5.519	5.458	5.465	5.502	5.583	5.586	5.505	5.471	5.550	5.546
Ca	0.002	0.000	0.002	0.001	0.000	0.000	0.000	0.004	0.000	0.000	0.000	0.000	0.000	0.005	0.000
Na	0.096	0.119	0.148	0.127	0.144	0.182	0.141	0.146	0.160	0.164	0.139	0.154	0.152	0.135	0.156
K	1.673	1.701	1.669	1.717	1.766	1.628	1.774	1.661	1.764	1.708	1.717	1.706	1.776	1.715	1.728
Sr	0.000	0.000	0.000	0.000	0.000	0.000	0.000	0.000	0.000	0.000	0.000	0.000	0.000	0.000	0.000
Ba	0.000	0.010	0.003	0.003	0.010	0.008	0.012	0.012	0.001	0.000	0.009	0.003	0.002	0.005	0.008
OH	2.343	1.688	1.989	2.141	2.268	2.040	2.110	1.487	1.801	1.526	1.972	1.593	1.902	1.769	1.763
F	1.639	2.288	1.994	1.833	1.729	1.954	1.873	2.493	2.176	2.452	2.001	2.376	2.076	2.209	2.215
Cl	0.017	0.024	0.017	0.026	0.003	0.005	0.017	0.020	0.023	0.021	0.027	0.031	0.022	0.023	0.022
XTi	0.042	0.042	0.049	0.043	0.041	0.038	0.045	0.047	0.042	0.039	0.034	0.044	0.043	0.037	0.050
XMg	0.969	0.971	0.964	0.968	0.966	0.970	0.968	0.967	0.966	0.973	0.975	0.972	0.969	0.975	0.977

Table B.1. Selected EPMA data of hydrothermal biotite (sample P62); bd: below detection; apfu: atoms per formula unit.

analysis	1	2	3	4	5	6	7	8	9	10	11	12	13	14	15
SiO_2	41.01	39.70	41.69	40.87	40.35	40.64	40.05	40.42	39.71	39.46	40.99	40.57	40.06	39.70	40.62
TiO_2	4.89	4.93	5.03	4.45	4.80	2.89	4.33	3.53	5.78	5.45	4.75	5.08	5.28	7.19	6.05
Al_2O_3	12.33	12.23	12.30	11.87	12.05	11.99	11.93	11.97	12.82	13.22	12.92	12.25	12.20	12.93	12.38
FeO	6.53	6.05	6.20	6.22	6.02	5.28	5.97	5.69	6.71	7.23	6.85	6.48	5.95	6.96	6.26
MnO	0.05	bdl	0.06	bdl	0.03	0.05	0.00	0.04	0.03	0.00	0.10	0.01	bdl	0.06	0.03
MgO	20.35	20.75	20.74	20.55	20.34	21.29	21.66	21.52	20.01	19.33	21.29	20.77	21.62	19.28	20.08
CaO	bdl	0.03	bdl	0.04	bdl	0.01	0.01	bdl	bdl	bdl	bdl	bdl	bdl	bdl	bdl
Na_2O	0.45	0.48	0.41	0.39	0.50	0.23	0.37	0.27	0.13	0.34	0.38	0.36	0.26	0.37	0.28
K_2O	9.78	9.39	9.70	9.90	10.00	9.87	9.77	9.58	9.85	10.26	10.31	10.31	10.11	9.12	9.52
BaO	0.22	0.24	0.22	0.16	0.27	0.17	0.21	0.22	0.44	0.12	0.27	0.09	0.13	0.17	0.31
F	2.52	2.85	3.03	2.40	3.41	2.13	2.36	2.82	1.41	1.82	2.40	2.64	2.53	2.03	2.02
Cl	0.28	0.19	0.26	0.16	0.21	0.11	0.12	0.21	0.19	0.19	0.23	0.15	0.19	0.20	0.16
Subt	99.69	98.44	99.09	99.55	98.89	99.90	99.16	98.65	98.77	98.55	98.67	998.41	99.31	99.31	100.90
O=F,Cl	1.24	1.33	1.05	1.48	0.92	1.02	1.23	0.64	0.81	1.06	1.14	1.11	0.90	0.90	0.89
Total	101.45	101.11	101.04	101.07	100.96	101.88	100.93	101.02	100.96	101.48	101.53	102.30	102.41	101.41	101.02

apfu							22(O)								
Si	5.917	5.841	5.921	5.866	5.991	5.942	5.976	5.782	5.767	5.760	5.870	5.870	5.717	5.717	5.807
Al iv	2.046	2.031	1.979	2.015	1.986	1.987	1.988	2.146	2.221	2.140	2.039	2.007	2.141	2.141	2.086
Al vi	0.000	0.000	0.000	0.000	0.000	0.000	0.000	0.000	0.000	0.000	0.000	0.000	0.000	0.000	0.000
Ti	0.526	0.530	0.473	0.512	0.305	0.460	0.374	0.617	0.584	0.502	0.539	0.554	0.760	0.760	0.650
Fe	0.718	0.726	0.736	0.714	0.620	0.705	0.670	0.797	0.862	0.805	0.765	0.695	0.818	0.818	0.748
Mn	0.000	0.008	0.000	0.003	0.007	0.000	0.005	0.003	0.000	0.011	0.001	0.000	0.008	0.008	0.004
Mg	4.389	4.540	4.543	4.513	4.878	4.562	4.729	4.236	4.107	4.460	4.372	4.498	4.037	4.037	4.279
Ca	0.005	0.000	0.006	0.000	0.001	0.001	0.000	0.000	0.000	0.000	0.000	0.000	0.000	0.000	0.000
Na	0.131	0.112	0.106	0.138	0.062	0.102	0.075	0.037	0.095	0.103	0.098	0.071	0.102	0.102	0.079
K	1.700	1.733	1.786	1.809	1.769	1.761	1.722	1.784	1.865	1.848	1.857	1.800	1.813	1.813	1.736
Sr	0.000	0.000	0.000	0.000	0.000	0.000	0.000	0.000	0.000	0.000	0.000	0.000	0.000	0.000	0.000
Ba	0.014	0.012	0.009	0.015	0.009	0.011	0.012	0.024	0.007	0.015	0.005	0.007	0.009	0.009	0.017
OH	2.674	2.597	2.888	2.421	3.028	2.916	2.694	3.322	3.133	2.879	2.786	2.839	3.051	3.051	3.049
F	1.279	1.343	1.073	1.530	0.946	1.055	1.256	0.633	0.820	1.067	1.179	1.117	0.902	0.902	0.913
Cl	0.046	0.061	0.038	0.050	0.026	0.029	0.050	0.045	0.046	0.054	0.035	0.044	0.048	0.048	0.038
XTi	0.093	0.091	0.082	0.089	0.053	0.080	0.065	0.109	0.105	0.087	0.095	0.096	0.135	0.135	0.115
XMg	0.859	0.862	0.861	0.863	0.887	0.866	0.876	0.842	0.827	0.847	0.851	0.866	0.832	0.832	0.851

Table B.1. Selected EPMA data of hydrothermal biotite (sample KMPR60); bd: below detection; apfu: atoms per formula unit.

analysis	1	2	3	4	5	6	7	8	9	10	11	12	13	14	15
SiO_2	38.46	39.11	35.76	38.99	38.47	40.17	40.49	39.92	38.95	39.85	40.17	39.87	40.40	40.22	40.86
TiO_2	5.05	4.66	5.47	4.60	4.02	3.91	4.20	3.80	3.93	4.62	3.87	4.50	4.03	3.72	3.59
Al_2O_3	13.00	13.47	16.32	13.48	12.51	11.85	12.53	12.00	12.52	12.57	11.36	12.46	12.06	12.03	11.47
FeO	11.31	11.79	13.66	11.87	13.45	12.36	12.51	12.56	12.87	12.70	11.85	12.98	13.21	12.41	11.95
MnO	0.04	0.07	0.16	0.06	0.24	0.13	0.15	0.08	0.08	0.05	0.05	0.15	0.12	0.07	bdl
MgO	17.20	16.69	13.79	17.17	16.87	17.56	17.52	17.89	17.24	17.28	18.09	17.19	17.52	17.57	18.36
CaO	0.00	0.03	0.03	bdl	bdl	bdl	0.01	0.01	bdl	0.02	bdl	bdl	0.03	bdl	bdl
Na_2O	0.25	0.29	0.38	0.29	0.27	0.19	0.18	0.26	0.18	0.22	0.08	0.24	0.23	0.19	0.21
K_2O	9.81	9.95	9.92	9.65	9.44	9.41	9.56	9.33	9.36	9.27	9.04	9.47	9.38	9.47	9.18

BaO	0.44	0.29	0.21	0.54	0.07	0.29	0.04	0.30	0.18	0.28	0.12	0.31	0.10	0.39	0.03
F	1.04	1.29	0.45	0.99	0.91	1.39	0.63	1.17	0.33	0.88	0.95	1.03	0.95	0.99	0.99
Cl	0.23	0.22	0.28	0.33	0.23	0.33	0.20	0.27	0.24	0.32	0.20	0.25	0.24	0.33	0.18
Subt	100.39	101.30	100.18	101.62	100.03	100.95	101.84	101.08	99.72	101.70	99.34	102.05	101.90	100.94	100.45
O=F,Cl	0.49	0.59	0.25	0.49	0.44	0.66	0.31	0.55	0.19	0.44	0.45	0.49	0.45	0.49	0.46
Total	99.90	100.71	99.93	101.13	99.60	100.29	101.53	100.53	99.52	101.25	98.89	101.56	101.44	100.45	99.99
apfu								22(O)							
Si	5.665	5.712	5.332	5.679	5.718	5.887	5.842	5.841	5.763	5.785	5.929	5.787	5.858	5.886	5.958
Al iv	2.257	2.288	2.668	2.314	2.192	2.047	2.131	2.069	2.183	2.151	1.976	2.132	2.061	2.075	1.972
Al vi	0.000	0.032	0.200	0.000	0.000	0.000	0.000	0.000	0.000	0.000	0.000	0.000	0.000	0.000	0.000
Ti	0.559	0.512	0.613	0.504	0.449	0.431	0.456	0.418	0.437	0.504	0.430	0.491	0.439	0.409	0.394
Fe	1.393	1.440	1.703	1.446	1.672	1.515	1.510	1.537	1.593	1.542	1.463	1.576	1.602	1.519	1.457
Mn	0.005	0.009	0.020	0.007	0.030	0.016	0.018	0.010	0.010	0.006	0.006	0.019	0.015	0.009	0.000
Mg	3.777	3.634	3.065	3.728	3.738	3.836	3.768	3.902	3.802	3.739	3.980	3.720	3.787	3.833	3.991
Ca	0.000	0.005	0.005	0.000	0.000	0.000	0.002	0.002	0.000	0.003	0.000	0.000	0.005	0.000	0.000
Na	0.072	0.081	0.109	0.082	0.077	0.054	0.051	0.075	0.051	0.061	0.022	0.069	0.063	0.054	0.060
K	1.843	1.854	1.887	1.793	1.790	1.759	1.759	1.741	1.766	1.716	1.702	1.753	1.735	1.768	1.708
Sr	0.000	0.000	0.000	0.000	0.000	0.000	0.000	0.000	0.000	0.000	0.000	0.000	0.000	0.000	0.000
Ba	0.025	0.016	0.012	0.031	0.004	0.016	0.002	0.017	0.010	0.016	0.007	0.018	0.006	0.023	0.002
OH	3.457	3.349	3.720	3.461	3.513	3.274	3.664	3.392	3.785	3.515	3.503	3.465	3.504	3.462	3.499
F	0.485	0.596	0.210	0.458	0.430	0.644	0.287	0.541	0.155	0.405	0.446	0.473	0.436	0.457	0.456
Cl	0.059	0.055	0.070	0.080	0.057	0.082	0.049	0.066	0.060	0.080	0.051	0.063	0.059	0.081	0.045
XTi	0.098	0.091	0.110	0.089	0.077	0.075	0.079	0.071	0.075	0.087	0.073	0.085	0.075	0.071	0.067
XMg	0.731	0.716	0.643	0.721	0.691	0.717	0.714	0.717	0.705	0.708	0.731	0.702	0.703	0.716	0.733

Table B.1. Selected EPMA data of hydrothermal biotite (sample KMSP80); bd: below detection; apfu: atoms per formula unit.

analysis	1	2	3	4	5	6	7	8	9	10	11	12	13	14	15
SiO_2	40.56	40.61	40.76	39.96	40.01	40.53	40.75	40.60	40.55	39.87	40.65	39.55	40.15	39.62	39.44
TiO_2	3.85	4.49	4.01	4.43	4.70	4.34	4.02	3.55	3.94	4.32	3.55	3.84	3.52	3.78	3.54
Al_2O_3	11.84	12.11	12.34	12.65	12.74	12.48	12.75	12.91	12.82	12.81	12.07	12.72	12.08	12.54	12.70

FeO	9.45	9.02	9.25	9.81	9.62	8.97	9.47	8.84	9.20	9.40	8.81	9.49	8.73	9.22	8.97
MnO	0.01	bdl	0.12	0.01	0.09	bdl	0.07	0.02	0.05	bdl	0.05	0.08	0.03	0.04	0.02
MgO	19.00	19.57	19.67	19.02	18.77	19.45	19.73	19.93	19.70	19.19	19.88	19.70	20.99	20.33	20.62
CaO	bdl	0.01	bdl	bdl	bdl	0.01	bdl	bdl	0.01	bdl	bdl	bdl	bdl	bdl	bdl
Na_2O	0.29	0.36	0.31	0.34	0.41	0.24	0.33	0.36	0.40	0.40	0.19	0.40	0.27	0.37	0.33
K_2O	9.78	9.08	9.34	9.31	9.58	9.26	9.56	9.49	9.79	9.59	9.61	9.41	9.11	9.65	9.63
BaO	0.02	0.11	0.18	0.21	0.09	0.20	0.09	bdl	0.15	0.09	0.08	0.26	0.07	0.15	bdl
F	1.12	1.56	1.30	0.71	0.86	0.60	0.89	1.19	0.67	1.15	1.15	0.52	0.96	1.19	0.74
Cl	0.12	0.26	0.14	0.22	0.24	0.16	0.26	0.17	0.16	0.18	0.19	0.29	0.23	0.16	0.24
Subt	100.68	100.53	100.94	100.42	100.78	100.11	99.66	98.26	100.59	99.91	100.09	100.83	99.67	98.01	98.87
O=F,Cl	0.50	0.72	0.58	0.35	0.42	0.29	0.43	0.32	0.52	0.53	0.28	0.46	0.54	0.37	0.53
Total	101.18	99.81	100.36	100.07	100.37	99.82	101.22	100.94	100.07	99.39	99.81	100.37	101.13	100.64	101.34
apfu								22(O)							
Si	5.933	5.866	5.866	5.789	5.781	5.850	5.823	5.812	5.773	5.900	5.752	5.891	5.812	5.813	5.748
Al iv	1.992	2.062	2.093	2.160	2.170	2.123	2.147	2.166	2.186	2.065	2.181	2.038	2.115	2.142	2.098
Al vi	0.000	0.000	0.000	0.000	0.000	0.000	0.000	0.000	0.000	0.000	0.000	0.000	0.000	0.000	0.000
Ti	0.413	0.488	0.434	0.483	0.511	0.471	0.432	0.425	0.470	0.387	0.420	0.379	0.407	0.381	0.542
Fe	1.128	1.090	1.113	1.189	1.163	1.083	1.132	1.103	1.138	1.069	1.154	1.045	1.103	1.074	1.126
Mn	0.001	0.000	0.015	0.001	0.011	0.000	0.009	0.006	0.000	0.006	0.010	0.003	0.005	0.002	0.014
Mg	4.256	4.214	4.220	4.107	4.043	4.185	4.203	4.209	4.142	4.327	4.271	4.479	4.336	4.399	4.198
Ca	0.000	0.002	0.000	0.000	0.000	0.002	0.000	0.002	0.000	0.000	0.000	0.000	0.000	0.000	0.002
Na	0.080	0.101	0.086	0.096	0.114	0.068	0.091	0.111	0.113	0.053	0.112	0.075	0.102	0.091	0.134
K	1.781	1.673	1.715	1.720	1.766	1.705	1.742	1.790	1.771	1.779	1.746	1.663	1.761	1.758	1.694
Sr	0.000	0.000	0.000	0.000	0.000	0.000	0.000	0.000	0.000	0.000	0.000	0.000	0.000	0.000	0.000
Ba	0.001	0.006	0.010	0.012	0.005	0.011	0.005	0.008	0.005	0.004	0.015	0.004	0.008	0.000	0.009
OH	3.466	3.223	3.375	3.621	3.549	3.689	3.535	3.657	3.430	3.425	3.690	3.509	3.423	3.606	3.435
F	0.506	0.713	0.592	0.324	0.393	0.273	0.403	0.304	0.527	0.528	0.239	0.436	0.538	0.336	0.524
Cl	0.028	0.064	0.034	0.055	0.058	0.038	0.062	0.039	0.043	0.047	0.071	0.055	0.038	0.058	0.040
XTi	0.071	0.084	0.075	0.084	0.089	0.082	0.075	0.074	0.082	0.067	0.072	0.064	0.070	0.065	0.092
XMg	0.790	0.795	0.791	0.776	0.777	0.794	0.788	0.792	0.784	0.802	0.787	0.811	0.797	0.804	0.788

Table B.2. Selected EPMA data of feldspar group minerals (sodic/potassic-calcic alteration 1-5; sodic/potassic alteration 6-10; propylitic alteration 11-15); bd: below detection; na = not analyzed; apfu: atoms per formula unit.

analysis	1	2	3	4	5	6	7	8	9	10	11	12	13	14	15
SiO_2	62.33	63.85	63.45	62.63	62.99	65.36	63.06	63.51	65.39	66.63	67.45	67.91	67.14	63.04	67.65
TiO_2	0.00	0.10	0.07	0.00	0.02	0.12	0.00	0.00	0.02	0.10	0.05	0.08	0.15	0	0.01
Al_2O_3	23.31	22.65	22.75	23.44	22.46	18.56	23.70	23.42	20.63	20.98	20.88	20.61	20.39	23.08	20.75
FeO	0.06	bdl	0.09	0.13	0.06	0.07	0.06	bdl	0.40	0.38	0.61	0.86	0.62	0.02	0.10
CaO	5.44	4.49	4.28	5.14	3.45	0.12	5.44	5.11	2.70	2.00	1.82	1.39	1.64	4.74	1.66
Na_2O	8.03	8.01	8.66	8.07	8.86	0.50	7.90	8.76	10.06	10.95	11.06	11.18	10.71	8.72	10.31
K_2O	0.99	1.20	0.91	1.05	0.74	16.00	1.02	0.41	0.08	0.10	0.20	0.04	0.13	0.12	0.22
BaO	bdl	0.26	bdl	0.11	bdl	0.35	0.32	bdl	0.11	0.10	0.12	0.01	0.03	0.03	0.05
F	na	na	na	na	na	na	na	na	0.23	0.15	bdl	bdl	bdl	0.196	bdl
Cl	na	na	na	na	na	na	na	na	0.10	0.02	0.0064	bdl	bdl	bdl	0.023
Total	100.16	100.55	100.20	100.56	98.58	101.08	101.50	101.21	99.72	101.42	102.21	102.10	100.82	99.96	100.80
apfu								8 (O)							
Si	2.767	2.816	2.806	2.770	2.822	2.993	2.767	2.781	2.886	2.893	2.912	2.928	2.929	2.784	2.940
Al	1.220	1.178	1.186	1.222	1.186	1.002	1.226	1.209	1.073	1.074	1.063	1.048	1.049	1.201	1.063
Ti	0.000	0.003	0.002	0.000	0.001	0.004	0.000	0.000	0.001	0.003	0.002	0.003	0.005	0.000	0.001
Fe	0.002	0.000	0.003	0.005	0.002	0.003	0.002	0.000	0.015	0.014	0.022	0.031	0.023	0.001	0.004
Ca	0.259	0.212	0.203	0.244	0.166	0.006	0.256	0.240	0.128	0.093	0.084	0.064	0.077	0.224	0.077
Na	0.691	0.685	0.743	0.692	0.770	0.044	0.672	0.744	0.861	0.922	0.926	0.935	0.906	0.747	0.869
K	0.056	0.067	0.051	0.059	0.042	0.934	0.057	0.023	0.004	0.006	0.012	0.003	0.007	0.007	0.013
Ba	0.000	0.004	0.000	0.002	0.000	0.006	0.005	0.000	0.002	0.002	0.002	0.000	0.001	0.001	0.001
F	0.000	0.000	0.000	0.000	0.000	0.000	0.000	0.000	0.032	0.021	0.000	0.000	0.000	0.027	0.000
Cl	0.000	0.000	0.000	0.000	0.000	0.000	0.000	0.000	0.008	0.002	0.000	0.000	0.000	0.000	0.002
Or	5.555	6.983	5.145	5.962	4.322	94.926	5.817	2.281	0.431	0.561	1.130	0.265	0.753	0.692	1.321
Ab	68.719	71.019	74.507	69.556	78.736	4.474	68.223	73.898	86.709	90.322	90.628	93.307	91.504	76.368	90.616
An	25.726	21.999	20.349	24.482	16.942	0.600	25.961	23.821	12.860	9.116	8.241	6.428	7.743	22.940	8.062

Table B.3. Selected EPMA data of chlorite from sodic/potassic-calcic (sample KMPR74, 1-10) and propylitic (KMPR88, 11-15) alteration; bd: below detection; apfu: atoms per formula unit.

analysis	1	2	3	4	5	6	7	8	9	10	11	12	13	14	15
SiO_2	29.63	29.36	32.95	29.69	30.23	29.60	28.97	29.89	29.67	28.58	29.04	29.05	29.00	29.05	29.19
TiO_2	0.18	0.10	0.02	0.05	0.18	0.06	0.11	0.00	0.13	0.02	0.11	0.02	0.08	0.13	0.00
Al_2O_3	17.63	17.86	17.69	18.03	18.90	18.59	19.79	17.11	17.29	17.69	18.32	17.32	17.44	17.77	17.54
FeO	16.93	15.55	14.75	17.81	14.85	17.60	13.60	19.10	18.64	20.07	18.87	19.25	20.95	17.43	18.76
MnO	0.25	0.17	0.22	0.30	0.27	0.26	0.11	0.50	0.53	0.67	0.27	0.36	0.47	0.36	0.32
MgO	22.82	23.36	21.86	19.40	20.97	21.24	23.76	21.25	20.38	19.89	20.65	20.55	19.78	21.22	20.32
CaO	0.06	0.21	0.33	0.19	0.29	0.09	0.06	0.05	0.14	bdl	0.06	0.06	0.18	0.17	0.08
Na_2O	bdl	0.03	0.02	bdl	0.04	0.05	bdl	0.03	0.02	bdl	bdl	bdl	bdl	0.06	0.04
K_2O	bdl	0.01	bdl	bdl	0.06	0.06	0.01	0.01	bdl	bdl	bdl	bdl	bdl	0.05	bdl
BaO	0.03	bdl	bdl	0.10	bdl	0.03	0.08	0.00	0.07	bdl	bdl	bdl	bdl	bdl	bdl
F	0.40	0.17	0.70	0.29	bdl	0.33	bdl	0.26	0.49	0.26	bdl	0.06	0.19	bdl	bdl
Cl	0.01	0.07	bdl	bdl	bdl	0.02	bdl	bdl	bdl	bdl	bdl	0.03	0.02	bdl	bdl
Cr2O3	0.05	0.02	0.05	0.01	bdl	0.01	0.02	bdl	bdl	bdl	0.02	0.04	0.04	bdl	bdl
Total	99.66	98.66	100.62	97.50	97.89	99.69	98.61	99.90	98.79	98.61	99.21	98.38	99.74	98.00	97.97
O=F,Cl	0.17	0.09	0.29	0.12	bdl	0.14	bdl	0.11	0.21	0.11	bdl	0.03	0.09	bdl	bdl
TOTAL	99.49	98.58	100.32	97.38	97.89	99.55	98.61	99.79	98.59	98.50	99.21	98.34	99.65	98.00	97.97
apfu								28 (O)							
Si	5.887	5.887	6.290	6.042	6.069	5.889	5.775	6.002	5.977	5.859	5.899	5.962	5.904	5.944	6.003
Al iv	2.113	2.113	1.710	1.958	1.931	2.111	2.225	1.998	2.023	2.141	2.101	2.038	2.096	2.056	1.997
Al vi	2.047	2.127	2.349	2.413	2.574	2.287	2.436	2.076	2.128	2.156	2.296	2.165	2.108	2.240	2.266
Ti	0.027	0.015	0.002	0.007	0.027	0.010	0.017	0.000	0.019	0.002	0.017	0.002	0.012	0.020	0.000
Cr	0.008	0.003	0.007	0.001	0.000	0.001	0.004	0.000	0.000	0.000	0.003	0.006	0.006	0.000	0.000
Fe^{3+}	0.169	0.107	0.647	0.385	0.379	0.237	0.138	0.149	0.289	0.124	0.129	0.112	0.114	0.108	0.144
Fe^{2+}	2.644	2.501	1.708	2.647	2.114	2.691	2.130	3.059	2.852	3.317	3.077	3.192	3.454	2.875	3.082
Mn	0.043	0.029	0.036	0.051	0.045	0.044	0.019	0.085	0.090	0.115	0.046	0.062	0.081	0.062	0.055
Mg	6.758	6.982	6.221	5.885	6.276	6.300	7.060	6.361	6.120	6.078	6.253	6.287	6.003	6.472	6.229
Ca	0.013	0.045	0.067	0.041	0.062	0.020	0.013	0.011	0.029	0.000	0.014	0.014	0.039	0.037	0.018
Na	0.000	0.026	0.018	0.026	0.029	0.038	0.000	0.026	0.012	0.001	0.000	0.000	0.000	0.051	0.032
K	0.002	0.005	0.000	0.000	0.030	0.032	0.004	0.007	0.000	0.000	0.002	0.002	0.000	0.026	0.000

Ba	0.005	0.000	0.000	0.017	0.000	0.004	0.012	0.000	0.011	0.000	0.000	0.000	0.000	0.000	0.000
F	0.500	0.210	0.844	0.378	0.000	0.411	0.000	0.331	0.623	0.336	0.000	0.084	0.249	0.000	0.000
Cl	0.007	0.051	0.000	0.000	0.010	0.013	0.000	0.000	0.000	0.000	0.000	0.020	0.015	0.000	0.003

Table B.4. Selected EPMA data of amphibole group minerals from the sodic/potassic-calcic (sample KMPR74, 1-10) and the propylitic (sample KMPR88, 11-15) alteration at Pagoni Rachi; bd: below detection; apfu: atoms per formula unit.

analysis	1	2	3	4	5	6	7	8	9	10	11	12	13	14	15
SiO^2	45.20	49.45	50.33	46.51	49.19	47.16	50.40	53.14	54.61	53.99	43.18	46.94	46.71	47.30	46.40
TiO^2	2.61	1.52	1.36	2.08	1.12	2.17	1.51	0.91	0.79	0.92	2.15	1.59	1.39	1.41	0.86
Al^2O^3	9.47	6.59	5.08	8.15	6.26	7.89	5.51	3.45	3.01	3.14	11.46	8.76	8.98	8.55	10.04
FeO	10.45	9.74	7.40	9.88	8.35	9.34	7.64	6.96	7.02	7.13	14.16	13.53	13.34	13.79	12.94
MnO	0.04	0.13	0.03	0.08	0.07	0.06	0.11	0.14	0.05	0.05	0.29	0.28	0.36	0.59	0.51
MgO	15.36	15.98	18.93	16.38	18.40	16.59	18.35	19.37	20.47	19.44	12.40	13.72	14.11	13.96	14.23
CaO	11.72	11.95	11.71	11.56	11.59	11.05	11.46	11.39	11.51	11.48	11.13	11.02	11.21	10.27	10.15
Na^2O	2.68	1.82	1.95	2.54	2.41	2.48	2.36	1.74	1.52	1.39	1.85	1.64	1.76	1.41	1.38
K^2O	0.78	0.57	0.35	0.90	0.61	0.70	0.44	0.35	0.29	0.46	0.61	0.56	0.58	0.48	0.38
BaO	0.09	bdl	0.13	0.11	0.08	0.14	bdl	bdl	0.06	0.10	0.27	0.12	bdl	bdl	0.30
F	0.49	0.65	0.46	0.38	0.72	0.80	0.71	0.77	0.36	0.69	0.21	bdl	0.08	0.23	bdl
Cl	0.15	0.12	0.21	0.16	0.09	0.12	0.18	0.18	0.13	0.06	0.03	0.05	0.09	bdl	0.06
Cr_2O_3	0.03	bdl	0.02	bdl	bdl	bdl	bdl	bdl	0.03	0.06	0.02	0.08	0.05	bdl	bdl
Total	98.77	98.53	97.96	98.73	98.89	98.50	97.96	98.40	99.65	98.92	98.25	98.29	98.65	97.99	97.24
apfu								23 (O)							
Si	6.527	7.108	5.931	6.686	6.959	6.761	7.132	7.452	7.457	7.513	6.315	6.741	6.682	6.737	6.603
Al iv	1.473	0.892	2.069	1.314	1.041	1.239	0.868	0.548	0.484	0.487	1.685	1.259	1.318	1.263	1.397
Al vi	0.139	0.225	0.222	0.067	0.003	0.094	0.051	0.022	0.000	0.028	0.290	0.223	0.196	0.172	0.287
Ti	0.284	0.164	0.196	0.225	0.119	0.234	0.160	0.096	0.081	0.097	0.237	0.172	0.150	0.151	0.092
Cr	0.004	0.000	0.002	0.000	0.000	0.000	0.000	0.000	0.003	0.007	0.002	0.009	0.005	0.000	0.000
Fe^{3+}	0.297	0.045	0.866	0.350	0.506	0.451	0.295	0.375	0.609	0.369	0.763	0.720	0.787	1.179	1.348
Fe^{2+}	0.965	1.126	0.000	0.837	0.482	0.669	0.609	0.441	0.193	0.461	0.969	0.904	0.809	0.464	0.193
Mn	0.005	0.016	0.003	0.010	0.009	0.007	0.014	0.016	0.006	0.006	0.036	0.034	0.044	0.071	0.062

Mg	3.307	3.424	3.948	3.510	3.881	3.545	3.871	4.049	4.167	4.033	2.703	2.937	3.009	2.964	3.019
Ca	1.813	1.840	1.755	1.781	1.757	1.697	1.737	1.711	1.684	1.712	1.744	1.695	1.718	1.567	1.548
Na	0.686	0.507	0.529	0.708	0.661	0.689	0.648	0.473	0.402	0.375	0.525	0.457	0.488	0.389	0.381
K	0.143	0.105	0.062	0.164	0.109	0.127	0.079	0.063	0.051	0.081	0.113	0.102	0.106	0.088	0.069
Ba	0.005	0.000	0.007	0.006	0.004	0.008	0.000	0.000	0.003	0.005	0.015	0.007	0.000	0.000	0.016
F	0.187	0.296	0.204	0.173	0.324	0.362	0.321	0.341	0.167	0.305	0.061	0.000	0.034	0.067	0.000
Cl	0.038	0.030	0.050	0.039	0.022	0.029	0.043	0.044	0.031	0.014	0.007	0.013	0.021	0.000	0.014

Table B.5. Selected EPMA data of epidote from sodic/potassic-calcic (sample KMPR74, 1-10) and propylitic (KMPR88, 11-15) alteration; bd: below detection; apfu: atoms per formula unit.

analysis	1	2	3	4	5	6	7	8	9	10	11	12	13	14	15
SiO_2	38.71	38.83	38.29	38.56	37.74	38.43	38.30	37.97	37.99	38.79	38.08	38.25	38.88	38.18	37.62
TiO_2	bdl	bdl	0.08	bdl	0.13	0.22	bdl	bdl	bdl	0.22	0.12	0.17	0.25	bdl	bdl
Al_2O_3	24.13	24.25	22.16	21.48	21.75	23.68	22.35	22.42	22.08	22.64	22.59	22.36	22.13	21.77	22.48
FeO	11.01	11.37	12.81	14.66	13.74	10.97	13.26	13.24	14.08	13.44	12.94	12.87	13.21	13.80	12.72
MnO	0.25	0.91	0.16	0.06	0.22	0.32	0.56	0.26	0.50	0.09	0.09	0.12	0.08	0.07	0.13
MgO	0.04	0.09	0.07	0.08	0.06	0.04	0.05	0.20	0.00	0.01	0.02	0.06	0.12	0.07	bdl
CaO	23.24	22.17	22.79	23.47	23.09	22.63	22.60	23.25	22.67	22.53	22.88	22.77	22.99	23.52	23.32
Total	97.38	97.63	96.36	98.31	96.73	96.29	97.12	97.34	97.32	97.72	96.72	96.60	97.66	97.40	96.27
apfu								12.5 (O)							
Si	3.237	3.247	3.292	3.302	3.268	3.250	3.282	3.251	3.274	3.294	3.266	3.281	3.304	3.282	3.246
Ti	0.000	0.000	0.005	0.000	0.009	0.014	0.000	0.000	0.000	0.014	0.008	0.011	0.016	0.000	0.000
Al	2.378	2.390	2.245	2.168	2.219	2.360	2.257	2.262	2.242	2.266	2.283	2.261	2.216	2.206	2.286
Fe^{3+}	0.346	0.358	0.414	0.472	0.448	0.349	0.427	0.427	0.456	0.429	0.418	0.415	0.422	0.446	0.413
Mn	0.018	0.065	0.011	0.005	0.016	0.023	0.040	0.019	0.037	0.007	0.007	0.008	0.006	0.005	0.010
Mg	0.005	0.012	0.009	0.010	0.007	0.005	0.007	0.025	0.000	0.001	0.002	0.008	0.015	0.009	0.000
Ca	2.082	1.986	2.099	2.153	2.142	2.050	2.075	2.133	2.093	2.049	2.102	2.093	2.093	2.166	2.156
X_{Fe} %	12.71	13.01	15.5	17.89	16.78	12.88	15.92	15.86	16.91	15.932	15.46	15.52	16.00	16.83	15.30

Table B.6. Selected EPMA data of sericite from sericitic alteration at Konos Hill (sample KMSP67, 1-9) and Pagoni Rachi (KMPR77a, 10-15) alteration; bd: below detection; apfu: atoms per formula unit.

analysis	1	2	3	4	5	6	7	8	9	10	11	12	13	14	15
SiO_2	49.15	50.11	49.86	49.69	50.12	50.63	50.12	49.89	49.78	50.36	51.03	49.89	49.69	50.31	50.32
TiO_2	0.08	0.12	0.09	0.09	0.06	0.09	0.11	0.13	0.11	0.09	0.08	0.06	0.09	0.09	0.11
Al_2O_3	31.93	30.35	32.96	32.15	33.42	31.89	31.12	29.98	31.01	31.89	29.45	33.12	30.58	33.46	31.26
FeO	0.57	0.45	0.89	0.45	0.38	0.49	0.56	0.45	0.36	0.42	0.12	0.48	0.26	0.24	0.18
MnO	0.04	0.04	bdl	0.08	bdl	0.02	bdl	0.06	0.01	bdl	0.06	0.11	0.04	0	bdl
MgO	1.48	1.75	2.01	2.012	1.63	1.21	0.98	0.78	1.46	2.21	0.98	0.76	2.011	2.12	2.01
CaO	0.09	0.11	0.09	0.11	0.12	0.04	0.21	0.04	0.09	0.01	0.11	0.15	0.11	0.06	0.09
Na_2O	0.46	0.38	0.41	0.96	0.78	1.12	0.89	0.65	0.48	0.18	0.96	0.56	0.48	0.65	0.62
K_2O	9.14	10.11	9.89	8.98	9.14	9.45	9.63	10.11	10.18	9.65	10.12	10.45	8.78	8.16	8.96
F	0.17	0.16	0.11	0.09	0.21	0.11	0.09	0.11	0.11	0.11	0.12	0.13	0.21	0.13	0.09
Cl	0.04	0.01	0.02	bdl	0.06	0.02	0.04	0.04	0.01	0.06	0.04	0.05	0.02	0.01	bdl
Total	93.15	93.491	96.33	94.612	95.812	95.07	93.75	92.24	93.6	94.98	93.07	95.76	92.271	95.2	93.64
apfu								22 (O)							
Si	6.589	6.721	6.500	6.560	6.517	6.660	6.697	6.785	6.671	6.622	6.868	6.552	6.699	6.540	6.681
Ti	0.008	0.012	0.009	0.009	0.006	0.009	0.011	0.013	0.011	0.009	0.008	0.006	0.009	0.009	0.011
Al	5.045	4.797	5.064	5.002	5.132	4.944	4.900	4.805	4.897	4.942	4.671	5.126	4.859	5.126	4.891
Fe^{2+}	0.064	0.050	0.097	0.050	0.041	0.054	0.063	0.051	0.040	0.046	0.014	0.053	0.029	0.026	0.020
Mn	0.005	0.005	0.000	0.009	0.000	0.002	0.000	0.007	0.001	0.000	0.007	0.012	0.005	0.000	0.000
Mg	0.296	0.350	0.391	0.396	0.317	0.237	0.195	0.158	0.292	0.433	0.197	0.149	0.404	0.411	0.398
Ca	0.013	0.002	0.013	0.016	0.017	0.006	0.030	0.006	0.013	0.001	0.016	0.021	0.016	0.008	0.013
Na	0.120	0.099	0.104	0.246	0.197	0.286	0.231	0.171	0.125	0.046	0.250	0.143	0.125	0.164	0.160
K	1.563	1.730	1.645	1.512	1.519	1.586	1.641	1.754	1.740	1.619	1.737	1.751	1.510	1.353	1.517
Cl	0.039	0.036	0.024	0.020	0.046	0.025	0.020	0.025	0.025	0.025	0.027	0.029	0.048	0.022	0.020
F	0.017	0.004	0.008	0.000	0.025	0.008	0.017	0.017	0.004	0.025	0.017	0.021	0.009	0.004	0.000

Table B.7. Selected EPMA data of members of the alunite–natroalunite solid solution (Konos Hill prospect). bdl: below detection limit; apfu: atoms per formula unit.

analysis	1	2	3	4	5	6	7	8	9	10	11	12	13	14	15
wt %															
Al_2O_3	37.90	37.66	39.47	36.54	37.19	37.40	37.65	36.80	36.96	38.08	42,41	36.95	38.24	40.44	39.95
FeO	0.46	0.30	0.23	0.12	0.28	0.17	0.02	0.10	0.07	bd	0.01	bdl	bdl	bdl	0.12
CaO	0.01	0.02	0.05	0.38	0.03	0.07	0.02	bdl	bdl	0.09	0.10	0.01	0.05	0.00	0.05
Na_2O	4.63	5.12	2.57	3.07	4.58	5.01	2.79	1.78	1.97	5.51	5.31	1.97	1.64	1.33	2.18
K_2O	3.52	3.59	3.02	4.91	3.90	3.41	5.75	7.10	6.86	2.6	1.95	7.02	4.71	4.44	3.69
BaO	0.15	0.37	0.21	0.21	bdl	bdl	0.16	bdl	0.12	bdl	bdl	0.46	bdl	bdl	0.38
SrO	bdl	bdl	bdl	0.38	bdl	bdl	0.19	bdl	bdl	bdl	bdl	0.05	bdl	bdl	0.07
La_2O_3	bdl	bdl	bdl	bdl	bdl	bdl	0.26	bdl	bdl	bdl	bdl	0.25	bdl	bdl	bdl
Ce_2O_3	bdl	bdl	bdl	bdl	bdl	bdl	bdl	bdl	0.19	bdl	bdl	0.36	bdl	bdl	0.15
Nd_2O_3	bdl	bdl	bdl	0.28	bdl	bdl	0.33	bdl	bdl	bdl	bdl	0.27	0.25	0.11	bdl
SO_3	34.74	35.16	36.72	34.05	34.24	34.57	34.73	33.69	34.52	34.46	35.48	33.66	33.93	36.46	35.05
Total	81.61	82.32	82.90	79.97	80.94	81.28	81.90	79.49	80.69	81.00	85.81	81.01	79.89	83.52	81.64
apfu								11 (O)							
Al	3.218	3.177	3.238	3.106	3.198	3.190	3.218	3.231	3.302	3.241	3.391	3.229	3.223	3.309	3.391
Fe	0.028	0.018	0.014	0.01	0.017	0.01	0.000	0.006	0.004	0.000	0.000	0.000	0.000	0.000	0.007
Ca	0.001	0.001	0.004	0.029	0.002	0.005	0.001	0.000	0.000	0.007	0.007	0.001	0.004	0.000	0.004
Na	0.646	0.708	0.317	0.335	0.649	0.704	0.392	0.258	0.279	0.772	0.701	0.283	0.228	0.181	0.296
K	0.324	0.332	0.298	0.447	0.363	0.315	0.532	0.675	0.644	0.240	0.169	0.664	0.430	0.400	0.331
Ba	0.004	0.010	0.006	0.006	0.002	0.004	0.004	0.000	0.003	0.004	0.004	0.013	0.021	0.008	0.010
Sr	0.000	0.000	0.011	0.006	0.006	0.000	0.008	0.000	0.000	0.005	0.009	0.002	0.010	0.000	0.003
La	0.000	0.000	0.000	0.000	0.022	0.007	0.007	0.000	0.000	0.000	0.005	0.007	0.002	0.011	0.000
Ce	0.003	0.000	0.012	0.000	0.010	0.003	0.000	0.000	0.005	0.000	0.001	0.010	0.000	0.001	0.004
Nd	0.000	0.000	0.000	0.000	0.003	0.000	0.009	0.000	0.000	0.000	0.000	0.007	0.007	0.003	0.000
S	1.878	1.889	1.789	1.716	1.879	1.891	1.890	1.894	1.904	1.868	1.816	1.873	1.738	1.855	1.847

Table B.8. EPMA data of electrum (1-7), native gold (8-22) and Ag-Au alloy (23-25) from the Pagoni Rachi prospect.

Sample KMPR74 1-6 (M-vein, potassic alter.); KMPR66 7-15 (D-type vein, sericitic alter.) ; bdl = below detection limit.															
analysis	1	2	3	4	5	6	7	8	9	10	11	12	13	14	15
wt%															
Au	87.20	88.41	87.75	86.76	87.19	87.47	87.92	96.75	96.87	97.91	96.38	98.85	95.45	94.90	95.31
Ag	12.45	12.33	12.61	12.61	12.08	11.99	12.19	2.04	2.11	2.13	1.93	1.73	4.47	5.33	5.57
Te	0.03	bdl	bdl	0.02	0.02	0.03	bdl	bdl	bdl	0.01	bdl	bdl	0.06	0.00	0.08
Bi	bdl	bdl	bdl	bdl	bdl	bdl	bdl	bdl	bdl	bdl	bdl	bdl	bdl	bdl	bdl
Cu	0.11	0.18	0.15	0.32	0.25	0.43	0.33	bdl	bdl	bdl	bdl	bdl	bdl	bdl	bdl
Fe	0.03	0.05	0.02	0.04	0.04	0.06	0.03	0.34	0.34	0.32	0.43	0.39	0.55	0.18	0.20
Total	99.82	100.98	100.53	99.75	99.57	99.98	100.47	99.12	99.32	100.37	98.75	100.96	100.54	99.51	101.15
apfu															
Au	0.790	0.792	0.788	0.782	0.791	0.788	0.790	0.952	0.951	0.951	0.950	0.956	0.903	0.897	0.897
Ag	0.206	0.202	0.207	0.207	0.200	0.197	0.200	0.037	0.038	0.038	0.035	0.031	0.077	0.097	0.095
Te	0.000	0.000	0.000	0.000	0.000	0.000	0.000	0.000	0.000	0.000	0.000	0.000	0.001	0.000	0.001
Bi	0.000	0.000	0.000	0.000	0.000	0.000	0.000	0.000	0.000	0.000	0.000	0.000	0.000	0.000	0.000
Cu	0.003	0.005	0.004	0.009	0.007	0.012	0.009	0.000	0.000	0.000	0.000	0.000	0.000	0.000	0.000
Fe	0.001	0.002	0.001	0.001	0.001	0.002	0.001	0.012	0.012	0.011	0.015	0.013	0.018	0.006	0.007
Sum	1.000	1.000	1.000	1.000	1.000	1.000	1.000	1.000	1.000	1.000	1.000	1.000	1.000	1.000	1.000

Table B.8. EPMA data of electrum (1-7), native gold (8-22) and Ag-Au alloy (23-25); (continued).

Sample KMPR66 16-22 (D-type vein, sericitic alter.); KMPR53 23-25 (E-type vein); bdl = below detection											
analysis	16	17	18	19	20	21	22	23	24	25	26
wt%											
Au	87.20	88.41	87.75	86.76	87.19	87.47	87.92	96.75	96.87	97.91	96.38
Ag	12.45	12.33	12.61	12.61	12.08	11.99	12.19	2.04	2.11	2.13	1.93
Te	0.03	bdl	bdl	0.02	0.02	0.03	bdl	bdl	bdl	0.01	bdl
Bi	bdl	bdl	bdl	bdl	bdl	bdl	bdl	bdl	bdl	bdl	bdl
Cu	0.11	0.18	0.15	0.32	0.25	0.43	0.33	bdl	bdl	bdl	bdl
Fe	0.03	0.05	0.02	0.04	0.04	0.06	0.03	0.34	0.34	0.32	0.43
Total	99.82	100.98	100.53	99.75	99.57	99.98	100.47	99.12	99.32	100.37	98.75
apfu											
Au	0.889	0.863	0.875	0.898	0.901	0.904	0.902	0.312	0.304	0.342	0.308
Ag	0.103	0.125	0.118	0.082	0.081	0.077	0.080	0.635	0.684	0.647	0.691
Te	0.001	0.001	0.000	0.000	0.000	0.001	0.000	0.001	0.000	0.000	0.000
Bi	0.000	0.000	0.000	0.000	0.000	0.000	0.000	0.000	0.000	0.000	0.000
Cu	0.000	0.000	0.000	0.000	0.000	0.000	0.000	0.000	0.000	0.000	0.000
Fe	0.007	0.012	0.007	0.019	0.018	0.018	0.018	0.052	0.011	0.009	0.002
Sum	1.000	1.000	1.000	1.000	1.000	1.000	1.000	1.000	0.999	0.998	1.001

Table B.9. Selected EPMA data of molybdenite from Sapes (Konos Hill).

Sample SP20; bdl = below detection limit.															
analysis	1	2	3	4	5	6	7	8	9	10	11	12	13	14	15
wt%															
Mo	59.07	60.27	60.21	60.76	60.18	57.92	58.05	58.46	58.21	58.02	59.35	59.74	58.04	58.45	57.92
Re	0.13	0.32	0.36	0.15	0.33	1.90	1.74	1.50	1.41	1.96	0.35	1.37	1.21	1.52	1.63
Cu	bdl	bdl	bdl	bdl	bdl	0.06	0.04	bdl	0.05	bdl	bdl	0.01	0.05	0.08	0.06
Fe	bdl	0.02	0.06	0.03	0.10	0.07	0.02	0.06	0.07	0.03	bdl	0.01	bdl	bdl	bdl
S	41.29	40.20	40.13	39.93	39.75	40.42	39.65	40.15	40.75	40.21	40.99	40.07	40.80	40.20	40.53
Total	100.49	100.81	100.76	100.87	100.36	100.36	100.49	100.16	100.48	100.22	100.69	101.19	101.10	100.25	100.15
apfu															
Mo	0.992	1.000	0.995	0.994	0.989	0.965	0.986	0.972	0.987	0.981	0.988	0.977	0.973	0.976	0.965
Re	0.001	0.003	0.003	0.001	0.003	0.016	0.015	0.013	0.012	0.017	0.003	0.012	0.010	0.013	0.015
Cu	0.000	0.000	0.000	0.000	0.000	0.001	0.001	0.000	0.001	0.000	0.000	0.000	0.001	0.002	0.001
Fe	0.000	0.000	0.002	0.001	0.003	0.002	0.000	0.002	0.002	0.001	0.000	0.000	0.000	0.000	0.000
S	2.007	1.997	2.001	2.004	2.005	2.015	1.998	2.013	1.998	2.001	2.009	2.011	2.003	2.009	1.999
Sum	3.000	3.000	3.000	3.000	3.000	3.000	3.000	3.000	3.000	3.000	3.000	3.000	2.988	3.000	2.979

Table B.9. Selected EPMA data of molybdenite from Sapes (Konos Hill); (continued).

Sample SP20; bdl = below detection limit.															
analysis	16	17	18	19	20	21	22	23	24	25	26	27	28	29	30
wt%															
Mo	58.38	58.64	59.81	59.40	60.62	60.14	60.48	57.92	58.35	58.40	58.81	59.48	59.01	59.55	59.74
Re	0.89	1.18	0.93	0.75	0.01	bdl	0.79	1.72	1.11	1.16	1.09	0.26	0.00	0.32	0.36
Cu	0.05	bdl	bdl	0.01	bdl	bdl	bdl	0.02	0.06	0.06	0.07	bdl	0.02	0.04	0.01
Fe	0.02	0.43	0.57	0.03	0.06	0.23	0.12	bdl	0.01	0.03	0.02	bdl	0.04	0.01	0.04

S	39.93	40.1	40.15	40.73	40.10	40.10	38.99	39.53	39.85	39.76	40.00	39.77	39.29	39.60	39.52
Total	99.27	100.25	100.46	100.92	100.79	100.46	100.38	99.19	99.37	99.40	99.98	99.51	98.37	99.51	99.67
apfu															
Mo	0.982	0.985	0.973	0.981	1.006	0.999	1.021	0.981	0.982	0.984	0.985	0.999	1.002	1.002	1.005
Re	0.008	0.010	0.008	0.006	0.000	0.000	0.007	0.015	0.010	0.010	0.009	0.002	0.000	0.003	0.003
Cu	0.001	0.000	0.000	0.000	0.000	0.000	0.000	0.001	0.001	0.001	0.002	0.000	0.001	0.001	0.000
Fe	0.001	0.012	0.016	0.001	0.002	0.007	0.004	0.000	0.000	0.001	0.000	0.000	0.001	0.000	0.001
S	2.009	1.993	2.003	2.006	1.992	1.994	1.969	2.003	2.007	2.004	2.004	1.999	1.996	1.994	1.990
Sum	3.000	3.000	3.000	2.994	3.000	3.000	3.000	3.000	3.000	3.000	3.000	3.000	3.000	3.000	3.000

Table B.9. Selected EPMA data of molybdenite from Pagoni Rachi.

Sample KMPR68 (M-type vein) 1-11; KMPR66 (D-type vein) 11-30; bdl = below detection limit.															
analysis	1	2	3	4	5	6	7	8	9	10	11	12	13	14	15
wt%															
Mo	60.14	59.37	58.68	58.91	58.62	58.56	55.90	59.77	59.10	60.25	58.08	58.01	59.34	58.77	59.62
Re	0.46	0.29	0.75	0.57	0.22	0.71	1.38	0.40	0.37	1.72	0.65	1.26	1.28	1.36	0.62
Cu	bdl	bdl	bdl	0.02	bdl	bdl	0.05	0.15	0.06	0.01	bdl	0.02	bdl	bdl	bdl
Fe	0.30	0.15	0.53	0.62	0.31	1.45	2.21	0.20	0.27	0.75	1.58	1.00	0.42	0.69	0.94
S	40.36	40.05	39.02	40.92	40.43	39.69	38.84	40.80	41.25	41.10	40.17	39.18	40.26	39.68	40.33
Total	101.26	99.86	100.98	101.02	99.58	100.41	98.38	101.33	101.04	103.82	100.47	99.47	101.30	100.50	101.52
apfu															
Mo	0.993	0.997	0.985	0.989	0.982	0.975	0.949	0.982	0.976	0.975	0.967	0.980	0.982	0.989	0.981
Re	0.004	0.002	0.006	0.005	0.002	0.006	0.012	0.003	0.003	0.014	0.005	0.011	0.011	0.011	0.005
Cu	0.000	0.000	0.000	0.000	0.000	0.000	0.001	0.004	0.001	0.000	0.000	0.000	0.000	0.000	0.000
Fe	0.009	0.004	0.015	0.017	0.009	0.041	0.064	0.006	0.008	0.021	0.044	0.029	0.012	0.019	0.027
S	1.994	1.996	1.993	1.989	2.008	1.978	1.973	2.005	2.012	1.990	1.984	1.980	1.995	1.981	1.987
Sum	3.000	3.000	3.000	3.000	3.000	3.000	3.000	3.000	3.000	3.000	3.000	3.000	3.000	3.000	3.000

Table B.9. Selected EPMA data of molybdenite from Pagoni Rachi (continued).

Sample KMPR66 15-30 (D-type vein); bdl = below detection limit.															
	16	17	18	19	20	21	22	23	24	25	26	27	28	29	30
wt%															
Mo	59.63	59.90	60.47	60.16	57.41	60.28	56.89	58.56	58.02	59.32	60.23	61.93	61.07	59.18	59.44
Re	2.08	1.02	1.41	0.99	2.49	1.52	2.53	3.15	2.88	0.58	0.68	0.10	0.28	1.24	1.48
Cu	0.02	bdl	0.05	bdl	0.01	bdl	0.01	bdl	0.03	bdl	0.05	bdl	bdl	0.05	bdl
Fe	0.75	0.79	0.86	0.98	0.29	0.52	0.33	0.51	0.41	0.26	0.27	0.19	0.16	0.59	0.13
S	39.41	40.51	39.30	40.42	38.33	40.31	38.74	40.40	40.28	40.11	40.97	40.76	40.61	40.50	40.52
Total	101.89	102.22	102.08	102.55	98.53	102.63	98.50	102.61	101.61	100.27	102.19	102.98	102.13	101.56	101.57
apfu															
Mo	0.994	0.982	1.006	0.985	0.990	0.990	0.977	0.966	0.963	0.988	0.984	1.008	1.001	0.975	0.981
Re	0.018	0.009	0.012	0.008	0.022	0.013	0.022	0.027	0.025	0.005	0.006	0.001	0.002	0.010	0.013
Cu	0.000	0.000	0.001	0.000	0.000	0.000	0.000	0.000	0.001	0.000	0.001	0.000	0.000	0.001	0.000
Fe	0.022	0.022	0.024	0.028	0.009	0.015	0.010	0.015	0.012	0.007	0.007	0.005	0.005	0.017	0.004
S	1.966	1.987	1.956	1.980	1.979	1.982	1.991	1.993	2.000	1.999	2.002	1.986	1.992	1.997	2.002
Sum	3.000	3.000	3.000	3.000	3.000	3.000	3.000	3.000	3.000	3.000	3.000	3.000	3.000	3.000	3.000

Table B.10. Selected EPMA data of chalcopyrite.

Sample KMPR74 1-10; KMPR66 10-15; bdl = below detection limit.															
analysis	1	2	3	4	5	6	7	8	9	10	11	12	13	14	15
wt%															
Cu	34.13	34.95	34.61	34.60	34.69	34.39	34.04	34.23	34.05	34.29	33.89	33.11	33.12	33.16	34.44
Fe	30.36	31.00	30.91	30.72	30.74	30.78	30.26	30.52	30.17	30.30	29.89	28.97	29.23	29.18	30.04
Au	bdl	bdl	bdl	0.02	0.04	bdl	bdl	bdl	bdl	0.08	0.08	bdl	bdl	bdl	0.04
Ni	bdl	bdl	bdl	bdl	bdl	bdl	bdl	bdl	bdl	bdl	bdl	bdl	bdl	bdl	bdl
Co	0.04	0.05	0.04	0.02	0.05	0.03	0.02	0.05	0.04	0.06	0.07	0.03	0.04	0.05	0.02
As	0.03	bdl	bdl	bdl	bdl	0.02	bdl	0.03	0.01	0.05	0.04	bdl	bdl	0.01	bdl
S	35.05	34.32	35.04	34.46	34.45	34.40	33.88	34.53	34.33	34.58	34.40	32.65	32.69	33.31	34.73
apfu															
Cu	0.988	1.011	0.994	1.004	1.005	0.999	1.004	0.996	0.998	0.998	0.995	1.012	1.010	1.001	1.002
Fe	1.000	1.020	1.010	1.014	1.014	1.018	1.015	1.010	1.006	1.004	0.999	1.008	1.014	1.003	0.994
Au	0.000	0.000	0.000	0.000	0.000	0.000	0.000	0.000	0.000	0.001	0.001	0.000	0.000	0.000	0.000
Ni	0.000	0.000	0.000	0.000	0.000	0.000	0.000	0.000	0.000	0.000	0.000	0.000	0.000	0.000	0.000
Co	0.001	0.002	0.001	0.001	0.002	0.001	0.001	0.001	0.001	0.002	0.002	0.001	0.001	0.002	0.000
As	0.001	0.000	0.000	0.000	0.000	0.000	0.000	0.001	0.000	0.001	0.001	0.000	0.000	0.000	0.000
S	2.011	1.968	1.995	1.982	1.979	1.982	1.980	1.992	1.994	1.995	2.002	1.979	1.975	1.994	2.003
Sum	4.000	4.000	4.000	4.000	4.000	4.000	4.000	4.000	4.000	4.000	4.000	4.000	4.000	4.000	4.000

Table B.10. Selected EPMA data of chalcopyrite (continued).

Sample KMPR68A 1-8; KMSP50c 9-15; bdl = below detection limit.															
analysis	1	2	3	4	5	6	7	8	9	10	11	12	13	14	15
wt%															
Cu	34.53	34.56	34.64	34.38	34.66	34.15	34.69	34.30	34.83	34.98	34.67	34.59	34.85	33.96	34.87
Fe	30.11	30.35	30.35	30.30	30.35	30.12	30.42	30.67	30.64	30.97	30.53	30.51	30.94	30.68	30.92
Au	0.03	bdl	bdl	bdl	bdl	bdl	bdl	bdl	bdl	bdl	bdl	bdl	bdl	bdl	bdl
Ni	bdl	bdl	bdl	bdl	bdl	bdl	0.07	0.05	0.01	0.03	0.07	0.12	0.31	0.38	0.18
Co	0.02	0.07	0.07	0.06	0.08	0.06	0.01	bdl	0.01	bdl	bdl	bdl	bdl	0.02	bdl
As	bdl	0.05	0.02	0.01	bdl	0.01	0.03	bdl	0.05	0.05	0.05	0.02	0.03	0.01	bdl
S	34.60	34.80	34.72	34.57	34.04	34.49	35.07	34.50	34.42	35.35	34.04	34.41	34.67	34.91	34.82
apfu															
Cu	1.005	1.000	1.004	1.000	1.014	0.998	0.002	0.001	0.000	0.001	0.001	0.000	0.001	0.000	0.000
Fe	0.997	1.000	1.000	1.003	1.010	1.002	0.994	1.012	1.008	1.001	1.013	1.005	1.010	1.002	1.008
Au	0.000	0.000	0.000	0.000	0.000	0.000	0.000	0.000	0.000	0.000	0.002	0.003	0.009	0.027	0.005
Ni	0.000	0.000	0.000	0.000	0.000	0.000	0.000	0.000	0.000	0.000	0.000	0.007	0.000	0.000	0.000
Co	0.001	0.002	0.002	0.002	0.002	0.002	0.001	0.001	0.001	0.001	0.001	0.001	0.001	0.000	0.001
As	0.000	0.001	0.000	0.000	0.000	0.000	2.005	1.990	1.981	2.001	1.972	1.982	1.980	1.994	1.986
S	1.997	1.997	1.994	1.994	1.973	1.998	0.997	0.995	1.007	0.994	1.010	1.001	1.000	0.975	1.000
Sum	4.000	4.000	4.000	4.000	4.000	4.000	3.999	4.000	3.998	3.999	4.000	4.000	4.000	3.999	4.000

Table B.11. Selected EPMA data of magnetite.

Sample KMSP81 (magmatic magnetite); bdl = below detection limit.															
wt%	1	2	3	4	5	6	7	8	9	10	11	12	13	14	15
MgO	0.02	0.02	bdl	bdl	0.01	0.02	bdl	0.03	bdl	bdl	bdl	0.02	0.01	bdl	0.01
CaO	0.04	0.04	0.04	0.07	0.05	0.34	0.12	0.16	0.14	0.02	0.12	0.04	0.03	0.04	0.01
MnO	bdl	bdl	bdl	bdl	bdl	bdl	bdl	bdl	bdl	bdl	bdl	bdl	bdl	bdl	bdl
FeO_{tot}	97.13	96.89	97.47	97.79	95.66	95.72	96.79	96.93	96.16	97.60	96.73	94.69	97.24	95.64	96.21
TiO_2	0.43	0.70	0.45	0.39	1.77	1.66	0.33	0.90	0.53	0.11	0.15	2.77	0.36	1.11	1.65
Al_2O_3	bdl	0.02	0.01	bdl	0.02	0.08	bdl	bdl	bdl	bdl	bdl	bdl	bdl	bdl	bdl
Cr_2O_3	0.05	0.05	0.08	0.02	0.01	0.04	0.04	0.08	0.07	0.07	0.06	0.04	0.04	0.04	0.08
NiO	bdl	bdl	bdl	bdl	bdl	bdl	0.01	bdl	bdl	bdl	0.04	bdl	bdl	0.01	bdl
V2O3	0.28	0.21	0.25	0.31	0.17	0.27	0.08	0.25	0.33	0.21	bdl	0.29	0.23	0.11	0.15
Total	97.95	97.98	98.49	98.67	97.69	98.64	97.45	98.36	97.25	98.04	97.20	98.11	97.93	96.961	98.11
apfu								4 (O)							
Ti	0.016	0.026	0.016	0.014	0.064	0.060	0.012	0.033	0.020	0.004	0.006	0.100	0.013	0.041	0.060
Al	0.000	0.001	0.001	0.000	0.001	0.005	0.000	0.000	0.000	0.000	0.000	0.000	0.000	0.000	0.000
Cr	0.002	0.002	0.003	0.001	0.000	0.002	0.002	0.003	0.003	0.003	0.002	0.002	0.002	0.002	0.003
Fe_{tot}	3.959	3.939	3.957	3.964	3.865	3.864	3.971	3.923	3.950	3.984	3.984	3.791	3.966	3.913	3.872
Mn	0.000	0.000	0.000	0.000	0.000	0.000	0.000	0.000	0.000	0.000	0.000	0.000	0.000	0.000	0.000
Ni	0.000	0.000	0.000	0.000	0.000	0.000	0.000	0.000	0.000	0.000	0.002	0.000	0.000	0.000	0.000
Mg	0.001	0.001	0.000	0.000	0.001	0.001	0.000	0.002	0.000	0.000	0.000	0.001	0.001	0.000	0.001
V	0.005	0.004	0.005	0.006	0.003	0.005	0.002	0.005	0.006	0.004	0.000	0.006	0.004	0.002	0.003
Sum	3.993	3.983	3.982	3.985	3.995	3.937	3.987	4.000	3.999	3.995	3.993	3.999	3.986	3.958	3.939

Table B.11. Selected EPMA data of magnetite (continued).

Sample KMPR74 (hydrothermal magnetite); bdl = below detection limit.															
wt%	1	2	3	4	5	6	7	8	9	10	11	12	13	14	15
MgO	bdl	0.01	bdl	bdl	bdl	bdl	bdl	bdl	bdl	0.01	0.02	bdl	bdl	0.01	bdl

MnO	bdl	bdl	0.01	bdl	bdl	bdl	bdl	bdl	bdl	bdl	bdl	bdl	bdl	bdl	bdl
FeO_{tot}	97.52	97.44	97.63	96.65	99.19	97.94	98.27	98.88	98.28	97.20	97.45	98.75	98.22	98.62	97.98
TiO_2	0.20	0.11	0.10	0.06	0.14	0.12	0.55	0.08	0.06	0.16	0.47	0.08	0.06	0.12	0.08
Al_2O_3	0.14	0.07	0.01	0.02	0.02	0.06	0.09	0.03	0.05	0.07	0.05	bdl	0.03	0.04	0.04
$Cr2O_3$	bdl	0.06	bdl	bdl	0.02	bdl	bdl	0.02	bdl	bdl	bdl	0.02	0.01	0.02	bdl
NiO	0.02	0.01	bdl	bdl	0.07	bdl	bdl	bdl	bdl	0.01	0.03	bdl	bdl	bdl	0.01
V_2O_3	0.29	0.27	0.27	0.22	0.17	0.33	0.22	0.23	0.19	0.21	0.18	0.09	0.15	0.22	0.22
Total	98.24	98.027	98.257	97.983	99.732	98.56	99.248	99.29	96.598	94.712	99.55	99.108	98.505	99.131	98.407
apfu							4 (O)								
Ti	0.007	0.004	0.004	0.002	0.005	0.004	0.020	0.003	0.002	0.006	0.017	0.003	0.002	0.004	0.003
Al	0.008	0.004	0.001	0.001	0.001	0.003	0.005	0.002	0.003	0.004	0.003	0.000	0.002	0.002	0.002
Cr	0.000	0.002	0.000	0.000	0.001	0.000	0.000	0.001	0.000	0.000	0.000	0.001	0.000	0.001	0.000
Fe_{tot}	3.967	3.976	3.986	3.989	3.981	3.980	3.948	3.986	3.988	3.977	3.955	3.991	3.990	3.982	3.986
Mn	0.000	0.000	0.000	0.000	0.000	0.000	0.000	0.000	0.000	0.000	0.000	0.000	0.000	0.000	0.000
Ni	0.001	0.000	0.000	0.000	0.003	0.000	0.000	0.000	0.000	0.000	0.001	0.000	0.000	0.000	0.000
Mg	0.000	0.001	0.000	0.000	0.000	0.000	0.000	0.000	0.000	0.001	0.001	0.000	0.000	0.001	0.000
V	0.006	0.005	0.005	0.004	0.003	0.006	0.004	0.004	0.004	0.004	0.004	0.002	0.003	0.004	0.004
Sum	3.989	3.999	3.996	3.997	3.994	3.994	3.978	3.996	3.996	3.992	3.981	3.997	3.997	3.994	3.996

Table B.11. Selected EPMA data of magnetite (continued).

Sample KMPR68a-b (hydrothermal magnetite); bdl = below detection limit.														
wt%	1	2	3	4	5	6	7	8	9	10	11	13	14	15
MgO	0.02	0.01	0.04	0.03	0.04	0.04	bdl	bdl	bdl	0.03	bdl	0.01	0.01	0.00
MnO	0.03	bdl	bdl	bdl	bdl	bdl	bdl	bdl	bdl	0.10	bdl	bdl	bdl	bdl
FeO_{tot}	95.58	95.92	95.29	95.54	95.78	95.55	95.76	96.36	95.86	95.96	95.41	96.68	95.78	96.00
TiO_2	0.40	0.30	0.57	0.38	0.33	0.25	0.28	0.18	0.47	0.44	0.76	0.45	0.21	0.49

Al_2O_3	0.41	0.38	0.42	0.37	0.38	0.46	0.45	0.23	0.39	0.33	0.46	0.35	0.22	0.25
Cr_2O_3	0.01	bdl	bdl	0.02	0.02	0.01	bdl	bdl	bdl	0.03	bdl	0.03	bdl	bdl
NiO	bdl	bdl	bdl	0.04	0.02	bdl	bdl	0.04	bdl	0.04	bdl	0.01	bdl	bdl
V_2O_3	0.18	0.19	0.15	0.17	0.20	0.23	0.08	0.22	0.19	0.17	0.32	0.11	0.23	0.16
Total	96.85	97.02	96.73	96.86	97.14	96.80	96.81	97.22	97.11	97.67	97.04	97.88	96.59	97.07
apfu							4 (O)							
Ti	0.011	0.021	0.014	0.012	0.009	0.010	0.007	0.017	0.016	0.028	0.016	0.008	0.018	0.015
Al	0.022	0.024	0.021	0.022	0.027	0.026	0.013	0.023	0.019	0.026	0.020	0.013	0.014	0.024
Cr	0.000	0.000	0.001	0.001	0.000	0.000	0.000	0.000	0.001	0.000	0.001	0.000	0.000	0.000
Fe_{tot}	3.941	3.916	3.931	3.934	3.933	3.939	3.961	3.928	3.926	3.898	3.932	3.960	3.939	3.928
Mn	0.000	0.000	0.000	0.000	0.000	0.000	0.000	0.000	0.004	0.000	0.000	0.000	0.000	0.001
Ni	0.000	0.000	0.002	0.001	0.000	0.000	0.002	0.000	0.002	0.000	0.000	0.000	0.000	0.000
Mg	0.000	0.003	0.002	0.003	0.003	0.000	0.000	0.000	0.002	0.000	0.001	0.001	0.000	0.001
V	0.004	0.003	0.003	0.004	0.005	0.002	0.004	0.004	0.003	0.006	0.002	0.005	0.003	0.006
Sum	3.978	3.967	3.994	3.976	3.977	3.977	3.987	3.971	3.974	3.959	3.973	3.986	3.999	3.973

Table B.12. Selected EPMA data of pyrite.

Sample KMSP20 (D-vein pyrite); bdl = below detection limit.															
analysis	1	2	3	4	5	6	7	8	9	10	11	12	13	14	15
wt%															
Fe	45.86	46.07	46.39	45.99	46.17	46.14	45.99	46.85	46.95	46.35	46.71	46.86	47.06	47.00	46.79
Cu	0.028	bdl	bdl	0.05	bdl	bdl	0.02	bdl	0.01	0.01	0.03	bdl	bdl	bdl	0.014
Ni	bdl	bdl	bdl	bdl	bdl	bdl	bdl	bdl	bdl	bdl	bdl	bdl	bdl	bdl	bdl
Co	0.09	0.07	0.07	0.05	0.09	0.09	0.07	0.11	0.07	0.06	0.07	0.06	0.05	0.10	0.09
Au	0.02	0.03	bdl	bdl	bdl	bdl	bdl	bdl	bdl	bdl	0.08	bdl	0.04	0.02	0.04
Se	bdl	bdl	bdl	bdl	bdl	bdl	bdl	bdl	bdl	bdl	bdl	bdl	bdl	bdl	bdl
As	0.01	0.11	0.07	0.04	0.19	0.01	bdl	0.01	bdl	0.13	0.03	0.02	0.04	bdl	0.02
S	52.55	52.57	53.19	53.09	52.68	52.75	52.53	52.86	52.91	52.73	54.15	53.69	53.26	53.69	53.55
Total	98.55	98.86	99.72	99.19	99.14	99.00	98.84	99.82	99.94	99.28	101.08	100.61	100.45	100.79	100.51
apfu															
Fe	1.000	1.003	1.000	0.996	1.003	1.002	1.000	1.011	1.012	1.005	0.993	1.001	0.997	1.003	1.001
Cu	0.001	0.000	0.000	0.001	0.000	0.000	0.000	0.000	0.000	0.000	0.001	0.000	0.000	0.000	0.000
Ni	0.000	0.000	0.000	0.000	0.000	0.000	0.000	0.000	0.000	0.000	0.000	0.000	0.000	0.000	0.000
Co	0.002	0.001	0.001	0.001	0.002	0.002	0.001	0.002	0.001	0.001	0.001	0.001	0.001	0.002	0.002
Au	0.000	0.000	0.000	0.000	0.000	0.000	0.000	0.000	0.000	0.000	0.000	0.000	0.000	0.000	0.000
Se	0.000	0.000	0.000	0.000	0.000	0.000	0.000	0.000	0.000	0.000	0.000	0.000	0.000	0.000	0.000
As	0.000	0.002	0.001	0.000	0.003	0.000	0.000	0.000	0.000	0.002	0.000	0.000	0.001	0.000	0.000
S	1.997	1.994	1.997	2.002	1.993	1.996	1.998	1.987	1.987	1.992	2.004	1.998	2.002	1.995	1.996
Sum	3.000	3.000	3.000	3.000	3.000	3.000	3.000	3.000	3.000	3.000	3.000	3.000	3.000	3.000	3.000

Table B.12. Selected EPMA data of pyrite (continued).

Sample KMSP8 (D-vein pyrite); bdl = below detection limit.															
analysis	1	2	3	4	5	6	7	8	9	10	11	12	13	14	15
wt%															
Fe	46.70	46.51	46.77	46.70	46.32	45.85	46.12	46.45	46.35	46.50	46.36	46.65	46.57	46.56	46.51
Cu	bdl	0.04	0.01	bdl	0.01	0.03	bdl	bdl	bdl	0.02	bdl	bdl	0.01	0.03	0.02
Ni	bdl	bdl	bdl	bdl	bdl	bdl	bdl	bdl	bdl	bdl	bdl	bdl	bdl	bdl	bdl
Co	0.07	0.07	0.08	0.09	0.05	0.09	0.09	0.11	0.14	0.12	0.11	0.09	0.11	0.12	0.09
Au	bdl	bdl	0.04	0.05	bdl	0.04	0.07	bdl	bdl	bdl	bdl	0.02	0.02	0.08	bdl
Se	bdl	0.06	bdl	bdl	bdl	bdl	bdl	bdl	bdl	bdl	bdl	bdl	bdl	bdl	bdl
As	bdl	0.01	bdl	0.0	0.06	0.5	0.01	0.002	bdl	0.01	0.03	0.01	0.04	0.01	0.02
S	53.81	53.81	54.24	54.03	53.82	53.32	52.57	53.51	53.33	53.38	53.42	53.27	53.31	53.14	53.43
Total	100.57	100.45	101.13	100.88	100.25	99.32	98.86	100.07	99.82	100.03	99.91	100.05	100.07	99.92	100.07
apfu															
Fe	0.997	0.994	0.993	0.994	0.991	0.991	1.004	0.997	0.998	0.999	0.997	1.003	1.001	1.003	0.999
Cu	0.000	0.001	0.000	0.000	0.000	0.000	0.000	0.000	0.000	0.000	0.000	0.000	0.000	0.001	0.000
Ni	0.000	0.000	0.000	0.000	0.000	0.000	0.000	0.000	0.000	0.000	0.000	0.000	0.000	0.000	0.000
Co	0.001	0.001	0.001	0.002	0.001	0.002	0.002	0.002	0.003	0.002	0.002	0.002	0.002	0.002	0.002
Au	0.000	0.000	0.000	0.000	0.000	0.000	0.000	0.000	0.000	0.000	0.000	0.000	0.000	0.000	0.000
Se	0.000	0.009	0.000	0.000	0.000	0.000	0.000	0.000	0.000	0.000	0.000	0.000	0.000	0.000	0.000
As	0.000	0.000	0.000	0.000	0.001	0.000	0.000	0.000	0.000	0.000	0.001	0.000	0.001	0.000	0.000
S	2.002	2.004	2.006	2.004	2.007	2.007	1.994	2.001	2.000	1.998	2.001	1.995	1.996	1.994	1.999
Sum	3.000	3.000	3.000	3.000	3.000	3.000	3.000	3.000	3.000	3.000	3.000	3.000	3.000	3.000	3.000

Table B.12. Selected EPMA data of pyrite (continued).

Sample KMPSP78 = 1-7; KMSP48 = 8-11; KMSP83 = 12-15; (E-vein pyrite); bdl = below detection limit.															
analysis	1	2	3	4	5	6	7	8	9	10	11	12	13	14	15
wt%															
Fe	48.37	47.33	47.08	46.4	47.03	46.42	47.07	45.84	45.89	46.67	46.69	46.52	46.42	46.76	46.86
Cu	0.07	0.05	0.04	0.16	0.04	0.23	bdl	bdl	bdl	bdl	bdl	0.02	0.01	0.03	0.06
Ni	bdl	bdl	bdl	bdl	bdl	bdl	bdl	bdl	bdl	bdl	bdl	bdl	bdl	bdl	bdl
Co	bdl	0.01	bdl	bdl	bdl	bdl	0.01	bdl	0.03	bdl	bdl	0.01	bdl	bdl	bdl
Au	0.01	bdl	0.02	0.01	bdl	0.01	bdl	bdl	bdl	bdl	bdl	bdl	bdl	0.01	0.01
Se	bdl	bdl	bdl	bdl	bdl	bdl	0.05	bdl	bdl	bdl	bdl	bdl	bdl	bdl	bdl
As	0.82	1.48	bdl	0.39	0.14	0.02	bdl	bdl	0.04	0.06	0.02	0.62	0.87	0.02	0.5
S	52.35	51.41	53.52	52.75	53.22	52.94	53.15	53.17	53.55	54 134	54 181	52.99	52.28	53.81	52.08
Total	99.46	100.28	100.68	99.74	100.52	100.72	100.28	101.15	101.57	100.86	100.93	100.55	99.58	100.53	100.78
apfu															
Fe	1.021	1.016	1.014	1.018	1.017	1.004	1.006	0.994	0.989	0.993	0.993	0.993	1.002	1.000	0.999
Cu	0.001	0.001	0.001	0.003	0.001	0.004	0.000	0.000	0.000	0.000	0.000	0.000	0.000	0.001	0.001
Ni	0.000	0.000	0.000	0.000	0.000	0.000	0.000	0.000	0.000	0.000	0.000	0.000	0.000	0.000	0.000
Co	0.000	0.000	0.000	0.000	0.000	0.000	0.000	0.000	0.001	0.000	0.000	0.000	0.000	0.000	0.000
Au	0.000	0.000	0.000	0.000	0.000	0.000	0.000	0.000	0.000	0.000	0.000	0.000	0.000	0.000	0.000
Se	0.000	0.000	0.000	0.000	0.000	0.000	0.007	0.000	0.000	0.000	0.000	0.000	0.000	0.000	0.000
As	0.013	0.024	0.000	0.006	0.002	0.000	0.000	0.000	0.001	0.001	0.000	0.000	0.000	0.000	0.000
S	1.963	1.959	1.984	1.972	1.979	1.990	1.993	2.006	2.009	2.006	2.007	2.007	1.998	1.999	1.999
Sum	3.000	3.000	3.000	3.000	3.000	3.000	3.000	3.000	3.000	3.000	3.000	3.000	3.000	3.000	3.000

Table B.12. Selected EPMA data of pyrite (continued).

Sample KMPR68a-b (M-vein pyrite); bdl = below detection limit.															
analysis	1	2	3	4	5	6	7	8	9	10	11	12	13	14	15
wt%															
Fe	45.93	46.15	46.21	46.06	46.01	46.17	45.59	45.83	46.61	46.51	46.45	46.38	46.62	46.46	46.53
Cu	bdl	bdl	bdl	bdl	bdl	bdl	bdl	0.01	bdl	bdl	0.01	bdl	bdl	bdl	bdl
Ni	bdl	bdl	bdl	bdl	bdl	bdl	bdl	0.03	bdl	bdl	bdl	bdl	bdl	bdl	bdl
Co	0.08	0.11	0.09	0.07	0.09	0.05	0.64	0.47	0.08	0.08	0.06	0.07	0.08	0.09	0.09
Au	bdl	0.10	bdl	bdl	bdl	bdl	bdl	0.03	0.02	bdl	bdl	0.01	0.01	bdl	bdl
Se	bdl	bdl	bdl	bdl	bdl	bdl	bdl	bdl	bdl	bdl	bdl	bdl	0.06	bdl	bdl
As	bdl	0.02	0.03	0.01	bdl	bdl	0.01	0.14	bdl	0.02	bdl	bdl	0.03	bdl	0.03
S	52.78	52.59	53.08	52.60	52.80	52.70	52.54	52.98	52.27	53.70	52.41	53.04	53.42	52.84	53.10
Total	98.80	99.01	99.41	98.77	98.94	98.99	98.77	99.49	98.98	100.31	98.93	99.50	100.15	99.39	99.75
apfu															
Fe	0.999	1.004	0.999	1.003	1.000	1.003	0.993	0.991	1.015	0.996	1.011	1.002	1.001	1.006	1.003
Cu	0.000	0.001	0.000	0.001	0.000	0.000	0.000	0.000	0.000	0.000	0.000	0.000	0.000	0.000	0.000
Ni	0.000	0.000	0.000	0.000	0.000	0.000	0.000	0.001	0.000	0.000	0.000	0.000	0.000	0.000	0.000
Co	0.002	0.002	0.002	0.001	0.002	0.001	0.013	0.010	0.002	0.002	0.001	0.001	0.002	0.002	0.002
Au	0.000	0.001	0.000	0.000	0.000	0.000	0.000	0.000	0.000	0.000	0.000	0.000	0.000	0.000	0.000
Se	0.000	0.000	0.000	0.000	0.000	0.001	0.000	0.000	0.000	0.000	0.000	0.000	0.001	0.000	0.000
As	0.000	0.000	0.000	0.000	0.000	0.000	0.000	0.002	0.000	0.000	0.000	0.000	0.000	0.000	0.000
S	1.999	1.992	1.999	1.995	1.998	1.995	1.994	1.996	1.983	2.003	1.987	1.996	1.997	1.992	1.994
Sum	3.000	3.000	3.000	3.000	3.000	3.000	3.000	3.000	3.000	3.000	3.000	3.000	3.000	3.000	3.000

Table B.12. Selected EPMA data of pyrite (continued).

Sample KMPR66/PR4 (D-vein pyrite); bdl = below detection limit.															
analysis	1	2	3	4	5	6	7	8	9	10	11	12	13	14	15
wt%															
Fe	46.83	46.74	46.09	46.21	46.51	46.13	46.40	46.24	46.47	46.56	47.01	46.41	46.33	46.84	46.25
Cu	bdl	bdl	bdl	bdl	bdl	bdl	bdl	bdl	bdl	0.01	bdl	bdl	bdl	0.04	bdl
Ni	bdl	bdl	bdl	bdl	bdl	bdl	bdl	bdl	bdl	0.20	bdl	0.01	bdl	bdl	bdl
Co	0.06	0.07	0.03	0.10	0.10	0.07	0.10	0.07	0.10	0.09	0.08	0.30	0.10	0.07	0.06
Au	bdl	bdl	0.01	bdl	bdl	bdl	bdl	bdl	0.06	bdl	0.16	bdl	0.03	bdl	bdl
Se	bdl	bdl	0.06	bdl	bdl	bdl	bdl	bdl	0.10	bdl	bdl	bdl	bdl	bdl	bdl
As	0.01	bdl	0.06	0.10	bdl	0.14	0.08	0.05	0.03	0.01	bdl	0.13	0.01	0.06	0.03
S	52.84	53.11	53.03	52.84	53.00	52.19	52.59	52.82	52.39	53.04	52.96	52.12	51.99	51.74	51.89
Total	99.74	99.93	99.23	99.25	99.73	98.52	99.20	99.23	99.05	99.92	100.23	98.97	98.45	98.75	98.23
apfu															
Fe	1.011	1.006	0.998	1.001	1.004	1.009	1.007	1.002	1.011	1.003	1.012	1.012	1.014	1.025	1.015
Cu	0.000	0.000	0.000	0.000	0.000	0.000	0.001	0.000	0.000	0.000	0.000	0.000	0.000	0.001	0.000
Ni	0.000	0.000	0.000	0.000	0.000	0.000	0.000	0.000	0.000	0.004	0.000	0.000	0.000	0.000	0.000
Co	0.001	0.002	0.001	0.002	0.002	0.001	0.002	0.002	0.002	0.002	0.002	0.006	0.002	0.001	0.001
Au	0.000	0.000	0.000	0.000	0.001	0.000	0.000	0.000	0.000	0.000	0.001	0.000	0.000	0.000	0.000
Se	0.000	0.000	0.001	0.000	0.000	0.000	0.000	0.000	0.001	0.000	0.000	0.000	0.000	0.000	0.000
As	0.000	0.000	0.001	0.002	0.000	0.002	0.001	0.001	0.000	0.000	0.000	0.002	0.000	0.001	0.000
S	1.988	1.992	2.000	1.995	1.993	1.988	1.989	1.995	1.986	1.991	1.985	1.979	1.983	1.972	1.983
Sum	3.000	3.000	3.000	3.000	3.000	3.000	3.000	3.000	3.000	3.000	3.000	3.000	3.000	3.000	3.000

Table B.12. Selected EPMA data of pyrite (continued).

Sample KMPR77a (D-vein pyrite); bdl = below detection limit.												
analysis	1	2	3	4	5	6	7	8	9	10	11	12
wt%												
Fe	46.13	46.10	46.45	46.22	46.17	46.54	46.06	46.20	46.40	46.14	46.05	46.12
Cu	bdl	bdl	bdl	bdl	bdl	bdl	bdl	bdl	bdl	bdl	bdl	0.02
Ni	bdl	bdl	bdl	bdl	bdl	bdl	bdl	bdl	bdl	bdl	bdl	bdl
Co	0.06	0.09	0.08	0.01	0.07	0.01	0.06	0.07	0.08	bdl	bdl	0.03
Au	0.06	bdl	bdl	0.08	0.08	0.07	0.05	0.07	0.07	0.08	0.08	0.09
Se	0.09	bdl	bdl	bdl	bdl	bdl	bdl	bdl	bdl	bdl	bdl	0.02
As	bdl	0.04	0.34	bdl	0.06	0.03	bdl	0.01	0.02	0.08	bdl	bdl
S	52.58	52.89	52.23	53.18	52.92	53.16	53.00	53.61	52.82	52.63	53.14	52.88
Total	98.83	99.13	99.13	99.53	99.30	99.82	99.17	99.96	99.43	98.93	99.26	99.14
apfu												
Fe	1.003	1.011	1.010	0.998	1.000	1.003	0.998	0.992	1.005	1.003	0.996	1.000
Cu	0.000	0.000	0.000	0.001	0.000	0.000	0.000	0.000	0.001	0.000	0.000	0.000
Ni	0.000	0.000	0.000	0.000	0.000	0.000	0.000	0.000	0.000	0.000	0.000	0.000
Co	0.001	0.002	0.002	0.002	0.002	0.001	0.001	0.001	0.001	0.002	0.002	0.002
Au	0.000	0.000	0.000	0.000	0.000	0.000	0.000	0.000	0.000	0.000	0.000	0.000
Se	0.001	0.000	0.000	0.000	0.000	0.000	0.000	0.000	0.000	0.000	0.000	0.000
As	0.000	0.001	0.006	0.000	0.001	0.000	0.000	0.000	0.000	0.001	0.000	0.000
S	1.996	1.987	1.983	2.000	1.997	1.995	2.001	2.006	1.992	1.994	2.002	1.998
Sum	3.000	3.000	3.000	3.000	3.000	3.000	3.000	3.000	3.000	3.000	3.000	3.000

Table B.12. Selected EPMA data of pyrite (continued).

Sample KMPR87 (E-vein pyrite); bdl = below detection limit.																
analysis	1	2	3	4	5	6	7	8	9	10	11	12	13	14	15	16
wt%																
Fe	45.68	46.50	46.72	46.35	46.38	46.47	46.53	46.65	46.33	46.89	46.22	47.07	47.07	46.44	46.68	46.66
Cu	bdl	bdl	0.02	bdl	bdl	bdl	0.02	0.04	0.05	bdl	bdl	0.02	0.01	0.02	bdl	0.03
Ni	bdl	bdl	bdl	bdl	bdl	bdl	bdl	bdl	bdl	bdl	bdl	bdl	bdl	bdl	bdl	bdl
Co	bdl	bdl	bdl	bdl	bdl	bdl	bdl	bdl	bdl	bdl	bdl	bdl	bdl	bdl	bdl	bdl
Au	bdl	0.01	bdl	bdl	bdl	bdl	0.02	bdl	bdl	bdl	bdl	bdl	bdl	bdl	bdl	bdl
Se	bdl	bdl	bdl	bdl	bdl	bdl	bdl	bdl	bdl	bdl	bdl	bdl	bdl	bdl	bdl	bdl
As	0.03	0.09	0.02	bdl	bdl	0.01	0.09	bdl	0.04	0.01	0.03	bdl	0.03	bdl	0.05	bdl
S	52.98	53.64	53.30	54.12	53.19	53.11	54.31	53.76	53.89	53.68	53.83	54.13	54.59	53.73	54.66	53.75
Total	98.70	100.26	100.09	100.49	99.58	99.59	100.96	100.49	100.34	100.58	100.08	101.21	101.71	100.22	101.46	100.46
apfu																
Fe	0.993	0.996	1.004	0.989	1.001	1.003	0.988	0.997	0.991	1.002	0.990	0.999	0.993	0.995	0.986	0.998
Cu	0.000	0.000	0.000	0.000	0.000	0.000	0.000	0.001	0.001	0.000	0.000	0.000	0.000	0.000	0.000	0.001
Ni	0.000	0.000	0.000	0.000	0.000	0.000	0.000	0.000	0.000	0.000	0.000	0.000	0.000	0.000	0.000	0.000
Co	0.000	0.000	0.000	0.000	0.000	0.000	0.000	0.000	0.000	0.000	0.000	0.000	0.000	0.000	0.000	0.000
Au	0.000	0.000	0.000	0.000	0.000	0.000	0.000	0.000	0.000	0.000	0.000	0.000	0.000	0.000	0.000	0.000
Se	0.000	0.000	0.000	0.000	0.000	0.000	0.000	0.000	0.000	0.000	0.000	0.000	0.000	0.000	0.000	0.000
As	0.000	0.001	0.000	0.000	0.000	0.000	0.001	0.000	0.001	0.000	0.000	0.000	0.000	0.000	0.001	0.000
S	2.006	2.002	1.995	2.011	1.999	1.997	2.010	2.002	2.008	1.998	2.009	2.001	2.006	2.005	2.012	2.002
Sum	3.000	3.000	3.000	3.000	3.000	3.000	3.000	3.000	3.000	3.000	3.000	3.000	3.000	3.000	3.000	3.000

Table B.13. Selected EPMA data of gypsum-vein hosted galena from Sapes (Konos Hill, analyses 1-9) and Pagoni Rachi (analyses 10-15) areas.

Sample SP50c 1-9; KMPR69 10-15; bdl = below detection limit.															
	1	2	3	4	5	6	7	8	9	10	11	12	13	14	15
wt%															
Pb	77.89	78.32	77.84	77.98	76.49	77.55	79.74	79.00	79.24	85.88	86.61	86.61	86.64	87.73	86.62
Ag	0.38	0.41	0.39	0.44	0.45	0.37	0.38	0.39	0.40	0.05	0.03	0.02	0.03	0.06	0.09
Bi	bdl	bdl	bdl	bdl	bdl	bdl	bdl	bdl	bdl	bdl	bdl	bdl	bdl	bdl	bdl
Te	1.08	bdl	bdl	bdl	bdl	bdl	bdl	bdl	bdl	bdl	bdl	bdl	bdl	bdl	bdl
Se	12.09	12.26	11.63	13.01	12.95	13.04	9.57	9.88	10.35	0.07	0.10	0.09	bdl	bdl	bdl
S	7.20	7.43	7.67	7.13	6.83	6.97	8.34	8.29	8.39	13.22	13.38	13.36	13.25	13.55	12.04
Total	98.63	99.33	98.40	99.59	98.05	99.12	98.82	98.38	99.13	99.22	100.11	100.08	99.92	101.34	98.75
apfu															
Pb	0.982	0.974	0.973	0.970	0.970	0.973	0.992	0.984	0.975	1.001	0.999	1.000	1.005	1.000	1.053
Ag	0.009	0.010	0.009	0.011	0.011	0.009	0.009	0.009	0.009	0.001	0.001	0.001	0.001	0.001	0.002
Bi	0.000	0.000	0.000	0.000	0.000	0.000	0.000	0.000	0.000	0.000	0.000	0.000	0.000	0.000	0.000
Te	0.022	0.019	0.018	0.020	0.027	0.024	0.016	0.017	0.015	0.000	0.000	0.000	0.000	0.000	0.000
Se	0.400	0.400	0.381	0.425	0.431	0.429	0.312	0.323	0.334	0.002	0.003	0.003	0.000	0.000	0.000
S	0.586	0.598	0.619	0.574	0.560	0.565	0.670	0.667	0.667	0.996	0.997	0.997	0.994	0.998	0.945
Sum	2.000	2.000	2.000	2.000	2.000	2.000	2.000	2.000	2.000	2.000	2.000	2.000	2.000	2.000	2.000

Table B.13. Selected EPMA data of E-vein hosted galena from Sapes (Konos Hill, analyses 1-7) and Pagoni Rachi (analyses 8-15) areas.

Sample SP50c 1-9; KMPR69 10-15; bdl = below detection limit.															
	1	2	3	4	5	6	7	8	9	10	11	12	13	14	15
wt%															
Pb	87.52	87.32	85.61	83.96	84.21	85.10	84.73	85.83	84.95	84.91	84.90	85.32	85.24	85.45	84.02
Ag	0.62	bdl	0.41	0.66	0.34	0.01	0.14	bdl	bdl	bdl	0.01	0.06	0.08	0.06	1.08
Bi	bdl	bdl	bdl	bdl	bdl	bdl	bdl	bdl	bdl	bdl	bdl	bdl	bdl	bdl	bdl
Te	0.06	bdl	bdl	bdl	0.08	bdl	bdl	bdl	bdl	bdl	bdl	bdl	bdl	bdl	bdl
Se	bdl	bdl	bdl	bdl	bdl	bdl	bdl	bdl	bdl	bdl	bdl	bdl	bdl	bdl	bdl
S	13.09	12.94	14.02	13.86	14.08	13.98	13.53	13.71	13.66	13.64	13.36	13.54	13.57	13.55	13.47
Total	101.03	100.80	100.12	98.57	98.74	99.30	98.51	99.61	98.76	98.57	99.08	99.12	99.06	99.39	99.81
apfu															
Pb	0.999	1.001	0.966	0.959	0.956	0.967	0.980	0.983	0.978	0.981	0.977	0.983	0.981	0.980	0.948
Ag	0.016	0.000	0.009	0.017	0.007	0.000	0.003	0.000	0.000	0.000	0.000	0.001	0.002	0.001	0.023
Bi	0.000	0.000	0.000	0.000	0.000	0.000	0.000	0.000	0.000	0.000	0.000	0.000	0.000	0.000	0.000
Te	0.000	0.000	0.000	0.000	0.000	0.000	0.000	0.000	0.000	0.000	0.000	0.000	0.000	0.000	0.000
Se	0.000	0.000	0.000	0.000	0.000	0.000	0.000	0.000	0.000	0.000	0.000	0.000	0.000	0.000	0.000
S	0.985	0.978	1.022	1.023	1.033	1.026	1.012	1.015	1.017	1.018	0.993	1.008	1.009	1.004	0.983
Sum	2.000	1.979	1.997	2.000	1.996	1.993	1.999	1.998	1.995	1.999	1.970	1.992	1.992	1.986	1.954

Table B.14. Selected EPMA data of sphalerite.

Sample KMSP78; bdl = below detection limit.															
analysis	1	2	3	4	5	6	7	8	9	10	11	12	13	14	15
wt%															
Zn	65.14	65.42	65.34	66.08	65.20	65.53	66.09	65.82	65.63	64.78	65.89	64.74	65.03	65.52	65.88
Fe	0.43	0.42	0.45	0.44	0.70	0.51	0.49	0.46	0.50	0.53	0.44	0.50	0.43	0.49	0.82
Cu	bdl	bdl	bdl	bdl	bdl	bdl	bdl	bdl	bdl	bdl	bdl	bdl	bdl	bdl	0.33
Co	bdl	bdl	bdl	bdl	bdl	bdl	0.01	bdl	bdl	bdl	0.02	0.01	bdl	bdl	0.01
Ge	bdl	bdl	bdl	bdl	bdl	bdl	bdl	bdl	bdl	bdl	bdl	bdl	bdl	bdl	bdl
Cd	1.26	1.64	1.53	1.23	1.91	1.67	1.30	1.54	1.68	1.87	1.34	1.98	2.28	2.03	0.01
In	bdl	bdl	bdl	bdl	bdl	bdl	bdl	bdl	bdl	bdl	bdl	bdl	bdl	bdl	0.09
S	32.91	32.87	33.22	33.34	32.72	32.76	32.60	33.23	32.94	33.01	32.88	32.36	32.39	32.20	33.31
Total	100.01	100.43	100.56	101.12	100.66	100.51	100.50	101.05	100.79	100.36	100.57	99.65	100.16	100.26	100.43
apfu															
Zn	0.975	0.977	0.971	0.976	0.973	0.978	0.987	0.975	0.976	0.967	0.981	0.977	0.978	0.986	0.975
Fe	0.008	0.007	0.008	0.008	0.012	0.009	0.009	0.008	0.009	0.009	0.008	0.009	0.008	0.009	0.014
Cu	0.000	0.000	0.000	0.000	0.001	0.001	0.000	0.000	0.000	0.000	0.000	0.000	0.000	0.000	0.005
Co	0.000	0.000	0.000	0.000	0.000	0.000	0.000	0.000	0.000	0.000	0.000	0.000	0.000	0.000	0.000
Ge	0.000	0.000	0.000	0.000	0.000	0.000	0.000	0.000	0.000	0.000	0.000	0.000	0.000	0.000	0.000
Cd	0.011	0.014	0.013	0.010	0.016	0.014	0.011	0.013	0.014	0.016	0.011	0.017	0.019	0.017	0.000
In	0.000	0.000	0.000	0.000	0.000	0.000	0.000	0.000	0.000	0.000	0.000	0.000	0.000	0.000	0.001
S	1.004	1.001	1.008	1.005	0.997	0.998	0.993	1.004	1.000	1.006	0.999	0.996	0.994	0.988	1.005
Sum	1.998	1.999	2.000	2.000	1.999	2.000	2.000	2.000	1.999	1.998	2.000	1.999	2.000	2.000	2.000
Mol % Fe	0.79	0.75	0.80	0.77	1.23	0.91	0.86	0.82	0.89	0.94	0.78	0.89	0.77	0.87	1.44

Table B.14. Selected EPMA data of sphalerite (continued).

Sample KMPR53 1-7; KMPR83 8-15; bdl = below detection limit.															
analysis	1	2	3	4	5	6	7	8	9	10	11	12	13	14	15
wt%															
Zn	66.48	66.10	66.45	66.28	66.50	66.97	66.75	65.41	65.51	65.87	65.26	66.23	65.09	63.67	65.46
Fe	0.15	0.14	0.13	0.19	0.16	0.33	0.53	0.17	0.19	0.09	0.56	0.14	0.10	0.06	0.17
Cu	0.01	0.01	bdl	bdl	bdl	bdl	bdl	0.04	0.04	bdl	0.46	0.03	0.05	bdl	0.02
Co	bdl	bdl	bdl	bdl	0.01	0.01	bdl	bdl	bdl	bdl	bdl	bdl	0.02	bdl	0.01
Ge	bdl	bdl	bdl	bdl	bdl	bdl	bdl	bdl	bdl	bdl	bdl	bdl	bdl	bdl	bdl
Cd	0.20	0.14	bdl	bdl	0.24	0.18	0.04	0.05	bdl	0.08	bdl	0.15	0.30	0.14	0.11
In	0.01	bdl	bdl	bdl	bdl	0.01	bdl	bdl	bdl	0.02	bdl	bdl	bdl	0.02	bdl
S	33.20	33.35	33.63	33.04	33.16	33.47	33.29	34.03	33.85	34.42	33.61	33.80	33.86	31.88	33.88
Total	100.05	99.80	100.48	99.50	100.08	100.98	100.61	99.76	99.60	100.56	99.93	100.37	99.41	95.80	99.72
apfu															
Zn	0.989	0.984	0.982	0.990	0.989	0.987	0.987	0.968	0.972	0.967	0.967	0.978	0.968	0.988	0.970
Fe	0.003	0.002	0.002	0.003	0.003	0.006	0.009	0.003	0.003	0.001	0.010	0.002	0.002	0.001	0.003
Cu	0.000	0.000	0.000	0.000	0.000	0.000	0.000	0.001	0.001	0.000	0.007	0.000	0.001	0.000	0.000
Co	0.000	0.000	0.000	0.000	0.000	0.000	0.000	0.000	0.000	0.000	0.000	0.000	0.000	0.000	0.000
Ge	0.000	0.000	0.000	0.000	0.000	0.000	0.000	0.000	0.000	0.000	0.000	0.000	0.000	0.000	0.000
Cd	0.002	0.001	0.002	0.000	0.002	0.001	0.000	0.000	0.000	0.001	0.000	0.001	0.003	0.001	0.001
In	0.000	0.000	0.000	0.000	0.000	0.000	0.000	0.000	0.000	0.000	0.000	0.000	0.000	0.000	0.000
S	1.007	1.012	1.013	1.007	1.006	1.006	1.004	1.027	1.024	1.030	1.016	1.018	1.027	1.009	1.024
Sum	2.000	1.999	1.999	2.000	2.000	2.000	2.000	1.999	2.000	1.999	2.000	2.000	2.000	2.000	1.999
Mol % Fe	0.26	0.25	0.23	0.33	0.29	0.58	0.92	0.30	0.34	0.15	0.98	0.25	0.17	0.12	0.30

Table B.16. EPMA data of enargite.

Sample KMSP67; bdl = below detection limit.						
analysis	1	2	3	4	5	6
wt%						
Cu	47.24	48.15	47.49	48.32	47.54	47.77
Ag	bdl	0.01	0.01	bdl	bdl	bdl
Fe	1.06	0.22	0.89	0.33	0.11	0.49
Sb	bdl	bdl	0.11	0.12	bdl	bdl
As	18.88	18.91	18.29	18.65	18.67	18.81
S	32.55	32.51	32.17	32.59	32.67	32.16
Total	99.73	99.8	98.96	100.01	98.99	99.23
apfu						
Cu	2.928	2.997	2.987	2.994	2.996	2.999
Ag	0.002	0.002	0.001	0.000	0.000	0.000
Fe	0.074	0.011	0.021	0.006	0.006	0.009
Sb	0.000	0.000	0.000	0.000	0.000	0.000
As	0.998	0.999	0.997	0.999	0.999	0.998
S	3.998	3.99	3.994	4.001	3.998	3.997
Sum	8.000	7.999	8.000	8.000	7.999	8.000

Table B.15. EPMA data of colusite.

Sample KMSP67; bdl = below detection limit.								
analysis	1	2	3	4	5	6	7	8
wt%								
Cu	47.24	47.15	47.49	47.32	47.54	47.77	47.44	47.04
Ag	0.01	0.01	0.01	bdl	bdl	bdl	0.02	bdl
Fe	bdl	bdl	bdl	0.04	0.02	bdl	bdl	bdl
Sb	6.33	6.52	6.27	5.20	6.38	5.47	4.55	5.31
As	6.92	7.03	7.30	8.49	6.65	8.47	9.01	8.83
V	3.29	3.17	3.24	3.20	3.21	3.25	3.24	3.20
Sn	6.67	6.32	6.18	4.76	6.82	4.62	4.36	4.42
S	30.55	30.34	30.43	31.18	30.12	30.87	31.10	31.13
Total	10.99	100.54	100.92	100.18	100.74	100.44	99.71	99.93
Chemical formula based on 13 (S+Se) pfu								
Cu	10.141	10.190	10.236	9.954	10.352	10.151	10.003	9.912
Ag	0.002	0.002	0.001	0.000	0.000	0.000	0.002	0.000
Fe	0.001	0.000	0.000	0.009	0.005	0.000	0.000	0.000
Sb	0.709	0.735	0.705	0.571	0.725	0.606	0.500	0.584
As	1.260	1.289	1.335	1.514	1.228	1.526	1.611	1.577
Bi	0.000	0.000	0.000	0.000	0.000	0.000	0.000	0.000
V	0.880	0.855	0.872	0.840	0.872	0.862	0.851	0.842
Sn	0.766	0.731	0.713	0.536	0.796	0.525	0.492	0.498
S	13.000	13.000	13.000	13.000	13.000	13.000	13.000	13.000

Table B.17. Selected EPMA data of tetrahedrite/tennantite group minerals.

Sample KMSP78; bdl = below detection limit.														
analysis	1	2	3	4	5	6	7	8	9	10	11	12	13	14
wt%														
Cu	38.67	38.94	39.32	39.07	38.81	39.36	40.69	39.01	38.55	39.73	39.87	41.96	39.23	39.37
Fe	2.16	2.80	2.95	2.82	3.01	3.14	3.68	2.44	2.89	3.22	3.66	2.53	3.19	2.71
Zn	8.00	5.59	5.30	5.69	7.06	5.38	5.28	5.92	5.38	7.89	7.40	7.93	8.31	8.46
Ag	0.24	0.24	0.36	0.29	0.12	0.19	0.10	0.24	0.24	0.10	0.04	0.04	0.06	0.10
Sb	15.91	16.13	16.12	16.03	12.79	11.38	6.06	17.82	17.92	8.27	5.03	5.64	7.73	6.54
As	9.54	9.47	9.54	9.56	11.68	12.73	16.38	8.31	8.19	14.80	16.59	11.85	15.02	16.07
S	26.16	25.44	25.67	25.63	26.48	26.72	27.43	26.35	25.74	27.25	27.68	29.74	27.36	27.72
Total	100.68	98.61	99.26	99.10	99.93	98.91	99.62	100.08	98.91	101.27	100.27	99.69	100.89	100.97
Chemical formula based on 13 (S+Se) pfu														
Zn	9.695	10.038	10.047	9.996	9.611	9.660	9.727	9.710	9.823	9.563	9.447	9.252	9.406	9.315
Fe	0.035	0.036	0.054	0.044	0.017	0.028	0.014	0.035	0.036	0.015	0.006	0.005	0.008	0.014
Cu	0.617	0.820	0.859	0.821	0.848	0.876	1.001	0.692	0.838	0.881	0.986	0.635	0.869	0.729
Co	1.950	1.401	1.315	1.415	1.699	1.284	1.227	1.432	1.333	1.846	1.705	1.699	1.936	1.945
Ge	2.081	2.169	2.149	2.140	1.653	1.458	0.756	2.314	2.382	1.039	0.622	0.649	0.967	0.808
Cd	2.028	2.070	2.067	2.074	2.453	2.650	3.321	1.754	1.771	3.022	3.333	2.216	3.054	3.225
Sum S	13.000	13.000	13.000	13.000	13.000	13.000	13.000	13.000	13.000	13.000	13.000	13.000	13.000	13.000

Appendix C. LA – ICP – MS DATA

Table C.1. LA – ICP- MS data of biotite (continued).

Sample B26 – Pervasive potassic alteration/Koryphes. Values in ppm; bdl = below detection limit.										
Spot	1	2	3	4	5	6	7	8	9	10
Li	66.68	71.99	129.02	84.66	104.48	114.75	117.84	135.04	168.05	118.03
Be	bdl	0.19	bdl	bdl	bdl	bdl	bdl	bdl	bdl	bdl
B	3.82	bdl	bdl	bdl	bdl	bdl	bdl	bdl	bdl	bdl
Ca	415.33	bdl	316.97	bdl	bdl	616.73	bdl	339.91	bdl	bdl
Sc	4.41	3.90	3.31	4.08	2.86	3.93	2.89	2.86	3.64	3.62
Ti	14742	13958	14042	14734	13971	14176	14068	14467	13598	14323
V	434	428	399	436	410	395	400	403	368	399
Cr	65	62	52	50	53	46	36	44	46	41
Mn	212	202	205	213	200	194	198	197	191	202
Co	1.08	1.11	1.34	1.63	1.17	1.28	0.70	1.39	1.02	1.75
Ni	bdl	bdl	bdl	bdl	bdl	bdl	bdl	bdl	bdl	bdl
Zn	23	22	18	22	22	17	20	21	18	21
Ga	25	25	21	26	23	21	23	21	20	23
Rb	563	555	542	586	547	537	554	555	529	571
Sr	5.63	5.67	4.40	5.41	5.03	3.97	3.89	4.75	3.17	4.10
Y	0.19	0.09	bdl	0.04	bdl	0.44	bdl	0.10	0.05	bdl
Zr	4.55	7.40	1.47	bdl	bdl	152.32	1.73	2.52	bdl	1.38
Nb	2.02	2.28	1517	2.32	1131	2.05	2.28	1.69	1679	1.93
Sn	0.27	bdl	bdl	bdl	bdl	bdl	0.28	bdl	bdl	bdl
Cs	5.62	5.78	4.84	5.41	5.13	5.37	5.43	5.22	4.69	5.63
Ba	454	561	323	568	385	366	377	348	280	363
La	0.02	0.04	0.01	0.02	0.01	0.03	0.04	0.04	<0.0143	0.02
Ce	0.05	0.04	0.01	bdl	bdl	0.05	0.06	0.10	0.04	0.01
Pr	0.01	0.01	0.00	0.01	0.01	bdl	bdl	0.00	bdl	bdl

Nd	0.02	0.06	bdl	bdl	bdl	bdl	bdl	0.06	0.03	bdl
Sm	bdl	bdl	0.01	0.06	bdl	bdl	0.08	0.02	bdl	0.02
Eu	bdl	0.03	bdl	0.00	bdl	bdl	bdl	bdl	bdl	bdl
Gd	bdl	bdl	bdl	bdl	0.01	bdl	bdl	bdl	bdl	bdl
Tb	bdl	bdl	bdl	bdl	bdl	bdl	bdl	bdl	bdl	bdl
Dy	bdl	bdl	bdl	0.02	bdl	0.07	bdl	bdl	bdl	bdl
Ho	bdl	bdl	bdl	bdl	bdl	0.02	bdl	bdl	bdl	bdl
Er	bdl	0.03	bdl	0.02	0.02	0.09	bdl	bdl	bdl	bdl
Tm	bdl	0.01	bdl	bdl	bdl	0.05	bdl	bdl	bdl	bdl
Yb	0.05	0.06	0.05	0.02	0.02	0.20	0.04	0.03	0.02	0.03
Lu	0.01	0.01	bdl	bdl	bdl	0.05	0.01	0.01	0.01	bdl
Hf	0.10	0.31	0.03	0.03	0.07	4.66	0.06	bdl	0.06	0.16
Ta	0.09	0.08	0.04	0.12	0.06	0.11	0.08	0.07	0.06	0.10
Pb	18	20	bdl	10	bdl	11	64	13	bdl	15
Pb	13	16	1.53	11	1.32	6.79	62	8.56	2.52	9.98
Th	0.23	0.23	0.03	0.04	0.03	1049	0.29	0.36	0.11	0.05
U	0.04	0.10	0.02	0.04	0.03	0.49	0.11	0.09	0.05	0.04

Table C.1. LA – ICP- MS data of biotite (continued).

Sample P62 – Selective potassic alteration/Koryphes. Values in ppm; bdl = below detection limit.										
Spot	1	2	3	4	5	6	7	8	9	10
Li	16.98	14.32	20.44	22.50	18.49	22.57	22.22	18.19	16.32	26.02
Be	0.59	bdl	bdl	bdl	bdl	bdl	0.45	bdl	0.45	0.56
B	bdl	bdl	bdl	bdl	bdl	3.43	bdl	bdl	bdl	bdl
Ca	bdl	bdl	bdl	bdl	408.74	bdl	bdl	bdl	bdl	606
Sc	12.59	18.20	12.95	10.43	12.58	10.61	11.78	12.00	18.79	8.48
Ti	28665	27234	31035	29557	29220	29415	30309	29049	23724	26593
V	1090	992	1634	692	654	616	673	1045	1036	654
Cr	57	48	254	42	44	36	50	69	47	37

Mn	271	284	249	254	257	272	251	256	264	248
Co	7.53	6.09	7.94	6.03	6.30	6.67	7.87	7.07	5.81	7.13
Ni	bdl	bdl	5.90	bdl	bdl	bdl	bdl	bdl	bdl	bdl
Zn	36	35	28	30	32	33	34	27	34	33
Ga	32	32	31	28	28	29	30	30	33	27
Rb	625	620	620	691	683	674	688	648	601	648
Sr	3.29	3.55	3.08	2.47	2.64	2.64	2.66	2.65	2.71	2.59
Y	bdl	bdl	0.16	0.06	bdl	bdl	0.15	0.10	0.11	0.28
Zr	2.00	4.43	bdl	1.69	1.55	1.54	bdl	1.87	3.70	1.87
Nb	13.67	19.59	3.46	14.06	15.73	15.33	18.65	8.31	21.55	14.13
Sn	2.70	3.67	1.43	2.34	1.89	3.01	2.55	1.63	3.36	2.63
Cs	10.32	12.03	10.04	9.10	9.18	8.25	8.50	10.12	12.24	9.07
Ba	833	878	835	609	653	713	662	754	871	603
La	0.02	0.03	0.03	0.02	bdl	0.02	0.01	0.03	0.01	0.02
Ce	0.06	bdl	0.03	bdl	bdl	bdl	bdl	0.01	bdl	0.06
Pr	bdl	0.01	0.01	0.01	bdl	bdl	bdl	0.02	bdl	bdl
Nd	0.02	0.04	bdl	0.01	0.05	0.01	0.03	0.05	0.01	bdl
Sm	0.03	bdl	0.01	bdl	bdl	0.01	bdl	0.05	bdl	0.03
Eu	bdl	0.02	bdl	0.02	0.01	0.02	bdl	bdl	bdl	bdl
Gd	0.03	bdl	0.05	bdl	bdl	0.04	bdl	bdl	bdl	0.07
Tb	0.01	bdl	bdl	bdl	0.00	bdl	bdl	bdl	bdl	0.01
Dy	bdl	bdl	bdl	0.01	bdl	0.01	0.02	0.01	bdl	0.09
Ho	bdl	bdl	bdl	bdl	bdl	0.00	0.01	0.00	0.01	0.02
Er	bdl	bdl	0.02	0.07	bdl	bdl	bdl	0.01	bdl	bdl
Tm	bdl	0.00	bdl	bdl	bdl	0.01	0.01	0.00	bdl	0.02
Yb	0.01	bdl	0.04	0.02	0.04	bdl	bdl	0.01	0.01	0.15
Lu	bdl	0.00	bdl	0.00	bdl	bdl	0.01	bdl	bdl	0.01
Hf	0.11	0.09	0.10	0.09	0.07	0.05	0.04	bdl	0.13	0.02
Ta	0.93	1205	0.28	0.96	1161	1202	1296	0.51	1264	1031
Pb	43	24	53	33	24	21	23	43	42	12

Pb	7.20	1.89	41.28	15	8.43	7.89	12	26	32	10
Th	0.00	0.00	0.02	bdl	0.00	bdl	0.01	0.01	0.00	0.03
U	0.03	0.04	0.02	0.01	0.01	0.02	0.02	0.02	0.06	0.02

Table C.1. LA – ICP- MS data of biotite (continued).

Sample KMPR60 –Potassic alteration/Pagoni Rachi. Values in ppm; bdl = below detection limit.										
Spot	1	2	3	4	5	6	7	8	9	10
Li	37.91	10.85	5.84	6.62	7.67	8.78	10.76	7.36	bdl	7.56
Be	bdl	bdl	bdl	bdl	bdl	bdl	bdl	1.70	bdl	bdl
B	bdl	bdl	bdl	bdl	bdl	bdl	bdl	bdl	bdl	bdl
Ca	2653	4162	1558	1176	801	3868	1955	bdl	1878	5931
Sc	20.77	21.68	35.19	38.21	47.15	15.90	38.13	51.21	20.70	22.53
Ti	2005	14292	20194	18897	23191	24169	22126	18796	19846	17260
V	230	340	360	346	359	614	530	645	281	314
Cr	31	bdl	28	bdl	bdl	22	38	bdl	bdl	bdl
Mn	2670	1268	692	701	676	906	990	960	935	763
Co	45.37	33.12	27.82	24.55	27.26	33.73	34.85	25.05	31.47	31.26
Ni	bdl	bdl	bdl	bdl	14.31	bdl	bdl	bdl	bdl	bdl
Zn	1156	474	224	218	206	278	291	283	308	237
Ga	53	41	41	39	35	44	45	35	27.36	30.15
Rb	63	454	450	488	469	373	474	412	427	378
Sr	40.41	9.12	11.14	1.70	11.19	58.73	39.87	8.90	49.27	66.80
Y	23.93	19.98	0.25	bdl	0.39	0.99	bdl	bdl	bdl	bdl
Zr	787	4.38	3.06	bdl	1.89	5.15	6.73	5.03	7.30	bdl
Nb	2.94	26.45	35.73	34.30	39.50	42.34	32.13	21.88	26.25	21.48
Sn	1.79	4.50	4.64	5.02	4.97	28.52	34.13	41.67	38.63	19.14
Cs	32.17	22.19	17.49	16.81	9.67	5.26	5.33	4.04	3.15	5.39
Ba	84	543	655	598	463	1334	1779	712	606	997
La	3.21	14.60	0.21	0.03	0.21	5.19	0.68	0.07	0.68	2.53

Ce	6.78	37.70	bdl	bdl	0.37	3.82	1.00	0.13	1.11	2.89
Pr	0.99	4.78	bdl	bdl	0.06	0.19	0.09	0.03	0.10	0.20
Nd	4.40	18.74	bdl	0.08	0.06	0.54	0.11	0.11	0.26	0.96
Sm	1.15	3.94	bdl	bdl	bdl	0.17	bdl	bdl	0.07	0.05
Eu	0.47	0.44	bdl	bdl	bdl	0.13	0.02	bdl	0.13	0.20
Gd	2.73	3.34	bdl	bdl	0.02	bdl	bdl	bdl	bdl	bdl
Tb	0.50	0.51	bdl	bdl	bdl	bdl	0.03	bdl	bdl	0.01
Dy	3.11	3.42	0.08	0.03	bdl	0.13	bdl	bdl	0.02	0.12
Ho	0.68	0.69	bdl	bdl	0.04	0.02	0.02	0.01	0.02	0.01
Er	2.12	1.51	0.04	0.01	0.05	0.07	bdl	0.07	bdl	0.07
Tm	0.47	0.14	bdl	bdl	0.02	0.02	0.03	bdl	bdl	bdl
Yb	4.22	1.17	0.03	0.02	0.05	0.27	0.04	0.06	0.07	bdl
Lu	0.58	0.24	0.03	bdl	0.01	0.06	0.03	bdl	0.04	0.02
Hf	22.48	0.14	bdl	0.19	0.17	0.39	0.27	0.11	0.35	0.24
Ta	0.16	1.67	2.49	2.33	3.28	1394	0.94	0.50	0.57	0.54
Pb	bdl	bdl	bdl	bdl	3.82	16	bdl	bdl	12.29	8.90
Pb	25	5.22	0.98	0.92	2.25	21	6.04	4.97	8.11	8.51
Th	5.35	1.92	0.02	0.03	0.04	0.12	0.06	0.04	bdl	bdl
U	12	0.96	0.15	0.16	0.12	0.44	0.38	0.18	0.22	0.09

Table C.1. LA – ICP- MS data of biotite (continued).

Sample KMPR80 –Potassic alteration/Papadokoryphi. Values in ppm; bdl = below detection limit.								
Spot	1	2	3	4	5	6	7	8
Li	47.34	46.72	61.40	53.28	51.43	56.99	57.83	54.76
Be	0.66	bdl	0.73	0.37	0.39	bdl	1.00	0.99
B	bdl	bdl	bdl	bdl	bdl	bdl	bdl	bdl
Ca	bdl	bdl	1443	585	bdl	1504	bdl	5853

Sc	7.83	5.51	9.92	5.94	8.44	7.25	7.72	9.15
Ti	27316	26684	17263	28771	31513	27275	23986	20143
V	141	107	118	128	148	127	129	113
Cr	bdl	bdl	bdl	12	9	26	bdl	24
Mn	389	325	1081	337	383	499	702	861
Co	62.56	67.56	63.69	66.09	64.05	55.36	63.87	62.16
Ni	57.14	48.86	49.77	45.03	50.05	43.64	55.26	47.99
Zn	48.19	50.49	101.70	44.59	59.77	68.61	84.96	89.37
Ga	36.85	27.93	36.12	35.60	44.46	34.69	35.20	31.22
Rb	891	919	580	951	916	773	651	648
Sr	3.41	1.96	1.99	5.30	7.87	23.43	3.67	2.70
Y	bdl	bdl	1.59	0.11	bdl	bdl	bdl	3.42
Zr	bdl	bdl	bdl	3.01	3.37	bdl	bdl	2.76
Nb	17.22	27.42	13.26	25.89	19.32	23.31	21.27	16.00
Sn	5.22	5.08	4.71	5.48	6.69	6.47	4.22	5.52
Cs	35.97	17.36	12.63	21.28	23.74	24.19	11.45	17.58
Ba	896	520	347	906	1059	748	473	373
La	bdl	bdl	0.24	0.01	0.02	0.05	bdl	0.26
Ce	0.02	bdl	0.85	0.01	0.02	0.03	bdl	0.57
Pr	bdl	0.01	0.11	bdl	bdl	0.01	0.01	0.06
Nd	0.04	0.76	0.74	0.02	bdl	bdl	bdl	0.37
Sm	bdl	bdl	0.24	bdl	bdl	0.10	bdl	0.30
Eu	bdl	0.02	0.13	bdl	0.02	0.04	bdl	0.07
Gd	bdl	bdl	0.19	0.04	bdl	bdl	0.02	0.46
Tb	0.01	0.02	0.05	0.00	bdl	0.01	bdl	0.12
Dy	bdl	0.07	0.33	0.02	bdl	bdl	bdl	0.70
Ho	bdl	0.08	0.07	0.01	0.00	bdl	bdl	0.17
Er	bdl	0.09	0.18	0.02	bdl	bdl	0.01	0.49
Tm	bdl	bdl	0.02	bdl	0.01	bdl	bdl	0.10
Yb	bdl	1.12	0.15	0.02	bdl	0.02	bdl	0.67

Lu	bdl	0.02	bdl	0.00	0.01	0.02	bdl	0.07
Hf	0.14	0.12	0.08	0.16	0.12	bdl	0.21	0.15
Ta	0.98	1.83	0.85	1.85	1332	1.41	2.05	1079
Pb	bdl	bdl	bdl	bdl	bdl	bdl	bdl	bdl
Pb	bdl	0.50	bdl	bdl	0.26	bdl	0.52	0.77
Th	0.01	0.02	0.05	bdl	0.01	0.02	0.05	0.14
U	0.07	0.02	0.06	0.05	0.05	0.03	0.04	0.10

Table C.2. LA – ICP – MS data of sphalerite.

KMSP78 (E-type vein, Konos Hill - Sapes). Values in ppm; bdl = below detection limit.										
Spot	1	2	3	4	5	6	7	8	9	10
Si	99	248	222	156	187	257	227	264	158	135
Mn	182	155	191	188	165	221	205	178	156	112
Fe	4148	3571	3413	3476	3639	4363	4332	3697	3622	2540
Co	0.23	0.42	2.07	2.27	5.03	7.13	6.46	3.61	2.47	0.53
Ni	bdl	bdl	bdl	bdl	bdl	bdl	bdl	bdl	bdl	bdl
Cu	18	16	23	51	31	14	13	31	18	25
Ga	52	12	13	31	1576	2.12	1852	9.72	6.50	9.61
Ge	7.25	2.44	2.34	4.56	0.48	bdl	bdl	0.98	0.46	1.31
As	1.42	bdl	bdl	bdl	bdl	bdl	bdl	bdl	bdl	bdl
Se	bdl	bdl	bdl	bdl	bdl	bdl	bdl	bdl	bdl	bdl
Mo	0.14	0.05	bdl	bdl	bdl	0.08	0.26	0.14	0.04	0.11
Ag	1.27	0.87	0.61	1.02	0.44	1.01	0.55	0.91	0.79	1.28
Cd	18543	16021	22796	20712	23610	39433	35896	20966	25989	12384
In	2049	0.81	1307	4.22	12	9.54	14	18	3.31	1979
Sn	8.60	8.79	4.12	8.26	21	4.47	2.43	6.53	9.22	6.41
Sb	3.00	0.27	bdl	0.51	bdl	bdl	0.07	0.67	bdl	2.79
W	0.01	bdl	bdl	bdl	bdl	bdl	0.01	bdl	bdl	bdl
Au	0.01	bdl	bdl	bdl	bdl	bdl	0.01	bdl	bdl	0.01
Tl205	0.01	0.01	bdl	bdl	bdl	0.01	0.01	bdl	bdl	0.04
Pb208	0.83	0.10	0.04	0.14	0.04	0.47	bdl	0.45	0.17	2.21
Bi209	bdl	bdl	bdl	bdl	bdl	0.01	bdl	bdl	bdl	bdl

Table C.2. LA – ICP – MS data of sphalerite (continued).

KMPR53 (E-type vein, Pagoni Rachi). Values in ppm; bdl = below detection limit.										
Spot	1	2	3	4	5	6	7	8	9	10
Si	298	292	236	247	178	203	243	153	191	211
Mn	1049	1014	1557	1856	2620	2066	1017	1157	1121	1141
Fe	3624	3009	4079	3533	4117	4106	3303	4177	4467	3563
Co	bdl	bdl	bdl	bdl	bdl	bdl	bdl	bdl	bdl	bdl
Ni	bdl	bdl	bdl	bdl	bdl	bdl	bdl	bdl	bdl	bdl
Cu	817	99	147	205	108	6.83	12	266	109	65
Ga	27	2.53	7.06	2.00	17	3.28	2043	6.38	7.42	21
Ge	bdl	bdl	bdl	bdl	bdl	bdl	bdl	bdl	bdl	51
As	bdl	bdl	bdl	bdl	bdl	bdl	0.59	bdl	bdl	0.71
Se	bdl	2.53	bdl	2.29	bdl	1.87	bdl	2.33	2.90	2.12
Mo	0.06	0.04	0.12	0.08	0.10	0.05	0.03	0.05	0.12	0.11
Ag	1.91	1.74	1.23	1.54	0.83	1.02	1.78	3.49	4.05	3.10
Cd	4194	4327	4008	3903	3731	4233	4577	4275	4547	3548
In	0.56	bdl	0.08	bdl	9.14	0.02	0.14	0.30	0.18	0.21
Sn	49	0.93	17	0.22	26	0.82	7.30	26	11	32
Sb	bdl	0.46	0.11	0.46	0.06	bdl	bdl	bdl	bdl	0.45
W	bdl	0.00	bdl	bdl	0.01	bdl	bdl	bdl	bdl	0.02
Au	0.01	bdl	bdl	bdl	bdl	bdl	0.01	0.03	bdl	0.04
Tl	bdl	bdl	bdl	bdl	bdl	bdl	bdl	bdl	bdl	bdl
Pb	0.32	6.05	0.88	0.55	0.05	0.04	1.73	1.11	6.53	2.12
Bi	0.01	0.02	0.01	bdl	bdl	bdl	0.01	bdl	bdl	0.09

Table C.3. LA – ICP – MS data of magnetite.

Sample KMPSP81 (magmatic magnetite). Values in ppm; bdl = below detection limit.															
Spot	1	2	3	4	5	6	7	8	9	10	11	12	13	14	15
Mg	1678	1656	998	1012	1237	962	612	1623	1427	1125	1652	1265	1678	1656	998
Al	4754	7841	6854	4611	4112	4512	4489	5412	4632	7845	7410	5674	4754	7841	6854
Si	4512	4656	8521	998	1123	991	1121	4151	2245	2564	3541	3021	4512	4656	8521
Ca	4125	2112	995	754	1241	1150	740	994	856	4125	2212	1745	4125	2112	995
Sc	2	2	3	2	4	2	2	2	3	3	2	2	2	2	3
Ti	21015	19845	9915	19900	21254	22545	20569	21457	22360	22525	20306	20455	21015	19845	9915
V	412	708	770	650	455	560	395	550	680	425	571	557	412	708	770
Cr	395	365	411	298	301	454	312	221	410	230	221	332	395	365	411
Mn	225	412	350	332	285	224	323	385	330	312	336	274	225	412	350
Co	20	19	26	20	24	27	20	20	22	20	22	21	20	19	26
Ni	31	22	21	25	20	19	22	23	27	23	20	23	31	22	21
Cu	4	2	2	3	4	5	8	6	4	6	6	4	4	2	2
Zn	34	38	79	65	40	45	60	48	33	39	74	50	34	38	79
Ga	9	12	14	15	13	12	17	21	22	20	14	16	9	12	14
Rb	2	2	4	3	2	3	3	2	2	5	2	3	2	2	4
Sr	4	4	8	4	6	7	4	4	6	8	7	5	4	4	8
Y	11	11	12	14	11	8	7	11	7	10	4	9	11	11	12
Zr	4	11	18	24	21	14	19	21	7	12	14	14	4	11	18
Nb	4	3	5	4	4	2	4	9	2	1	5	5	4	3	5
Mo	bdl	bdl	bdl	1	1	bdl	1	bdl	2	1	bdl	1	bdl	bdl	bdl
Sn	58	97	36	45	74	45	49	54	78	99	74	59	58	97	36
Ba	4	11	10	11	4	5	6	4	2	4	4	9	4	11	10
Hf	0.06	1.18	0.09	0.12	0.10	0.08	0.85	0.14	0.12	0.14	0.09	0.06	0.06	1.18	0.09
Ta	bdl	bdl	bdl	1	bdl	bdl	bdl	bdl	bdl	1	bdl	bdl	bdl	bdl	bdl
W	4	2	1	2	2	2	2	3	3	3	2	3	4	2	1
Pb	25	12	12	14	18	21	36	21	14	28	31	20	25	12	12

Table C.3. LA – ICP – MS data of magnetite (continued).

Sample KMPR74 (hydrothermal magnetite). Values in ppm; bdl = below detection limit.															
Spot	1	2	3	4	5	6	7	8	9	10	11	12	13	14	15
Mg	1078	643	3613	3583	451	1896	1099	3613	3613	1152	1560	2154	1451	3121	1623
Al	6808	3371	6282	6565	2002	4764	2556	5674	5385	3356	4400	4454	5125	4855	4542
Si	3741	6095	6345	4345	1982	5502	4210	3505	6679	4252	4121	3320	4451	4236	4425
Ca	2739	2189	1206	3810	1337	3509	910	3810	4158	3810	2259	2540	2454	2980	3520
Sc	4	15	6	12	10	23	11	15	10	18	14	10	12	11	12
Ti	1405	1424	1305	1498	1372	1459	2215	1423	11517	1325	1987	2415	1995	2080	2870
V	1799	1658	1077	1722	1749	1701	1519	3079	1720	1814	2101	1915	1412	1995	1495
Cr	24	24	24	14	21	25	20	28	26	24	19	16	21	24	28
Mn	992	559	2672	1576	412	1047	723	474	611	479	451	652	1425	1010	1232
Co	5	5	14	5	5	7	11	11	4	4	9	11	4	4	6
Ni	14	19	15	15	15	15	16	16	18	14	14	16	17	16	14
Cu	29	bdl	bdl	30	bdl	bdl	25	152	bdl	8	bdl	21	bdl	22	32
Zn	3494	4004	1860	2314	3016	3187	3140	2578	2920	2753	2004	3012	3025	2945	3645
Ga	34	40	33	35	31	35	35	36	31	35	32	31	35	31	31
Rb	1	19	bdl	bdl	bdl	1	bdl	8	2	7	4	6	2	4	
Sr	1	3	bdl	bdl	13	57	1	bdl	72	31	18	11	21	16	22
Y	1	2	bdl	bdl	bdl	10	1	bdl	bdl	1	2	1	bdl	bdl	bdl
Zr	bdl	3	bdl	bdl	bdl	23	bdl	bdl	bdl	15	11	7	bdl	bdl	bdl
Nb	bdl	9	3	5	2	40	1	2	3	30	bdl	18	21	bdl	11
Mo	1	1	6	2	4	4	3	1	3	3	1	1	2	5	1
Sn	41	38	28	30	30	40	26	39	39	39	35	32	29	34	39
Ba	1	2	bdl	bdl	2	9	1	10	11	7	bdl	6	bdl	4	bdl
Hf	2	0.25	0.10	0.17	<0.092	1.23	0.09	0.16	0.12	0.32	0.25	0.26	0.30	bdl	bdl
Ta	bdl	1	1	1	bdl	3	bdl	bdl	bdl	2	bdl	bdl	1	2	bdl
W	bdl	5	bdl	1	bdl	9	4	1	1	7	bdl	4	bdl	bdl	9
Pb	5	14	bdl	5	1	20	2	1	1	12	6	bdl	11	bdl	9

Table C.3. LA – ICP – MS data of magnetite (continued).

Sample KMPR68 (hydrothermal magnetite). Values in ppm; bdl = below detection limit.															
Spot	1	2	3	4	5	6	7	8	9	10	11	12	13	14	15
Mg	1274	5135	550	663	3258	1701	1106	2534	6896	3270	4420	3195	1984	1245	2420
Al	5328	5370	4881	4920	5370	5370	5370	5977	5370	3354	5124	5235	4986	4758	5548
Si	2772	3843	bdl	1338	1481	4072	2110	3322	6247	5197	1452	3987	3322	3864	4252
Ca	1071	1504	1188	bdl	bdl	1511	980	bdl	bdl	2065	1120	1078	1215	1451	2064
Sc	4	2	4	2	1	3	1	18	5	3	2	4	11	3	3
Ti	4255	4852	4120	3096	3175	1845	2120	3120	4100	1155	1815	3506	2451	4557	3856
V	1654	1695	1689	1689	1696	1622	1754	3079	1684	1695	1689	1653	1632	1645	1780
Cr	21	22	20	16	25	20	20	20	21	18	21	16	23	24	17
Mn	954	690	2199	815	902	1389	986	1157	637	794	1145	1065	856	1125	987
Co	15	13	21	9	10	17	3	14	12	11	9	12	8	15	9
Ni	15	18	19	19	12	17	13	16	21	14	14	19	20	14	14
Cu	19	10	84	75	bdl	146	24	156	35	9	45	95	14	17	114
Zn	181	159	865	952	182	2163	1754	168	452	180	2096	1452	1896	1457	994
Ga	15	13	25	16	17	24	14	17	11	14	35	12	12	14	11
Rb	1	bdl	bdl	3	bdl	7	1	3	3	2	bdl	2	bdl	4	bdl
Sr	30	7	5	23	2	9	6	13	5	5	10	19	8	18	9
Y	3	2	2	1	8	2	1	27	15	53	4	11	2	35	4
Zr	bdl	bdl	bdl	bdl	bdl	bdl	bdl	4	bdl	10	6	bdl	2	bdl	bdl
Nb	2	1	1	1	3	bdl	bdl	5	8	55	bdl	bdl	12	21	6
Mo	2	5	1	3	5	3	8	4	9	5	1	1	6	1	3
Sn	7	8	5	7	11	10	11	18	10	39	13	11	9	19	11
Ba	7	5	3	3	4	5	8	6	3	7	5	3	3	8	5
Hf	0.03	0.04	0.07	0.03	0.14	bdl	bdl	0.23	0.19	0.65	0.95	0.22	bdl	0.22	bdl
Ta	bdl	bdl	bdl	bdl	1	bdl	bdl	bdl	2	7	bdl	bdl	1	bdl	bdl
W	bdl	bdl	bdl	bdl	1	bdl	1	14	2	44	12	1	4	4	bdl
Pb	16	10	128	74	14	39	114	34	28	28	35	12	54	75	77

Table C.4. LA – ICP – MS data of pyrite.

KMSP20 (D-type vein, Konos Hill-Sapes). Values in ppm; bdl = below detection limit.															
Spot	1	2	3	4	5	6	7	8	9	10	11	12	13	14	15
Mn	bdl	bdl	1	bdl	bdl	1	1	1	bdl	bdl	1	bdl	1	1	1
Co	7	127	65	1	7	1395	269	99	689	1	15	412	23	470	225
Ni	7	22	bdl	bdl	4	11	bdl	bdl	bdl	bdl	bdl	46	bdl	bdl	18
Cu	7	9	3	1	2	0	bdl	0	bdl	bdl	bdl	1	bdl	1	1
Zn	bdl	2	2	3	bdl	bdl	3	3	bdl	bdl	bdl	bdl	bdl	bdl	bdl
Ga	bdl	bdl	bdl	bdl	bdl	bdl	bdl	0	bdl	bdl	bdl	0	bdl	bdl	bdl
Ge	1	1	bdl	bdl	bdl	bdl	bdl	bdl	bdl	bdl	1	bdl	bdl	bdl	bdl
As	bdl	bdl	bdl	53	374	342	7	567	1577	53	226	bdl	508	53	285
Se	40	54	131	26	113	233	165	83	103	21	21	31	52	108	212
Mo	bdl	bdl	bdl	bdl	bdl	bdl	bdl	bdl	bdl	bdl	bdl	bdl	bdl	bdl	bdl
Ag	bdl	bdl	bdl	bdl	bdl	bdl	bdl	bdl	bdl	bdl	bdl	bdl	bdl	bdl	bdl
Cd	bdl	bdl	bdl	bdl	bdl	bdl	bdl	bdl	bdl	bdl	bdl	bdl	bdl	bdl	bdl
In	bdl	bdl	bdl	bdl	bdl	bdl	bdl	bdl	bdl	bdl	bdl	bdl	bdl	bdl	bdl
Sn	bdl	bdl	bdl	bdl	bdl	bdl	bdl	bdl	bdl	bdl	bdl	bdl	bdl	bdl	0.21
Sb	bdl	bdl	bdl	bdl	bdl	bdl	bdl	bdl	bdl	bdl	bdl	bdl	bdl	bdl	0.11
W	bdl	bdl	bdl	bdl	bdl	bdl	0.04	bdl	bdl	bdl	bdl	bdl	bdl	bdl	bdl
Au	bdl	bdl	bdl	bdl	bdl	bdl	bdl	bdl	bdl	bdl	bdl	bdl	bdl	bdl	bdl
Tl	0	bdl	bdl	bdl	bdl	bdl	bdl	bdl	bdl	bdl	bdl	bdl	bdl	bdl	0.01
Pb	bdl	bdl	bdl	bdl	bdl	bdl	bdl	bdl	bdl	bdl	bdl	bdl	bdl	0.15	bdl
Bi	bdl	bdl	bdl	bdl	bdl	bdl	bdl	bdl	bdl	bdl	bdl	bdl	bdl	bdl	bdl

Table C.4. LA – ICP – MS data of pyrite (continued).

KMSP78 (E-type vein, Konos Hill-Sapes). Values in ppm; bdl = below detection limit.												
Spot	1	2	3	4	5	6	7	8	9	10	11	12
Mn	1	1	0	3	5	12	13	11	5	12	9	6
Co	227	457	282	2	1	0.30	118	12	4	2	4	108
Ni	142	628	188	2	2	bdl	35	8	12	4	3	458
Cu	30	5	26	351	317	206	40	65	41	110	30	110
Zn	bdl	bdl	11	22	49	5	4	32	14	19	9	16
Ga	0	bdl	0	1	1	1	bdl	1	1	2	1	0.92
Ge	1.09	0.92	0.98	1.28	2.20	0.75	0.80	2.12	1.80	1.00	1.22	1.12
As	4403	688	8152	11745	14518	16429	7601	988	4408	11453	9845	8756
Se	bdl	bdl	bdl	bdl	bdl	bdl	bdl	bdl	bdl	bdl	bdl	bdl
Mo	10	6	15	1	1	0	1	4	1	1	2	3
Ag	1	6	1	18	19	10	4	5	14	12	7	9
Cd	bdl	bdl	41	0	1	bdl	14	21	4	8	12	15
In	0.156	bdl	bdl	0.0451	0.038	bdl	bdl	0.04	0.25	0.08	0.04	0.11
Sn	0.291	bdl	bdl	0.86	0.96	0.421	bdl	0.183	9	0.47	0.59	1.41
Sb	82	2	27	265	292	210	49	145	82	208	75	128
W	0.0	0.1	0.0	0.2	0.4	0.2	0.1	0.2	0.4	0.2	0.2	0.20
Au	0.8	0.1	0.8	0.3	0.4	0.5	0.8	0.9	1.1	0.4	0.7	0.67
Tl	15	0	2	16	16	14	3	12	18	9	12	7
Pb	327	34	102	776	898	574	168	412	568	225	329	418
Bi	42	0	0	1	1	0	9	1	1	2	1	11

Table C.4. LA – ICP – MS data of pyrite (continued).

KMPR68a-b (M-type vein, Pagoni Rachi). Values in ppm; bdl = below detection limit.																
Spot	1	2	3	4	5	6	7	8	9	10	11	12	13	14	15	16
Mn	bdl	1	bdl	1	3	1	bdl	5	4	bdl	1	bdl	1	4	9	1
Co	4.53	12.53	3.60	3.13	0.88	0.60	3.80	0.71	0.58	12	0.49	3.33	2.96	1.15	3.44	5.52
Ni	27	3	15	7	3	bdl	bdl	4	11	4	77	18	15	15	53	22
Cu	bdl	bdl	bdl	bdl	bdl	bdl	bdl	1	2	bdl	0	bdl	1	0	1659	10
Zn	bdl	2.33	2.50	2.71	2.04	bdl	2.09	2.57	2.58	3.21	3.37	2.37	2.68	3.14	2750	2.79
Ga	bdl	bdl	bdl	bdl	bdl	bdl	bdl	bdl	bdl	bdl	bdl	bdl	bdl	bdl	bdl	bdl
Ge	bdl	bdl	bdl	bdl	bdl	bdl	bdl	bdl	1	bdl	bdl	bdl	1	1	bdl	bdl
As	90	6	39	34	52	44	7	233	131	3	51	43	31	213	45	233
Se	89	11	113	125	107	11	16	95	124	22	105	92	93	137	20	66
Mo	bdl	bdl	bdl	bdl	bdl	bdl	bdl	bdl	bdl	bdl	bdl	bdl	bdl	bdl	9	0
Ag	bdl	bdl	bdl	bdl	bdl	bdl	bdl	bdl	bdl	bdl	bdl	bdl	bdl	bdl	2	bdl
Cd	bdl	bdl	bdl	bdl	bdl	bdl	bdl	bdl	bdl	bdl	bdl	bdl	bdl	bdl	27	bdl
In	bdl	bdl	bdl	bdl	bdl	bdl	bdl	bdl	bdl	bdl	bdl	bdl	bdl	bdl	0.20	bdl
Sn	bdl	bdl	bdl	bdl	0.17	bdl	bdl	bdl	bdl	bdl	bdl	bdl	bdl	bdl	bdl	bdl
Sb	bdl	bdl	bdl	bdl	bdl	bdl	bdl	0.59	1.08	bdl	bdl	bdl	bdl	bdl	0.26	bdl
W	bdl	bdl	bdl	bdl	0.24	bdl	bdl	bdl	bdl	bdl	bdl	bdl	bdl	bdl	bdl	bdl
Au	bdl	bdl	bdl	bdl	bdl	0.02	bdl	bdl	0.03	0.17	bdl	bdl	bdl	bdl	0.61	0.06
Tl	bdl	bdl	bdl	bdl	bdl	bdl	bdl	bdl	bdl	bdl	bdl	bdl	bdl	bdl	bdl	bdl
Pb	12	bdl	0	bdl	1	bdl	bdl	62	129	bdl	10	1	bdl	1	83	20
Bi	1	bdl	bdl	bdl	bdl	bdl	bdl	3	5	bdl	bdl	bdl	bdl	bdl	1	bdl

Table C.4. LA – ICP – MS data of pyrite (continued).

KMPR66/PR4 (D-type vein, Pagoni Rachi). Values in ppm; bdl = below detection limit.															
Spot	1	2	3	4	5	6	7	8	9	10	11	12	13	14	15
Mn	bdl	1	2	bdl	2	2	1	bdl	bdl	bdl	3	1	bdl	1	1
Co	326	123	44	4	104	335	1	1	0	576	4	1	0	8	1
Ni	5	8	38	17	10	39	13	5	8	35	24	34	113	41	6
Cu	1	bdl	bdl	bdl	bdl	71	9824	bdl	bdl	bdl	1	10	1	53	bdl
Zn	bdl	bdl	bdl	bdl	bdl	bdl	bdl	bdl	bdl	bdl	bdl	bdl	bdl	bdl	bdl
Ga	bdl	bdl	bdl	bdl	bdl	bdl	bdl	bdl	bdl	bdl	0	bdl	bdl	bdl	bdl
Ge	1	bdl	bdl	bdl	bdl	bdl	bdl	bdl	bdl	1	bdl	bdl	bdl	bdl	bdl
As	485	2086	489	1182	3745	1339	93	218	91	180	2366	2563	592	1269	2101
Se	108	42	98	47	116	83	187	61	45	68	79	92	117	68	60
Mo	bdl	bdl	bdl	bdl	2	10	0	bdl	bdl	bdl	17	16	bdl	16	bdl
Ag	bdl	bdl	bdl	bdl	bdl	bdl	bdl	bdl	bdl	bdl	bdl	bdl	bdl	bdl	bdl
Cd	bdl	bdl	bdl	bdl	bdl	bdl	bdl	bdl	bdl	bdl	bdl	bdl	bdl	bdl	bdl
In	bdl	0.03	bdl	bdl	bdl	bdl	0.03	bdl	bdl	bdl	0.04	bdl	bdl	bdl	bdl
Sn	bdl	bdl	bdl	bdl	bdl	bdl	bdl	bdl	bdl	bdl	0.13	bdl	bdl	bdl	bdl
Sb	bdl	bdl	bdl	bdl	bdl	bdl	bdl	bdl	bdl	bdl	0.38	bdl	bdl	bdl	bdl
W	bdl	bdl	0	bdl	bdl	bdl	bdl	bdl	bdl	0.03	bdl	0.05	bdl	bdl	bdl
Au	bdl	bdl	0.06	bdl	0.21	0.26	bdl	bdl	bdl	0.29	0.41	0.17	0.18	0.15	bdl
Tl	bdl	bdl	0.01	0.01	bdl	bdl	bdl	bdl	bdl	bdl	bdl	bdl	bdl	bdl	bdl
Pb	3	0	3	0	4	2	0	0	0	0	2	2	4	1	bdl
Bi	1	bdl	bdl	bdl	5	4	0	0	bdl	1	3	3	1	2	bdl

Table C.4. LA – ICP – MS data of pyrite (continued).

KMPR75a (D-type vein, Pagoni Rachi). Values in ppm; bdl = below detection limit.							
Spot	1	2	3	4	5	6	7
Mn	3	6	1	bdl	1	3	1
Co	99	466	1	5	3	33	2
Ni	5	8	28	22	3	5	bdl
Cu	5	125	27	bdl	bdl	2	1
Zn	4	3	bdl	bdl	bdl	4	bdl
Ga	1	bdl	0	bdl	bdl	0	bdl
Ge	bdl	bdl	bdl	bdl	bdl	2	bdl
As	3449	702	762	478	522	510	436
Se	71	64	120	146	166	72	88
Mo	bdl	bdl	bdl	bdl	bdl	33	0
Ag	bdl	bdl	bdl	bdl	bdl	bdl	bdl
Cd	bdl	bdl	bdl	bdl	bdl	bdl	bdl
In	bdl	bdl	bdl	bdl	bdl	bdl	bdl
Sn	bdl	bdl	bdl	bdl	bdl	bdl	bdl
Sb	0.54	0.57	0.13	bdl	bdl	bdl	0.19
W	bdl	bdl	bdl	bdl	bdl	bdl	0.23
Au	4.35	0.09	0.04	bdl	bdl	0.05	bdl
Tl	bdl	bdl	bdl	bdl	bdl	0	0
Pb	18	18	5	0	0	4	7
Bi	5	18	2	bdl	0	1	4

Table C.4. LA – ICP – MS data of pyrite (continued).

KMPR53ii (E-type vein, Pagoni Rachi). Values in ppm; bdl = below detection limit.												
Spot	1	2	3	4	5	6	7	8	9	10	11	12
Mn	264	2	1	bdl	1	122	45	104	52	32	4	12
Co	46	41	1	9	198	45	74	47	52	41	62	41
Ni	11	12	4	5	30	52	47	41	38	25	41	25
Cu	19	6	7	13	7	12	31	24	29	9	17	14
Zn	1015	45	bdl	3	bdl	41	2012	12	19	9	84	21
Ga	3	bdl	bdl	bdl	2	4	1	bdl	1	4	bdl	2
Ge	1	1	bdl	2	bdl	1	2	1	3	2	2	1
As	121	41	7	114	4	112	95	89	74	25	47	32
Se	11	33	54	15	63	18	24	45	20	31	12	18
Mo	3	0	bdl	bdl	bdl	4	2	bdl	bdl	2	bdl	2
Ag	1	bdl	1	0.96	1	0.32	1	2	1	2	2	0.74
Cd	6	0.92	0.61	bdl	bdl	1	1	1	3	1	2.1	0.96
In	bdl	bdl	bdl	bdl	bdl	0.1	bdl	bdl	bdl	bdl	bdl	bdl
Sn	bdl	bdl	0.14	bdl	bdl	bdl	bdl	bdl	bdl	0.2	bdl	bdl
Sb	1.77	0.23	0.55	0.53	0.37	0.25	0.17	0.21	bdl	0.86	0.4	0.46
W	bdl	0.02	bdl	0.01	bdl	0.04	0.09	bdl	bdl	bdl	bdl	bdl
Au	0.33	0.09	bdl	0.12	bdl	0.31	0.22	0.19	bdl	0.19	0.3	bdl
Tl	0.10	0.16	0.06	0.13	bdl	0.21	0.21	0.16	0.17	0.12	0.12	0.17
Pb	220	83	620	129	51	44	50	224	34	45	65	75
Bi	5.15	0.41	5.3	26	0.14	4	12	8	7451	17	6	4.8

Appendix D. Geochemical analyses of magmatic rocks. Major elements in wt%; trace elements in ppm.

Samples 1-10 granodiorite porphyry; 11-15 monzodiorite.															
	1	2	3	4	5	6	7	8	9	10	11	12	13	14	15
SiO_2	60.62	61.44	64.12	61.88	63.01	61.84	60.46	59.05	59.37	61.82	55.43	57.39	57.98	56.61	58.32
Al_2O_3	16.54	16.32	14.38	16.68	15.29	16.41	17.24	17.06	17.15	16.74	14.87	14.17	16.58	14.95	15.31
Fe_2O_3	5.69	5.21	3.49	4.68	5.05	4.89	5.64	5.42	5.63	5.53	6.64	6.7	5.01	6.11	5.49
MgO	2.75	2.81	3.12	2.55	3.31	2.99	2.93	2.75	2.96	2.46	4.34	5.47	2.65	4.86	5.48
CaO	4.42	4.27	4.16	5.09	2.77	4.12	4.14	4.76	4.56	5.33	6.48	5.32	5.25	6.32	5.45
Na_2O	3.12	3.1	3.35	5.61	2.05	2.88	3.44	3.82	3.34	3.19	2.47	2.96	2.36	2.27	2.98
K_2O	2.53	2.71	3.96	3.28	2.83	1.98	2.78	1.99	2.34	2.06	3.26	3.02	2.24	3.45	3.12
TiO_2	0.57	0.63	0.63	0.58	0.53	0.46	0.51	0.5	0.51	0.5	0.67	0.69	0.47	0.65	0.53
P_2O_5	0.13	0.12	0.14	0.13	0.12	0.11	0.11	0.11	0.12	0.1	0.19	0.16	0.11	0.19	0.21
MnO	0.11	0.1	0.03	0.06	0.13	0.12	0.11	0.12	0.09	0.09	0.14	0.05	0.14	0.11	0.09
Cr_2O_3	0.01	0.01	0.02	0.01	0.02	0.04	0.01	0.01	0.01	0.02	0.02	0.04	0.01	0.01	0.01
LOI	3.3	3.1	2.3	2.3	4.6	3.2	2.4	5.2	3.7	2	5.2	3.8	7	3.2	2.9
Sum	99.75	99.82	99.70	99.82	99.73	99.04	99.79	99.82	99.80	99.82	99.72	99.72	99.82	98.72	99.88
Ba	926	856	740	148	1191	956	622	278	536	476	731	784	449	741	644
Be	1	1	2	2	<1	2	<1	2	2	<1	2	3	5	3	2
Ce	45	45	46	46	45	45	38	37	41	40	39	38	39	39	37
Co	14	12	50	5	12	11	11	10	12	10	21	19	10	10	11
Cs	0.5	1	1.9	1	4.8	2.5	6	8.3	14.3	1.3	1.5	2.3	20.4	11.6	9.8
Dy	2.9	2.4	2.86	3.28	3.28	3.6	3.01	2.96	3.05	3.02	3.19	3.34	2.95	3.35	2.98
Er	2.01	2	1.99	2.06	1.89	1.88	1.82	1.77	1.85	1.89	1.95	1.95	1.73	1.79	1.65
Eu	0.81	0.76	0.77	0.87	0.79	0.81	0.79	0.68	0.8	0.79	0.87	0.87	0.87	0.91	0.88
Ga	16	14	14	17	13	12	16	15	17	15	15	12	15	15	15
Gd	3.17	3.11	3.36	3.36	3.61	3.48	2.93	2.73	3.38	3.09	3.4	3.7	3.12	3.4	3.21
Hf	3.4	4	5.6	3.4	4.7	3.8	3.1	3	3	3.2	3.5	4.3	3	3.6	3.4

Ho	0.64	0.61	0.64	0.67	0.67	0.61	0.68	0.56	0.68	0.59	0.66	0.7	0.57	0.58	0.63
La	24.2	23	21	24	27	25	18	18	19	20	19	19	19	19	18
Lu	0.3	0.35	0.31	0.31	0.27	0.31	0.28	0.27	0.3	0.26	0.3	0.26	0.28	0.29	0.28
Nb	6.1	6.4	9.8	6.4	7.8	6.9	6	5.7	6.6	6.1	7.2	7.4	5.9	5.6	6.1
Nd	17	17	20	17	19	18	15	13	15	15	15	15	15	15	16
Pr	4.76	5.11	5.39	4.76	5.16	5.12	3.98	3.8	4.26	4.17	4.17	4.22	4.21	4.28	4.17
Rb	54	57	97	70	91	79	69	32	70	52	85	92	86	84	80
Sc	2.8	4.9	15	3.1	4.9	7	3.9	8.4	8.1	2.5	4.6	6	4.2	2.8	3.1
Sm	3.24	3.31	3.7	3.25	3.69	3.12	2.83	3.19	3.21	3.05	3.42	3.67	3.08	3.07	3.12
Sn	1	1	3	1	3	2	2	1	1	2	2	2	2	1	2
Sr	365.8	364	231	571	139	256	356	278	369	347	347	287	215	284	236
Ta	0.5	0.6	1.3	0.8	0.7	0.5	0.6	0.6	0.5	0.6	0.6	0.7	0.4	0.4	0.5
Tb	0.5	0.48	0.54	0.54	0.55	0.51	0.5	0.44	0.52	0.5	0.56	0.58	0.46	0.56	0.52
Th	10.4	15	17	11	15	17	7	8	7	8	11	12	7	8	7
Tm	0.29	0.3	0.3	0.29	0.3	0.31	0.29	0.29	0.29	0.29	0.29	0.3	0.29	0.28	0.24
U	4	3.6	3.8	3.7	4.9	3.7	2.8	3	3.2	2.8	3.9	3.4	3.1	3.2	3.6
V	136	128	120	135	107	145	127	125	129	119	149	146	114	112	142
W	4.7	4.5	3.96	4.9	7.5	5.4	4.9	5.1	7.1	6.9	4.2	8.1	3.2	4.2	3.8
Y	16.6	18	18	17	19	19	16	15	18	16	17	18	16	17	17
Yb	1.94	1.92	1.93	1.89	1.85	1.84	1.8	1.68	1.93	1.81	1.84	1.85	1.69	1.65	1.78
Zr	116.4	121	208	123	158	145	93	102	107	106	114	149	112	121	119

Appendix D. Geochemical analyses of magmatic rocks. Major elements in wt%; trace elements in ppm (continued).

Samples 15-19 sericitic-altered microgranite porphyry; 20 potassic-altered microgranite porphyry											
	16	17	18	19	20		16	17	18	19	20
SiO_2	77.38	76.32	72.46	72.58	71.65	Ho	0.61	0.49	0.59	0.53	0.56
Al_2O_3	14.3	14.46	15.49	15.96	12.9	La	27	22	23	22	23
Fe_2O_3	0.41	0.51	1.02	1.89	1.24	Lu	0.32	0.31	0.3	0.34	0.34
MgO	0.93	0.78	0.91	0.45	1.11	Nb	9.8	8.9	9.2	9.5	9.4
CaO	0.11	0.21	0.18	0.12	1.45	Nd	17	15	17	14	12
Na_2O	0.16	0.32	0.42	0.46	0.21	Pr	5.1	4.91	4.84	4.47	4.48
K_2O	3.46	3.12	3.12	3.98	7.08	Rb	121	132	142	137	253
TiO_2	0.27	0.21	0.17	0.12	0.17	Sc	6	4	3	4	3
P_2O_5	0.07	0.5	0.39	0.17	0.05	Sm	2.99	2.45	2.78	2.63	2.67
MnO	0.01	0.01	0.03	0.06	0.06	Sn	3	1	2	2	2
Cr_2O_3	0.01	0.01	0.01	0.01	0.02	Sr	11	14	11	19	91
LOI	2.7	2.9	4.2	3.6	3.7	Ta	1.5	1.2	1.1	1.6	1.6
Sum	99.80	99.34	99.39	99.39	99.62	Tb	0.46	0.48	0.39	0.42	0.39
Ba	164	215	178	212	1313	Th	19	16	19	19	20
Be	3	2	2	1	<1	Tm	0.29	0.29	0.31	0.28	0.29
Ce	49	44	46	49	44	U	4.1	4.8	3.9	4.9	10
Co	40	42	40	40	51	V	36	31	25	19	16
Cs	0.9	0.6	0.8	1	5.6	W	4.24	4.1	4.21	4.8	5.11
Dy	2.69	2.21	2.56	2.36	2.48	Y	18	18	17	17	18
Er	1.91	1.88	1.71	1.91	1.72	Yb	1.95	1.92	1.98	1.87	2.09
Eu	0.5	0.45	0.51	0.47	0.52	Zr	148	145	124	125	88
Ga	13	12	11	12	11						
Gd	2.82	2.12	2.89	2.45	2.39						
Hf	4.1	3.6	3.2	3.4	2.7						

Appendix E. Geochemical analyses of mineralized rocks. Values in ppm; bdl = below detection, na = not analyzed.

Samples KMSP series.															
KMSP-	1	3	4a	4b	7	17b	35	36	37	43	44	45	46	47	48
Ag	0.06	0.01	0.03	0.03	0.02	0.04	0.51	0.07	0.06	0.11	0.79	0.05	0.18	0.22	0.94
As	1.4	3.6	0.1	1.9	12	53	1981	4021	73	3.5	219	8.6	315	9.6	53
Au	0.02	0.02	0.03	0.05	0.04	0.01	0.02	0.01	0.01	0.01	0.03	0.01	0.03	bdl	0.1
Bi	0.94	0.38	0.93	1.19	2.38	1.76	14	2.05	2.2	0.25	7.93	1.69	2.58	4.38	14
Cd	0.02	bdl	bdl	0.02	bdl	bdl	0.34	0.09	bdl	0.06	0.16	0.03	0.03	0.03	6.57
Co	11	15	25	24	26	16	46	34	6	2.8	2.7	17	0.7	10	2.9
Cr	128	3.7	97	5.4	138	4.7	146	20	223	115	255	145	178	148	332
Cu	64	7.92	3	20	9.04	15	11	89	17	69	53	8.28	41	50	99
Ga	4.3	0.5	1	1.1	4.3	7.2	0.8	1.8	1.6	13	2.75	7.94	5.34	11	3.43
Ge	0.1	bdl	bdl	0.1	bdl	bdl	0.2	0.2	bdl	bdl	bdl	bdl	bdl	bdl	bdl
In	bdl	bdl	bdl	bdl	bdl	bdl	0.1	0.28	0.07	0.1	0.04	0.02	0.19	0.22	0.58
Li	7.6	0.2	0.3	0.8	7.6	6.1	0.4	0.3	0.8	4.1	46	9.7	41.5	37.3	23.9
Mo	2.31	4.55	35	6.99	0.51	0.92	6.19	0.68	3.43	12	14	19	3.41	1.51	9.48
Ni	10	3.4	8.7	9.4	110	3.6	36	41	7.9	8.3	22	10.5	3.8	12	12
Pb	3.98	1.57	2.68	2.71	5.21	7.72	11	13	7.43	5.98	94	11	8.58	5.48	145
Pd	bdl	bdl	bdl	bdl	bdl	bdl	bdl	bdl	bdl	na	na	na	na	na	na
Pt	bdl	bdl	bdl	bdl	bdl	0.002	bdl	bdl	bdl	na	na	na	na	na	na
Re	0.049	0.014	0.651	0.033	0.005	0.002	bdl	bdl	bdl	0.015	bdl	0.025	bdl	bdl	bdl
Sb	0.05	0.04	bdl	bdl	0.04	0.11	32	82	7.77	0.35	39	3.2	29	16	15
Se	2.5	8	5.6	10.5	4.1	0.6	2.7	2	1.6	1.5	0.4	2.2	2.5	0.7	0.4
Sn	0.30	bdl	0.10	0.21	bdl	0.21	0.12	0.17	0.31	2.91	0.45	2.52	0.71	1.50	0.70
Te	0.40	0.10	0.55	0.62	0.18	1.89	18	1.81	3.56	1.28	9.05	1.7	1.78	4.02	0.9
Tl	0.03	0.04	0.04	0.05	0.07	bdl	0.65	1.32	0.15	0.58	0.52	0.33	1.09	0.85	0.53
U	3.3	0.92	0.97	1.24	0.56	0.45	0.25	0.2	0.32	4.6	0.6	2.4	0.9	0.6	0.7

V	21	3	5	6	25	68	19	53	12	72	29	84	29	55	33
W	bdl	bdl	bdl	bdl	bdl	0.1	1.35	3.43	0.89	3.3	32	1.4	4.1	51	1.4
Zn	14.9	1.3	2.4	2.6	4.5	34	78	94	9.8	15	30	45	3.3	33	1328

KMSP-	49	50	51	54	58	59	60	61	62	63	64	65	66	67	68
Ag	0.05	0.03	bdl	0.02	0.04	0.17	0.12	0.05	0.09	3.35	0.02	0.04	0.03	0.035	bdl
As	10	2	1.5	8.7	3.9	13	7.6	3.3	29	1121	3.4	17.5	1.8	6.4	0.9
Au	0.008	bdl	bdl	0.005	0.028	bdl	0.007	bdl	0.008	0.924	0.031	0.141	0.029	0.042	bdl
Bi	0.38	0.14	0.48	3.26	1.02	0.52	1.6	0.69	2.52	2.99	2.92	1.81	1.45	2.12	1.44
Cd	0.12	bdl	bdl	0.03	0.11	0.04	0.03	0.2	0.09	13	0.17	0.12	0.09	0.1	0.03
Co	41	5.2	3.8	bdl	29	2.9	53	22	17	9.6	24	11	23	12	17
Cr	135	42	16	44	58	61	168	103	229	143	123	14	14	11	63
Cu	51	2.01	3.27	8.07	135	30	104	141	36	31	14	46	11	43	9.47
Ga	8.04	17	15	16	15	16	18	20	7.38	5.47	20	6.97	20	18	17
Ge	bdl	bdl	bdl	bdl	bdl	bdl	bdl	bdl	bdl	bdl	bdl	bdl	bdl	bdl	bdl
In	bdl	0.03	bdl	0.03	bdl	0.03	0.13	0.04	0.04	0.22	0.01	bdl	0.04	bdl	0.02
Li	14	4.1	3.6	2.6	3.3	8.9	9.4	14	11	45	8.7	2	0.5	9.7	14
Mo	4.05	5.47	1.79	1.54	4.63	1.76	1.12	1.9	18	128	47	17	0.82	6.19	1.5
Ni	48	1.8	1.4	0.6	11	8.3	235	52	13	6.2	41	3.7	10	2.7	29
Pb	11	2.79	1.22	1.08	6.07	9.46	9.26	4.06	12	603	6.34	42	13	19	4.64
Pd	na	na	na	na	na	na	na	na	na	na	na	na	na	na	na
Pt	na	na	na	na	na	na	na	na	na	na	na	na	na	na	na
Re	0.012	bdl	0.018	bdl	0.061	bdl	bdl	bdl	0.023	0.021	0.187	0.065	bdl	0.034	0.022
Sb	1.25	0.1	0.11	0.32	0.16	2.58	0.77	0.23	3.32	31	0.39	0.56	1.66	1.12	0.24
Se	4.51	1.10	0.9	7	4.71	3.45	5.31	3.11	1.61	2	4.61	8.12	10	6.91	3.42
Sn	0.52	1.20	1.81	0.80	1.31	0.80	2	1.20	2	0.80	4.11	2.40	4.50	8.82	1.31
Te	0.41	0.32	0.08	0.21	0.52	0.21	3.58	0.38	1.79	18	0.19	0.27	0.08	0.11	0.38

Tl	0.47	0.58	0.55	0.26	0.46	1.68	0.28	1.35	0.45	4.38	0.87	0.14	2.07	0.2	1.15
U	0.6	1.9	1.3	1.3	3	2.1	1.6	2.3	2.7	1	2.2	1.9	1.6	5.3	4.2
V	44	100	112	118	97	83	77	182	78	80	107	79	156	108	177
W	0.7	1.1	0.7	0.6	0.6	0.5	1.6	0.6	1.2	2.2	1.4	0.7	0.3	1.1	1.7
Zn	48.5	8.7	3.9	3.1	20	13	6	62	5	790	17	16	9.2	7.9	29

KMSP-	69	70	71	72	73	74	75	76	77	78	79	80b		81	84
Ag	0.19	0.16	0.13	0.23	0.22	0.04	0.12	0.13	0.05	2.61	0.21	0.17	0.07	0.26	0.37
As	15	18	34	18	3.9	5.9	67	66	1.6	550	74	69	9.5	108	296
Au	0.044	0.021	0.364	0.187	0.039	0.027	bdl	0.053	0.006	0.051	0.063	0.022	0.008	0.176	0.029
Bi	2.03	2.97	2.42	2.08	6.79	1.79	13.4	9.22	0.99	0.34	0.35	1.55	0.1	3.11	1.12
Cd	0.02	0.06	0.03	0.02	0.03	0.09	bdl	0.02	bdl	282.44	0.3	0.43	0.02	bdl	0.28
Co	0.3	0.3	bdl	0.4	0.4	0.2	bdl	0.7	4.2	3.7	1.2	13.7	14.5	27.1	8.4
Cr	38	24	34	52	44	13	10	24	17	125	263	107	96	206	289
Cu	9.88	6.67	7.39	4.49	32	8.58	14	13	16	300	2.54	3.92	6.08	8.43	23
Ga	5.12	4.22	6.72	11	14	17	17	16	12	3.4	6.16	15	17	6.08	4.52
Ge	bdl	bdl	bdl	bdl	bdl	bdl	bdl	bdl	bdl	bdl	bdl	bdl	bdl	bdl	bdl
In	bdl	bdl	0.01	bdl	0.03	0.03	0.02	0.03	bdl	0.14	0.01	bdl	0.1	bdl	0.02
Li	0.7	0.6	0.7	0.8	0.6	0.7	1.4	2	3.6	12.3	17.1	30.6	15.7	18	32.6
Mo	3.56	2.36	2.36	3.76	19	5.95	1.3	4.55	4.43	2.16	3.48	2.02	1.22	48.75	6.53
Ni	1.3	1.1	0.7	2.4	1.6	0.5	0.7	1.8	1.8	4.1	4.6	5.5	10.7	6.5	9.8
Pb	110	116	122	93	16	59	93	87	3.59	977	12	33	7.64	59	73.2
Pd	na	na	na	na	na	na	na	na	na	na	na	na	na	na	na
Pt	na	na	na	na	na	na	na	na	na	na	na	na	na	na	na
Re	bdl	bdl	bdl	bdl	bdl	0.011	bdl	bdl	0.006	0.013	bdl	0.012	0.024	bdl	0.005
Sb	5.07	1.88	1.93	5.34	4.89	0.56	4.91	7.35	0.56	93	16	4.15	1.23	15	23
Se	2.5	4.4	14	5.9	26	6.5	2.5	11	3.1	0.3	bdl	1.5	0.5	1.7	bdl

Sn	3.7	2.1	2	1.6	4.6	18	1	2.5	5.8	0.5	1	2.2	4	0.4	0.4
Te	0.23	0.12	0.16	0.21	0.71	0.16	0.78	1.83	0.18	1.01	0.43	1.02	0.72	1.15	0.75
Tl	0.06	0.07	0.07	bdl	0.18	2.39	bdl	0.07	1.08	1.34	1.38	2.66	0.85	1.09	0.83
U	1.9	2	1.3	1.5	2.3	1.7	2.7	3.8	1.6	0.6	1.4	1.1	1.2	0.5	0.4
V	78	102	107	105	105	184	134	120	113	39	31	186	135	82	46
W	0.8	1.9	0.9	1.7	0.8	1.4	1.3	2.3	0.9	1.7	1.4	4.6	1.3	1.3	1
Zn	4.4	2.5	2	4.3	5.8	7.4	11.7	6.6	3.1	5867	7.2	61	39	57	56

KMSP-	85	86
Ag	0.16	0.24
As	177	127
Au	0.026	0.02
Bi	1.56	1.47
Cd	0.04	bdl
Co	12	18
Cr	216	222
Cu	22	3.09
Ga	11	6.62
Ge	0	0
In	0.02	0.06
Li	31	19
Mo	38	7.64
Ni	24	7.8
Pb	18	19
Pd	na	na
Pt	na	na

	85	86
Re	0.025	0.005
Sb	22	2.03
Se	0.9	0.7
Sn	1.3	0.6
Te	1.1	1.09
Tl	0.88	1.28
U	1.4	0.8
V	88	69
W	3.6	2
Zn	68	49

Samples KMPR series. bdl = below detection, na = not analyzed.

KMPR-	3	4	5	6	7	8	9	10	11	12	13	14	15	16	17
Ag	0.26	0.44	0.41	0.32	0.06	0.31	0.06	0.16	0.16	0.48	0.26	0.12	0.45	0.32	0.43
As	32	130	33	7.3	59	44	8.6	3.6	30	23	50	14	45	7.2	12
Au	0.186	0.095	0.127	0.204	0.124	0.165	0.088	0.199	0.135	0.075	0.128	0.065	0.235	0.218	0.057
Bi	0.16	1.75	1.32	0.11	1.16	3.22	1.08	0.69	2.23	2.12	1.78	0.89	0.81	1.25	3.58
Cd	0.19	0.55	1.86	0.56	0.06	bdl	0.03	bdl	0.05	bdl	bdl	0.03	0.01	bdl	0.04
Co	11.4	4.3	8.9	10.7	2.4	2	0.2	0.2	1.2	0.2	0.2	2.6	0.1	1.3	0.5
Cr	66	3	131	4.7	89	2.80	71	2.85	106	3.81	4.51	229	5.32	72	3
Cu	235	123	215	319	158	109	259	68	89	174	96	33	49	207	144
Ga	2.9	1.1	1.4	6.2	1.4	1.6	1.1	2.8	2.7	1.4	2	1.9	0.9	6	4.2
Ge	bdl	bdl	bdl	bdl	bdl	bdl	bdl	bdl	bdl	bdl	bdl	bdl	bdl	bdl	bdl
In	0.04	0.03	0.11	0.07	0.05	0.06	0.08	bdl	bdl	0.08	0.08	0.08	bdl	0.05	0.02
Li	6.6	4.7	1.9	11	1.4	1	0.6	0.5	0.8	0.9	0.5	0.6	0.6	2.6	1.2
Mo	68	7.09	3.73	42	40	51	53	35	20	21	8.55	2.25	9.53	24	8.76
Ni	4.4	2	3.2	2.8	1.9	0.8	1	0.8	1.7	1	0.7	2.7	0.9	1.1	1
Pb	15.8	203	30	17	131	13	12	6.06	21	34	43	12	27	14	58
Pd	0.015	bdl	bdl	bdl	bdl	bdl	0.014	bdl	bdl	bdl	bdl	bdl	bdl	bdl	bdl
Pt	bdl	bdl	bdl	bdl	0.003	bdl	bdl	0.003	bdl	bdl	bdl	bdl	0.003	bdl	bdl
Re	0.962	0.144	0.018	0.503	0.004	0.048	0.044	0.025	0.009	0.005	0.003	0.002	0.005	0.014	0.005
Sb	0.12	10	2.53	0.06	18	2.22	0.15	0.05	1.07	0.19	0.81	0.42	5.21	0.03	0.04
Se	2.8	0.9	1.1	2	2.3	0.5	1	0.8	4.1	1.4	2	0.3	2.3	2.7	1.2
Sn	0.5	0.9	0.6	1.2	0.3	0.3	bdl	0.3	0.4	0.2	0.4	0.4	0.2	0.4	0.3
Te	0.7	0.66	1.58	0.38	0.35	0.69	0.69	0.15	1.48	1.27	2.19	0.5	0.2	0.26	1.14
Tl	0.12	3.63	0.25	0.07	0.05	0.05	0.05	0.03	0.08	0.07	0.08	0.07	0.11	0.07	0.06
U	0.61	0.24	0.85	1.16	0.44	0.2	0.72	0.14	0.25	0.12	0.16	0.15	0.11	0.54	0.38
V	31	11	30	55	20	20	25	26	27	20	39	19	6	58	49

W	0.13	0.18	0.13	0.06	0.17	0.11	bdl	bdl	0.11	0.08	0.12	0.17	bdl	bdl	bdl
Zn	78	107	88	133	124	100	9	3.6	118	4.9	3.8	59	2	20	75.6

KMPR-	18	19	21	22	23	24	25	26	27	28	32	33	34	36	37
Ag	0.13	0.01	0.14	0.27	0.16	0.08	0.09	0.30	0.70	0.06	0.02	0.11	0.13	0.25	0.10
As	35	0.4	3.6	90.1	23.9	12.1	28.1	15.8	27.3	27.5	6.4	13.5	19.7	2.4	0.9
Au	0.118	0.087	0.278	0.127	0.143	0.112	0.164	0.168	0.301	1.123	0.041	0.281	0.168	0.058	0.036
Bi	1.46	0.95	0.98	0.23	1.24	1.31	1.55	0.74	1.47	1.24	0.45	1.43	1.24	0.39	0.13
Cd	0.21	bdl	0.06	0.45	0.02	0.03	bdl	bdl	bdl	bdl	bdl	bdl	0.26	1.42	0.09
Co	3.1	bdl	5.6	1.3	0.5	0.1	0.1	0.1	0.3	0.3	0.2	17.1	13	10	8.9
Cr	3.3	54	4.6	3.8	147	3	113	3.2	105	9.1	67	1.9	71	4.3	3.9
Cu	139	3.26	225	75	76	73	70	30	135	168	7.51	198	140	297	75
Ga	2	1.5	6.7	1.8	2.5	2.2	2.2	2.1	1.4	3.1	0.7	1.3	1.2	3.8	6.9
Ge	bdl	bdl	0.2	bdl	bdl	bdl	bdl	bdl	bdl	bdl	bdl	bdl	bdl	0.2	bdl
In	0.06	bdl	0.06	bdl	bdl	bdl	0.04	bdl	bdl	0.02	bdl	bdl	0.03	bdl	bdl
Li	1.1	1	6.6	2.3	1	1	0.6	0.5	1.3	0.8	1	2.2	1.5	5.1	8.2
Mo	7.25	3.7	19	18.4	4.5	6.09	6.73	15	37	58	164	8.54	12	3.86	1.85
Ni	1.6	0.5	1.9	1.2	2	0.5	1.4	0.5	1.8	0.9	0.8	3.9	4.5	1.6	3.7
Pb	60	8.48	4.51	20	19	8.69	9.04	4.98	3.64	16	6.89	15	14	193	5.85
Pd	bdl	bdl	bdl	bdl	bdl	bdl	bdl	bdl	bdl	0.011	0.029	bdl	bdl	bdl	bdl
Pt	bdl	bdl	bdl	bdl	bdl	bdl	bdl	bdl	0.004	bdl	bdl	bdl	bdl	bdl	bdl
Re	0.003	0.003	0.055	0.015	0.003	0.003	0.003	0.007	0.016	0.01	0.097	0.114	0.11	0.062	0.019
Sb	0.85	0.69	0.05	7.6	1.18	0.53	1.68	0.48	0.27	0.15	0.08	0.27	0.33	0.09	bdl
Se	0.6	3.6	0.3	0.1	1	1.2	2.6	2.5	4.3	1.1	2.2	1.4	0.6	1.9	bdl
Sn	0.6	0.2	1.1	1.1	1.1	0.2	0.2	0.2	0.1	0.2	0.1	bdl	0.2	0.5	0.5
Te	0.75	0.06	0.14	0.11	1.16	0.56	2.68	0.22	0.72	0.57	0.21	0.83	0.53	0.26	0.05
Tl	0.04	0.06	0.03	0.59	bdl	0.04	0.08	0.04	0.06	0.05	0.03	0.26	0.22	0.04	0.04

U	0.41	0.43	0.67	0.59	0.19	0.12	0.1	0.09	0.12	0.19	0.2	0.66	0.75	0.77	0.76
V	37	7	60	50	34	22	23	15	30	31	14	43	20	31	54
W	0.17	0.06	0.09	0.22	0.12	0.07	0.09	0.05	bdl	bdl	0.05	bdl	bdl	bdl	bdl
Zn	400	2	40	44	4	2	1.95	1.46	4.61	5.30	1.32	64	44	248	47

KMPR-	40	41	43	44	47	51	52	55	56	57	58	59	60	61	62
Ag	0.10	0.09	0.16	0.08	0.05	0.11	0.12	0.05	0.12	0.09	0.20	0.06	0.14	0.15	0.03
As	4.2	2.9	4.2	1.9	1.4	4.2	1	1	11	9.4	3.1	5.3	2	1.5	2.8
Au	0.057	0.046	0.136	0.033	0.036	0.051	0.458	0.061	0.106	0.064	0.023	0.188	0.039	0.029	0.194
Bi	0.4	0.37	0.41	0.38	0.07	0.33	0.48	0.39	1.22	0.36	0.44	0.75	0.03	0.1	0.67
Cd	0.05	0.05	0.85	0.17	0.08	2.22	0.06	0.04	bdl	0.22	2.06	1.09	0.22	0.18	bdl
Co	9.6	11.4	7.8	13	8.3	8.4	11	8	1.3	2.4	7.7	8.1	7.4	7.1	0.9
Cr	57	6.4	73	2.9	4.4	60	15	70	2.3	97	2.6	79	3.8	61	2.3
Cu	68	108	107	17	46	67	122	66	27	50	10	35	163	89	14
Ga	7.2	5.9	4.3	3.3	7.7	7.3	7	6.9	1.5	1.6	1.6	1.2	4.3	5.3	3.3
Ge	0.1	0.1	bdl	bdl	bdl	bdl	bdl	bdl	bdl	bdl	bdl	bdl	0.2	0.2	bdl
In	0.05	0.04	bdl	bdl	bdl	0.12	bdl	bdl	bdl	bdl	bdl	bdl	0.05	0.12	bdl
Li	13	11	11	7	8	11	12	10	1.8	1.2	2.5	1.3	7.3	12	1
Mo	1.1	1.35	4.06	14	1.88	0.64	4.93	1.5	8.68	18	14	9.57	0.81	1.61	2.67
Ni	4.6	3.8	3.3	2.5	3.3	3.5	5.9	3.6	0.8	2.1	3.2	3.8	2.3	2.5	0.5
Pb	7.26	4.96	128	9.22	2.1	9.25	7.53	9.53	17	25	67	165	8.91	5.01	21
Pd	bdl	bdl	bdl	bdl	bdl	bdl	bdl	bdl	bdl	bdl	bdl	bdl	bdl	bdl	bdl
Pt	bdl	0.002	bdl	bdl	bdl	bdl	bdl	bdl	bdl	bdl	bdl	bdl	bdl	bdl	0.002
Re	0.009	0.022	0.07	0.331	0.012	0.005	0.074	0.024	0.004	0.005	0.002	0.002	bdl	0	0.003
Sb	0.03	0.04	0.04	0.03	bdl	0.03	bdl	bdl	0.36	0.63	0.17	0.27	0.05	bdl	0.05
Se	1.3	1.4	0.6	1	bdl	0.3	0.7	0.3	1.1	2	2.1	3.5	bdl	bdl	3.2
Sn	0.8	0.7	0.8	0.3	0.5	1	0.6	0.4	0.4	0.3	0.4	0.2	1.7	1	0.3

Te	0.07	0.07	0.16	0.16	0.04	0.18	0.05	bdl	0.2	0.11	0.18	0.43	bdl	0.02	0.17
Tl	bdl	0.03	0.06	0.11	0.04	0.09	0.07	0.05	0.03	0.04	0.05	0.06	bdl	bdl	0.09
U	0.68	0.76	0.91	0.3	0.71	0.69	0.7	0.86	0.18	0.51	0.26	0.29	0.63	0.6	0.32
V	93	79	53	41	62	82	87	65	21	31	35	22	71	70	34
W	0.07	0.1	bdl	bdl	bdl	bdl	0.06	bdl	bdl	bdl	bdl	bdl	0.18	0.05	bdl
Zn	36	35	154	54	57	138	30	22	34	61	183	249	46	48	6.2

KMPR-	63	64	66	67	68	68b	69	70	71	73	74	75a	75b	76	77a
Ag	0.10	0.08	1.74	0.24	0.35	0.48	0.43	0.21	0.32	14	0.22	0.18	0.86	0.33	1.10
As	9.3	4.7	409	15	4.7	30	42	18	46	3981	8.9	29	193	11	239
Au	0.103	0.173	6.302	0.238	0.254	0.284	0.113	0.09	0.189	0.208	0.679	0.158	3.941	0.044	0.808
Bi	0.69	1.12	1.8	0.08	0.07	0.24	1.55	1.22	0.61	6.35	0.4	0.21	1.95	0.73	2.21
Cd	0.06	0.02	0.1	0.28	0.22	2.89	0.04	bdl	bdl	174	0.33	0.34	0.15	1.92	0.2
Co	0.4	0.7	56	11	11	13	0.3	0.3	0.6	5.8	18	6.8	32	11	9.5
Cr	2.1	69	222	3.8	7.4	124	2.7	93	2.6	280	126	168	229	139	248
Cu	52	30	208	266	355	545	18	165	121	>10000	573	283	290	17	174
Ga	0.9	3.7	0.9	4.9	7.2	4.5	1.2	2.3	1.7	6.78	15	7.79	6.73	13	14
Ge	bdl	bdl	0.4	bdl	0.3	bdl	bdl	bdl	bdl	na	na	na	na	na	na
In	bdl	0.03	0.05	bdl	0.04	0.03	bdl	0.17	0.04	1.14	0.22	0.05	0.07	0.02	0.21
Li	1	2.10	2.81	9.30	8.44	8	0.41	0.51	0.72	9.71	16	21	28	18	5.11
Mo	5.36	8.07	35	66	50	53	12	17	18	2.42	8.31	67	90	3.69	18
Ni	0.6	0.8	18.4	3.4	4.3	5	0.2	1.2	0.4	35	5.6	3.9	10.9	5.3	12
Pb	13	14	16	24	7.55	78	25	19	29	>10000	26	116	19	784	47
Pd	bdl	bdl	bdl	0.011	bdl	bdl	bdl	bdl	bdl	na	na	na	na	na	na
Pt	bdl	bdl	bdl	bdl	bdl	bdl	bdl	bdl	bdl	na	na	na	na	na	na
Re	0.006	0.003	0.572	>1	0.666	0.678	0.002	0.007	0.002	0.012	0.037	0.966	>1	0.029	0.034
Sb	0.29	0.06	0.39	0.08	0.03	0.07	2.09	0.05	0.28	890	1.23	0.81	2.56	0.34	6.48

Se	1.5	0.7	56	1.4	1.5	4.3	2.5	1.1	4.2	2.3	bdl	2.8	29	4.7	24
Sn	0.1	0.5	0.8	0.7	0.8	0.6	0.2	0.6	0.1	2.5	4.8	1.8	4.7	2.2	3.7
Te	0.25	0.24	5.53	0.46	0.19	0.86	0.2	0.34	0.2	4.53	bdl	1.02	5.68	0.74	1.5
Tl	0.04	0.02	0.13	0.14	0.05	0.08	0.12	0.06	0.05	7.85	0.17	0.62	0.76	0.91	1.3
U	0.31	0.15	0.11	0.65	0.93	0.94	0.25	0.16	0.14	0.7	1.7	1.3	1	1.7	1.5
V	27	48	14	50	59	38	9	32	21	26	115	61	87	86	84
W	bdl	bdl	0.84	0.06	0.07	0.14	bdl	bdl	0.05	1.1	1.3	5.6	13	1.2	2.3
Zn	16	14	48	103	106	208	5.2	3.2	14	>10000	83	57	128	392	37

KMPR-	77b	78	79	83	84	87	89	90	91	92	93	94	95
Ag	0.33	8.18	86	0.81	0.21	0.92	0.16	0.09	6.30	1.05	0.20	0.12	bdl
As	57	369	2028	8.3	3.5	95	310	47	49	396	279	81	111
Au	0.084	0.138	0.816	0.115	0.015	0.281	0.087	0.01	0.122	0.042	0.008	0.011	0.005
Bi	0.6	1.13	8.3	0.66	2.38	1.95	1.07	1.17	1.81	20	0.39	2.39	0.39
Cd	0.51	12	68	38	0.51	1.07	0.05	na	0.35	0.03	0.1	0.13	0.02
Co	11.7	4.2	5	5.9	9.7	4.5	42	2.7	2	204	9.9	46	0.7
Cr	73	234	329	173	111	252	236	229	282	229	126	258	93
Cu	28	343	226	28	5.37	35	29	5.21	25	6.04	4.29	6.86	7
Ga	6.35	25	68	4.41	6.1	0.76	12	4.76	32.5	1.98	6.91	3.61	12
Ge	na	na	na	na	na	na	na	na	na	na	na	na	na
In	0.03	2.88	12	0.03	bdl	0.02	0.13	bdl	2.5	0.02	0.04	bdl	bdl
Li	9.7	37	24	15	9.1	24	43	11	53	11	44	16	6.3
Mo	1.97	1.95	4.59	49	51	31	7.18	11	11	15	2.94	5.71	4.98
Ni	3.8	13	27	3.5	3.6	4.3	161	6.7	14	38	41	40	3.1
Pb	56	426	>10000	3167	47	417	14	16	1779	22	6.9	9.29	1.67
Pd	na	na	na	na	na	na	na	na	na	na	na	na	na
Pt	na	na	na	na	na	na	na	na	na	na	na	na	na

Re	0.004	bdl	0.005	0.196	0.054	bdl	bdl	0.007	bdl	0.007	bdl	bdl	bdl
Sb	2.91	125	1166	4.13	1.24	11	10	3.34	19	4.38	19	18	4.81
Se	2.40	2.70	1.50	3.90	1.60	1.90	0.71	na	3.50	86.6	0.30	4.20	5.80
Sn	1.1	2.2	18.2	1.8	2.5	0.2	1.3	1	1	0.10	0.72	0.30	1.61
Te	2.55	6.6	6.75	0.54	1.96	0.64	0.13	1.3	0.48	12.56	0.32	1.54	0.85
Tl	0.73	9.93	18	0.53	0.84	0.08	1.69	1.61	0.35	0.1	1.41	1.1	0.87
U	1	4.40	96	0.70	0.90	0.30	3	0.50	7.80	1	0.90	0.71	0.82
V	53	86	66	45	59	6	89	39	66	17	63	30	72
W	1.2	4	46	2.1	0.8	0.2	2	1.1	4.3	1.8	1.7	26	1.4
Zn	110	4309	566	5145	92	217	50	15	311	49	54	287	3.8

Appendix F – Mineralogical content of selected samples defined by XRD analyses.

No.	Sample code	Mineral phases identified:
1	KMSP-2	Quartz, muscovite, pyrite
2	KMSP-3	Quartz, muscovite
3	KMSP-4b	Quartz, muscovite, pyrite, kaolinite
4	KMSP-5	Quartz, muscovite, pyrite
5	KMSP-6	Quartz, muscovite, albite
6	KMSP-8	Quartz, albite, clinochlore, muscovite
7	KMSP-16	Albite, quartz, clinochlore, epidote
8	KMSP-23	Muscovite, pyrite
9	KMSP-26a	Alunite, quartz
10	KMSP-26b	Quartz, alunite, pyrophyllite
11	KMSP-26c	Quartz, alunite, kaolinite
12	KMSP-26d	Quartz, alunite, natroalunite
13	KMSP-27	Alunite, quartz
14	KMSP-28	Quartz, alunite
15	KMSP-30	Quartz, alunite, natroalunite, kaolinite
16	KMSP-31	Quartz, alunite, natroalunite
17	KMSP-43	Quartz, albite, clinochlore
18	KMSP-50	Quartz, muscovite, illite, albite
19	KMSP-51	Muscovite, quartz
20	KMSP-61	Albite, biotite, clinochlore, quartz, pyrite
21	KMSP-64	Quartz, clinochlore, muscovite, pyrite
22	KMSP-65	Quartz, pyrophyllite, kaolinite, pyrite
23	KMSP-67	Quartz, kaolinite, pyrite
24	KMSP-69	Quartz, alunite
25	KMSP-70	Quartz, alunite
26	KMSP-74	Quartz, alunite, muscovite
27	KMSP-75	Quartz, alunite
28	KMSP-76	Quartz, alunite
29	KMSP-77	Quartz, alunite, muscovite
30	KMSP-80b	Calcite, quartz, muscovite, pyrite, montmorillonite
31	KMSP-81	Albite, clinochlore, tremolite, muscovite, quartz
32	KMSP-82	Albite, clinochlore, tremolite, quartz
33	KMPR-3	Quartz, muscovite
34	KMPR-4	Quartz, muscovite, kaolinite
35	KMPR-6	Quartz, muscovite, albite
36	KMPR-8	Quartz, albite, tremolite, muscovite
37	KMPR-21	Quartz, albite, clinochlore
38	KMPR-34	Quartz, muscovite, calcite, kaolinite
39	KMPR-41	Quartz, chlorite, albite
40	KMPR-48	Quartz, muscovite
41	KMPR-49	Quartz, muscovite, pyrite
42	KMPR-51	Quartz, albite, actinolite
43	KMPR-64	Quartz, pyrite, muscovite, chlorite, montmorillonite

44	KMPR-67	Quartz, albite, clinochlore, muscovite
45	KMPR74	Quartz, albite, actinolite, clinochlore
46	KMPR77a	Quartz, muscovite
47	KMPR87	Quartz, muscovite, kaolinite

Appendix G – Mineralogical content of selected samples defined by SWIR analyses.

No.	Sample code	Mineral phases
1	KMSP-1	Muscovitic Illite, Mg-chlorite
2	KMSP-2	Muscovite
3	KMSP-3	Muscovite
4	KMSP-4a	Kaolinite, illite, muscovite, goethite
5	KMSP-4b	Kaolinite, illite, muscovite, goethite
6	KMSP-9	Paragonite, jarosite, Mg-chlorite, goethite
7	KMSP-10	Muscovite
8	KMSP-11	Muscovitic illite, Fe-Mg chlorite
9	KMSP-12	Palygorskite, gypsum
10	KMSP-13	Muscovitic illite, Mg chlorite
11	KMSP-14	Muscovitic illite, Mg chlorite
12	KMSP-15	Kaolinite, hematite
13	KMSP-18	Paragonite, montmorillonite
14	KMSP-19	Montmorillonite, siderite
15	KMSP-20	Muscovite, Mg-chlorite
16	KMSP-21	Paragonite, montmorillonite
17	KMSP-23	Paragonie, montmorillonite, siderite
18	KMSP-24	Muscovitic illite, Fe-Mg chlorite
19	KMSP-27	K-alunite
20	KMSP-28	K-alunite
21	KMSP-29	Na-alunite
22	KMSP-30	Na-alunite
23	KMSP-31	Na-alunite
24	KMSP-33	Fe-Mg chlorite
25	KMSP43	Montmorillonite, ankerite
26	KMSP50	Muscovitic illite, montmorillonite
27	KMSP51	Muscovitic illite
28	KMSP57	Epidote
29	KMSP58	Kaolinite
30	KMSP61	Fe-Mg chorite, montmorillonite
31	KMSP64	Paragonite
32	KMSP65	Pyrophyllite
33	KMSP67	Kaolinite
34	KMSP69	K-alunite
35	KMSP74	Muscovitic illite, pyrophyllite
36	KMSP77	Paragonite
37	KMSP80a	Ankerite, kaolinite
38	KMSP81	Mg chlorite, epidote
39	KMSP87	Epidote, muscovitic illite
40	KMPR-3	Kaolinite, montmorillonite
41	KMPR-6	Fe-Mg chlorite
42	KMPR-15	Muscovitic illite, montmorillonite
43	KMPR-19	Paragonitic Illite, kaolinite, goethite, hematite

44	KMPR-25	Kaolinite, montmorillonite, goethite
45	KMPR-31	Paragonitic illite, kaolinite
46	KMPR-34	Kaolinite
47	KMPR-37	Fe-Mg chlorite, montmorillonite
48	KMPR-38	Fe-Mg chlorite, montmorillonite
49	KMPR-41	Montmorillonite, ankerite
50	KMPR-49	Kaolinite, muscovitic illite
51	KMPR-50	Kaolinite, muscovitic illite
52	KMPR-52	Paragonite, dolomite
53	KMPR-53	Muscovite, kaolinite
54	KMPR-57	Kaolinite, dickite
55	KMPR-64	Montmorillonite, kaolinite, goethite
56	KMPR-67	Muscovitic illite, kaolinite
57	KMPR-68	Fe-Mgchlorite, montmorillonite
58	KMPR68b	Montmorillonite, kaolinite
59	KMPR72	Kaolinite, montmoillonite
60	KMPR74	Fe-Mg chlorite, muscovitic illite
61	KMPR75a	Kaolinite
62	KMPR77a	Muscovite
63	KMPR80	Fe-Mg chlorite
64	KMPR81	Fe-Mg chlorite, montmorillonite
65	KMPR82	Muscovitic illite
66	KMPR83	Muscovite, dolomite
67	KMPR84	Biotite
68	KMPR87	Kaolinite, muscovitic illite
69	KMPR88	Biotite, epidote